

STRUCTURAL HEALTH MONITORING OF THE FIRST GEOSYNTHETIC REINFORCED  
SOIL – INTEGRATED BRIDGE SYSTEM IN HAWAII

A THESIS SUBMITTED TO THE GRADUATE DIVISION OF THE  
UNIVERSITY OF HAWAI‘I AT MĀNOA IN PARTIAL FULFILLMENT  
OF THE REQUIREMENTS FOR THE DEGREE OF

MASTER OF SCIENCE

IN

CIVIL ENGINEERING

MAY 2014

By

Joseph Brandin Lawrence

Thesis Committee:

Phillip Ooi, Chair Person  
Horst G. Brandes  
Peter G. Nicholson

## ABSTRACT

Geosynthetic reinforced soil is defined as closely-spaced ( $\leq 12$  inches; typically 8 inches) alternating layers of geosynthetic reinforcement and compacted soil. A geosynthetic reinforced soil - integrated bridge system (GRS-IBS) consists of three main components; a reinforced soil foundation (RSF), a GRS abutment, and an integrated approach. GRS-IBS is being promoted by the Federal Highway Administration (FHWA) where GRS abutments are used to support single span bridge superstructure in their Everyday Counts Initiative, which is focused on accelerating implementation of proven, market-ready technologies. There are many advantages of GRS abutments over traditional concrete abutment walls but two of the more notable ones are: (1) elimination of the need to form, pour and wait for the concrete to cure resulting in accelerated construction and significant cost savings; and (2) reduced carbon footprint with less concrete and hence cement (production of 1 ton of cement releases 1 ton of CO<sub>2</sub> into the atmosphere) utilized in the abutment walls.

The first GRS-IBS in Hawaii was recently constructed in Lahaina, Maui. The superstructure was instrumented with strain gages to measure the effects of concrete shrinkage and the GRS abutments were instrumented to measure footing vertical pressures, lateral pressures behind the end wall and the GRS facing, bridge footing settlement and lateral displacement of the GRS facing. All gages were monitored remotely with the aid of a data acquisition system. From the recorded data, it was observed that (1) the bridge superstructure continually undergoes thermal expansion and contraction; (2) overall the superstructure compressive strains tend to increase and the end wall lateral pressures tend to decrease with time, which is an indication of superstructure concrete shrinkage; (3) the total footing settlement did not exceed 0.9 inch at the time of writing; (4) the measured pressures underneath the footing are consistent with the estimated stress from the superstructure; during construction and (5) the footing cyclically undergoes rotation about a transverse axis causing the vertical pressures to fluctuate cyclically while the lateral pressures behind the bridge end wall are also undergoing pressure cycles consistent with the effects of thermal loading. A finite element analysis was performed to compare results with the measured field data. The analysis yielded nearly identical trends for footing settlement and facing lateral pressure. This helped verify that the observed trends and measured values are reasonable.

## **ACKNOWLEDGMENTS**

The author would like to thank the Federal Highway Administration (FHWA) for sponsoring this research through their Innovative Bridge Research and Deployment program. Input from Mr. Michael Adams (FHWA) on the design of the instrumentation system was invaluable, for which the author is greatly indebted. The author would also like to thank Ms. Melia Iwamoto for helping with installation and data collection throughout the project. Lastly, Professor Ooi for his advice and support throughout the entire investigation

The author acknowledges KSF Inc. for designing the GRS-IBS over the Kauaula Stream. The assistance and coordination provided by the contractor Goodfellow Brothers Inc. with installation and protection of the instruments is invaluable and greatly appreciated. Geokon Inc. helped troubleshoot the data acquisition system, for which the author is most grateful. The review of this work by the thesis committee consisting of Professors Phillip Ooi, Horst Brandes, and Peter Nicholson is also greatly appreciated.

## Table of Contents

Abstract.....	ii
Acknowledgments.....	iii
1 Introduction.....	1
1.1 Overview.....	1
1.2 Benefits.....	1
1.3 Objectives.....	4
1.4 Organization.....	5
2 Literature Review.....	6
2.1 Material.....	6
2.1.1 Facing Elements.....	6
2.1.2 Backfill Material.....	9
2.1.3 Geosynthetics.....	10
2.2 Lateral Earth Pressure on Wall Facing.....	11
2.2.1 Wu (2007).....	12
2.2.2 Soong and Koerner (1997).....	13
2.2.3 German Geotechnical Society (2011).....	14
2.3 Mechanically Stabilized Earth versus Geosynthetic Reinforced Soil.....	15
2.3.1 Reinforcement spacing.....	15
2.3.2 Reinforcement Length.....	15
2.3.3 Vertical Capacity.....	16
2.3.4 Deformations.....	17
2.3.5 Reinforcement Rupture.....	19
2.3.6 Reinforcement Pullout.....	20
2.3.7 Connection Requirement.....	20
2.3.8 Limiting Eccentricity.....	20
2.4 Case Studies of Monitored Bridges on GRS Abutments.....	21
3 Kauaula Stream Bridge.....	31
3.1.1 Project Overview.....	31
3.1.2 Subsurface Stratigraphy.....	35
3.1.3 GRS Abutment Materials.....	35
3.1.4 Construction Sequence.....	39



4	Instrumentation .....	51
4.1	Pressure Cells.....	51
4.1.1	Vertical Earth Pressure Cells .....	55
4.1.2	Nano concrete tiles.....	57
4.1.3	Lateral Earth Pressure Cells .....	61
4.2	Inclinometer .....	64
4.3	Strain Gage.....	71
4.4	Deformation Meter.....	77
4.5	PVC pipe and Cable Layout.....	81
4.6	Data Acquisition System.....	86
4.6.1	Layout .....	87
4.6.2	Datalogger.....	89
4.6.3	AVW200 and AVW206 Modules.....	89
4.6.4	Multiplexer.....	90
4.6.5	Radio modem .....	91
4.6.6	Cellular modem.....	92
4.6.7	Solar panel power supply .....	92
4.7	Software .....	94
4.8	Total Station.....	94
5	Data Analysis .....	96
5.1	Vertical Pressure Below Footing .....	96
5.1.1	Vertical Pressures During Construction.....	96
5.1.2	Post-Construction Vertical Pressures.....	98
5.2	Settlement .....	103
5.3	Lateral Pressure.....	104
5.3.1	CMU .....	104
5.3.2	End Wall .....	119
5.4	Lateral Displacement of Facing Blocks .....	130
5.4.1	Displacements During Construction .....	130
5.4.2	Post-Construction Displacements .....	133
5.5	Superstructure Strain.....	138
5.5.1	Concrete Cylinder .....	138

5.5.2	Wearing Surface.....	139
5.5.3	Precast Planks .....	140
5.5.4	Tub Girders .....	140
5.5.5	Strain Gage Temperature .....	154
5.6	Verification of GRS-IBS Behavior.....	157
6	Finite Element Analysis .....	160
6.1	Software and Model Parameters .....	160
6.2	Modeling the Construction Sequence .....	163
6.3	Comparison of Calculated and Measured Behavior.....	168
7	Summary and Conclusions .....	172
7.1	Project Summary.....	172
7.2	Conclusions.....	172
7.3	Main Contributions .....	175
7.4	Recommendations for Future Research .....	176
8	References.....	177
	APPENDIX A: BORING LOGS (Hirata and associates, 2009).....	181
	APPENDIX B: TECHNICAL SHEET (Mirafi, 2014) .....	194
	APPENDIX C: SAMPLE CALCULATIONS.....	195

## List of Figures

Figure 1 Typical GRS-IBS Cross Section (Adams et al. 2011a) .....	2
Figure 2 Rigid, Partially Deformable and Flexible Facing Elements (German Geotechnical Society, 2011) .....	7
Figure 3 GRS Walls with Different Facings. (Wu, 1994).....	8
Figure 4 CMU Blocks Commonly Used as Facing for GRS abutments (Adams et al. 2011b) .....	9
Figure 5 Recommended Gradations for Well-Graded and Open Graded Granular Backfill (Adams et al. 2011b) .....	10
Figure 6 (a) A Rigid Block with no Lateral Deformation, Versus (b) a Reinforced Soil Mass (Wu et al. 2010) .....	11
Figure 7 Bin Pressure Diagram (Wu, 2001) .....	12
Figure 8 Wall Facing Stresses due to Non-Reinforced Backfill Zones (Soong and Koerner, 1997).....	13
Figure 9 Photograph of a GRS Performance Test Before Loading (Adams et al. 2011a).....	16
Figure 10 Comparison of Performance Test Results and In-Service Settlement of GRS Abutments (Adams et al. 2011b).....	17
Figure 11 Comparison of Predicted Lateral Deformation to Measured Data for an In-Service GRS Abutment (Adams et al. 2011b).....	18
Figure 12 Schematic of the Instrumented GRS Integrated Bridge System (Warren et al. 2010) .....	22
Figure 13 Schematic of Olympic Avenue GRS Bridge Abutment in Buchanan County, Iowa with Geosynthetic Wrapped Sheets Flexible Facing (Vennapusa et al. 2012) .....	24
Figure 14 Abutment Settlement Readings (Vennapusa et al. 2012) .....	24
Figure 15 Plan View of the 250 <sup>th</sup> Street Bridge Abutments in Buchanan County, Iowa (Vennapusa et al. 2012) .....	25
Figure 16 Cross-Sectional View of the GRS Fill Material (Vennapusa et al. 2012) .....	26
Figure 17 Plan View of the Concrete Footing (Vennapusa et al. 2012) .....	26
Figure 18 Location of Kauaula Stream Bridge .....	32
Figure 19 Original Design (Kai Hawaii, Inc. 2011).....	33
Figure 20 Valued Engineered Design (KSF Inc. 2011) .....	34
Figure 21 GRS Backfill .....	35
Figure 22 Grain Size Distribution of GRS Backfill .....	37
Figure 23 Compaction Curve of Backfill Finer than 3/4" .....	37
Figure 24 Mohr Coloumb Failure Envelope for GRS backfill .....	38
Figure 25 Maui CMU Block .....	39
Figure 26 Drilling Hole for Inclinator Casing.....	40
Figure 27 Backfill Placement on Abutment 2.....	41
Figure 28 Compaction of Backfill Using a Hand Tamper .....	41
Figure 29 Compaction of Backfill by Vibratory Roller .....	42
Figure 30 Nuclear Gage Testing .....	42
Figure 31 Geosynthetic Burned Through Using a Torch.....	43
Figure 32 Styrofoam Placed in Front of Abutment 1 Prior to Placement of Rip Rap .....	44
Figure 33 Completed Abutment 2 with Concrete Footing.....	44
Figure 34 Concrete Floor Pour for Tub Girder .....	46
Figure 35 Precast Concrete Plank Layout (KSF, Inc. 2011).....	46

Figure 36 Hydraulic lift Raising the Tub Girder onto Two Steel Beams used as a Guide .....	47
Figure 37 Large Backhoe Pushing Tub Girder .....	47
Figure 38 Placement of Precast Concrete Planks on Tub Girders .....	48
Figure 39 End Walls and Wing Walls Completed.....	48
Figure 40 Integrated Approach Construction.....	49
Figure 41 Completed GRS-IBS at Kauauala Stream.....	50
Figure 42 Abutment 1 Fatback Layout .....	52
Figure 43 Abutment 2 Fatback layout.....	53
Figure 44 Abutment 2 Earth Pressure Cell Layout .....	54
Figure 45 Geokon 4800 Earth Pressure Cell (Geokon Inc. 2013) .....	55
Figure 46 Shallow Hole for Earth Pressure Cells .....	56
Figure 47 Earth Pressure Cells Placed on a Flat Layer of Sand.....	56
Figure 48 Nano Concrete Tile.....	57
Figure 49 Locations of Nano Concrete Tiles at Abutment 1 .....	58
Figure 50 Locations of Nano Concrete Tiles at Abutment 2 .....	59
Figure 51 Nano Concrete Tiles Set Down on Plastic Sheeting Which Was Then Folded Over To Sandwich Them .....	60
Figure 52 Geokon 4810 Lateral Earth Pressure Cell (Geokon Inc. 2013) .....	62
Figure 53 Fatback Cell Fastened to CMU Block.....	63
Figure 54 Sand Placed in Front of Fatback Cell for Protection .....	63
Figure 55 Fatback Cells Fastened to End Wall.....	64
Figure 56 Geokon 6300 Inclinometer (Geokon Inc. 2013).....	65
Figure 57 Geokon Glue-Snap Inclinometer Casing (Geokon Inc. 2013).....	66
Figure 58 Abutment 1 Inclinometer Layout .....	67
Figure 59 Abutment 2 Inclinometer Layout .....	68
Figure 60 Inclinometer Casing Protruding Above Ground.....	70
Figure 61 Inclinometers Installed into Glue-Snap Casing .....	70
Figure 62 Geokon 4200 Concrete Embedded Strain Gage (Geokon Inc. 2013).....	72
Figure 63 Abutment 1 Strain Gage Layout.....	73
Figure 64 Abutment 2 Strain Gage Layout.....	74
Figure 65 Concrete Cylinder.....	75
Figure 66 Strain Gage Fastened to Rebar Using Plastic Straps .....	76
Figure 67 Strain Gage Cables Daylighting from the Floor of the Tub Girder .....	77
Figure 68 Geokon 4430 Deformation Meter (Geokon Inc. 2013) .....	78
Figure 69 Abutment 1 Deformation Meter Layout.....	79
Figure 70 Abutment 2 Deformation Meter Layout.....	80
Figure 71 Grout Mixture Poured into PVC Pipe Housing Deformation Meter .....	81
Figure 72 PVC Pipe System Under the Middle Tub Girder .....	82
Figure 73 Steel Straps Used to Hold up PVC Pipes .....	82
Figure 74 Typical Layout of PVC Pipe System for Each Abutment.....	83
Figure 75 Typical Cross-Section of Middle Tub Girder's PVC Pipe Layout.....	84
Figure 76 Typical Cross-Section of Outer Tub Girders' PVC Pipe Layout .....	85
Figure 77 J-Box at Abutment 1 Containing the Wireless Transmitters (WT1 on left and WT2 on right)..	88

Figure 78 J-Box at Abutment 2 Containing the Three Multiplexers (Bottom Row) and One Datalogger (Top) .....	88
Figure 79 CR1000 Datalogger (Campbell Scientific Inc. 2013).....	89
Figure 80 AVW200 Module (Campbell Scientific Inc. 2013).....	90
Figure 81 AVW206 Module (Campbell Scientific Inc. 2013).....	90
Figure 82 Vibrating Wire Multiplexer (Geokon Inc. 2013).....	91
Figure 83 RF401 Spread Spectrum Radio (Campbell Scientific Inc. 2013).....	91
Figure 84 Raven X Cellular Modem (Campbell Scientific Inc. 2013) .....	92
Figure 85 One 65 Watt Solar Panel at Abutment 2.....	93
Figure 86 Two 20 Watt Solar Panels at Abutment 1 .....	93
Figure 87 TS11 Leica Total Station (www.surveyequipment.com, 2013) .....	94
Figure 88 Mini-Prism with L-Bracket (www.sccsurvey.co.uk, 2013) .....	95
Figure 89 Vertical Pressure for Each EP Cell During Construction .....	97
Figure 90 Average Vertical Pressure During Construction .....	97
Figure 91 Vertical Pressure as a Function of Time.....	99
Figure 92 Vertical Pressure and Ambient Temperature vs Time.....	100
Figure 93 Dummy EP Cell.....	101
Figure 94 Daily Pressure Fluctuations in EP Cell vs Dummy Cell .....	102
Figure 95 Daily Ambient and Instrument Temperature .....	102
Figure 96 Settlement vs Time .....	103
Figure 97 Measured Lateral Pressures vs Rankine Active, At Rest Pressures, Wu, and Soong and Koerner Estimations (FB 6 at Abutment 1) .....	106
Figure 98 Measured Lateral Pressures vs Rankine Active, At Rest Pressures, Wu, and Soong and Koerner Estimations (FB 7 at Abutment 1) .....	107
Figure 99 Measured Lateral Pressures vs Rankine Active, At Rest Pressures, Wu, and Soong and Koerner Estimations (FB 8 at Abutment 1) .....	107
Figure 100 Abutment 1 Lateral Pressure During Construction .....	110
Figure 101 Abutment 2 Lateral Pressure During Construction .....	110
Figure 102 Abutment 1 Lateral Pressure as a Function of Time .....	114
Figure 103 Abutment 2 Lateral Pressure as a Function of Time .....	114
Figure 104 Ambient Temperature versus Time .....	115
Figure 105 Abutment 1 Lateral Pressure and Ambient Temperature vs Time .....	116
Figure 106 Abutment 2 Lateral Pressure and Ambient Temperature vs Time .....	116
Figure 107 Lateral Pressure vs Temperature .....	117
Figure 108 Measured Pressure vs Gage Temperature.....	118
Figure 109 FB9 Lateral Pressure vs Depth .....	119
Figure 110 FB10 Lateral Pressure vs Depth .....	120
Figure 111 FB11 Lateral Pressure vs Depth .....	120
Figure 112 FB12 Lateral Pressure vs Depth .....	121
Figure 113 FB13 Lateral Pressure vs Depth .....	121
Figure 114 Abutment 1 Outer Tub Girder Lateral Pressures as a Function of Time.....	122
Figure 115 Abutment 1 Middle Tub Girder Lateral Pressures as a Function of Time .....	123
Figure 116 Abutment 2 Outer Tub Girder Lateral Pressures as a Function of Time .....	123

Figure 117 Abutment 2 Middle Tub Girder Lateral Pressures as a Function of Time .....	124
Figure 118 Abutment 1 Outer Tub Girder Lateral Pressure and Ambient Temperature vs Time .....	127
Figure 119 Abutment 1 Middle Tub Girder Lateral Pressure and Ambient Temperature vs Time .....	128
Figure 120 Abutment 2 Outer Tub Girder Lateral Pressure and Ambient Temperature vs Time .....	128
Figure 121 Abutment 2 Middle Tub Girder Lateral Pressure and Ambient Temperature vs Time .....	129
Figure 122 Abutment 1 Middle Tub Girder Instrument and Ambient Temperature vs Time.....	129
Figure 123 Abutment 2 Middle Tub Girder Instrument and Ambient Temperature vs Time.....	130
Figure 124 Lateral Deflection vs Depth During Construction at (a) Abutment 1 and (b) Abutment 2 ....	132
Figure 125 Abutment 1 Lateral Displacement as a Function of Time .....	133
Figure 126 Abutment 2 Lateral Displacement as a Function of Time .....	134
Figure 127 Abutment 1 Lateral Displacement and Ambient Temperature vs Time .....	134
Figure 128 Abutment 2 Lateral Displacement and Ambient Temperature vs Time .....	135
Figure 129 Concrete Cylinder Strain (SG 31) as a Function of Time.....	138
Figure 130 Concrete Cylinder (SG 31) Strain and Ambient Temperature vs Time.....	139
Figure 131 Strain in Top Surface vs Time .....	141
Figure 132 Strain in Pre-Cast Planks vs Time .....	141
Figure 133 Strain in West Walls of Tub Girders vs Time .....	142
Figure 134 Strain in East Walls of Tub Girders vs Time.....	142
Figure 135 Strain in Floors of Tub Girders vs Time.....	143
Figure 136 Wearing Surface Strain and Ambient Temperature vs Time.....	149
Figure 137 Pre-Cast Plank Strain and Ambient Temperature vs Time.....	150
Figure 138 West Wall Strain and Ambient Temperature vs Time.....	150
Figure 139 East Wall Strain and Ambient Temperature vs Time .....	151
Figure 140 Tub Girder Floor Strain and Ambient Temperature vs Time .....	151
Figure 141 Temperatures in Tub Girder 3 on Abutment 1 Side .....	154
Figure 142 Temperatures in Tub Girder 2 on Abutment 1 Side .....	155
Figure 143 Temperatures in Tub Girder 1 on Abutment 1 Side .....	155
Figure 144 Temperatures in Tub Girder 3 on Abutment 2 Side (SG17 in the precast planks stopped working).....	156
Figure 145 Temperatures in Tub Girder 2 on Abutment 2 Side .....	156
Figure 146 Temperatures in Tub Girder 1 on Abutment 2 Side .....	157
Figure 147 Vertical Pressure Variation Over One Day .....	158
Figure 148 Lateral Pressure Variation Over One Day .....	159
Figure 149 Abutment Fill's $E_{50}$ as a Function of Depth .....	161
Figure 150 Construction Sequence .....	168
Figure 151 Predicted vs Measured Displacements .....	170
Figure 152 Calculated vs Measured Lateral Pressures on the Facing.....	170
Figure 153 Calculated vs Measured Settlement.....	171

## List of Tables

Table 1 Summary of in-service GRS-IBS and their Cost Benefits (Adams et al. 2011a, Warren et al. 2012, Venapusa et al. 2012).....	3
Table 2 Adjustment Factors (German Geotechnical Society, 2011).....	14
Table 3 Summary of Monitored Bridges Founded on GRS.....	28
Table 4 Construction sequence and timeline .....	39
Table 5 Components of the Data Acquisition System .....	86
Table 6 List of Instruments Terminating at Abutment 2.....	87
Table 7 List of Instruments Terminating at Abutment 1.....	87
Table 8 Calculated Vertical Pressure vs Measured Pressure .....	98
Table 9 Estimated Weights of Bridge Components.....	98
Table 10 Monthly Summary of Vertical Pressure .....	99
Table 11 Settlement Recorded .....	104
Table 12 Rankine Active and At Rest Earth Pressures (FB6) .....	108
Table 13 Rankine Active and At Rest Earth Pressures (FB7) .....	108
Table 14 Rankine Active and At Rest Earth Pressures (FB8) .....	109
Table 15 Abutment 1 Wu and Soong and Koerner Lateral Pressures.....	109
Table 16 Abutment 1 Measured Lateral Pressure .....	111
Table 17 Abutment 2 Measured Lateral Pressure .....	111
Table 18 Monthly Average Lateral Pressure .....	113
Table 19 Monthly Lateral Pressure Range.....	113
Table 20 Abutment 1 End Walls Average Lateral Pressure .....	125
Table 21 Abutment 1 End Walls Lateral Pressure Range.....	125
Table 22 Abutment 2 End Walls Average Lateral Pressure .....	126
Table 23 Abutment 2 End Walls Lateral Pressure Range.....	126
Table 24 Abutment 1 Average Lateral Displacement.....	136
Table 25 Abutment 1 Lateral Displacement Range .....	136
Table 26 Abutment 2 Average Lateral Displacement.....	137
Table 27 Abutment 2 Lateral Displacement Range .....	137
Table 28 Concrete Cylinder (SG 31) Strain Monthly Summary.....	139
Table 29 Average Strain in Wearing Surface .....	144
Table 30 Range of Strains in Wearing Surface.....	144
Table 31 Average Strain in Precast Planks .....	145
Table 32 Range of Strains in Precast Planks.....	145
Table 33 Average Strain in West Walls of Tub Girders .....	146
Table 34 Range of Strains in West Walls of Tub Girders.....	146
Table 35 Average Strain in East Walls of Tub Girders .....	147
Table 36 Range of Strains in East Walls of Tub Girders .....	147
Table 37 Average Strain in Floors of Tub Girders .....	148
Table 38 Range of Strains in Floors of Tub Girders.....	148
Table 39 Comparison of Measured and Calculated Strains Over Half a Temperature Cycle.....	153
Table 40 Material Input Parameters for Finite Element Analysis.....	162
Table 41 Geotextile Input Parameters for Finite Element Analysis.....	163

# 1 INTRODUCTION

## 1.1 Overview

The majority of highway bridges constructed today are supported on deep foundations (Adams et al. 2011a). However, deep foundations are costly and often require specialty contractors to construct. The Federal Highway Administration (FHWA), during the Bridge of the Future initiative, developed the Geosynthetic Reinforced Soil Integrated Bridge System (GRS-IBS) (Adams et al. 2011a) to minimize costs for constructing single span bridges throughout the United States. If deep foundations are not required, the GRS-IBS can be an attractive option because it requires no specialty contractors and can be constructed quicker than conventional concrete cantilever abutment wall-supported bridges.

GRS-IBS consists of three main components; a reinforced soil foundation (RSF), a GRS abutment, and an integrated approach (Figure 1). The RSF is constructed using compacted granular fill reinforced with geosynthetics. The purpose of the RSF is to provide embedment and increase the bearing width and capacity. The GRS abutment is constructed using alternating layers of compacted granular fill and  $\leq 12$ -inch (typically 8-inch)-spaced layers of geosynthetic reinforcement. Every layer of reinforcement is frictionally connected to the facing element, which is typically a concrete masonry unit (CMU) block. The top 3 to 4 facing elements are normally pinned and grouted. The reinforcement spacing in the top 5 courses is usually halved to meet serviceability requirements in the lateral direction. The integrated approach is also constructed using GRS. It creates a transition to the superstructure and alleviates the “bump-at-the-end-of-the-bridge” that is caused by differential settlement of the abutment and the approach roadway.

## 1.2 Benefits

GRS-IBS is cost effective since common materials and construction techniques are utilized to build a bridge rather expeditiously. The speedy construction can be attributed to its simplicity and flexibility of the design as well as availability of off-the-shelf materials and equipment. The faster construction time causes less road closures, disruptions, and lower labor costs. GRS-IBS also has the potential for reduced maintenance costs due to elimination of the “bump-at-the-end-



of-the-bridge” as well as fewer parts (bridge bearings and joints) to maintain. The potential savings can range from 25-60% compared to a conventional bridge as summarized in Table 1.

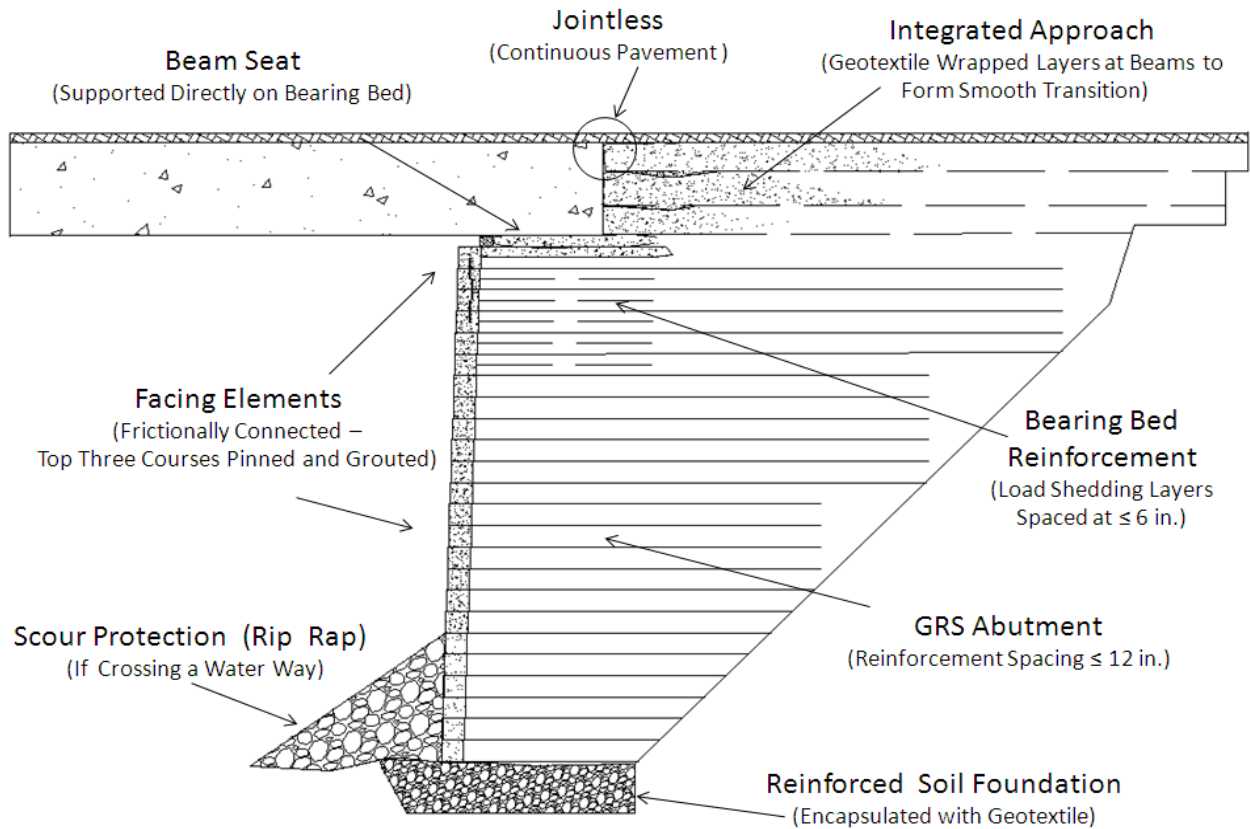


**Figure 1 Typical GRS-IBS Cross Section (Adams et al. 2011a)**

Advantages of choosing GRS-IBS over conventional bridges include (Adams et al 2011a, Wu et al 2006):

- Reduced carbon footprint with less concrete and hence cement (production of 1 ton of cement releases 1 ton of CO<sub>2</sub> into the atmosphere) utilized in the conventional reinforced concrete abutment walls
- GRS abutment flexibility causing more tolerance to foundation settlement
- Construction is rapid and does not require any specialty contractors
- Lateral earth pressures are much lower behind the GRS abutment compared to conventional reinforced concrete abutment.

- GRS abutments, when properly designed and constructed, alleviate differential settlement between foundation and approach roadway.
- GRS abutments, when properly designed and constructed, are very stable and have high ductility. This means that GRS abutments are less likely to experience sudden catastrophic collapses compared to conventional reinforced concrete abutments.
- Construction is less dependent on weather than conventional bridges.
- Design is flexible and can be easily modified for unseen site conditions.

**Table 1 Summary of in-service GRS-IBS and their Cost Benefits (Adams et al. 2011a, Warren et al. 2012, Venapusa et al. 2012)**

Road Name	Year	Bridge Length (ft)	Project Cost	
			GRS Option	Conventional
Bowman (Defiance County, Ohio)	2005	82	\$259,000	\$338,000
			Savings: \$79,000 (23% reduction)	
Glenburg (Defiance County, Ohio)	2006	52	\$159,000	\$180,000
			Savings: \$21,000 (12% reduction)	
Fountain Street (Defiance County, Ohio)	2006	37	\$104,000	\$137,500
			Savings: \$33,500 (24% reduction)	
Behnfeldt (Defiance County, Ohio)	2006	54	\$120,600	\$157,600
			Savings: \$37,000 (23% reduction)	
Farmer Mark (Defiance County, Ohio)	2006	32	\$78,800	\$120,900
			Savings: \$42,100 (35% reduction)	
Vine Street (Defiance County, Ohio)	2006	33	\$85,800	\$118,000
			Savings: \$32,200 (27% reduction)	
Tiffin River (Defiance County, Ohio)	2010	140	\$890,000	\$1,190,000
			Savings: \$300,000 (25% reduction)	
Olympic Avenue (Buchanan County, Iowa)	2010	73	\$48,500	\$105,000
			Savings: \$56,500 (54% reduction)	
250th Street (Buchanan County, Iowa)	2010	69	\$43,000	\$105,000
			Savings: \$62,000 (59% reduction)	

### 1.3 Objectives

Due to the infancy of this technology, it is imperative to monitor and analyze the behavior of any new GRS-IBS. In this research, an instrumentation system was designed and installed to monitor the behavior of the first GRS-IBS in Hawaii built over the Kauaula Stream in Lahaina, Maui.

The following are the research objectives:

- a. Perform a literature review on GRS-IBS.
- b. Design a remote monitoring system to gage the performance of the new GRS-IBS crossing at Kauaula Stream in Lahaina, Maui consisting of the following instruments:

<b>Instrument</b>	<b>Purpose is to Measure</b>
Earth Pressure Cells (EP) and Nanoconcrete Tiles	Bearing pressure on the GRS below the footing of the south abutment.
Total Station and Prisms	Settlement of the GRS-IBS during and post-construction.
Deformation meters	Compression over the depth of the GRS.
Inclinometer	Lateral deflection of the facing blocks
Lateral Pressure Cells (Fatback “FB” Cells)	Horizontal stresses on the facing blocks along the bridge centerline. It is known that the lateral pressure behind a GRS abutment is less than in a conventional retaining wall. Also, horizontal stresses on the bridge end wall at the centerline and at both ends to study the effects of skew, if any.
Strain gages	Strains in the superstructure during and post-construction.

- c. Design, purchase, install and monitor instruments during and post-construction. Major construction events that can impact instrumentation readings will be monitored and documented.
- d. Report the observed behavior of the GRS-IBS and the associated major construction events in a final report

## 1.4 Organization

This report is organized as follows:

- Chapter 2 contains a literature review on GRS-IBS. This chapter describes the materials needed to build a GRS-IBS, presents proposed methods of estimating lateral pressures acting on the facing blocks, discusses differences between mechanically stabilized earth (MSE) and GRS, and summarizes case studies of other GRS-IBS.
- Chapter 3 presents construction details of the Kauaula stream GRS-IBS.
- Chapter 4 describes the instruments used to monitor the GRS-IBS, their layout and installation. It also describes the data acquisition hardware, software, and configuration for remote monitoring.
- Chapter 5 discusses the data collected during and post-construction.
- Chapter 6 describes a finite element analysis conducted on the GRS-IBS. This analysis is compared to the field data gathered.
- Chapter 7 contains the summary, conclusions and recommendations for future research.
- The Appendix contains boring logs for the Kauaula Stream Bridge, data sheets provided by the manufacturers for the geosynthetic reinforcement, and calculations for material properties used in the finite element analysis.

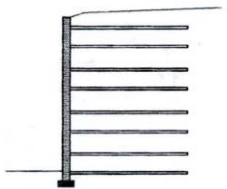
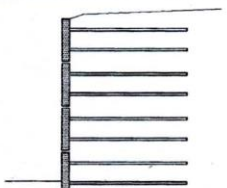
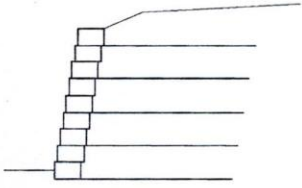
## 2 LITERATURE REVIEW

### 2.1 Material

GRS abutment construction is simple and can be summarized in 3 steps that are essentially repeated until the finish wall height is reached: (1) Place a row of facing elements, (2) Tamp a layer of compacted granular fill behind the facing, and (3) Unroll a layer of geosynthetic reinforcement on top of the facing and granular fill. Not included above is that the top few courses of facing are pinned and grouted and the backfill is more heavily reinforced to meet serviceability requirements in terms of lateral deflection. The materials utilized in each of the three steps are not proprietary and are easily obtainable. They are described in the following sub-sections.

#### 2.1.1 Facing Elements

The main purpose of the facing element is to provide a form for compacting the granular fill and prevent the soil from sloughing due to surface water runoff and/or rain. The German Geotechnical Society (2011) categorized facing elements as: (a) rigid or non-deformable; (b) partially deformable; or (c) flexible or deformable (Figure 2). Rigid facing elements can be, but not limited, to pre-cast concrete or cast-in-place concrete walls. Wrapped geosynthetic sheets are considered flexible while gabions, timbers, or concrete blocks that are not rigidly attached are considered partially deformable. Various types of facing elements summarized by Wu (1994) are shown in Figure 3.

Type of facing element	Description
<b>Non-deformable facing elements</b>	
 <p>Full height panels</p>	The elements are pre-manufactured such that they cover the entire height of the reinforced retaining structure in one piece.
 <p>Partial height panels</p>	Partial height panels are usually 1 m to 2 m high and 100 mm to 200 mm thick.
 <p>Block elements, moulded bricks</p>	Facing elements of precast concrete blocks (e.g. modular blocks, segmented blocks) or connected natural stones.

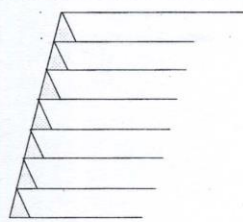
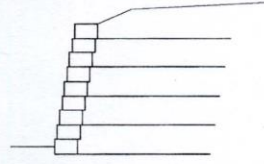
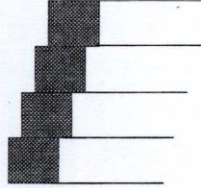
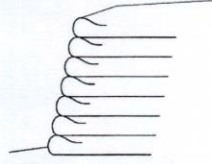
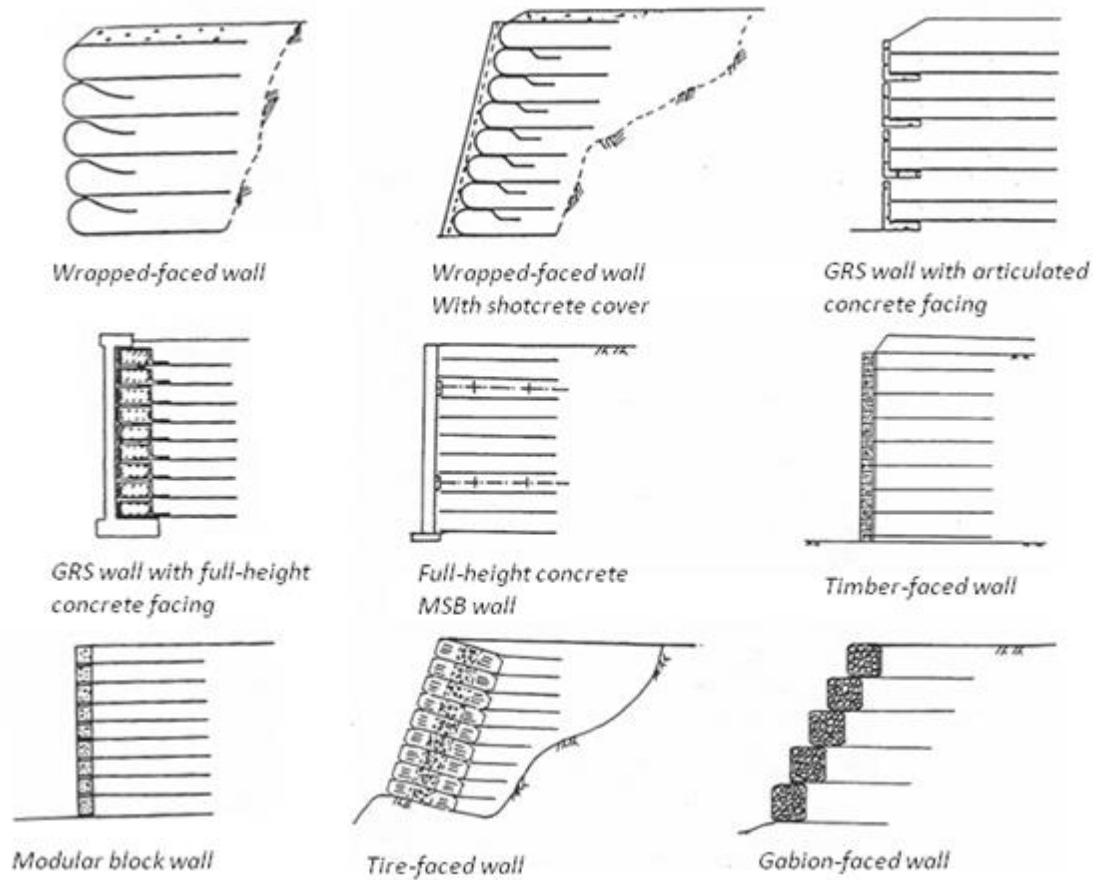
<b>Partially deformable facing elements</b>	
 <p>Welded steel wire mesh</p>	Facing elements made from open, welded steel wire mesh sections and designed to fit the angle of the slope.
 <p>Block elements, moulded bricks</p>	Facing elements of precast concrete blocks (e.g. modular blocks, segmented blocks) or natural stones which can move relative to each other.
 <p>Gabions</p>	Gabions are usually manufactured from galvanised, welded wire mesh and filled with stones or crushed rock. The gabion dimensions are generally between 0.5 m to 1.0 m high, 2 m to 3 m long and 0.5 m to 1.0 m deep.
<b>Deformable facing elements</b>	
 <p>Wrap-around method</p>	Wrap-around method or padded wall method. The full width of the reinforcement protrudes from the front of the reinforced fill structure and wrapped around the front of a layer of fill material.

Figure 2 Rigid, Partially Deformable and Flexible Facing Elements (German Geotechnical Society, 2011)



**Figure 3 GRS Walls with Different Facings. (Wu, 1994)**

Japan Railways constructed numerous GRS bridge abutments using rigid facing elements (Tateyama et al. 1994; Tatsuoka, 1997). These GRS abutments experienced little deformation under service as well as earthquake loads. Numerous GRS bridge abutments using partially deformable {although Wu et al. (2006) termed them as flexible} facing have been constructed and investigated in the US. These bridge abutments were reported to exhibit satisfactory deformations under service loads (Wu et al. 2006).

Abutment construction utilizing rigid facing elements tend to be more time consuming and expensive than the non-rigid variety. Therefore, split face concrete masonry unit (CMU) with nominal dimensions of 8 inches by 8 inches by 16 inches are increasingly being used as a facing

element for GRS-IBS (Adams et al. 2012). They are lightweight, economical, and are likely to ensure compaction in every 8–inch-thick lift (Figure 4).



**Figure 4 CMU Blocks Commonly Used as Facing for GRS abutments (Adams et al. 2011b)**

### ***2.1.2 Backfill Material***

Adams et al. (2011b) provide the following guidelines for selection of an appropriate backfill material:

- Should consist of crushed hard, durable particles of fragments of stone or gravel and be free from organic or deleterious material or other soft particles that have poor durability
- Should be well-graded or open graded (Figure 5)
- Should have angular particles and have a friction angle not less than 38°



- Maximum particle size should not exceed 2 inches to avoid damage to the geosynthetic while compacting
- Should be easily compacted, have the ability to drain, and have good workability.

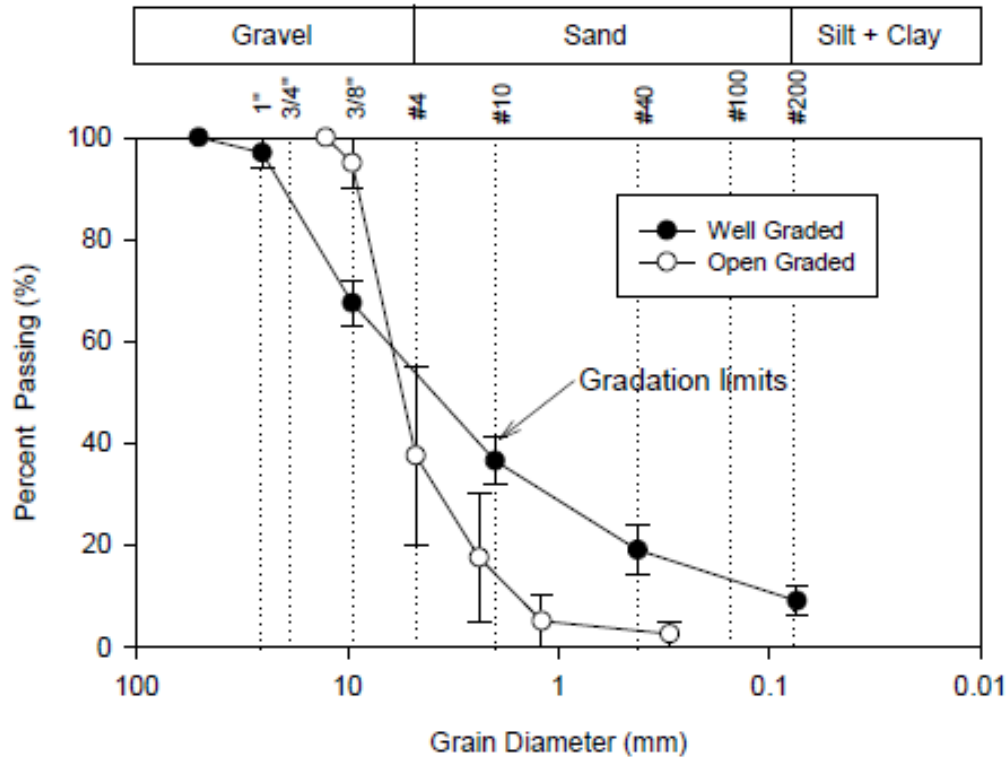


**Figure 5 Recommended Gradations for Well-Graded and Open Graded Granular Backfill (Adams et al. 2011b)**

### 2.1.3 Geosynthetics

As of 2012, all in service GRS-IBSs utilized biaxial woven polypropylene (PP) geotextile (Adams et al. 2011b). This type of geotextile is low cost, easy to place, and has the ability to provide the friction connection between the facing blocks and the geosynthetic. Adams et al. (2011b) recommended the following requirements for the geosynthetic material:

- Should have an ultimate wide width tensile strength of at least 4,800 lb/ft in accordance with ASTM D4595 for geotextiles and ASTM D6637 for geogrids
- Should use biaxial geosynthetic to eliminate construction placement errors and ensure approximately the same strength in both directions

- Should have documented sliding coefficients for various soil types or project specific soils in accordance with ASTM D 5321
- Should follow industry standards on the hydrolysis resistance of polyester, oxidative resistance of PP and high density polyethylene, and stress cracking resistance of HDPE for all components of the geosynthetic
- Should have minimum UV resistance when measured in accordance with ASTM D4355

## 2.2 Lateral Earth Pressure on Wall Facing

The lateral earth pressure acting on a GRS facing may not follow classical earth pressure theory. This is because the reinforcement restrains the soil from moving laterally. If a rigid body undergoes no lateral deformation under its own weight and external loads (Figure 6a), then a facing placed in front of it would not experience any lateral pressure from the rigid body. In reality, the reinforced soil mass is not infinitely rigid. Hence, the lateral pressure on the facing is not zero. Instead, they can be estimated using the procedures described below.

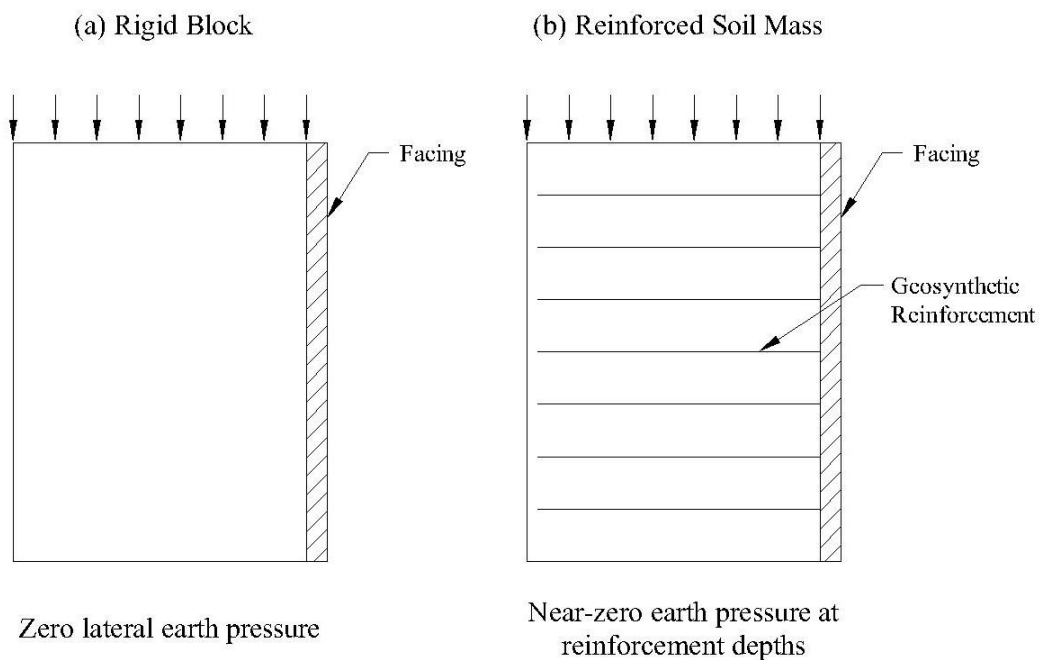


**Figure 6 (a) A Rigid Block with no Lateral Deformation, Versus (b) a Reinforced Soil Mass (Wu et al. 2010)**

### 2.2.1 Wu (2007)

Wu (2007) postulated based on evidence from numerous case studies that the lateral thrust against the facing is independent of the wall height. Since the reinforcement effectively restrains lateral deformation of the soil, the lateral pressure on the facing is quite small in comparison to the lateral stress predicted from classical earth pressure theory. Its magnitude depends on the reinforcement spacing, the soil shear strength parameters and the rigidity of the facing. Termed "bin pressure," Wu (2001) proposed that the bin pressure diagram is near zero at the reinforcement elevation and increases with depth below the reinforcement before decreasing to near zero at the reinforcement layer below (i.e.; at the base of the facing). However, because the reinforcement may deform slightly and there may be imperfect bonding between the soil and reinforcement at the wall face, Wu (2001) proposed the bin pressure diagram as shown in Figure 7. The lateral thrust is estimated using Equation 1 (Wu, 2001) and is a function of the reinforcement spacing and the soil strength parameters.

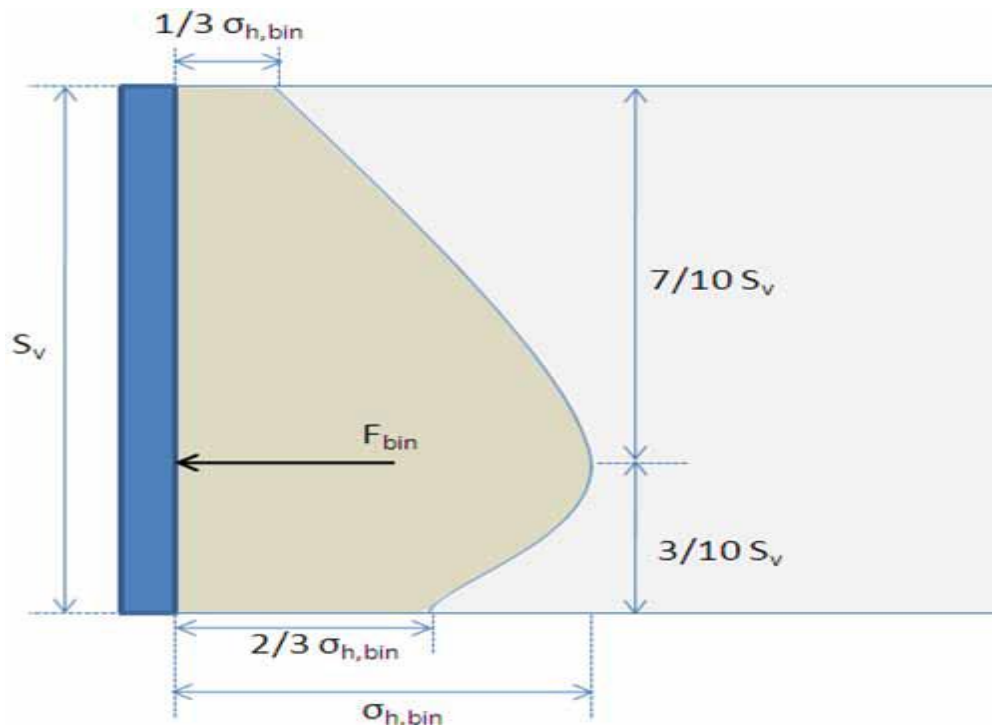


Figure 7 Bin Pressure Diagram (Wu, 2001)

$$F = 0.72\gamma S_v^2 \tan^2(45^\circ - \phi/2) \quad (1)$$

where  $\gamma$  = unit weight of soil,  $S_v$  = reinforcement spacing and  $\phi$  = friction angle of soil.

### 2.2.2 Soong and Koerner (1997)

Soong and Koerner (1997) proposed another way of evaluating the lateral pressure on the facing when the reinforcement is connected to the middle of the back of the facing as shown in Figure 8. While the reinforcements stabilize most of the soil mass through interface friction, Soong and Koerner (1997) postulated that there is a small zone of soil bearing against the wall facing that is not restrained by the reinforcement-mobilized friction. Assuming that each layer acts independently from those above and below, they proposed a lateral earth pressure distribution as shown in Figure 8. The magnitude of the connection force can be estimated using Equation 2.

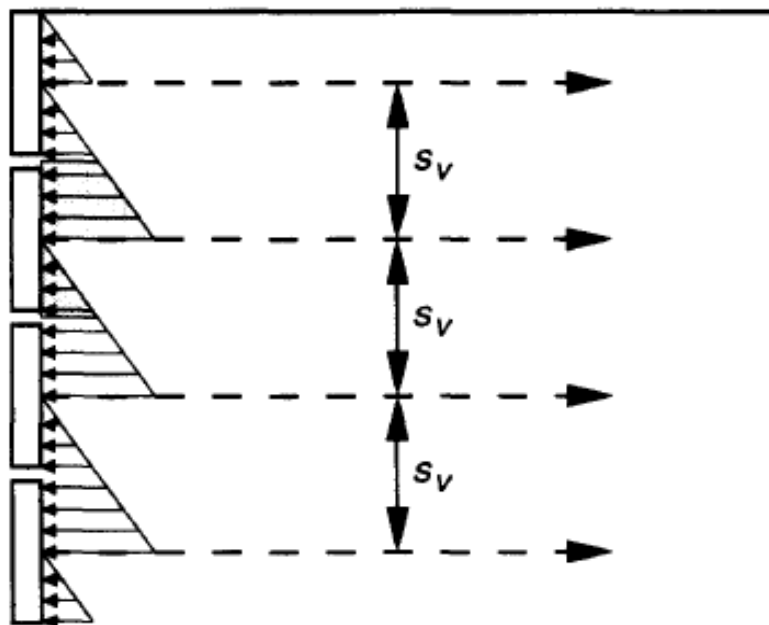


**Figure 8 Wall Facing Stresses due to Non-Reinforced Backfill Zones (Soong and Koerner, 1997)**

$$F = 0.5\gamma S_v^2 \tan^2(45^\circ - \phi/2) \quad (2)$$

Soong and Koerner's (1997) proposed thrust is approximately 69% of the value proposed by Wu (2001).

### 2.2.3 German Geotechnical Society (2011)

Unlike the recommendations of Soong and Koerner and Wu, the German Geotechnical Society (2011) proposed Equation 3 that estimates a facing lateral pressure ( $\sigma_{\text{facing}}$ ) that increases with depth. Equation 3 can be utilized for non-deformable or rigid, partially deformable and deformable or flexible facing elements through the use of different adjustment factors as summarized in Table 2 (German Geotechnical Society, 2011).

$$\sigma_{\text{facing}} = \eta_g \cdot K_{\text{ag}} \cdot \gamma \cdot H \cdot \gamma_g + \eta_q \cdot K_{\text{aq}} \cdot q \cdot \gamma_q \cdot S_v \quad (3)$$

where  $\eta_g, \eta_q$  = adjustment factors (Table 2)

$K_{\text{ag}}$  = Coulomb active lateral pressure coefficient for soil

$\gamma$  = soil unit weight

$\gamma_g, \gamma_q$  = load factors found in German Standard DIN 1054 where  $\gamma_g$  = load factor for soil weight = 1.35 and  $\gamma_q$  = load factor for surcharge = 1.5

$K_{\text{aq}}$  = Coulomb active lateral pressure coefficient for surcharge

$q$  = surcharge

$S_v$  = reinforcement spacing

**Table 2 Adjustment Factors (German Geotechnical Society, 2011)**

	Adjustment Factor		Wall Friction Angle	
	$\eta_g$		$\eta_q$	$\delta$
	$0 < h \leq 0.4H$	$0.4H < h \leq H$		
Non-deformable facing elements	1	1	1	Analogous to DIN 4085
Partially deformable facing elements	1	0.7	1	$1/3\phi$ to $1\phi$
Deformable facing elements	1	0.5	1	0

$h$  = depth below top of reinforced soil

$H$  = Wall height

## **2.3 Mechanically Stabilized Earth versus Geosynthetic Reinforced Soil**

Mechanically stabilized earth (MSE) walls and abutments differ from GRS in 8 different aspects: (1) reinforcement spacing, (2) reinforcement length, (3) vertical capacity, (4) deformations, (5) reinforcement strength, (6) pullout, (7) connection requirements, and (8) limiting eccentricity.

### ***2.3.1 Reinforcement spacing***

According to the American Association of State Highway and Transportation Officials (AASHTO 2010) and the FHWA's Geotechnical Engineering Circular (GEC) No. 11 (Berg et al. 2009), the maximum reinforcement spacing for MSE is 0.8 m (32 inches). There is no limit on having a smaller spacing, but there is no incentive for doing so. This is due to the code suggesting that a 0.2-m-(8-inch-)spacing with 70 kN/m (4800 lb/ft) reinforcement strength will behave the same as a system with a 0.6-m-(24-inch-)spacing and 210 kN/m (14400 lb/ft) reinforcement strength. On the other hand, the maximum reinforcement spacing for a GRS is 12 inches (Adams et al. 2011a and b). Due to the closely spaced reinforcement, the GRS exhibits a composite behavior. The GRS reinforcement in addition to providing tensile resistance also lowers lateral deformation, increases lateral confinement, suppresses soil dilation during shear, enhances locked in compaction induced stresses, increases ductility of the soil mass, and reduces migration of fines. Consequently, the bearing capacity of footings on a GRS is larger and the lateral thrusts on a GRS facing are smaller than those for a MSE.

### ***2.3.2 Reinforcement Length***

MSE abutment specifications require the reinforcement length to be at least 70% of the wall height unless the MSE is underlain by a competent foundation stratum ( $SPT-N > 50$  blows/ft). However for a GRS-IBS, the reinforcement can be as low as 30% of the wall height or 6.0 ft, whichever is greater (Adams et al. 2011a and b). The length of the reinforcement does not have to be uniform throughout the height of the abutment. The length and schedule is to be determined by external stability (i.e. direct sliding, bearing capacity and global stability).

### 2.3.3 Vertical Capacity

One of the major differences between GRS and MSE is the availability of a procedure to estimate the vertical bearing capacity of a footing supported on a GRS. This is not provided for in MSE specifications. Performance testing or mini-pier experiments (Figure 9) are large-scale laboratory tests on a GRS column that has the same backfill strength, reinforcement, and facing elements as a GRS wall in the field (Adams et al. 2011a). A database of these performance tests can be used to validate a semi-empirical expression derived by Pham (2009) for estimating the bearing capacity of a footing on a GRS wall (Equation 4).



**Figure 9 Photograph of a GRS Performance Test Before Loading (Adams et al. 2011a).**

$$q_{ult} = \left( \sigma_h + 0.7 \frac{s_v}{d_{max}} \frac{T_f}{S_v} \right) K_p + 2c \sqrt{K_p} \quad (4)$$

where  $q_{ult}$  = nominal vertical footing bearing capacity on a GRS wall

$\sigma_h$  = lateral stress

$S_v$  = reinforcement spacing

$d_{max}$  = maximum aggregate size

$T_f$  = ultimate wide width reinforcement tensile strength

$K_p$  = Rankine passive earth pressure coefficient

c = soil cohesion.

For a GRS wall with CMU facing,  $\sigma_h$  = lateral stress exerted by the facing on the GRS mass, defined by Pham (2009) as:

$$\sigma_h = \gamma_{bl} D \tan \delta \tag{5}$$

where  $\gamma_{bl}$  = bulk unit weight of facing block = weight of block/volume of block assuming it is not hollow, D = depth of facing block perpendicular to the wall face and  $\delta$  = friction angle between geosynthetic reinforcement and the top and bottom surface of the facing block.

### 2.3.4 Deformations

Vertical deformation or settlement of a loaded GRS wall can be estimated using a stress-strain curve from an appropriate performance test. This method has been verified by 5 in-service GRS-IBSs in Defiance County, Ohio (Figure 10).

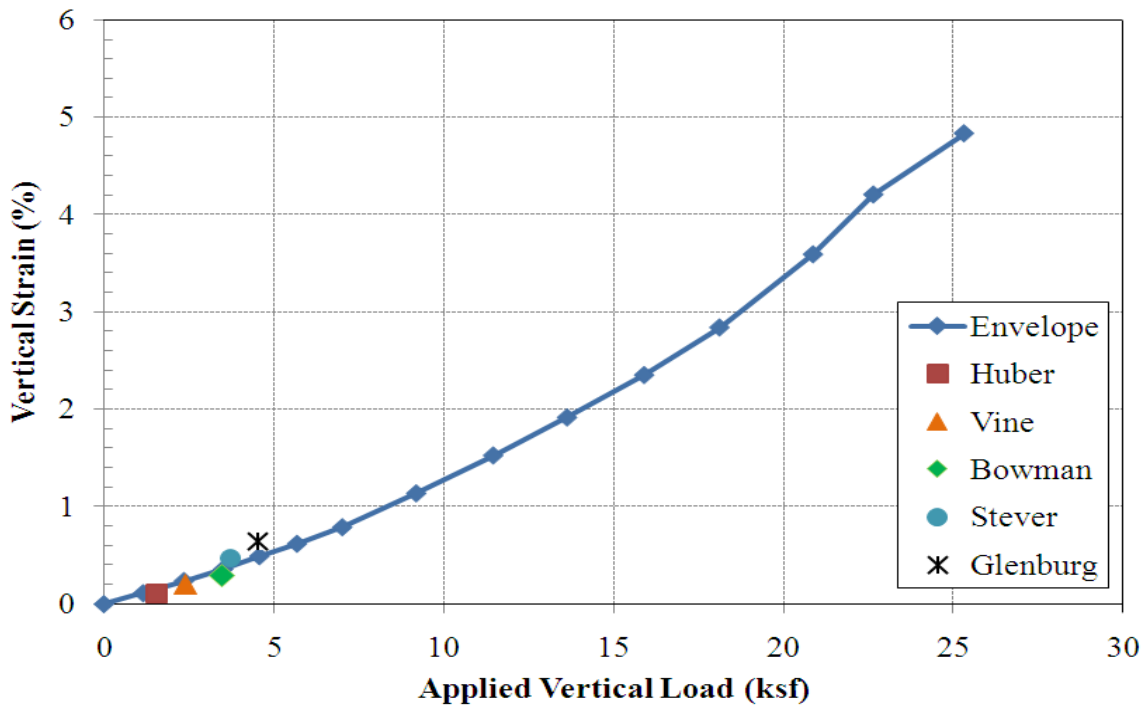


**Figure 10 Comparison of Performance Test Results and In-Service Settlement of GRS Abutments (Adams et al. 2011b)**



Lateral deformation is estimated using the vertical deformation from the performance test coupled with the theory of zero volume change proposed by Adams et al. (2002) which states that the volume of soil pushed vertically down by the footing is equal to the volume of soil pushed outward laterally. The resulting lateral deformation is as follows:

$$\rho_h = \frac{2b_{q,vol}\rho_v}{H} \quad (6)$$

$\rho_h$  = maximum lateral deformation

$b_{q,vol}$  = setback distance from wall to edge of footing plus the bearing width

$\rho_v$  = maximum vertical deformation

H = height of the abutment.

The postulate of zero volume change has been shown to be valid for GRS structures over a large range of stresses (Figure 11).

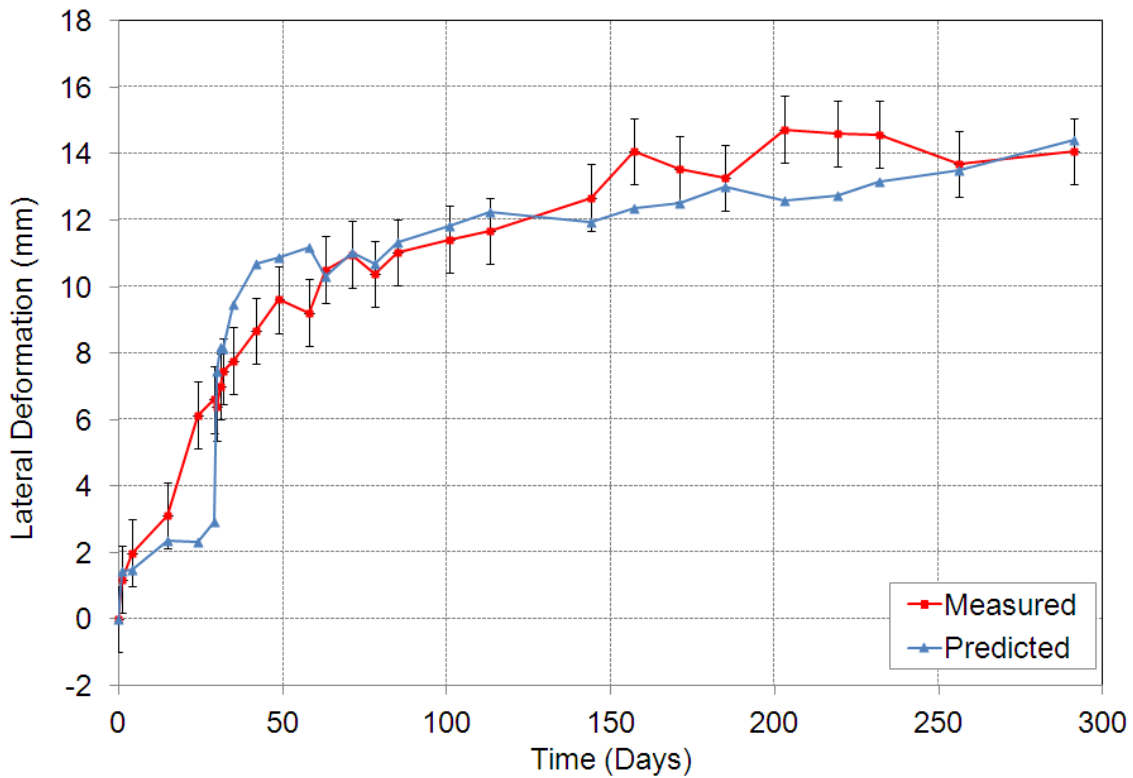


**Figure 11 Comparison of Predicted Lateral Deformation to Measured Data for an In-Service GRS Abutment (Adams et al. 2011b)**

### 2.3.5 Reinforcement Rupture

In the current bridge design specifications for MSE (AASHTO 2010 and Berg et al. 2009), the maximum factored reinforcement tension ( $T_{\max}$  defined in Equation 7) must be less than the factored reinforcement tensile resistance ( $T_r$  defined in Equation 8).

$$T_{\max} = \sigma_h S_v \quad (7)$$

$$T_r = \frac{\psi T_f}{RF_{ID} \times RF_{CR} \times RF_D} \quad (8)$$

where  $\sigma_h$  = factored lateral earth pressure at the reinforcement layer calculated using classical earth pressure theories for the soil ignoring the reinforcement

$S_v$  = reinforcement spacing

$\psi$  = resistance factor for the reinforcement wide width tensile strength

$T_f$  = ultimate reinforcement wide width tensile strength

$RF_{ID}$  = installation damage reduction factor

$RF_{CR}$  = creep reduction factor

$RF_D$  = durability reduction factor.

For GRS-IBS design, Adams et al. (2011a) proposed that the following two criteria need to be met. First, the required reinforcement strength (Equation 9 intended for cohesionless backfill) must be lower than the allowable reinforcement strength (Equation 10). Second, the required reinforcement strength must be lower than the reinforcement strength at 2% strain (Adams et al. 2011a).

$$T_{req} = \left( \frac{\sigma_h}{\frac{S_v}{0.7 \cdot 6d_{\max}}} \right) S_v \quad (9)$$

$$T_{all} = \frac{T_f}{3.5} \quad (10)$$

where  $T_{req}$  = required reinforcement strength

$\sigma_h$  = factored lateral earth pressure at the reinforcement layer

$S_v$  = reinforcement spacing

$d_{max}$  = maximum grain size

$T_{all}$  = factored long-term reinforcement strength

$T_f$  = ultimate reinforcement wide width tensile strength.

Adams et al. (2011a) utilized a single factor of safety of 3.5 when estimating  $T_{all}$  instead of 3 separate reduction factors for  $T_f$  and a load factor for  $\sigma_h$  as required in AASHTO.

### **2.3.6 Reinforcement Pullout**

MSE guidelines require internal stability with respect to the pullout mode of failure (AASHTO 2010, Berg et al. 2009). On the other hand pullout failure is not considered a possible failure mode for GRS (Adams et al. 2011b). This is due to the belief that closely spaced reinforcements make the GRS mass behave more as a composite material. Also, no pull out failure has been observed in numerous GRS performance tests loaded to failure.

### **2.3.7 Connection Requirement**

MSE design practice requires the connection strength between the reinforcement and the facing to be larger than the maximum tension in the reinforcement caused by lateral earth pressures. GRS design does not have this requirement (Adams et al. 2011b). The lateral earth pressures are low on the facing elements (as explained in Section 2.2). Therefore a frictional connection is sufficient, eliminating the need for mechanical connections (Adams et al. 2011b).

### **2.3.8 Limiting Eccentricity**

In the current AASHTO Bridge Design Specifications, the practice of calculating the ratio of stabilizing moment to overturning moment as a check for overturning of bridge abutments and

MSE walls has been replaced by the resultant location (or limiting eccentricity) criteria coupled with a check for bearing pressure. AASHTO limits the resultant force for walls with footing on soil and rock to lie within the middle third and middle half, respectively for allowable stress design or ASD (middle half and middle three quarter for LRFD).

The base of a GRS mass is relatively flexible and the notion that it can support bending stresses with tensile contact pressures for liftoff developing (i.e.; when the resultant force lies outside the middle third) seems counterintuitive. Therefore, overturning about the toe caused by earth pressures behind the GRS and/or loading on its top is not deemed a possibility. No overturning failures have been observed in MSE or GRS. Lastly, in a GRS-IBS, the bridge superstructure acts as a giant strut that restrains any overturning from occurring.

#### **2.4 Case Studies of Monitored Bridges on GRS Abutments**

Construction related information and measured performance of three instrumented in-service bridges on GRS, the Tiffin River Bridge in Ohio (Warren et al. 2010), Olympic Avenue Bridge in Iowa (Vennapusa et al. 2012) and 250<sup>th</sup> Street Bridge in Iowa (Vennapusa et al. 2012) are described in detail below. Table 3 is a summary of these three bridges as well as other bridges on GRS abutments that were monitored predominantly for movements.

##### *Tiffin River Bridge, Ohio (Warren et al. 2010)*

The Tiffin River Bridge is currently the longest in-service GRS-IBS at a span of 140 ft (Adams et al. 2011a). The north and south abutment heights are 18 feet and 20.5 feet, respectively. For the top 5 feet of each abutment, solid core CMU blocks were utilized to prevent freeze-thaw conditions. The remainder of the abutment height utilized hollow core CMU blocks. The backfill used was AASHTO No. 89 crushed stone that was compacted to at least 95% relative compaction. Two different types of geotextile reinforcement were utilized. The primary geotextile used for every layer had a wide width tensile strength equal to 70 kN/m (4800 lb/ft). The secondary geotextile, which was installed between the primary reinforcements, had a wide width tensile strength equal to 35 kN/m (2400 lb/ft) (Figure 12).

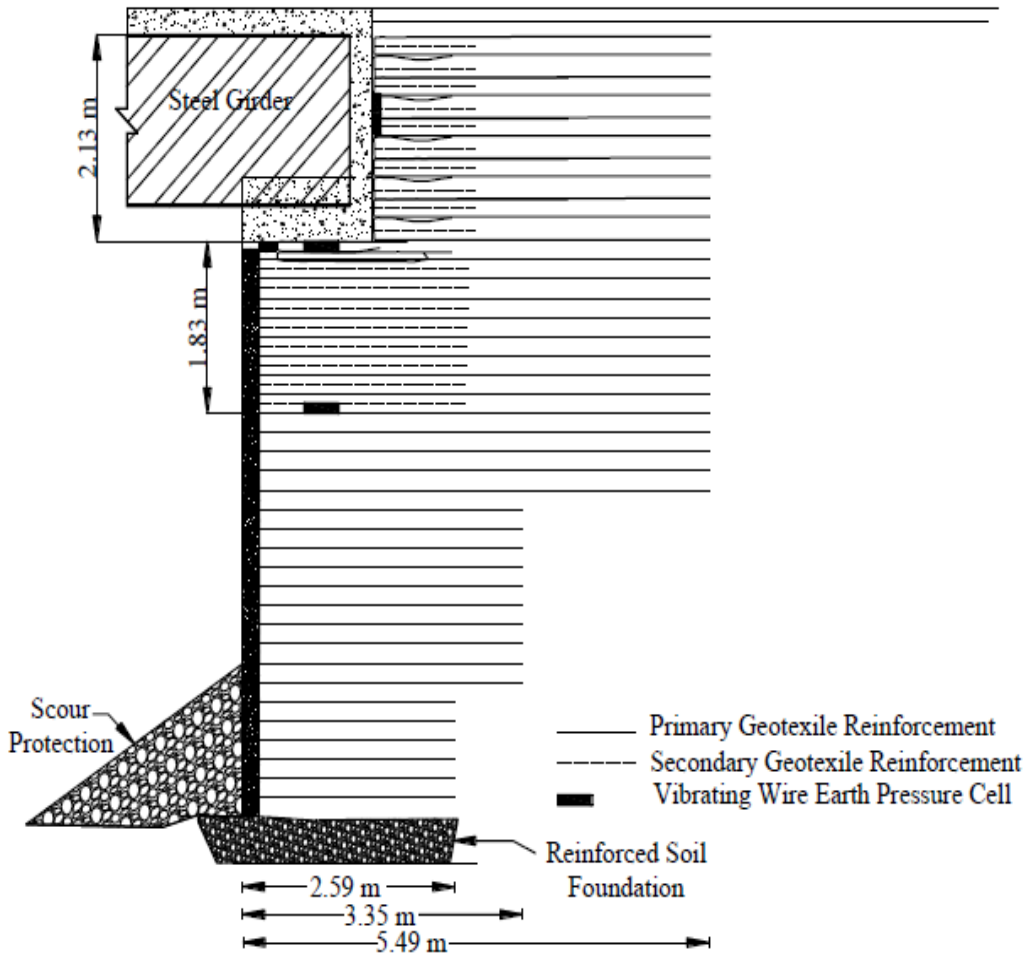


**Figure 12 Schematic of the Instrumented GRS Integrated Bridge System (Warren et al. 2010)**

Three different types of vibrating wire instruments were installed in the GRS-IBS during construction. First, earth pressure cells were installed to measure the vertical pressure under the footing at two depths: 6 feet below the girder footing and directly below the girder footing (Figure 12). Second, lateral earth pressure cells were installed at the mid-height of the bridge rear wall to measure the lateral pressure at each bridge end (Figure 12). Third, strain gages were installed on the steel girders to evaluate the variation of strain during thermal cycles. All the instruments installed were connected to a datalogger and modem which allowed the instruments to be monitored remotely.

Based on the measured data over a span of 10 months, the following conclusions were made:

- As the temperature increased, the steel expanded and increased the lateral pressure on the GRS abutment wall.
- The vertical pressure was inversely proportional to the strain temperature. As the steel girder expanded, the vertical pressures decreased slightly.
- The measured strains increased with increasing temperature and vice versa.

*Olympic Avenue Bridge, Buchanan County, Iowa (Vennapusa et al. 2012)*

The Olympic Avenue Bridge has a span of 73 feet and was built to replace an existing timber abutment back wall bridge. The GRS abutment consisted of compacted backfill wrapped in layers of geosynthetic, and was sloped with a grouted rip rap facing for scour protection (Figure 13). The lift thickness of the loose backfill was about 8 inches and the compacted thickness was targeted to be 7 in. The geosynthetic used was Mirafi® 500X, a woven polypropylene geotextile with an ultimate tensile strength of about 1200 lb/ft in the machine direction and 1440 lb/ft in the cross-machine direction.

Bridge abutment elevations were monitored shortly after construction completion for about a year and two months. The elevations were obtained from the north and south abutment footings (Figure 14). The maximum settlement of 0.7 in was observed at the north abutment. No transverse differential settlement was observed in either abutment.

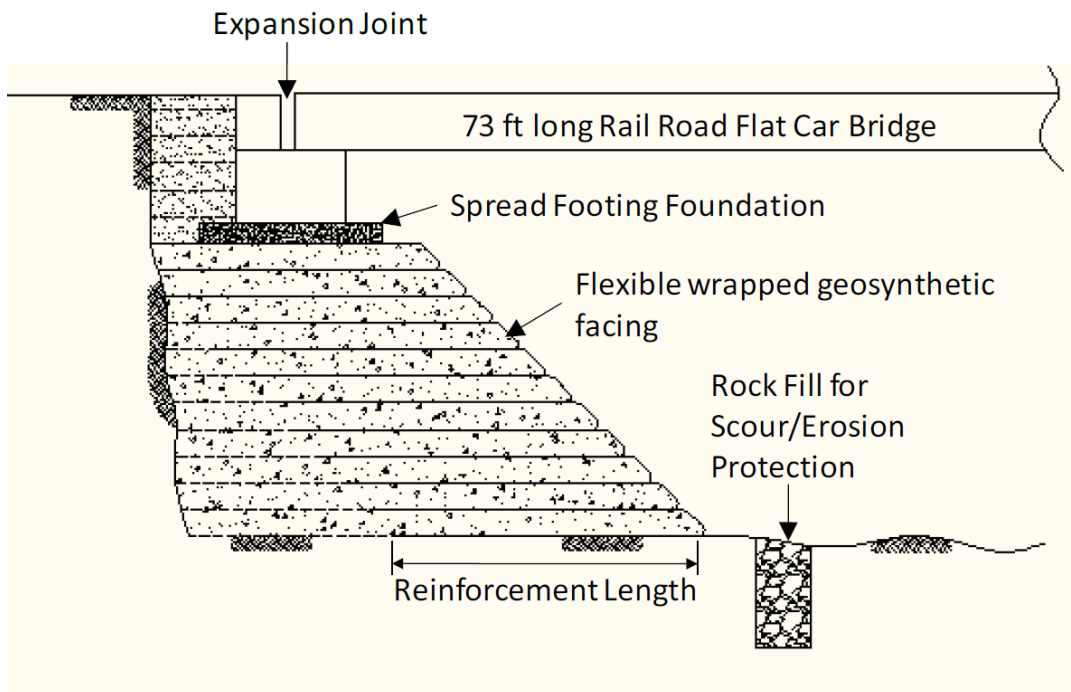


**Figure 13 Schematic of Olympic Avenue GRS Bridge Abutment in Buchanan County, Iowa with Geosynthetic Wrapped Sheets Flexible Facing (Vennapusa et al. 2012)**

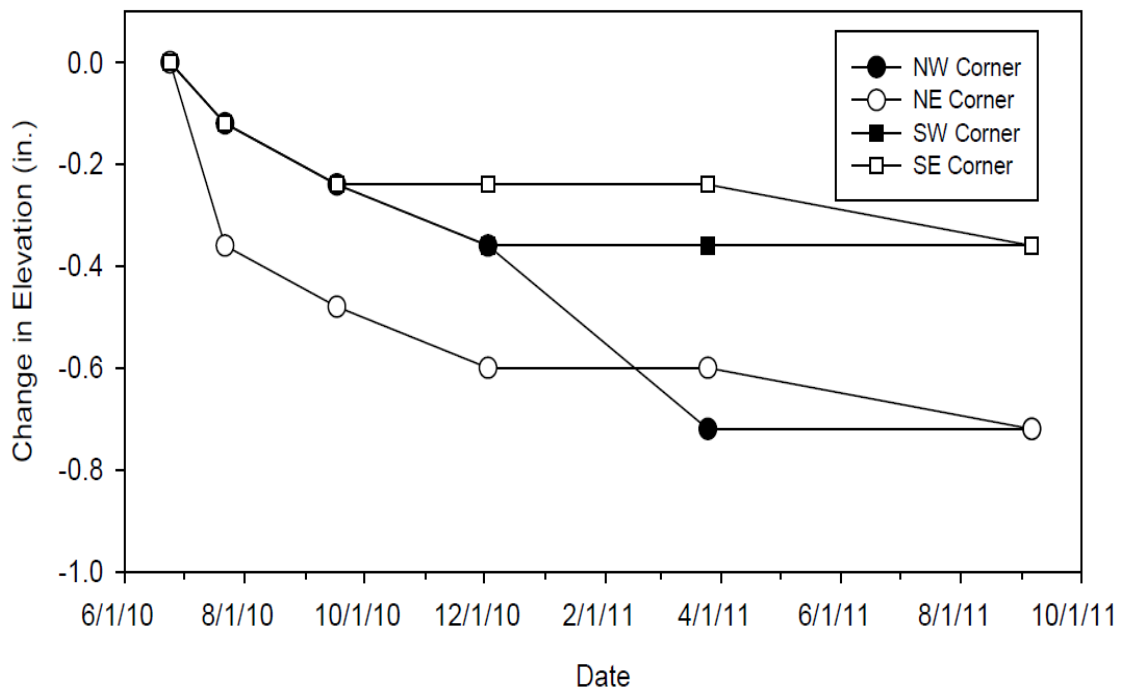


**Figure 14 Abutment Settlement Readings (Vennapusa et al. 2012)**

250<sup>th</sup> Street Bridge, Buchanan County, Iowa (Vennapusa et al. 2012)

The 250<sup>th</sup> Street Bridge is a 69 foot long bridge built on GRS abutments to replace an existing steel bridge. The east and west abutments were built 11 feet away from the previous concrete abutments. A trench of about 7.4 feet wide by 4.6 feet deep was excavated and filled with the GRS abutment (Figure 15). Sheet piles were installed on the north and south portions of the excavation to protect the GRS abutment from scour. The GRS fill material used was well-graded gravel with sand (GW) according to USCS classification system and A-1-a according to the AASHTO classification system. The field relative compaction was on average about 94% based on standard Proctor with an average moisture content of 6.1%. The GRS abutment was constructed in 7 inch lifts of compacted backfill that was wrapped in geosynthetic. Similarly to the Olympic Avenue Bridge, Mirafi® 500X geosynthetic was used.

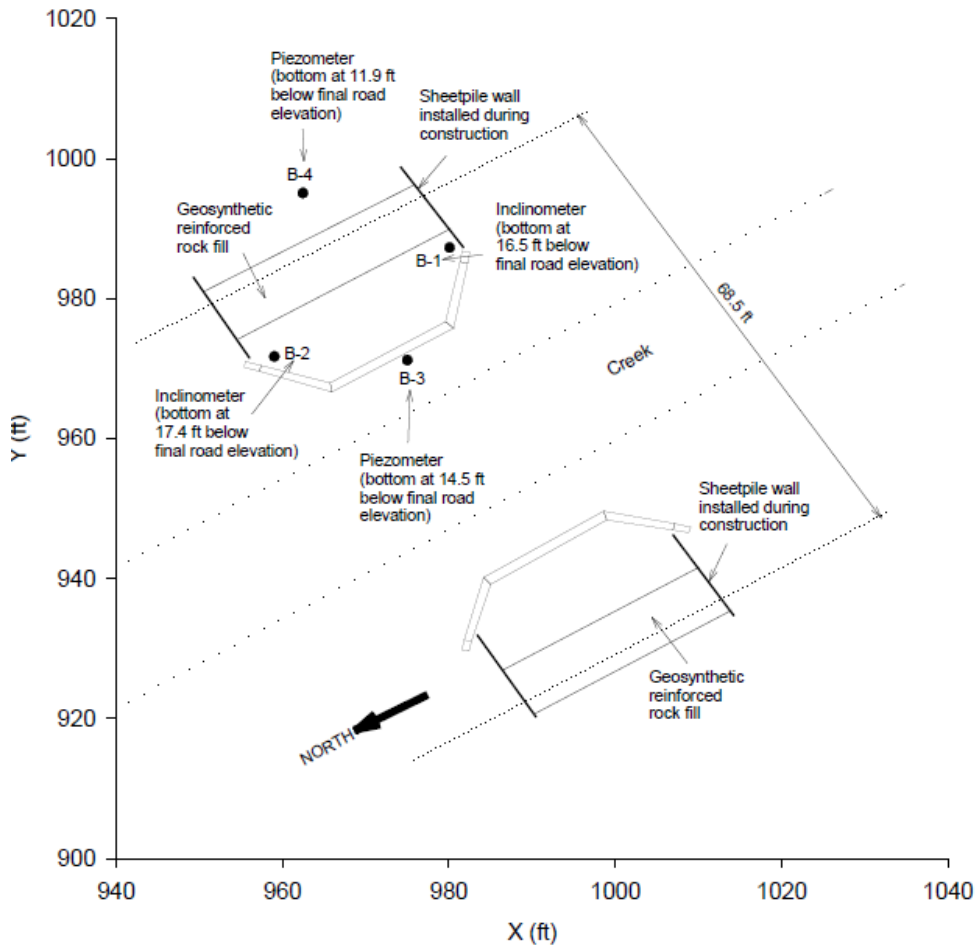
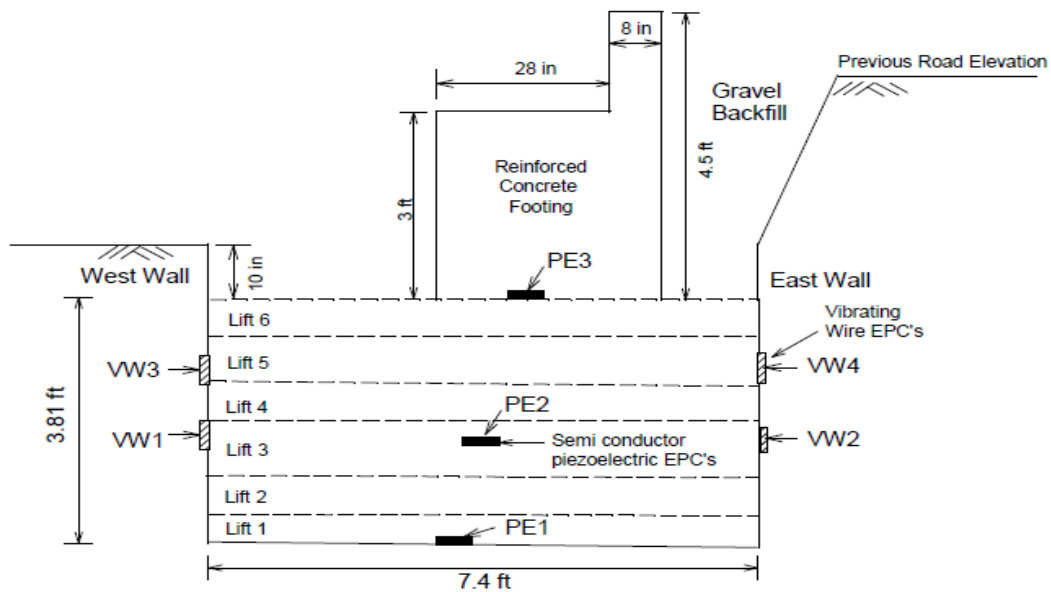


Figure 15 Plan View of the 250<sup>th</sup> Street Bridge Abutments in Buchanan County, Iowa (Vennapusa et al. 2012)



In-situ testing and a yearlong observation of the bridge were conducted. Soil borings were drilled at four locations (B-1 to B-4, Figure 15). Inclinerometers were installed at locations B-1 and B-2 to monitor lateral ground movements during and after construction. Piezometers were installed at B-3 and B-4 to monitor pore water pressures in the foundation soils. Semiconductor earth pressure cells were installed at PE1, PE 2, and PE 3 (Figure 16) under the center of the footing to measure total vertical stress in the abutment. Vibrating wire earth pressure cells were installed at seven locations, two each against the west and east side trench walls to measure the lateral stresses at the interface of GRS fill material and the existing abutment fill (Figure 16). The last three vibrating wire earth pressure cells were installed directly beneath the footing to measure vertical stresses (Figure 17).



**Figure 16 Cross-Sectional View of the GRS Fill Material (Vennapusa et al. 2012)**

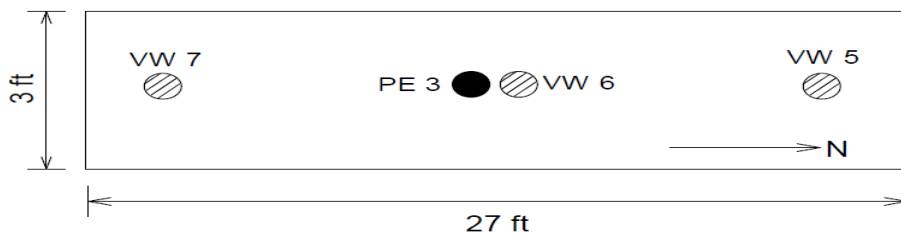


**Figure 17 Plan View of the Concrete Footing (Vennapusa et al. 2012)**

Bridge live load (LL) tests were conducted at three different times; shortly after construction completion, two months after construction completion, and one year after construction completion. LL tests involved driving a loaded test truck with single axle at the front and a tandem axle in the back with a known weight and axle spacing over the bridge. Earth pressure cell readings were then taken when the truck was at specific locations. The loaded truck was also placed at the center of the bridge while the deflections of the bridge were measured using total station survey equipment.

Based on the measured data, the following conclusions were made:

- The earth pressure cells below the footing indicated that the dead load was almost fully transferred down to the bottom of the GRS fill.
- The horizontal to vertical stress ratio was less than 0.25, thus indicating low lateral stress on the soil surrounding the GRS fill material.
- Bridge abutment elevation monitoring since the end of construction to about 1 year after completion of construction indicated maximum settlements of  $\leq 0.7$  inches with transverse differential settlements of  $\leq 0.2$  inches at each abutment.
- Static LL tests indicated non-uniform deflections transversely across the bridge at the center span when the truck was positioned along the edges. This suggests poor load transfer across the bridge. The maximum measured deflection was close to but less than the AASHTO allowable deflection. However, it must be noted that the AASHTO allowable limits are based on a 72 kip three-axle test truck, while the test truck used in this study weighed about 52 to 53 kips.
- Peak increase in vertical stresses in the GRS fill material was observed when the test truck was positioned directly above the footing. Peak increase in lateral stresses in the GRS/existing soil interface was observed when the test truck was positioned directly on or within 20 feet of the footing.

**Table 3 Summary of Monitored Bridges Founded on GRS**

Case	Date Built	Abutment Height	Span	Backfill	Reinf. Type	Reinf. Spacing	Facing Type	Maximum Settlement	Lateral Movement of Wall Face	Note
Founders/ Meadows Bridge <sup>1,2,3</sup>	June 1999	19.36 ft and 14.76 ft	34.5 m (113 ft) for both spans	CDOT class 1 Backfill $c = 0$ $\phi = 39^\circ$ $\gamma = 141 \text{ lb/ft}^3$	Geogrid $T_{ult} = 10.78 \text{ kip/ft}$	16 inches	Mechanically connected CMU blocks	0.43 inches	0.55 inches	First major bridge in the United States built on footings supported by a GRS abutment. Built as a two-span bridge
Lake Mami <sup>1,4</sup>	Fall 2000	3.5 ft to 6.5 ft	67 ft	Poorly Graded Sand (SP)	PPL geotextile with $T_{ult} = 2400 \text{ lb/ft}$	6 inches	Wrapped Geotextile behind an old rock-masonry wall	0.24 inches	Not Reported	
Twin Lakes <sup>1,4</sup>	Fall 2000	Not Reported	71 ft	Poorly Graded Sand (SP)	PPL geotextile with $T_{ult} = 2100 \text{ lb/ft}$	6 inches	Wrapped Geotextile behind an old rock-masonry wall	0.38 inches	Not Reported	

Case	Date Built	Abutment Height	Span	Backfill	Reinf. Type	Reinf. Spacing	Facing Type	Maximum Settlement	Lateral Movement of Wall Face	Note
Bowman Road <sup>1,5</sup>	Oct. 2005	16.91 ft and 16.47 ft	79 ft	$c=0$ $\phi = 48^\circ$ $\gamma = 110$ lb/ft <sup>3</sup>	Woven geotextile with with $T_{ult} = 4800$ lb/ft and $T_{ult} = 2100$ lb/ft	8 inches and 4 inches	CMU Blocks	0.07 ft	0.02 ft	
Vine Street <sup>1</sup>	Oct. 2006	12.36 ft and 10.36 ft	50 ft	Not Reported	Not Reported	Not Reported	CMU Blocks	0.035 ft	0.011 ft	
Glenburg Road <sup>1</sup>	May 2006	13.22 ft and 12.80 ft	30.6 ft	Not Reported	Not Reported	Not Reported	CMU Blocks	0.107 ft	0.027 ft	
Huber Road <sup>1</sup>	Aug. 2007	17.30 ft and 16.16 ft	79 ft	Not Reported	Not Reported	Not Reported	CMU Blocks	0.004 ft	0.005 ft	

Case	Date Built	Abutment Height	Span	Backfill	Reinf. Type	Reinf. Spacing	Facing Type	Maximum Settlement	Lateral Movement of Wall Face	Note
Tiffin River Bridge <sup>1,6</sup>	July 2009	20.52 ft and 18.00 ft	140 ft	$c = 0$ $\phi = 48^\circ$ $\gamma = 110$ lb/ft <sup>3</sup>	Nonwoven geotextile with $T_{ult} = 4800$ lb/ft and $T_{ult} = 2400$ lb/ft	8 inches and 4 inches	Solid core CMU for and Hollow core CMU	Not Reported	0.047 ft	Largest in-service GRS-IBS in the US
Olympic Avenue Bridge <sup>1,7</sup>	July 2010	≈ 6.4 ft	73 ft	Not Reported	Woven geotextile with $T_{ult} = 1200$ lb/ft MD and $T_{ult} = 1400$ CMD	7 inches	Wrapped Geotextile	0.7 inches	Not Reported	
250th Street Bridge <sup>1,7</sup>	Oct. 2010	≈ 3.8 ft	69 ft	$c = 0$ $\phi = 48^\circ$ $\gamma = 110$ lb/ft <sup>3</sup>	Woven geotextile with $T_{ult} = 1200$ lb/ft MD and $T_{ult} = 1400$ CMD	7 inches	Wrapped Geotextile	0.5 inches	0.4 inches	

1. Adams et al. 2011a

2. Abu-Hejleh et al. 2001

3. Abu-Hejleh et al. 2003

4. Keller and Devin 2003

5. Adams et al. 2007

6. Warren et al. 2010

7. Vennapusa et al. 2012

### 3 KAUAULA STREAM BRIDGE

#### *3.1.1 Project Overview*

The Kauaula Stream Bridge forms part of a new access road in Lahaina, Maui (Figure 18) that includes 1.67 miles of roadway, 1 bridge, 1 tunnel and 8 culverts. The single span bridge was originally designed having 7 AASHTO concrete girders as its superstructure supported on reinforced concrete abutments founded on deeply embedded spread footings (Figure 19). However, the Contractor (Goodfellow Brothers) value engineered the bridge to utilize GRS-IBS (Figure 20). UHM personnel were on-site to observe construction as well as install monitoring instruments (EPs, FBs, inclinometers, strain gages, and deformation meters). Bridge construction and instrumentation installation occurred between January 2012 and May 2013.

The Kauaula Stream Bridge has a single 109-foot-long span. It is skewed ( $31^\circ$ ) and super-elevated as shown in Figures 20b and c. The value-engineered bridge was designed having 3 separate tub girders as its superstructure connected by numerous precast concrete planks. A 5-inch-thick cast-in-place topping was poured on the planks to serve as the wearing surface. The tub girders/precast planks/topping are integral with the concrete footing; i.e.; there is a full moment connection between the superstructure and sub-structure.



**Figure 18 Location of Kauaula Stream Bridge**

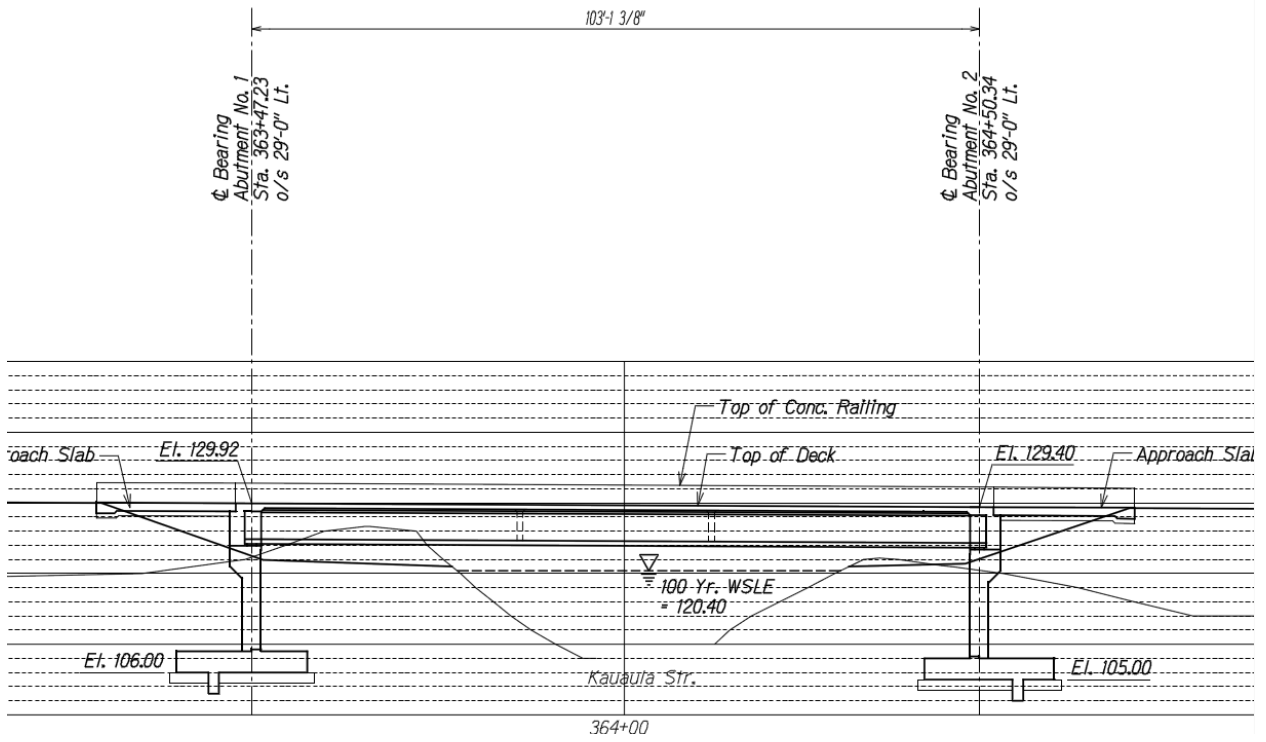
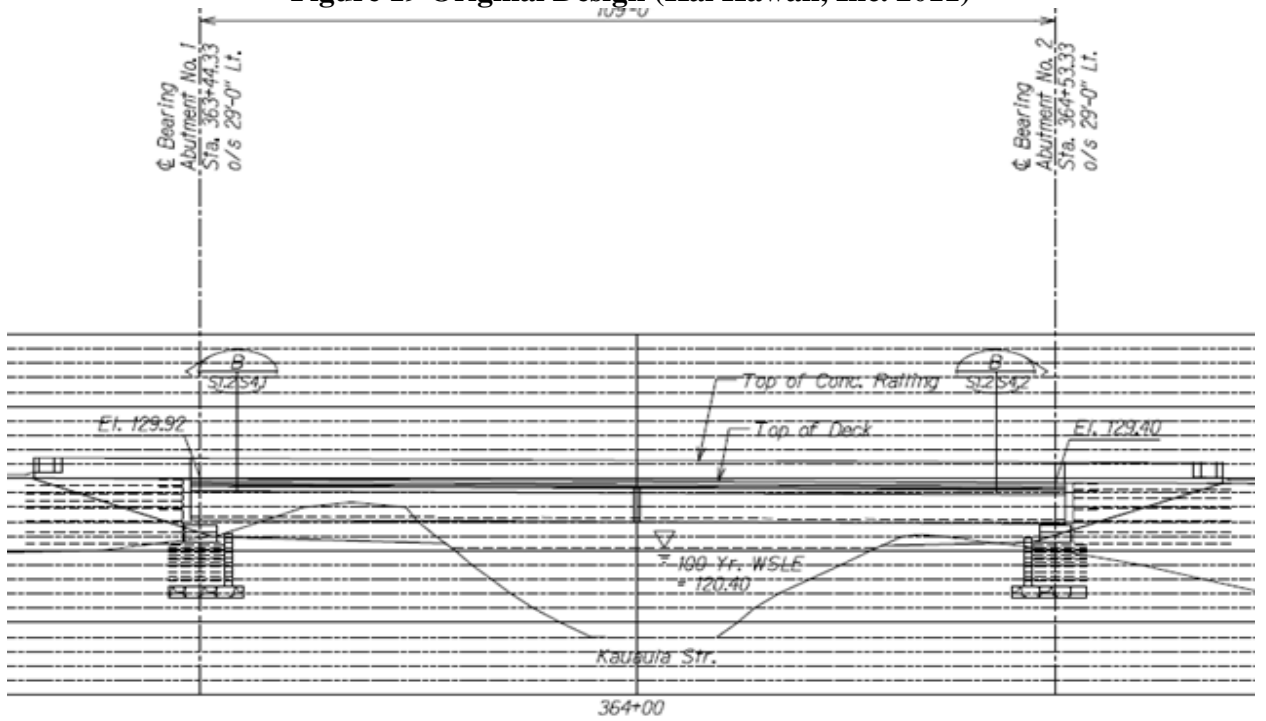
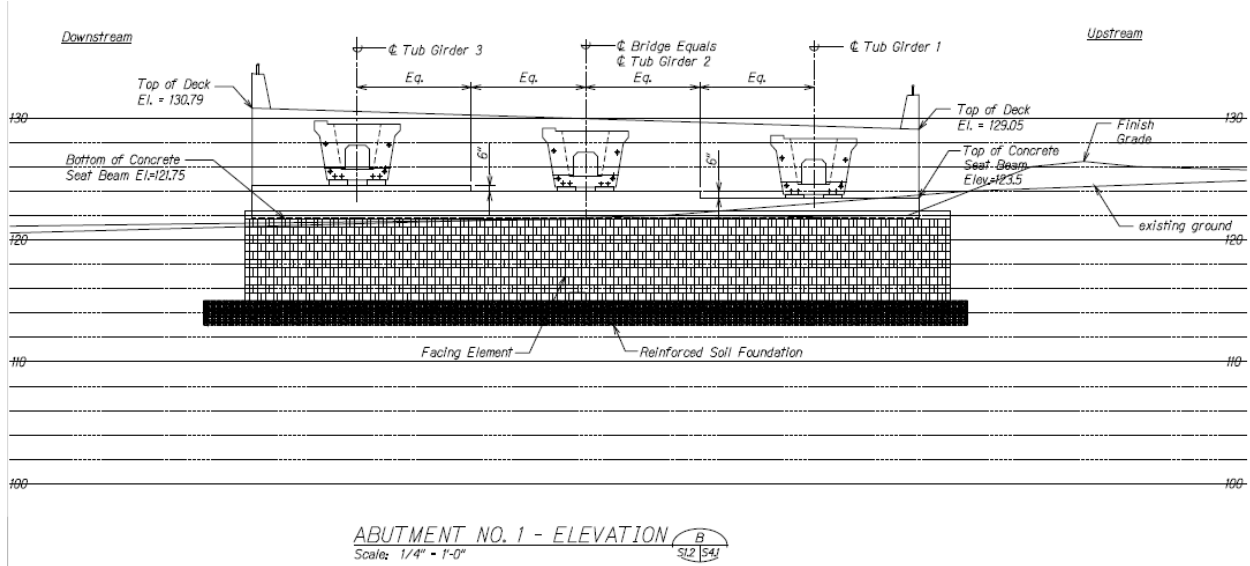


Figure 19 Original Design (Kai Hawaii, Inc. 2011)

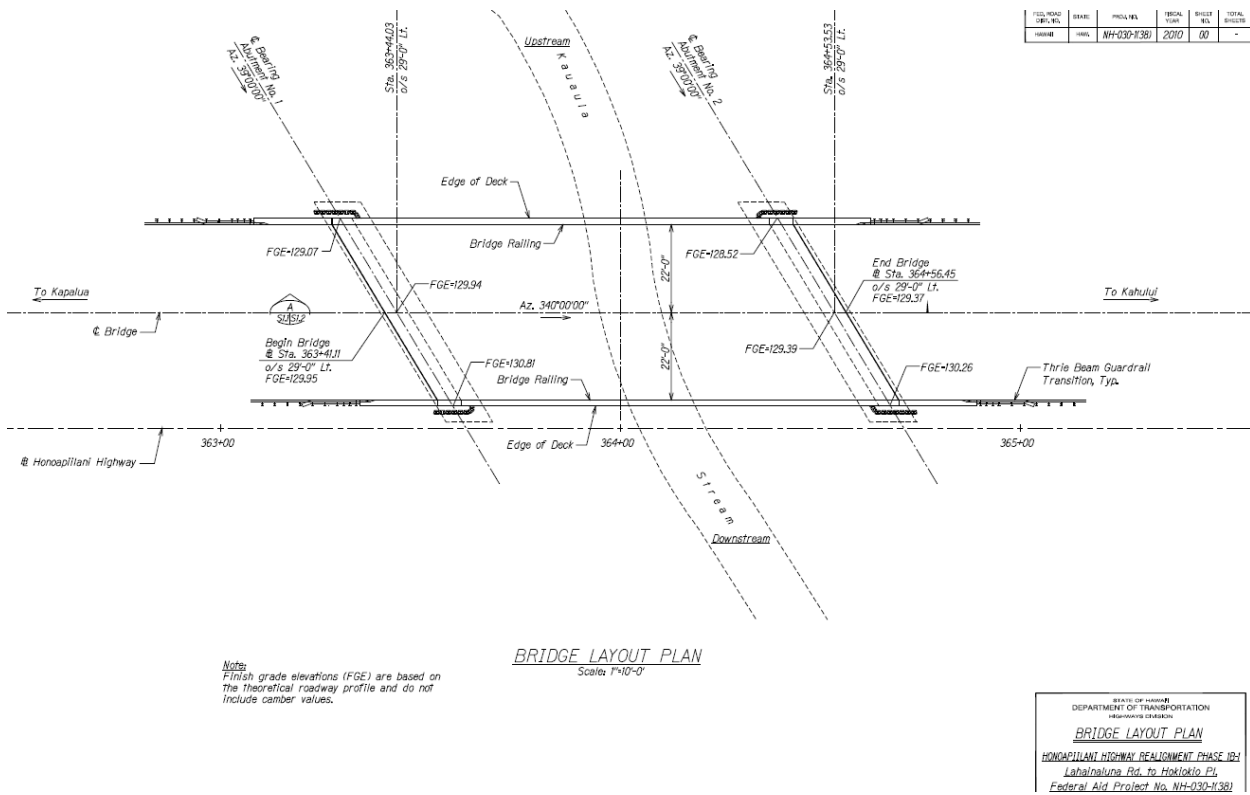


(a)





(b)



(c)

Figure 20 Valued Engineered Design (KSF Inc. 2011)

### ***3.1.2 Subsurface Stratigraphy***

Four borings were drilled by Hirata and Associates. B-22 through B-25 were drilled at the abutment locations (Appendix A). The surface soil consisted of reddish brown and clayey silt and silty clay (ML) in a medium stiff to stiff condition (Hirata and Associates, Inc, 2009). The ML extended from depths of 12 inches to 4.5 feet. Beneath the surface soil and extending down to the maximum depth drilled of about 85 feet, older alluvium (cobble and boulder layer) was encountered. The cobbles and boulders were hard and were densely packed in a matrix of silt, sand, and gravel. In some sections, the silt and sand matrix was partially to completely cemented and was medium hard to hard.

### ***3.1.3 GRS Abutment Materials***

#### ***Backfill***

The GRS backfill was a Class B basalt aggregate that met the State of Hawaii Department of Transportation's specifications for 1.5 inch maximum nominal untreated base course (Figure 21). Three 5 gallon buckets of the oven dried backfill were sent to FHWA's Turner-Fairbank Highway Research Center to conduct the following tests.

1. Grain size distribution in accordance with ASTM D6913
2. Standard Proctor in accordance with Method C of ASTM D698
3. Consolidated drained direct shear tests on fully saturated specimens in a 12 inch x 12 inch x 8 inch shear box in accordance with ASTM D3080.



**Figure 21 GRS Backfill**

The backfill grain size distribution is shown in Figure 22. From this curve,  $D_{60} = 0.37$  in,  $D_{30} = 0.13$  in,  $D_{10} = 0.021$  in,  $C_u = 17.6$ ,  $C_c = 2.2$  and % fines = 3% making this backfill a GW based on the Unified Soil Classification System and A-1-a based on the AASHTO soil classification system.

Using a 6-inch-diameter mold, a standard Proctor compaction test was performed on the material that passed the  $\frac{3}{4}$  inch sieve. The soil was compacted in 3 lifts with each lift receiving 56 blows of a 5.5-lb hammer. The optimum water content,  $w_{opt}$ , was estimated to be about 9% and the maximum dry unit weight  $\gamma_{d\ max} \approx 136$  pcf (Figure 23). The optimum water content of the on-site backfill is expected to be lower since the material larger than  $\frac{3}{4}$  inch was removed in this test. Oversize correction was not performed because oven drying of the backfill precluded the determination of the natural water content necessary for the correction. Later on, the field inspector informed UHM personnel that the HDOT-approved values of maximum dry unit weight and optimum water content were  $\gamma_{d\ max} = 145$  pcf and  $w_{opt} = 7\%$ , respectively.

Consolidated drained direct shear tests were conducted in a 12 inch x 12 inch x 8 inch high shear box. The specimens were compacted to a relative compaction = 90% to 91% based on Standard Proctor (123 pcf – 124 pcf) at a water content of 9%. Then the specimens were saturated, consolidated, and sheared to failure. Normal stresses of 7.5 psi, 15 psi and 30 psi were applied during the consolidation phase. A gap of  $D_{85}$  (~0.63 inch) was created between the two halves of the box prior to shear and the specimens were sheared at a rate of 0.015 in/min. The shear tests resulted in a non-linear Mohr-Coulomb failure envelope (Figure 24). Assuming a linear failure envelope, the peak friction angle  $\phi_{peak}$  was determined to be  $53.8^\circ$  while the cohesion was 8.23 psi or 1185 psf. The fully softened friction angle  $\phi_{fs}$  was determined to be  $49^\circ$ .

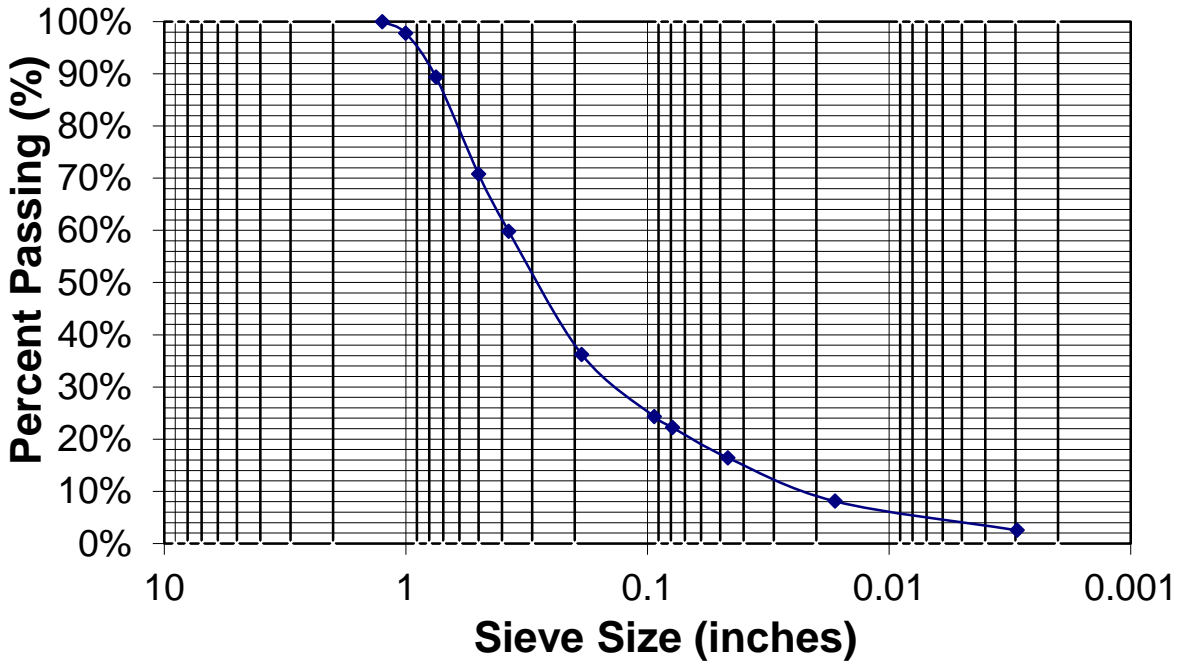


Figure 22 Grain Size Distribution of GRS Backfill

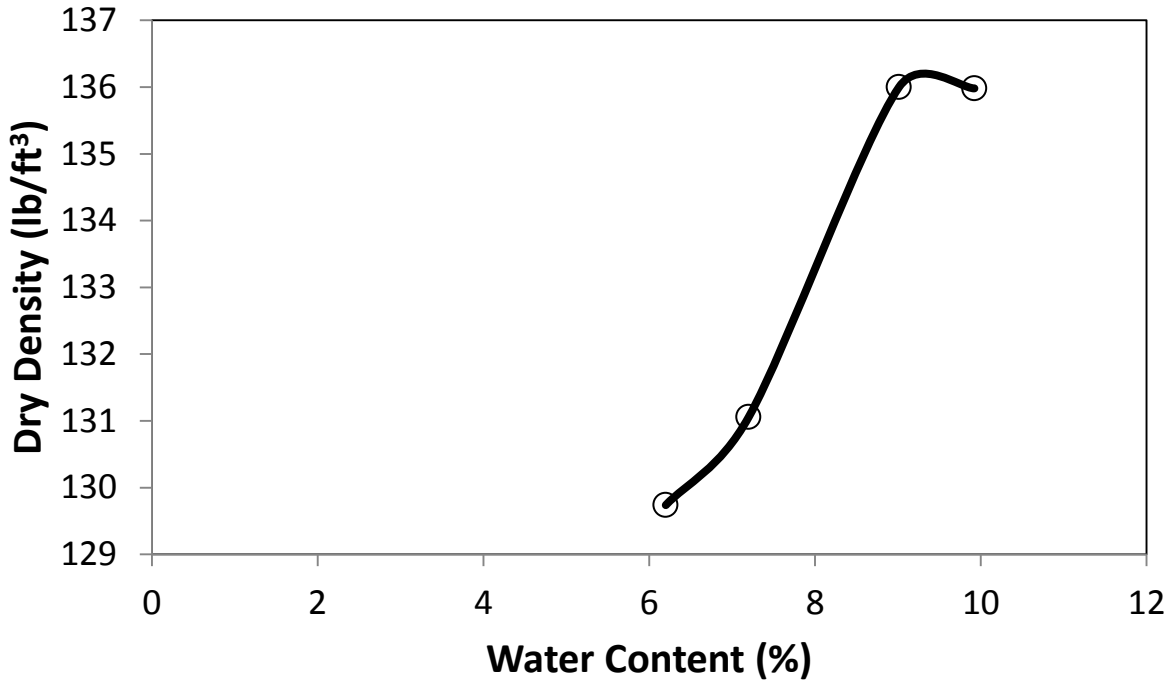
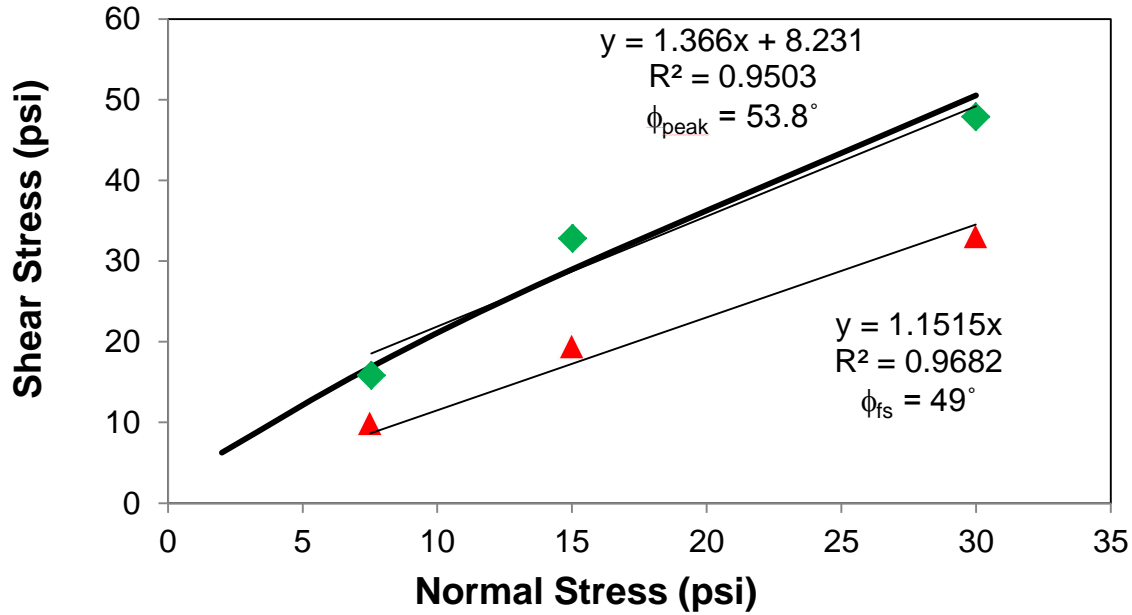


Figure 23 Compaction Curve of Backfill Finer than 3/4 inch



**Figure 24 Mohr Coloumb Failure Envelope for GRS backfill**

*Geosynthetic*

The geosynthetic used was a woven Mirafi® PET 70/70 composed of high-tenacity polypropylene multifilament yarns, which are woven into a stable network such that the yarns retain their relative position. Mirafi® PET 70/70 is also inert to biological degradation and resistant to naturally encountered chemicals, alkalis, and acids ([www.tencate.com](http://www.tencate.com)). The ultimate wide-width tensile strength,  $T_f$ , of this geosynthetic material is 4800 lbs/ft in the machine and cross machine directions as stated by the manufacturer’s technical data sheet (Appendix B).

*Facing Elements*

The facing elements for the GRS abutments were Maui CMU blocks (Figure 25), each having nominal dimensions of 8 inch high by 16 inch long by 12 inch wide and weighed approximately 75 lbs.



**Figure 25 Maui CMU Block**

### **3.1.4 Construction Sequence**

Construction of the Kauaula Stream Bridge began in January 2012 and was completed in May 2013. Because the bridge formed only one component of a 1.67 mile highway, construction of the bridge was not continuous and spanned over approximately 1.5 years. A list of key construction events and dates is summarized in Table 4.

**Table 4 Construction sequence and timeline**

Construction Event	Date
Construction of reinforced soil foundation	January 2012
Completion of GRS abutments	March 2012
Rip rap placed in front of GRS abutments	April 2012
Footings poured	July 2012
First tub girder completed	July 30, 2012
Second tub girder completed	September 15, 2012
Precast planks poured	October 2012
First tub girder launched	December 12, 2012
Second tub girder launched	December 27, 2012
Third tub girder launched	January 3, 2013
Precast planks placed on girders	January 2013
End walls, wing walls, and top deck completed	February 2013
Integral approaches completed	March 2013
Bridge completed	May 2013

The reinforced soil foundation was constructed in January 2012 by excavating a trench in the existing ground below the bottom of each GRS abutment and compacting the fill in between layers of geosynthetic. Shortly after the RSF was completed, a 6-inch-diameter, 12-foot-deep hole was drilled through the RSF into the cobbles and boulders at both abutments to facilitate installation of the inclinometer casings (Figure 26). Then, the first 15 feet of inclinometer casing was installed in the drilled hole and the annular space backfilled with soil and rodded.

Construction of the GRS abutments began by laying CMU blocks in a line. Using the CMU blocks as a form, each lift was backfilled to the top of the CMU blocks (Figure 27). The layer of backfill was then compacted using a hand tamper near the facing, and a vibratory roller further away from the facing (Figures 28 and 29). A nuclear gage was used to ensure relative compaction was at least 95% and water content was about 7% for each lift (Figure 30). After compaction, the geosynthetic reinforcement was placed over the lift. This process was repeated for the first 5 lifts.



**Figure 26 Drilling Hole for Inclinometer Casing**





**Figure 27 Backfill Placement on Abutment 2**



**Figure 28 Compaction of Backfill Using a Hand Tamper**





**Figure 29 Compaction of Backfill by Vibratory Roller**



**Figure 30 Nuclear Gage Testing**

For the top 5 CMU blocks, the height of each lift was halved with a geosynthetic placed over each lift; i.e.; geosynthetic frequency was doubled. The geosynthetic between the CMU blocks was burned off for the top 4 courses (Figure 31) to allow the CMU blocks to be pinned and grouted. After completion of each GRS abutment, styrofoam blocks were placed in front of the facing to protect it from any impact due to rip rap placement (Figure 32).

Two concrete footings, each 55 feet long, 5 feet wide and 2.25 feet thick on average, were then constructed at each abutment to support the three tub girders. Figure 33 displays the completed concrete footing at Abutment 2.



**Figure 31 Geosynthetic Burned Through Using a Torch**





**Figure 32 Styrofoam Placed in Front of Abutment 1 Prior to Placement of Rip Rap**



**Figure 33 Completed Abutment 2 with Concrete Footing**

The concrete tub girders were constructed by first erecting wooden forms and placing the steel reinforcement inside. Then, the tub girder floor was poured (Figure 34) followed by the tub girder walls several days later. After the concrete has cured sufficiently, the form was re-used to construct the next tub girder.

During construction of the tub girders, concrete planks for the top deck were formed and poured. There were two types of planks. The B planks spanned over the tub girder walls, while the A planks spanned between girders as shown in Figure 35.

The tub girders were launched by first lifting each girder using a hydraulic lift onto two steel beams that served as a guide rail (Figure 36). After attaching guidewheels that travel on the steel rail at the bottom of the girder, a large backhoe slowly pushed the girder across the Kauaula Stream onto the opposite concrete footing (Figure 37). When the tub girder was in place, the hydraulic lift system was used again to lower the tub girder onto the footings.

The concrete planks were then placed on top of the girders (Figure 38) followed by fabrication of the top deck and wing and end wall reinforcement. Concrete was poured to construct the end walls first, the top deck second and finally the wing walls (Figure 39).



**Figure 34 Concrete Floor Pour for Tub Girder**

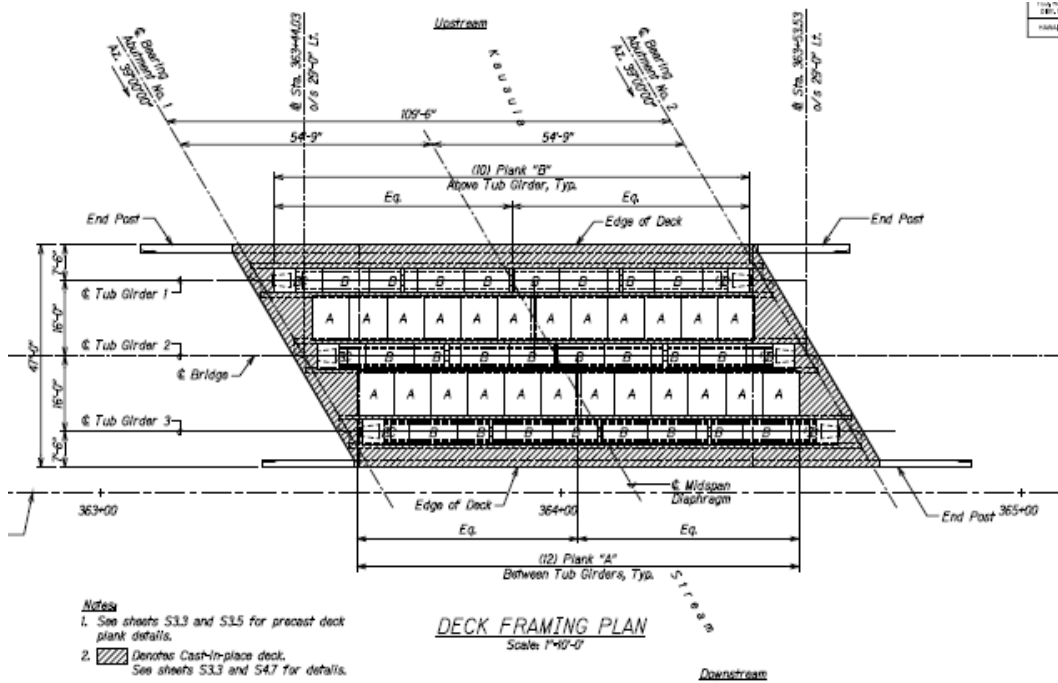


**Figure 35 Precast Concrete Plank Layout (KSF, Inc. 2011)**





**Figure 36 Hydraulic lift Raising the Tub Girder onto Two Steel Beams used as a Guide**



**Figure 37 Large Backhoe Pushing Tub Girder**





**Figure 38 Placement of Precast Concrete Planks on Tub Girders**



**Figure 39 End Walls and Wing Walls Completed**

After the wing and end wall concrete was properly cured, the integrated approach was compacted in 6 inch lifts using the same backfill material as the GRS abutment. Using a hand tamper close to the walls and a vibratory roller further away, each lift was compacted to at least 95% relative compaction (Figure 40). The geosynthetic spacing was 12 inches for the approach. Upon completion of the integrated approach, the guardrails were erected. Figure 41 displays the completed GRS-IBS.



**Figure 40 Integrated Approach Construction**





**Figure 41 Completed GRS-IBS at Kauaula Stream**

## 4 INSTRUMENTATION

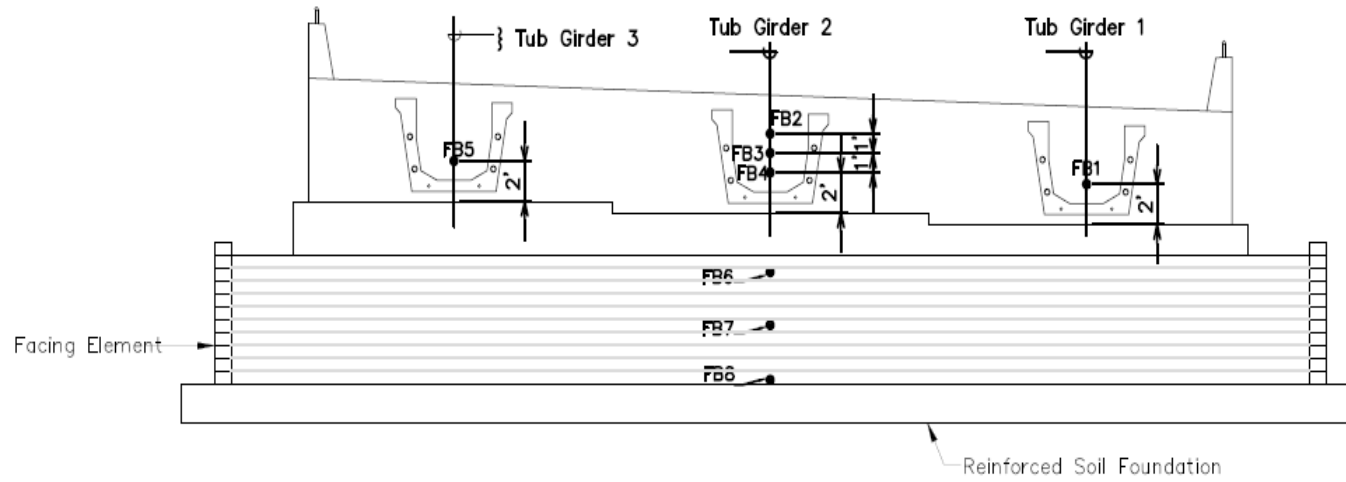
A list of instrument types used to monitor the behavior of the Kauaula Stream Bridge during and post-construction was previously provided in Section 1.3. This section details the instruments, their function and method of installation. It also includes a description of the data acquisition system which collects and stores the data and provides a means of remote access to the data via a modem.

### 4.1 Pressure Cells

Vibrating wire pressure cells were used to monitor: (a) static lateral pressures exerted by the GRS on the facing elements and the end walls and (b) static vertical pressures exerted by the bridge footing on the GRS. Two types of vibrating wire pressure cells were utilized: Geokon 4800 earth pressure (EP) cell for measuring vertical earth pressures and Geokon 4810 lateral earth pressure cell (or Fatback “FB” cell). These hydraulic-type pressure cells consist of two flat plates welded together at the periphery, separated by a small gap filled with hydraulic fluid. Changes in the fluid pressure due to any external loading are measured by a pressure transducer. Also housed in the pressure transducer is a thermistor for temperature measurement. In fact, all instruments described in this section have thermistors to measure temperature with one exception (nano concrete tiles). The layout of the EP and FB cells is shown in Figures 42, 43, and 44. EP cells were only installed at Abutment 2, which is at a lower elevation than Abutment 1.

Downstream  
←

Upstream  
→

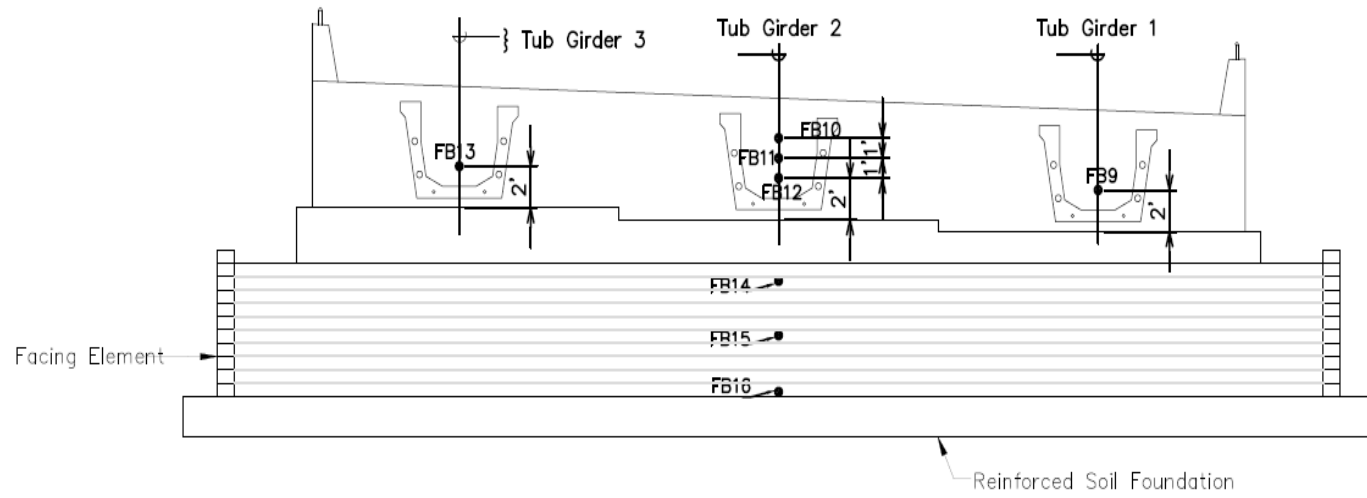


ABUTMENT NO. 1 – SECTION "Fat Back" Pressure Cells  
Scale: 1/4" = 1'-0"

**Figure 42 Abutment 1 Fatback Layout**

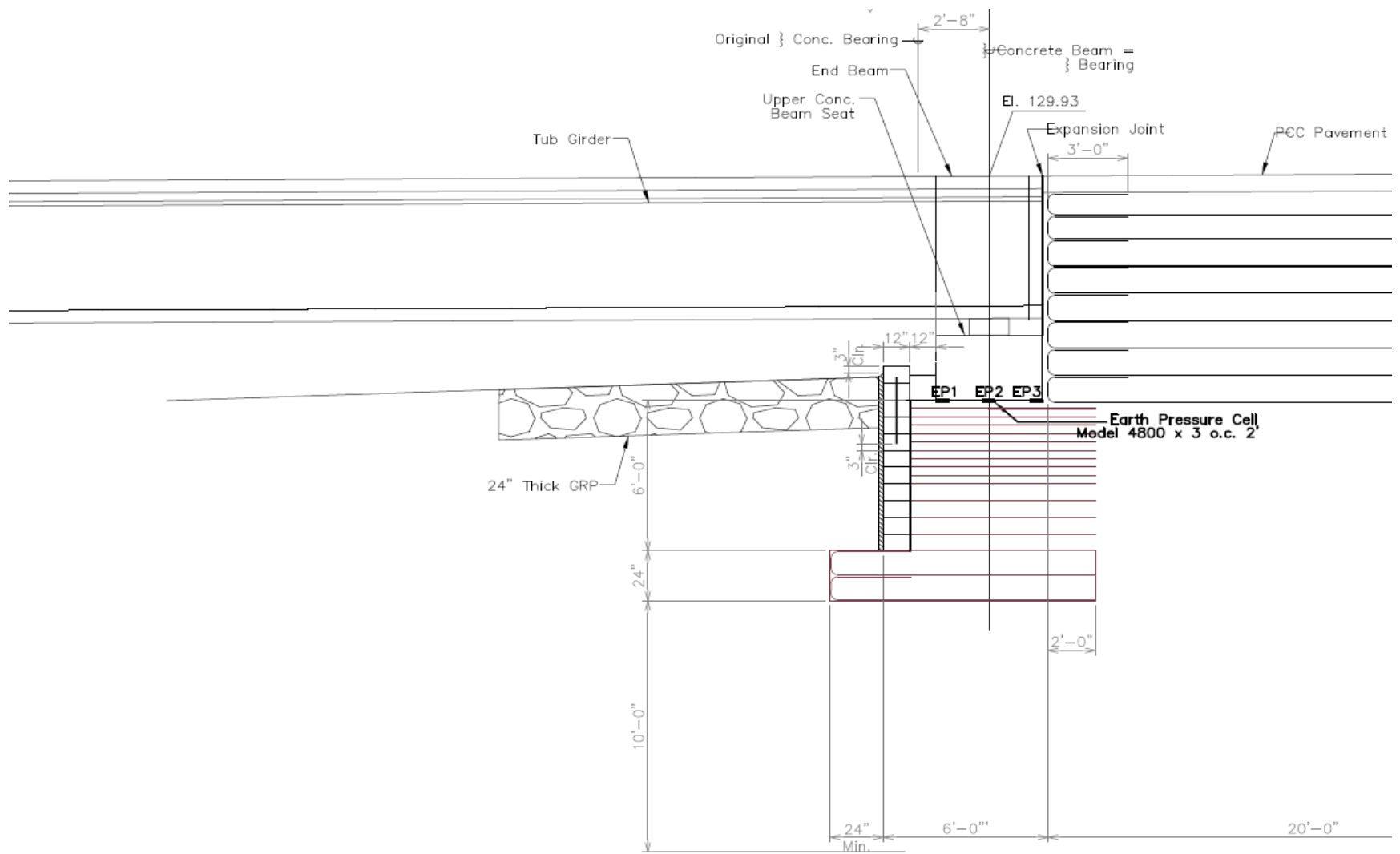
Downstream  
←

Upstream  
→



ABUTMENT NO. 2 – SECTION "Fat Back" Pressure Cells

**Figure 43 Abutment 2 Fatback layout**



ABUTMENT 1 Earth Pressure Cell

**Figure 44 Abutment 2 Earth Pressure Cell Layout**

#### **4.1.1 Vertical Earth Pressure Cells**

Three EP cells were installed directly under the concrete footing along the centerline of the middle tub girder at Abutment 2 to measure the vertical pressures during and after construction (Figure 44). Each EP cell has a pressure capacity of 50 psi, a diameter of 9 inches and a thickness of 0.236 inches (Figure 45).



**Figure 45 Geokon 4800 Earth Pressure Cell (Geokon Inc. 2013)**

EP installation was conducted as follows:

1. A shallow hole was excavated at the EP cell location (Figure 46).
2. After setting the EP cells down, a 1- to 2-inch-thick layer of sand was placed on top of the EP cells to create a level surface and to protect the instrument from excessive point loading from the gravelly portion of the concrete footing. Each EP cell was then placed 2 feet apart and aligned with the middle tub girder (Figure 47)
3. The EP cell cables were bundled with the FB, inclinometer, and deformation meter cables and then run through a PVC pipe leading to a data collection housing as described in Section 4.5.





**Figure 46 Shallow Hole for Earth Pressure Cells**



**Figure 47 Earth Pressure Cells Placed on a Flat Layer of Sand**

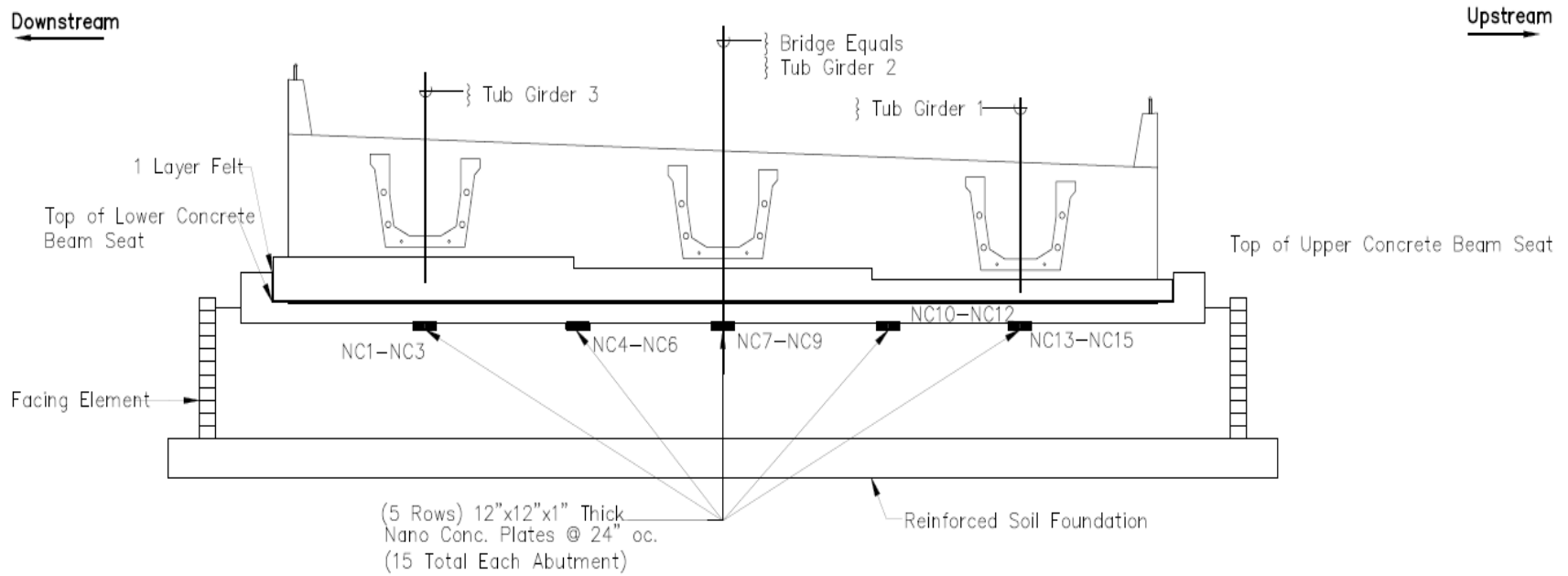
#### **4.1.2 Nano concrete tiles**

At each abutment, 15 nano concrete (NC) tiles were installed to measure vertical pressures exerted by the bridge footing on the GRS (Figure 49 and 50). The NC is composed of a concrete mix injected with a nanomaterial additive that transforms the NC into a smart sensing concrete (Oceanit, 2013 – see Figure 48). By monitoring the change in impedance of the NC from the zero reading, the vertical pressures exerted on the NC tile can be estimated.



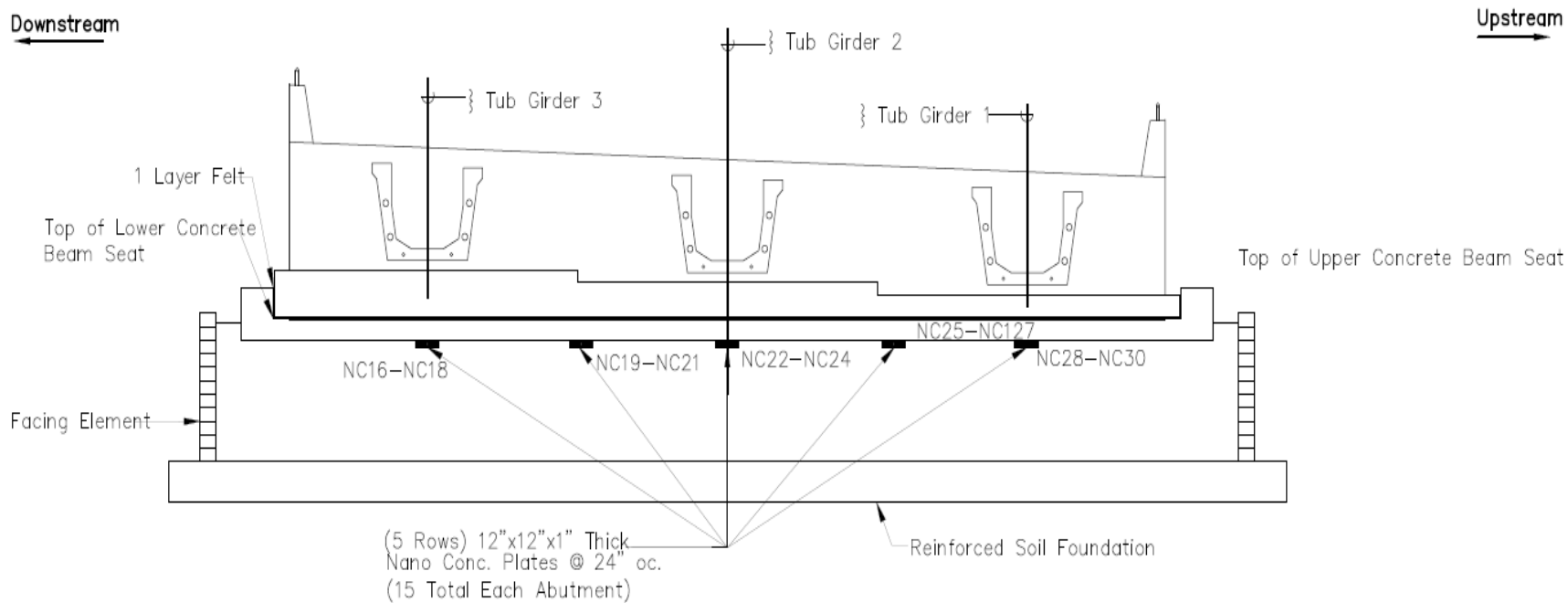
**Figure 48 Nano Concrete Tile**





ABUTMENT NO. 1 – SECTION Nano Conc. Tile

**Figure 49 Locations of Nano Concrete Tiles at Abutment 1**



ABUTMENT NO. 2 – SECTION Nano Conc. Tile

**Figure 50 Locations of Nano Concrete Tiles at Abutment 2**

NC tile installation was conducted as follows:

1. Shallow holes were excavated at the desired NC tile locations. (Figure 46).
2. Each NC tile was placed between two plastic sheets to minimize any exposure to moisture. Then, a 1- to 2-inch-thick layer of sand was placed on top to create a level surface and to protect the instrument from excessive point loading from the gravelly portion of the concrete footing. The NC tiles were spaced 2 feet apart and aligned with the tub girders (Figure 51)
3. The NC cable was run to daylight on the stream side of the footing.



**Figure 51 Nano Concrete Tiles Set Down on Plastic Sheeting Which Was Then Folded Over To Sandwich Them**

The NC tiles were connected in series and if any of the connections or any NC tiles along the chain were damaged, the tiles before it in the series would not work. Unfortunately this is what happened, no vertical pressures were recorded, and the NC tiles will not be discussed hereafter.

#### ***4.1.3 Lateral Earth Pressure Cells***

A total of 16 FBs (Figure 52) were installed in the GRS-IBS. Each FB has a capacity of 50 psi and a diameter of 6 inches. Specifically designed to measure soil pressures against a structural face, the fatback cells have a thick plate that stiffens the back of the cell so that its stiffness is more compatible with that of the structure that it is mounted to. At each abutment, a total of 3 FBs were installed on the back of the first, fifth, and ninth CMU blocks from the bottom along the centerline of the middle tub girder. A total of five FBs were installed directly behind each end wall. One FB was installed on the end wall behind each outside tub girder and three behind the middle tub girder at each abutment (Figure 42 and 43). Lateral pressures could change as a result of the following:

1. Compaction-induced pressures and increase in soil height during construction
2. Traffic loading
3. Seismic-induced pressures
4. Cyclic thermal expansion and contraction
5. Superstructure concrete shrinkage

These FBs were used to monitor the lateral pressure induced by the GRS on the facing elements and end walls during and after construction, to monitor the lateral pressures induced as a result of primarily items 1, 4, and 5 above and to assess the impact of skew on the lateral pressures on the end walls.



**Figure 52 Geokon 4810 Lateral Earth Pressure Cell (Geokon Inc. 2013)**

FB installation behind the CMU blocks was conducted as follows:

1. Each FB was fastened to a CMU block with an electric drill and concrete screws (Figure 53)
2. The CMU block with the FB was aligned with the centerline of the abutment.
3. Sand was placed in front of the FB to protect the instrument from excessive contact pressures due to point loading from any gravel in the backfill (Figure 54).
4. The cables of each FB were run along the backfill side of the CMU blocks to the top, bundled with the deformation meter, inclinometer, and EP cables and then run through a PVC pipe to the data collection system described in Section 4.5.



**Figure 53 Fatback Cell Fastened to CMU Block**

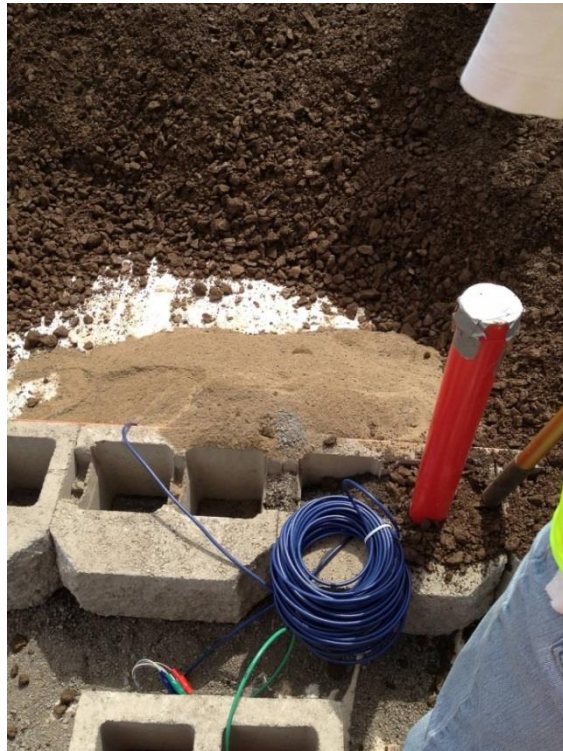


**Figure 54 Sand Placed in Front of Fatback Cell for Protection**



FB installation behind the end walls was conducted as follows:

1. Each FB was fastened to the end walls with an electric drill and concrete screws (Figure 55).
2. The cables were taped to the end wall and directed to a hole through the end wall to reach the data acquisition system on the other side.
3. As each layer of the integral abutment was filled and compacted, sand was placed in front of the FBs to protect the instrument from experiencing excessive contact pressures due to point loading from any gravel in the backfill.



**Figure 55 Fatback Cells Fastened to End Wall**

#### **4.2 Inclinator**

Geokon 6300 vibrating wire in-place inclinometers were installed to measure the lateral deflection of the facing elements of both GRS abutments during and after construction. The inclinometers were placed into a glue-snap, pre-placed casing installed in a borehole drilled at the center of each abutment (Figures 56 and 57). Designed for long-term monitoring, the basic

principle is the utilization of tilt sensors to measure inclination over segments in a borehole drilled into the structure to be studied. The bottom of the inclinometer casing is embedded 10 ft in a firm stratum to establish a point of fixity. For reference purposes, this point of fixity is deemed immobile. Noted as older alluvium, this firm stratum consists of cobbles and boulders in a matrix of silt, sand and gravel.

The tilt sensor consists of a pendulous mass which is supported by a vibrating wire strain gage and an elastic hinge. The strain gage senses any change in force caused by the rotation of the center of gravity of the mass (Geokon Inc. 2013). The full layout of the inclinometer system is shown in Figures 58 and 59. The inclinometers were spaced closer together (every 2 feet) in the upper 10 feet of the GRS abutment facing, which is considered the zone of interest, and further apart (every 4 feet) below that.

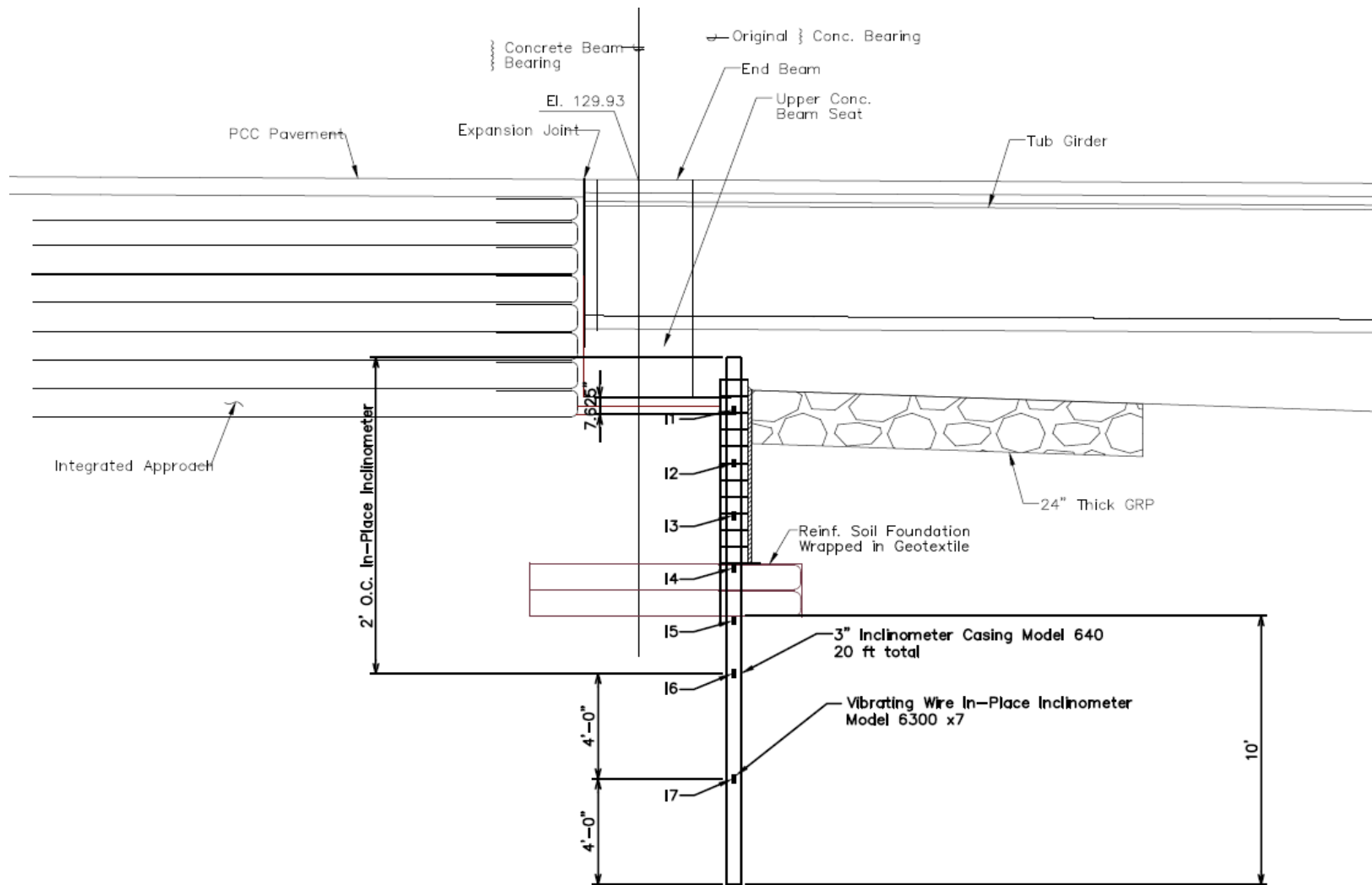


**Figure 56 Geokon 6300 Inclinometer (Geokon Inc. 2013)**





**Figure 57 Geokon Glue-Snap Inclinometer Casing (Geokon Inc. 2013)**



ABUTMENT 1 Inclinerometer

**Figure 58 Abutment 1 Inclinerometer Layout**

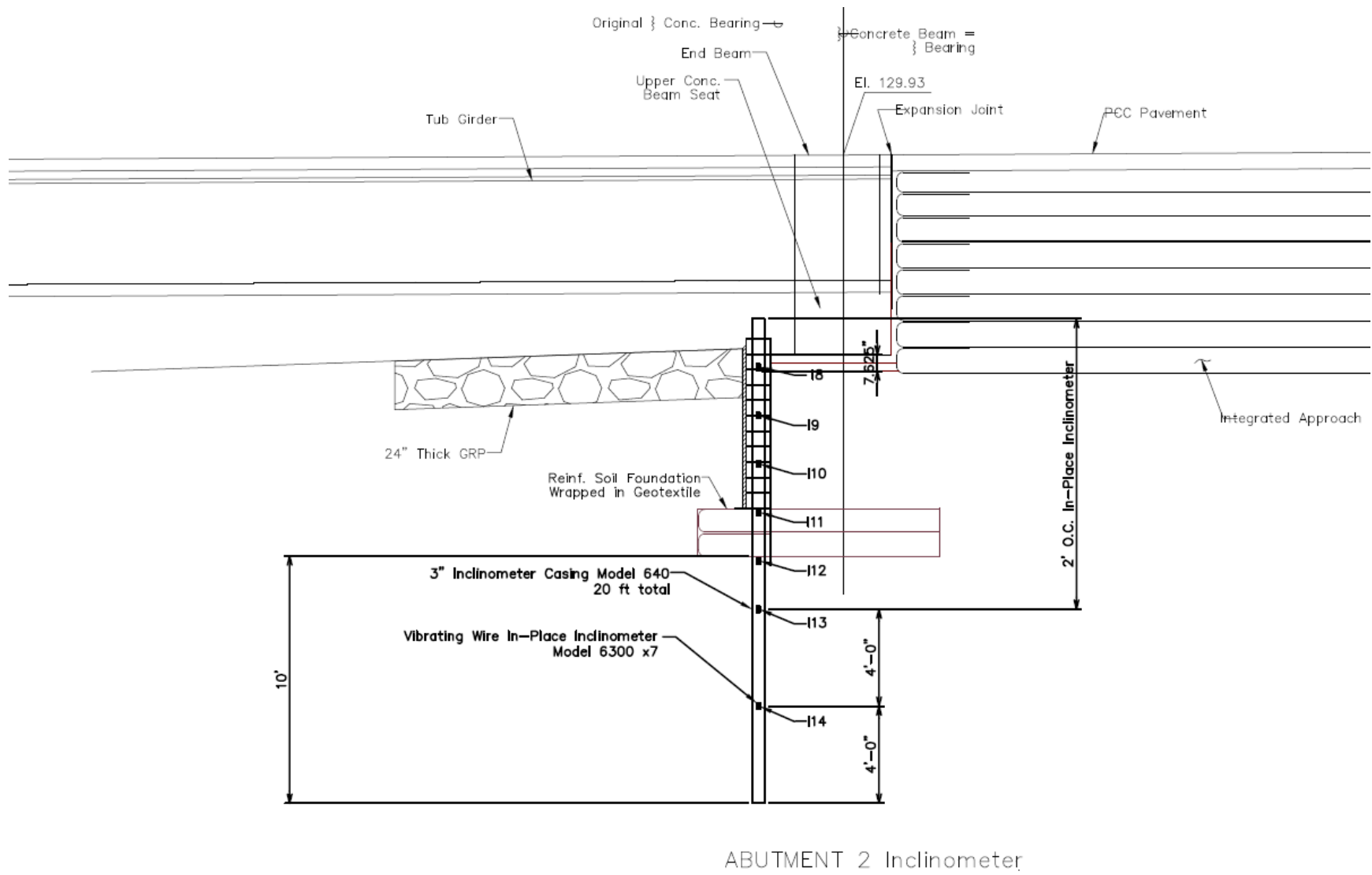


**Figure 59 Abutment 2 Inclinometer Layout**

Inclinometer and casing installation was conducted as follows:

1. A 6-inch-diameter hole was drilled through the RSF about 10 ft into the cobbles and boulders at both abutments to facilitate installation of the inclinometer casings (Figure 26). Three five-foot inclinometer casing segments were glue-snapped together and placed into that hole leaving 3 feet of inclinometer casing extending above ground. The annular space of the inclinometer casing below ground was backfilled with soil and rodded
2. As the GRS abutments were constructed, small incisions were made in the geotextile at each lift to allow the inclinometer casing to pass through (Figure 60).
3. When the GRS abutment reached the top of the initial 15 feet of inclinometer casing, the last five-foot segment was glue-snapped on.
4. After completion of the GRS abutment, the string of inclinometers were assembled and rolled down the grooves of the inclinometer casing with the “A” direction pointing towards the stream (Figure 61).
5. Inclinometer cables were bundled up with the FB, deformation meter, and EP cables, then run through a PVC pipe to the data acquisition system as described in Section 4.5.



**Figure 60 Inclinometer Casing Protruding Above Ground**



**Figure 61 Inclinometers Installed into Glue-Snap Casing**

### 4.3 Strain Gage

Thirty Geokon 4200 strain gages (SG) were installed to measure strains induced in the tub girders, precast planks and wearing surface (Figure 62). Five strain gages were installed at the middle third points of each girder. They were all attached to the rebar at the following locations: (a) at the center of the floor; (b) at the top of both walls of each tub girder; (c) at the center of the deck planks between the tub walls; and (d) in the wearing course (Figures 63 and 64). Strains are measured with the aid of a steel wire tensioned between two end blocks that are firmly in contact with the mass concrete. Deformations in the concrete will cause the two end blocks to move relative to one another, altering the tension in the steel wire. This change in length is measured as a change in resonant frequency of the wire when an electrical pulse is sent to pluck it. An additional strain gage (SG31) was installed in an unreinforced 6-inch-diameter concrete cylinder to measure the shrinkage-induced strains in the concrete used to pour the tub girders over time. The concrete used to manufacture the precast planks and tub girders has a design 28-day compressive strength of 8000 psi and a water cement ratio of 0.4. 128 ounces of Masterlife shrinkage reducing admixture was added to each cubic yard of concrete for the precast planks and tub girders to reduce concrete shrinkage. This cylinder is placed in the same junction box that houses the data acquisition system at Abutment 2 (Figure 65). The concrete used to manufacture the wearing surface is similar to the concrete described above with the following two differences:

- (1) The 28-day design compressive strength is 6000 psi; and
- (2) 4 lbs of 1/8-inch Anticrak Hd and 6 lbs of 67/36 Anticrak Hd alkali resistant glass fiber were added per cubic yard of concrete.

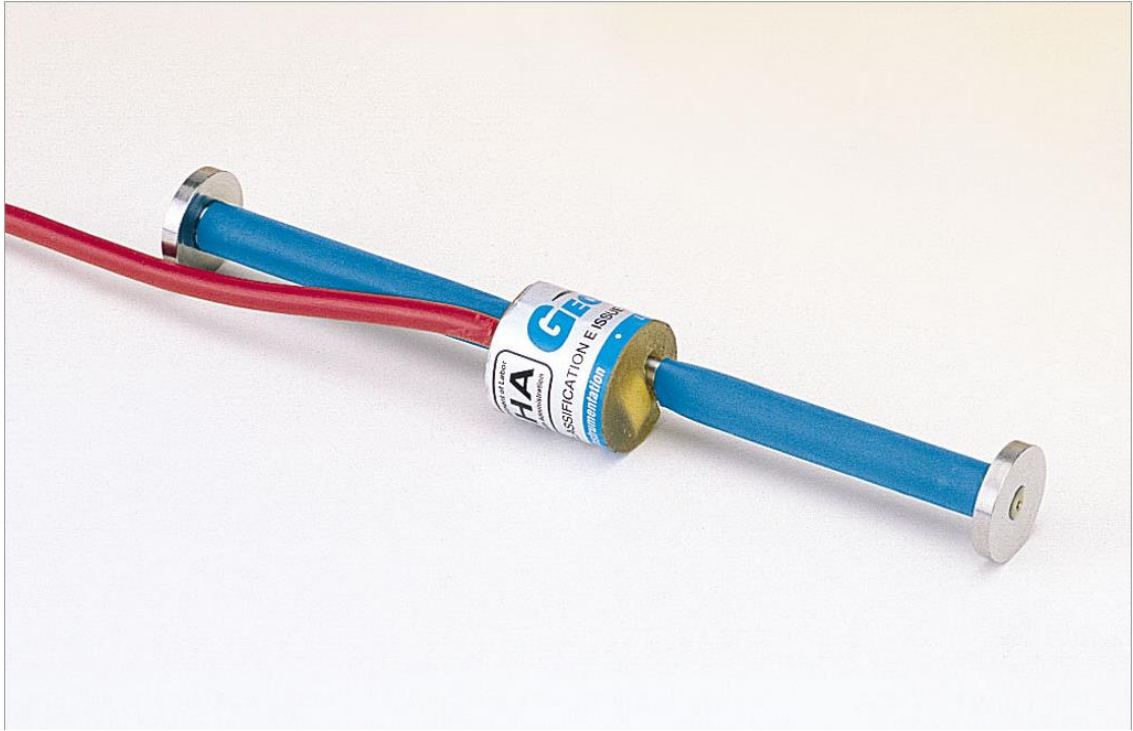


**Figure 62 Geokon 4200 Concrete Embedded Strain Gage (Geokon Inc. 2013)**

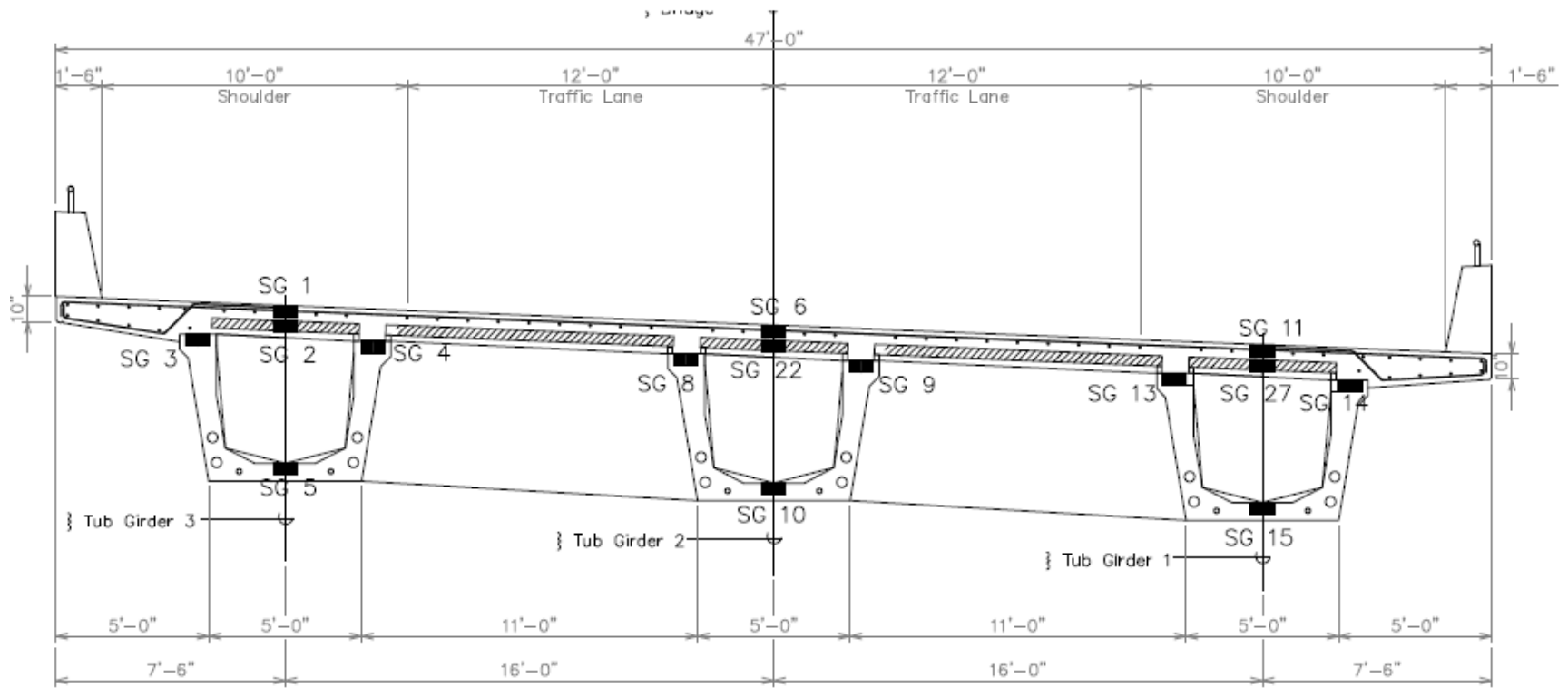


**Figure 63 Abutment 1 Strain Gage Layout**



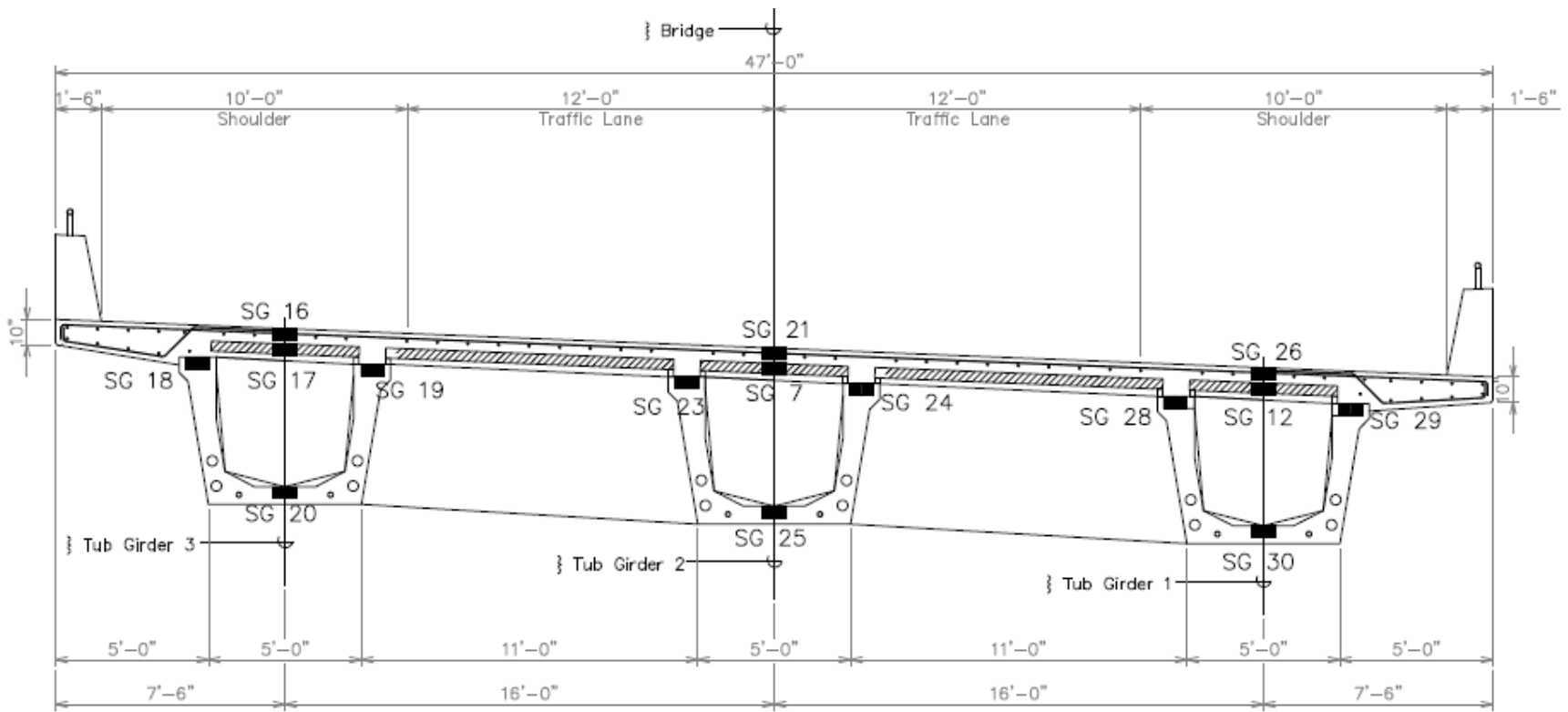


**Figure 64 Abutment 2 Strain Gage Layout**



**Figure 65 Concrete Cylinder**

Strain gage installation was conducted as follows:

1. Two  $\frac{1}{2}$  inch x  $\frac{1}{2}$  inch x  $\frac{1}{2}$  inch wooden blocks were prepared for each strain gage.
2. The strain gage was fastened to the rebar using plastic straps along with the wooden blocks as shown in Figure 66.
3. With the aid of plastic straps, the cables of each strain gage were fastened to the rebar and were configured to daylight on the inside floor of the tub girders (Figure 67). It was necessary to keep the cables on the inside of the tub girder so that they will not be damaged or in the way during the girder launch.

4. After the girder launch, the cables were run through a pipe through the floor of the tub girder to a PVC pipe network for protection as described in Section 4.5. The cables terminate in the data acquisition system.



**Figure 66 Strain Gage Fastened to Rebar Using Plastic Straps**



**Figure 67 Strain Gage Cables Daylighting from the Floor of the Tub Girder**

#### **4.4 Deformation Meter**

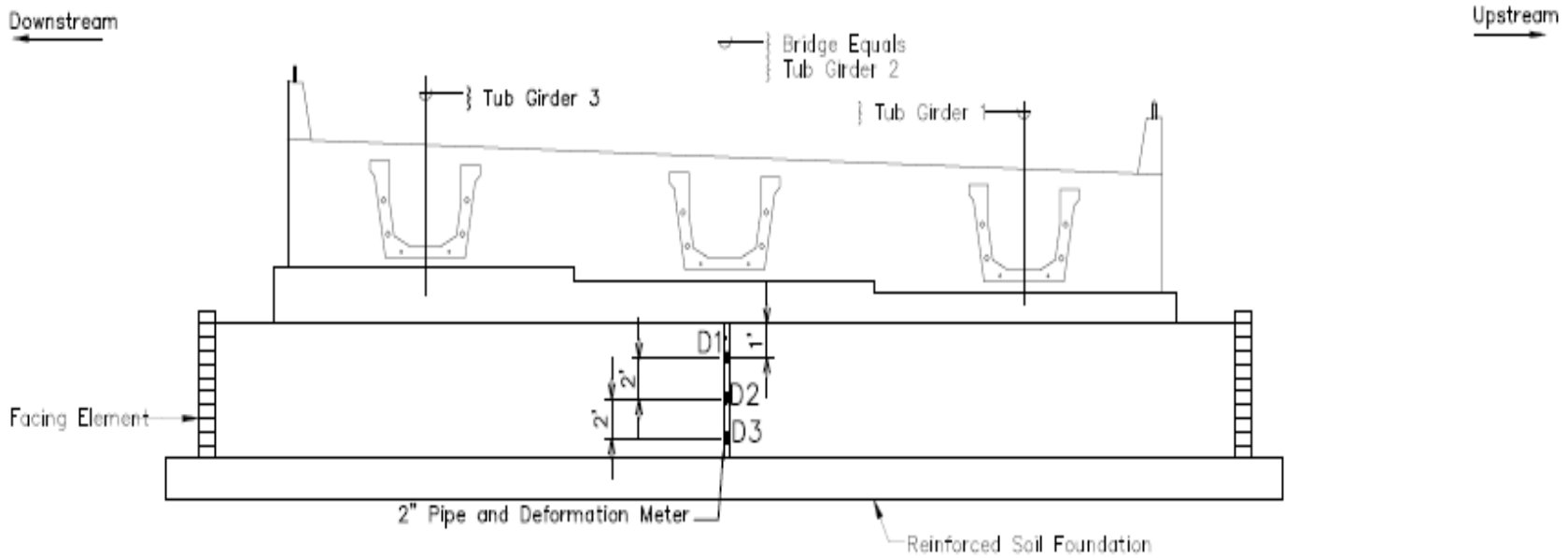
Three Geokon 4430 deformation meters were installed below the center of each footing at each abutment (Figure 68) to measure the compression over the depth of the GRS. The deformation meter sensor is attached to a 2-inch-diameter flange at one end and connected to another flange at the other end inside a 2-foot-long, 1-inch-diameter rod. The sensor and rod are covered by a PVC tube. Any vertical ground deformation will cause the flanges to move. This movement is detected by the sensor and conveyed to a readout system. The deformation meters were installed in a 2.5 inch PVC pipe filled with grout to keep the deformation meters in place. The layout of the deformation meters is shown in figures 69 and 70 for abutments 1 and 2, respectively. However, shrinkage of the cement gout meant that caused the PVC pipe experienced the majority of the compression and the deformation meters read mostly 0. The deformation meters will not be discussed hereafter.



**Figure 68 Geokon 4430 Deformation Meter (Geokon Inc. 2013)**

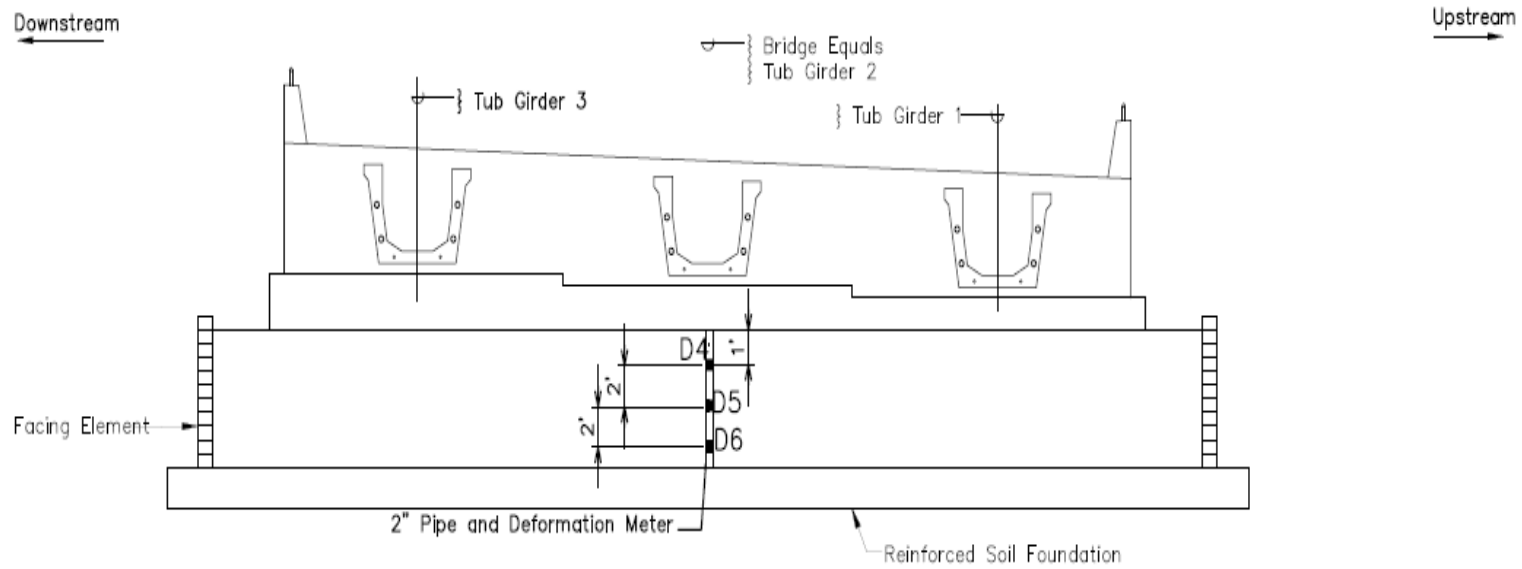
Installation of the deformation meters was conducted as follows:

1. The GRS backfill was compacted around a 2.5-inch diameter Schedule 80 PVC pipe at the center of each abutment footing. With the bottom of the PVC pipe located on top of the RSF, this pipe is used to house the three deformation meters stacked consecutively on top of each other giving a total GRS monitored height of about 6 feet.
2. After consecutively stacking the deformation meters in a line, the instruments were lowered into their proper places inside the PVC pipe.
3. The PVC pipe was grouted using a 50:50 mix of cement and water by volume as shown in Figure 71.
4. After the grout cured, the deformation meter cables were bunched up with the FB, inclinometer and EP cables, and then run through a PVC pipe to the data acquisition system as described in Section 4.5.



ABUTMENT NO. 1 – SECTION Deformation Meter

**Figure 69 Abutment 1 Deformation Meter Layout**



ABUTMENT NO. 2 – SECTION Deformation Meter

**Figure 70 Abutment 2 Deformation Meter Layout**





**Figure 71 Grout Mixture Poured into PVC Pipe Housing Deformation Meter**

#### **4.5 PVC pipe and Cable Layout**

A continuous 3-inch-diameter PVC pipe system utilizing 90 degree elbows, T fittings and toilet flanges housed the network of cables (Figure 72). The cables in the pipe system were ultimately connected to multiplexers at Abutment 2 or wireless transmitters at Abutment 1. Three PVC pipes at each abutment were also attached to the underside of the tub girders to house the SG cables that emanate from the inside of the tub girders. These PVC pipes were fastened to the tub girders utilizing steel straps and concrete screws (Figure 73). All cables inside this network of PVC pipes lead to a steel junction box (J-box) fastened to each end wall between Tub Girder 2 (ocean or west side) and Tub Girder 3 (middle) as shown in Figure 74. The PVC pipe configurations for the middle and the outer tub girders are shown in Figures 75 and 76, respectively.





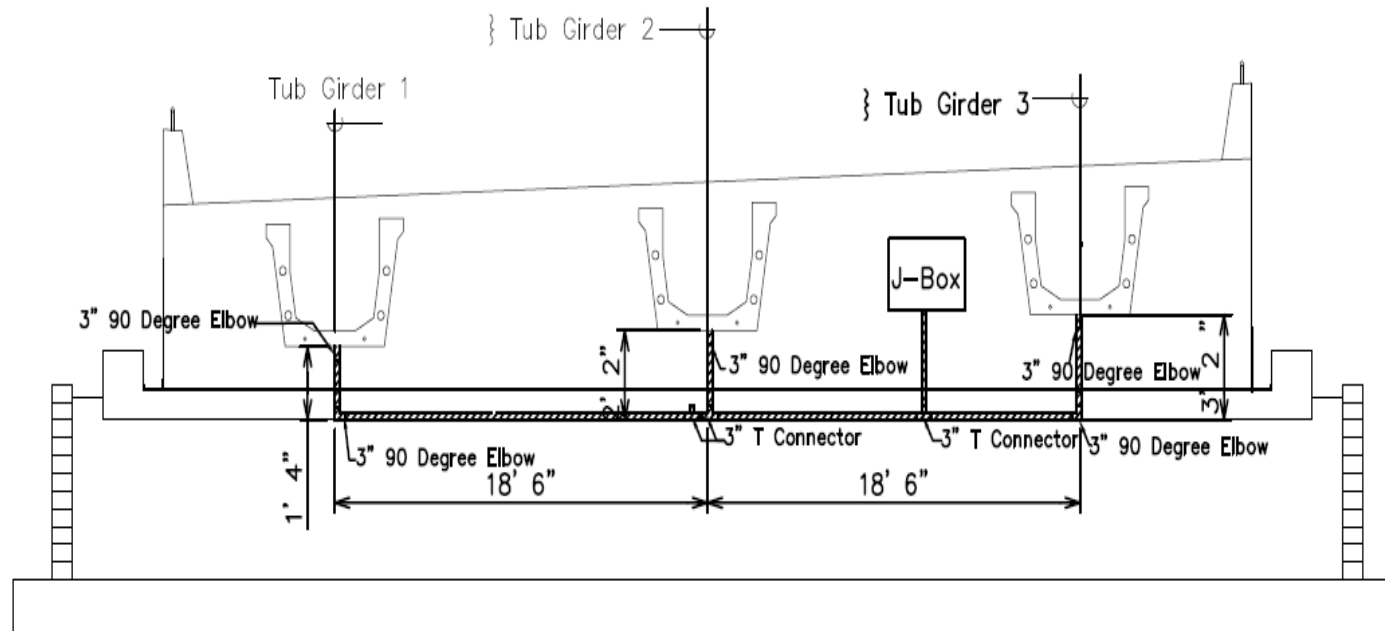
**Figure 72 PVC Pipe System Under the Middle Tub Girder**



**Figure 73 Steel Straps Used to Hold up PVC Pipes**

Upstream  
←

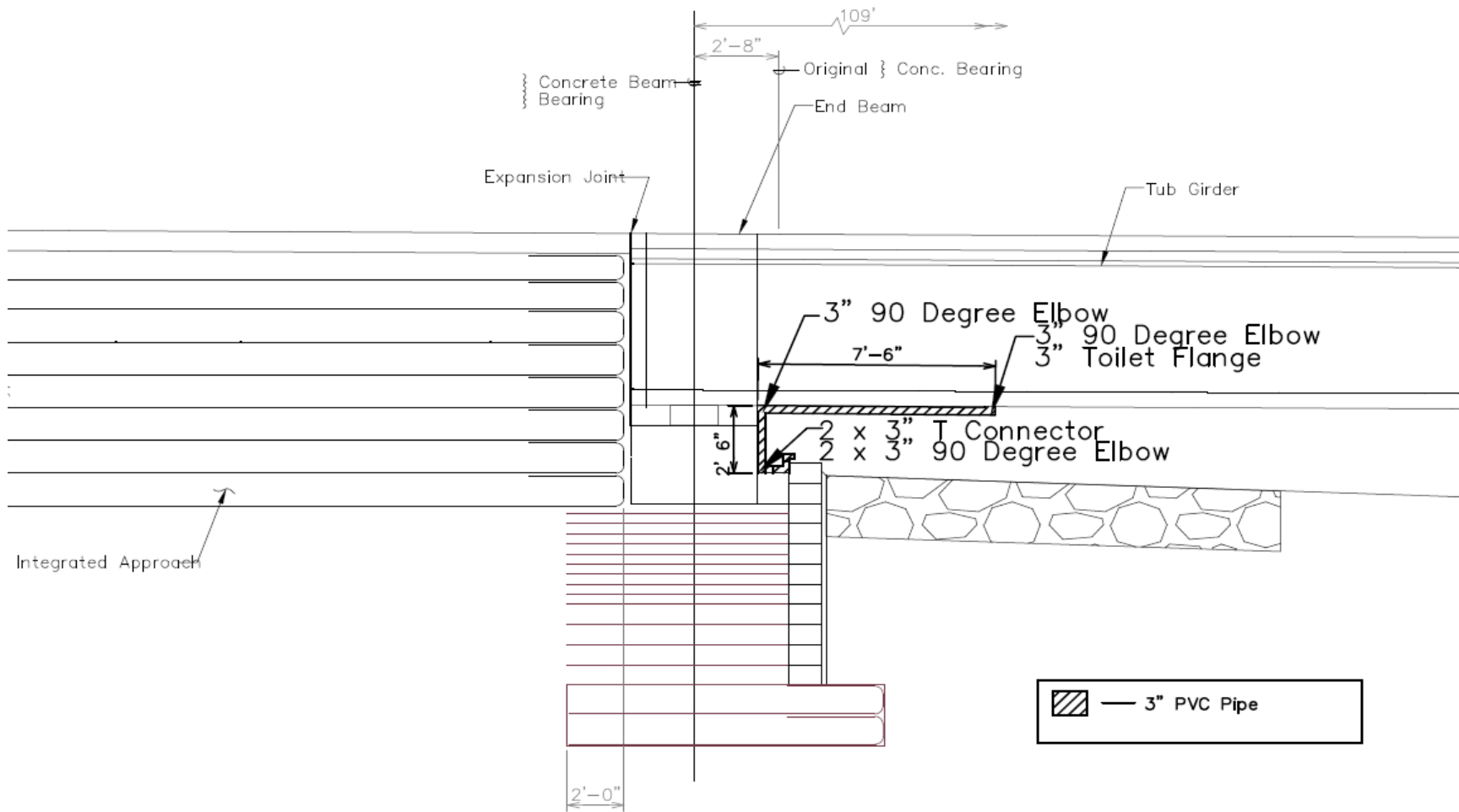
Downstream  
→



▨ — 3" PVC Pipe

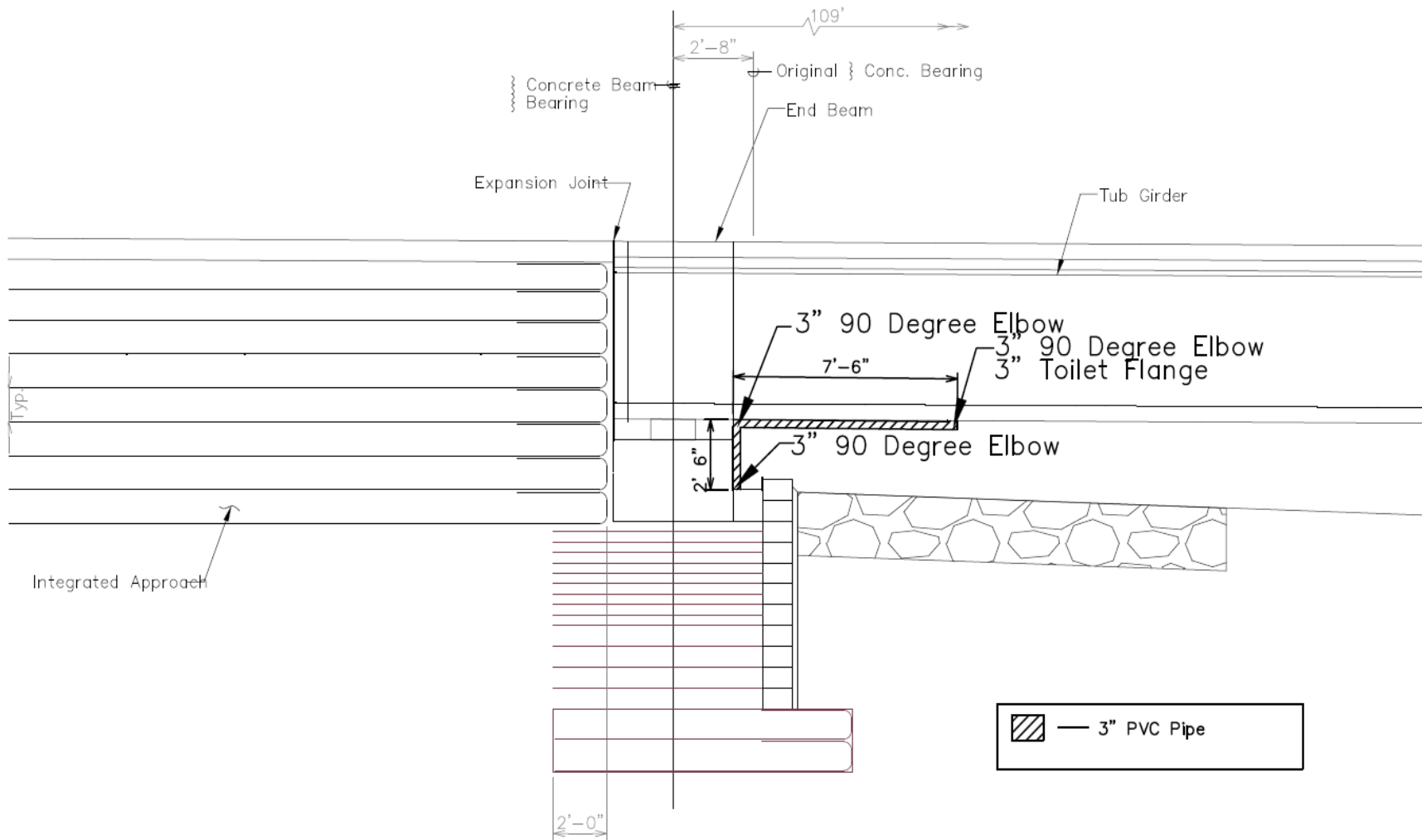
TYP SECTION PVC PIPE LAYOUT  
NOT TO SCALE

**Figure 74 Typical Layout of PVC Pipe System for Rach Abutment**



TYP Middle Tub  
NOT TO SCALE

**Figure 75 Typical Cross-Section of Middle Tub Girder's PVC Pipe Layout**



TYP. Outer Tub Girder  
 NOT TO SCALE

**Figure 76 Typical Cross-Section of Outer Tub Girders' PVC Pipe Layout**

#### 4.6 Data Acquisition System

The data acquisition system consists of the components shown in Table 5. All instruments terminate at one of two J-boxes at either Abutments 1 or 2. The data from Abutment 1 is transmitted to the CR1000 data logger at Abutment 2 via two wireless transmitters (Figure 77). The CR1000 data logger stores all data collected from both abutments and can be programmed to collect data at specified times and frequency. A MultiLogger software can then be used to establish a remote connection to the data acquisition system via a cellular modem to download the data.

**Table 5 Components of the Data Acquisition System**

<b>Component</b>	<b>Quantity</b>	<b>Purpose</b>	<b>Location</b>
CR1000 data logger	1	Digitize and store data from vibrating wire instruments	Abutment 2
AVW200	3	Interface between multiplexers and CR1000 (direct connection)	Abutment 2
AVW206	2	Interface between multiplexers and CR1000 (wireless)	Abutment 1
AM16/32 multiplexer	5	Increase the capacity of AVW200 and AVW206 from 1 to 16 instruments	Abutment 1 and 2
RF401 spread spectrum data radio modem	1	Wirelessly connects AVW206 modules at Abutment 1 to the data logger at Abutment 2	Abutment 2
Raven X cellular modem	1	Allows wireless connection to the data logger via internet	Abutment 2
Solar panels for power supply	3	Provides power to charge 12 Volt batteries required for the data logger at Abutment 2 and wireless transmitters at Abutment 1	Abutments 1 and 2

#### 4.6.1 Layout

The data acquisition system was installed in two separate J-boxes. The J-box at Abutment 2 (Figure 78) houses the main data logger, 3 multiplexers, 3 AVW200 modules, radio modem, and cellular modem. The cables of the instruments shown in Table 6 terminate at Abutment 2.

**Table 6 List of Instruments Terminating at Abutment 2**

<b>Instrument</b>	<b>Numbering</b>	<b>Quantity</b>	<b>Multiplexer</b>
Earth Pressure Cells	EP1 - EP3, Dummy EP cell	4	MUX 3
Deformation meters	D 4 – 6	3	MUX 3
Inclinometer	I 8 – 14	7	MUX 2
Lateral Pressure Cells	FB 9 – 16	8	MUX 2
Strain gages	SG 16-31	16	MUX 1
<b>Total</b>		<b>38</b>	

All instrument cables at Abutment 2 end up in one of three multiplexers which are wired to the CR 1000 data logger.

The J-box at Abutment 1 houses two multiplexers, each connected to an AVW206 module (Figure 79). Using radio frequency, the AVW206 modules relay all data from the instruments at Abutment 1 to the data logger at Abutment 2. The cables of the instruments shown in Table 7 terminate at Abutment 1.

**Table 7 List of Instruments Terminating at Abutment 1**

<b>Instrument</b>	<b>Numbering</b>	<b>Quantity</b>	<b>Wireless Transmitter (WT)</b>
Deformation meters	D 1 – 3	3	D1 on WT1 D2 on WT2 D3 omitted
Inclinometer	I 1 – 7	7	WT2
Lateral Pressure Cells	FB 1 – 8	8	WT2
Strain gages	SG 1-15	15	WT1
<b>Total</b>		<b>33</b>	



**Figure 77 J-Box at Abutment 1 Containing the Wireless Transmitters (WT1 on left and WT2 on right)**



**Figure 78 J-Box at Abutment 2 Containing the Three Multiplexers (Bottom Row) and One Datalogger (Top)**



#### 4.6.2 Datalogger

A Campbell Scientific CR1000 data logger was utilized to control all sensors, telecommunications, data digitization, and storage of all data as well as programs on-board (Figure 79). The data logger has input/output connections for multiplexers (i.e.; the AVW200 modules), communication peripherals (cellular modem and radio modem) and is powered by a battery charged by a solar panel.



**Figure 79 CR1000 Datalogger (Campbell Scientific Inc. 2013)**

#### 4.6.3 AVW200 and AVW206 Modules

Three AVW200 and two AVW206 modules were utilized as interfaces between the instruments and the data logger (Figures 80 and 81). These modules allow measurements from each vibrating wire instrument to be acquired while significantly reducing the amount of noise introduced from external sources.

The AVW200 serve as a direct interface between the multiplexers and the data logger, while the AVW206 was connected wirelessly. The AVW206 utilize a spread spectrum radio and a 900 MHz Omni direction  $\frac{1}{2}$  wave whip antenna to transmit the data from Abutment 1 to the data logger at Abutment 2. This wireless configuration eliminated the need for a second data logger and cell phone modem.





**Figure 80 AVW200 Module (Campbell Scientific Inc. 2013)**



**Figure 81 AVW206 Module (Campbell Scientific Inc. 2013)**

#### **4.6.4 Multiplexer**

Multiplexers increase the capacity of each AVW module from 1 to 16 instruments (Figure 82). Each of the five multiplexers was programmed to return measured values to the data logger every 4 hours.

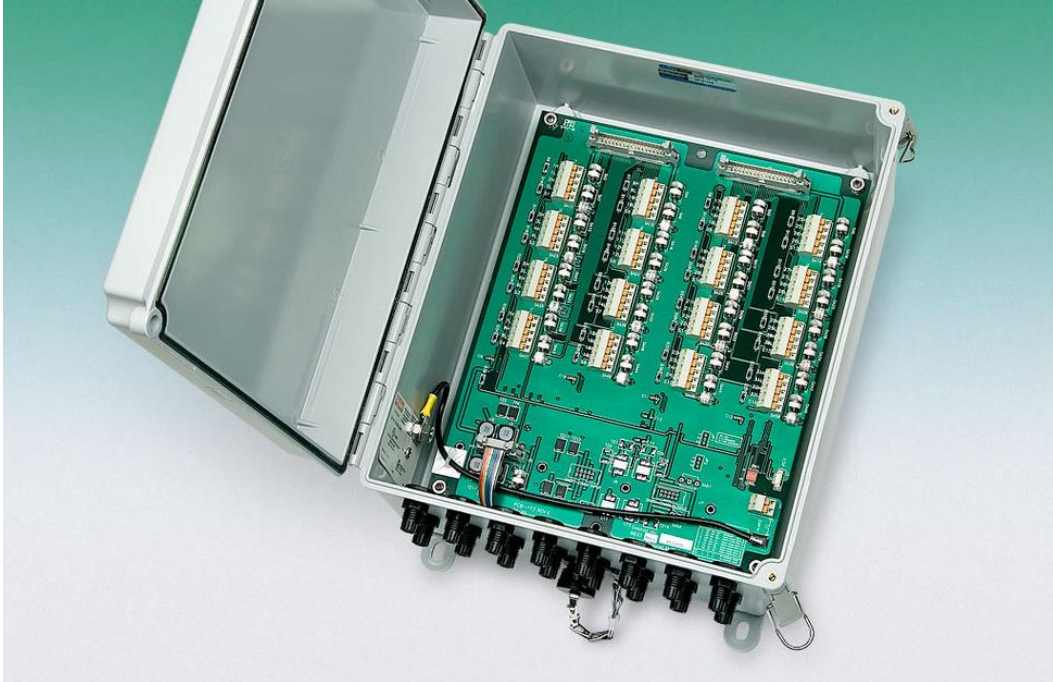


**Figure 82 Vibrating Wire Multiplexer (Geokon Inc. 2013)**

#### **4.6.5 Radio modem**

The RF401 spread spectrum radio modem is a wireless data communication device connected to the data logger and is used to receive data from the AVW206 modules at Abutment 1 (Figure 83).

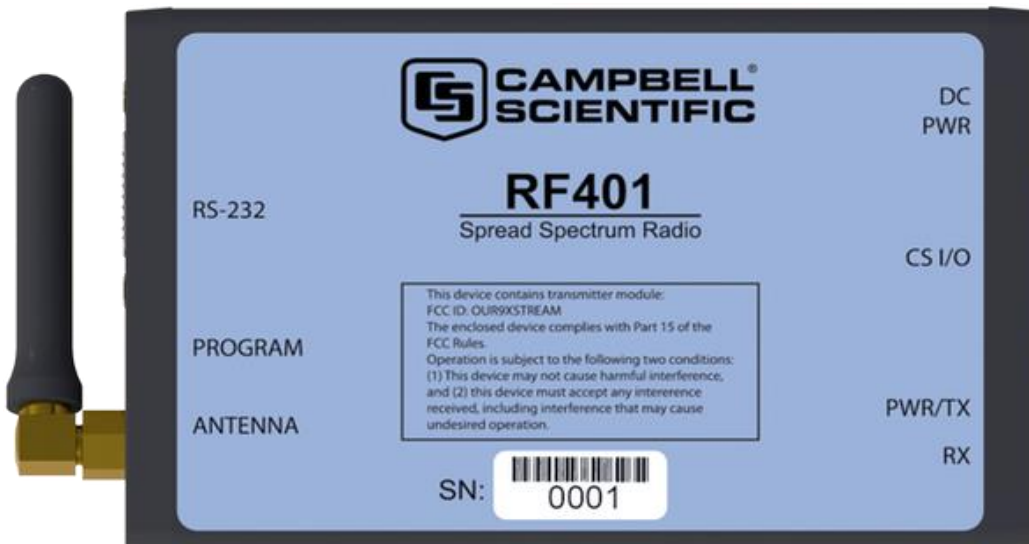


**Figure 83 RF401 Spread Spectrum Radio (Campbell Scientific Inc. 2013)**

#### **4.6.6 Cellular modem**

The Raven X cellular modem (Figure 84) enables the data logger to be accessed through a wireless service network. The modem was configured so that communications with the CR1000 data logger could be made through the internet using TCP/IP communication protocol. A Dynamic IP address was created using the phone number provided by Verizon Wireless.



**Figure 84 Raven X Cellular Modem (Campbell Scientific Inc. 2013)**

#### **4.6.7 Solar panel power supply**

Three solar panels were utilized to provide photovoltaic power to charge three lead acid batteries. Two 20 Watt solar panels were used to charge the batteries at each AVW206-multiplexer at Abutment 1 while a 65 Watt solar panel was used to charge the battery for the data logger and cellular and radio modem at Abutment 2. The solar panels were mounted onto a 21-foot-long, 2 3/8-inch-outside diameter steel pole that was attached to the bridge wing wall with the aid of two triple-legged brackets (Figures 85 and 86). Each bracket is etch-primed with an oven baked final black coating and has a stand-off distance of 12 inches. Each bracket was fastened to the wing wall using 10 lag bolts.



**Figure 85 One 65 Watt Solar Panel at Abutment 2**

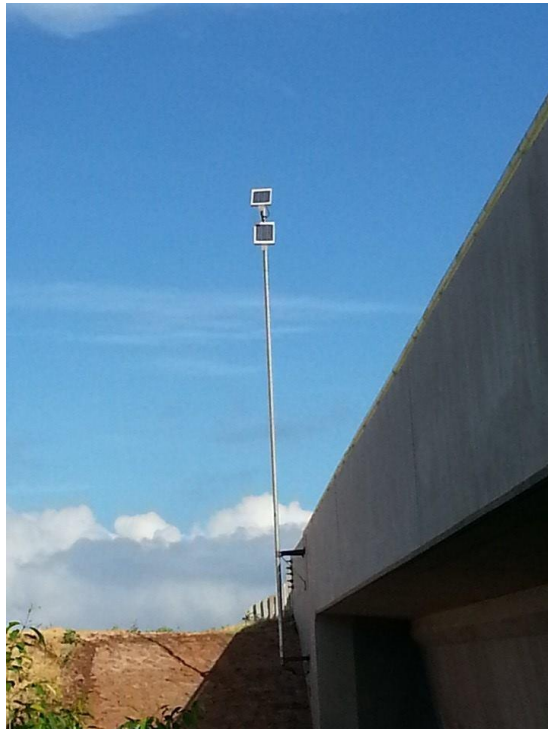


**Figure 86 Two 20 Watt Solar Panels at Abutment 1**

#### 4.7 Software

The Canary Systems MultiLogger Suite 5.0 was used to communicate with and control the data logger. The MultiLogger Suite 5.0 consists of a group of desktop applications, data server, and a web client that runs under Microsoft Internet Information Services (IIS) (Canary Systems). The Multilogger Suite was programmed to do the following: setup network configuration, monitor system, backup system, and collect data. Each individual instrument had to be defined in the software.

The IP address of the modem is needed to setup network connection. Data was monitored and backed up periodically (typically every two weeks). Remote data collection began when the data acquisition system was first installed under the bridge (March 8, 2013).

#### 4.8 Total Station

Settlement of the bridge footings on the GRS abutments was monitored using a TS11 total station and Leica Prisms with L-brackets (Figures 87 and 87). The prisms served as targets for the total station and were installed on the centerline of each footing. Measurements of settlement were taken at key loading events and periodically after construction completion. These readings are not automated and as such, the reading frequency is significantly less than the other instruments.



**Figure 87 TS11 Leica Total Station (www.surveyequipment.com, 2013)**



**Figure 88 Mini-Prism with L-Bracket ([www.sccsurvey.co.uk](http://www.sccsurvey.co.uk), 2013)**

## 5 DATA ANALYSIS

The first five subsections discuss data on the following: (1) vertical pressure below the footing, (2) settlement of the bridge footing supported on the GRS, (3) lateral pressure on the CMU facing and end walls, (4) lateral deflection of the GRS facing, and (5) strain in the superstructure. The sixth subsection describes the relationship between the readings.

### 5.1 Vertical Pressure Below Footing

Sections 5.1.1 and 5.1.2 summarize the vertical pressures below the Abutment 2 footing during and post-construction, respectively.

#### 5.1.1 Vertical Pressures During Construction

The vertical pressure during construction and the associated loading events are summarized in Figure 90 and Table 8. The EP cells were installed at Abutment 2 on May 7, 2012. No load was experienced by the EP cells until footing construction was completed. The pressures due to the footing registered between 169 and 357 psf with an average of 269 psf, equivalent to a 1.8-ft-thick concrete footing. The footing at the location of the EP cells was actually 2.25 ft thick. This corresponds to a surcharge of 338 psf.

On December 12, 2012 the first tub girder was launched across the Kauaula stream. It was observed that the EP cells experienced a slight decrease in average vertical pressure to 170 psf (Figure 90). This decrease was due to rotation of the footing or footing “liftoff” in the transverse direction. On January 10, 2013 all three tub girders were launched across the Kauaula stream. The average pressure increased to 1580 psf. On January 22, 2013 when the majority of the planks were installed on the three tub girders, the vertical pressure increased to an average of 2035 psf. Upon completion of the wing walls and end walls on February 28, 2013 the vertical pressure increased to an average of 3763 psf. Figure 89 shows that the vertical pressure in EP 3 was the highest after the end wall was poured and after backfilling behind Abutment 2. Installed on the backfill side, it is logical that EP 3 was affected most by the vertical pressure due to the wing walls and backfill (Figure 44). When the bridge was completed on April 24, 2013, the pressure increased to an average of 3883 psf. This drop in pressure of about 71 psf can be



considered as reasonable as it is within the range of daily pressure fluctuation observed at the bridge as shown in Figure 91.

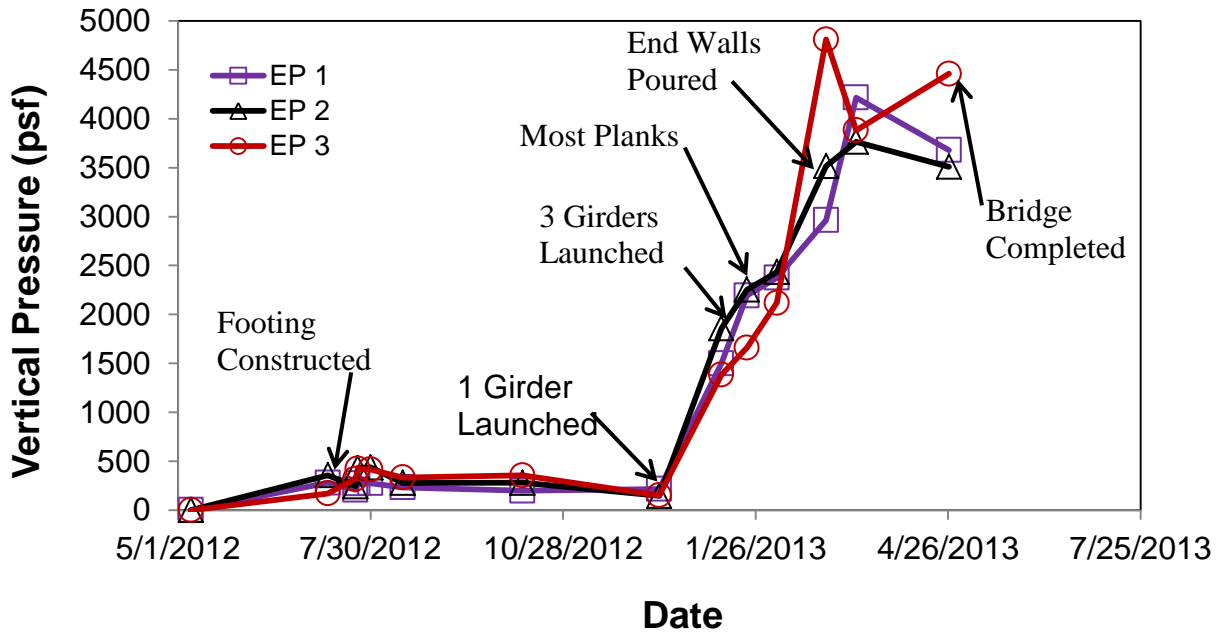


Figure 89 Vertical Pressure for Each EP Cell During Construction

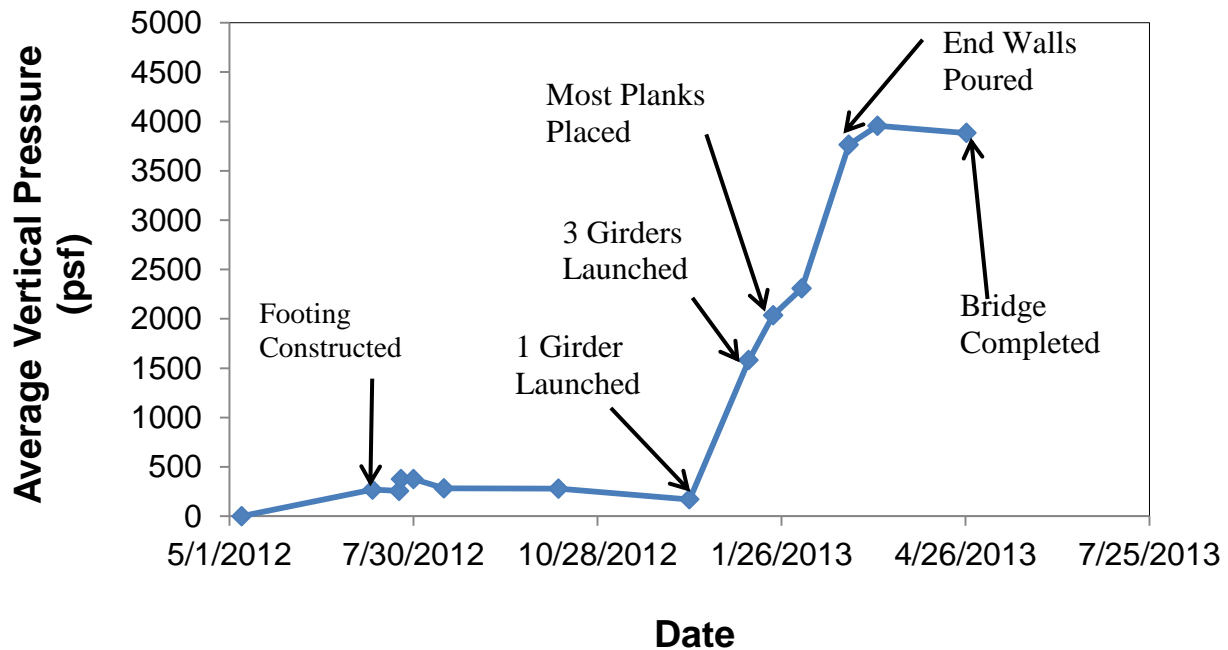


Figure 90 Average Vertical Pressure During Construction

To validate the EP cell readings, the measured pressures were compared to calculated values. The bridge dead load due to the various bridge components is estimated in Table 9. Table 8 displays the measured vertical pressures versus the calculated values utilizing the information from Table 9. The absolute difference between the calculated and the measured pressures ranged from -20 to +7%, excluding the 1 girder launch. As explained previously, the large discrepancy in the calculated and measured stress during this construction event can be attributed to a rotation of the footing since the first tub girder launched was on the mountain (east) side of the footing.

**Table 8 Calculated Vertical Pressure vs Measured Pressure**

<b>Construction Event</b>	<b>Calculated Pressure (psf)</b>	<b>Average Measured Pressure (psf)</b>	<b>Percent Difference (%)</b>
<b>Footing Completed</b>	338	269	-20
<b>1 Girder Launched</b>	735	170	-77
<b>3 Girders Launched</b>	1530	1580	+3
<b>Most Planks Placed</b>	1897	2036	+7
<b>End Walls Poured</b>	3525	3763	+6
<b>Bridge Completed</b>	3778	3883	+3

**Table 9 Estimated Weights of Bridge Components**

<b>Bridge Component</b>	<b>Volume (ft<sup>3</sup>)</b>	<b>Unit Weight of Concrete (pcf)</b>	<b>Weight (lbs)</b>
<b>Footing</b>	619	150	92813
<b>1 Tub Girder</b>	1458	150	218610
<b>All Planks</b>	1512.4	150	226860
<b>End Walls</b>	1514	150	227100
<b>Wearing Surface + Planks</b>	4289	150	643313
<b>All Jersey Barriers</b>	926	150	1389000

### **5.1.2 Post-Construction Vertical Pressures**

Figure 91 displays the data collected from each EP cell starting on April 26, 2013 till September 19, 2013. EP 1 readings fluctuated the most while EP 3 readings fluctuated the least during this

period. A possible explanation for these fluctuations is provided below. A summary of the monthly EP data can be found in Table 10.

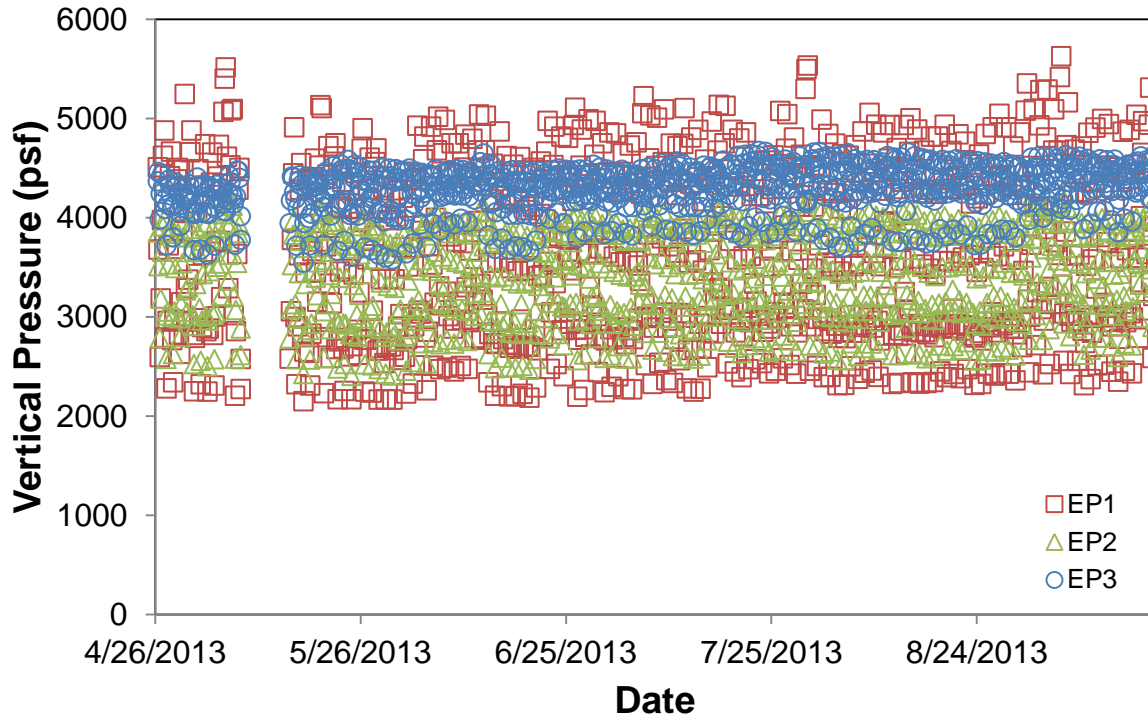


**Figure 91 Vertical Pressure as a Function of Time**

**Table 10 Monthly Summary of Vertical Pressure**

Month	Average Vertical Pressure (psf)			Pressure Range (psf)					
	EP1	EP2	EP3	EP1		EP2		EP3	
				Max	Min	Max	Min	Max	Min
<b>April</b>	3568	3360	4177	5248	2278	4070	2576	4459	3722
<b>May</b>	3524	3335	4188	5515	2148	4205	2406	4583	3546
<b>June</b>	3557	3366	4261	5109	2186	4066	2456	4646	3638
<b>July</b>	3606	3401	4315	5534	2246	4186	2578	4672	3811
<b>August</b>	3516	3373	4315	5354	2312	4113	2558	4663	3700
<b>September</b>	3749	3501	4378	5626	2311	4231	2596	4636	3854

All EP cells displayed cyclic behavior as a function of ambient temperature (Figure 92). The ambient temperature was downloaded from the NOAA website for the Kapalua airport, which is approximately 8 miles north of the Kauaula Stream Bridge. The vertical pressure approaches a maximum when the temperature decreases to a minimum and vice versa. It is postulated that changes in pressure can be attributed to thermal contraction and expansion of the Kauaula Stream Bridge. As the temperature increases to a maximum in the afternoon, the bridge expands and hogs causing the footing on the stream side to lift off and the pressure to drop. The EP cells closer to the stream, EP1 and EP2, experienced a larger fluctuation in pressure compared to EP3, which is farthest from the stream.

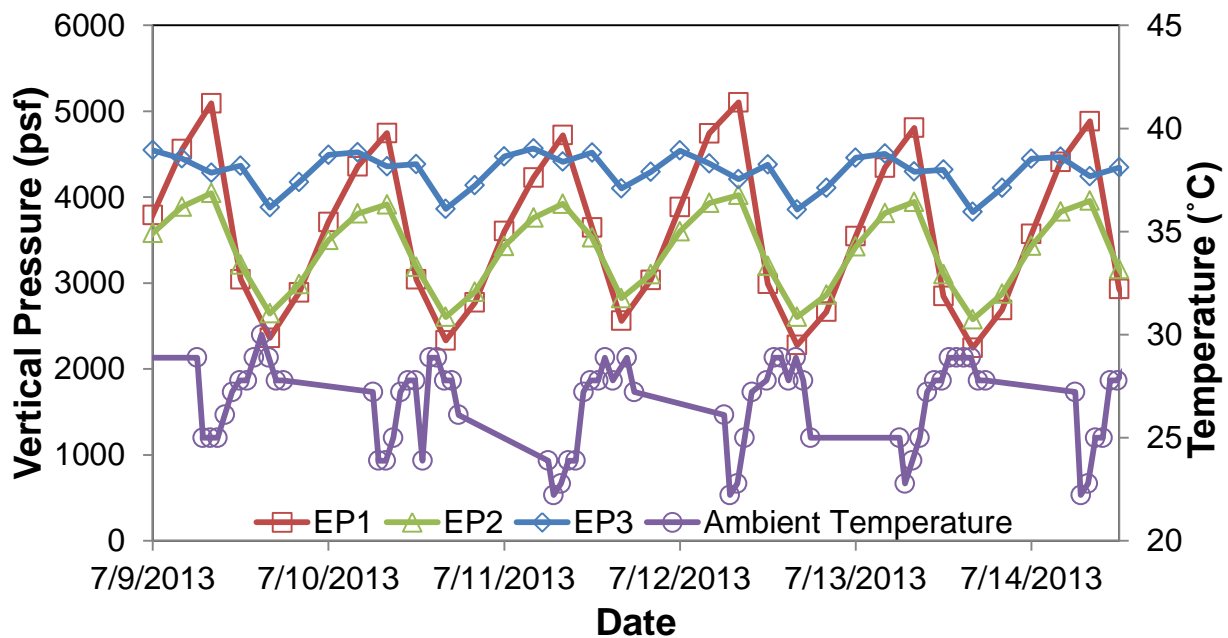


**Figure 92 Vertical Pressure and Ambient Temperature vs Time**

To verify that cycling of the vertical pressures is not due to noise, a dummy EP cell was placed inside the Abutment 2 J-box. The dummy EP cell was covered with bubble wrap to insulate it from temperature changes and was connected to the data acquisition system (Figure 93). Figure 94 displays the pressure fluctuations of all four EP cells with the dummy cell essentially reading zero constantly. Figure 95 displays the instrument temperatures compared to the ambient temperature for a 4 day period in July 2013. EP cells 1, 2 and 3 installed under the footing show little to no temperature variation while the dummy cell shows temperatures ranging from 28.7 °C

to 30.6 °C. The ambient pressure ranged from 22 °C to 30 °C. The dummy cell data suggests that there is little noise from the data acquisition system and the vertical pressure fluctuations in EP cells 1 to 3 appear to be temperature-induced.



**Figure 93 Dummy EP Cell**

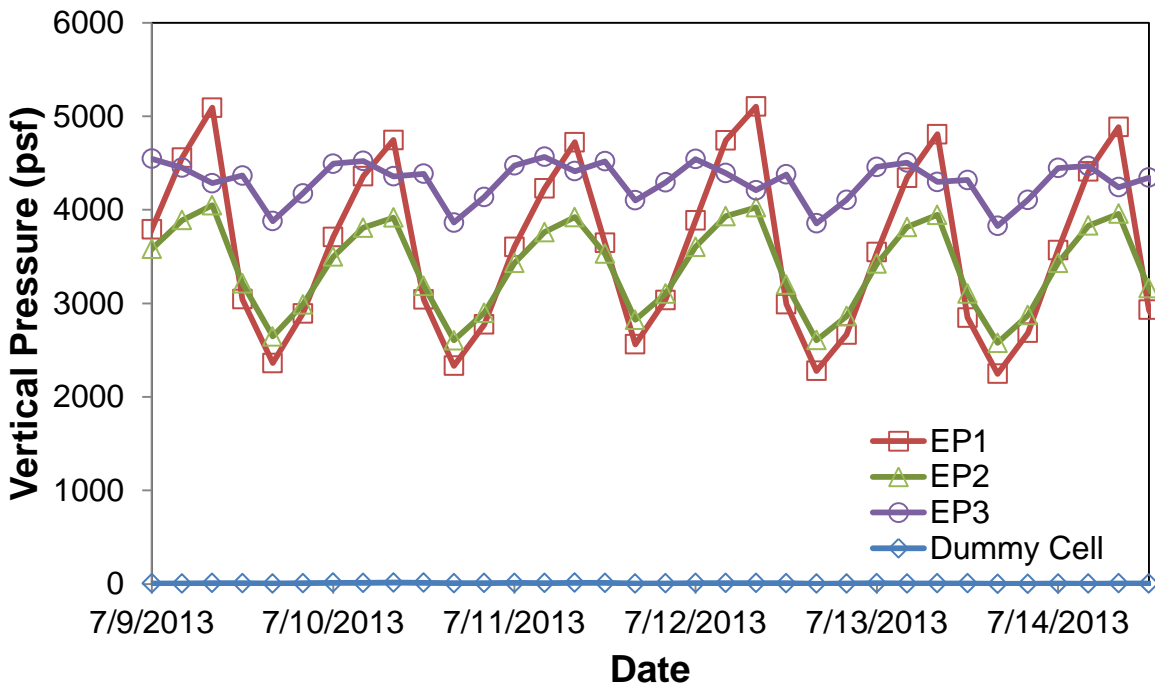


Figure 94 Daily Pressure Fluctuations in EP Cell vs Dummy Cell

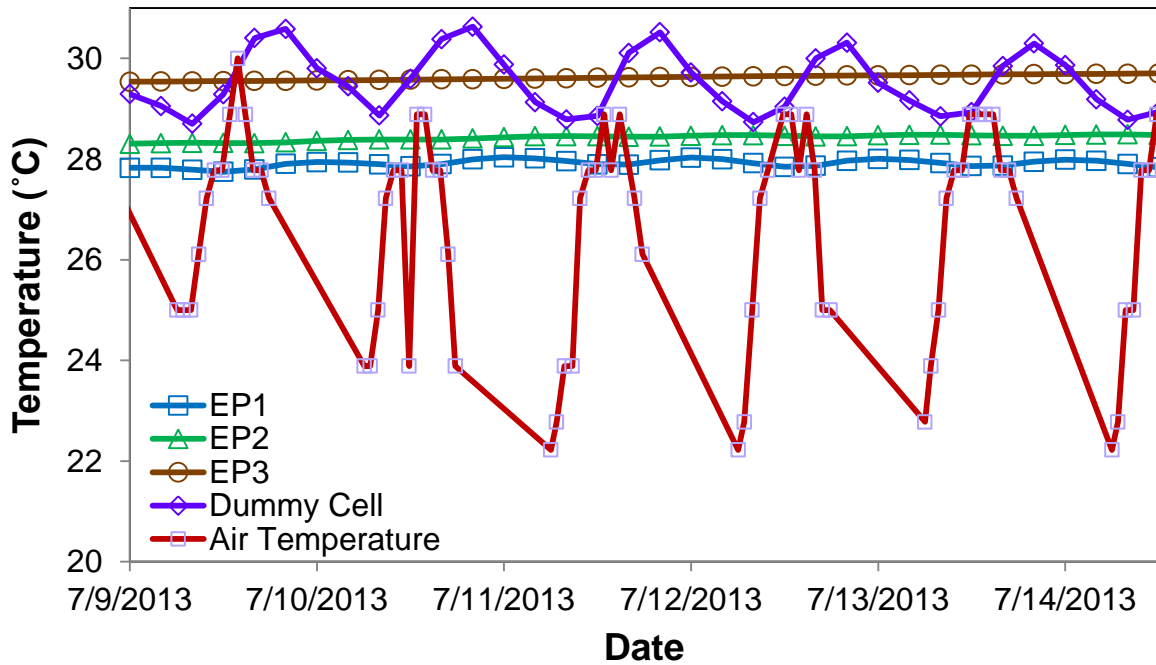
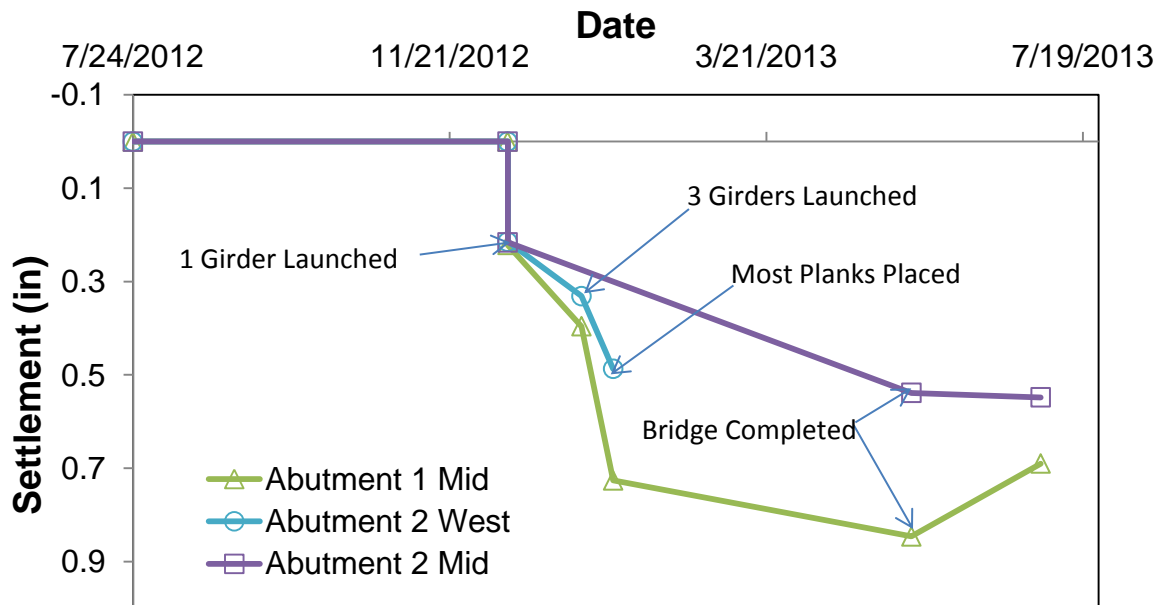


Figure 95 Daily Ambient and Instrument Temperature

## 5.2 Settlement

Total settlement of the Kauaula Stream Bridge abutment footings was monitored utilizing a Leica TS11 total station and Leica Prisms with L-brackets. Initially 4 points were monitored: 3 points on the Abutment 2 footing (middle, mountain (east) side, and ocean (west) side); 1 point in the middle of the Abutment 1 footing. However, the line of sight to the east side of Abutment 2 was blocked by beams and other construction appurtenance. This point was eventually abandoned. The remaining points were surveyed with the total station at key loading events annotated in Figure 96. At the time of writing, the results indicate that the Abutment 1 footing settled the most (0.7 to 0.85 inches) while the Abutment 2 footing had a maximum settlement of 0.55 inches.



**Figure 96 Settlement vs Time**

Table 11 summarizes all the footing settlement measured. Blacked out entries indicate that points could not be surveyed because the line of sight to the points were blocked by beams and other construction appurtenance. Eventually, the Abutment 2 West survey point also had to be abandoned because the L-bracket was removed and the screw hole concreted by the contractor for aesthetic purposes prior to turning the bridge over to the owner.



**Table 11 Settlement Recorded**

Date	Construction Event	Displacement (in)		
		Abutment 1 Mid	Abutment 2 Mid	Abutment 2 West
12/13/2012	Zero Readings Prior to Girder Launch	0		
12/13/2012	After Girder 1 Launch	0.22	0.22	0.21
1/10/2013	After All 3 Girders Launched	0.40		0.33
1/22/2013	Most Planks Placed	0.73		0.49
5/15/2013	Bridge Completed	0.85	0.54	
7/3/2013	Two Months after Completion	0.69	0.55	

### 5.3 Lateral Pressure

The lateral earth pressure measurements behind the CMU and behind the end walls are discussed in sections 5.3.1 and 5.3.2, respectively.

#### 5.3.1 CMU

Sections 5.3.1.1 and 5.3.1.2 discuss the lateral pressures behind the CMU during and post-construction, respectively.

##### 5.3.1.1 Lateral Pressures During Construction

Lateral earth pressure readings were recorded behind the CMU blocks as each lift was constructed. Lateral pressure cells were placed on the first, fifth and ninth CMU blocks from the bottom of the GRS wall. The lateral pressures were compared to Rankine active and at-rest values. To calculate the lateral pressures, the soil unit weight,  $\gamma$ , was estimated using Equation 11, the dry unit weight ( $\gamma_d$ ) and water content ( $w$ ).  $\gamma_d$  and  $w$  were measured using a nuclear gage for each lift during construction. Then,  $\sigma_v$  was calculated using Equation 12. The at-rest earth pressure coefficient ( $K_o$ ) was calculated using Equation 13 where  $\phi$  = friction angle of the soil backfill. The Rankine active earth pressure coefficient ( $K_a$ ) was calculated using Equation

14. Finally the Rankine active and at-rest pressures were calculated using Equation 15, where  $K = K_o$  for at-rest and  $K = K_a$  for Rankine active earth pressures. The calculated at-rest, Rankine active earth pressures, Wu and Soong and Koerner pressures are shown in Tables 12-15.

$$\gamma = \gamma_d(1 + w) \quad (11)$$

$$\sigma_v = \sum_{i=1}^n (\gamma_i z_i) \quad (12)$$

$$K_o = 1 - \sin\phi \quad (13)$$

$$K_a = \frac{1 - \sin\phi}{1 + \sin\phi} \quad (14)$$

$$\sigma_h = K \sigma_v \quad (15)$$

At a depth of one foot of soil above the fatbacks, two different lateral earth pressure trends were observed. FB 8 (Figure 99) read essentially negligible lateral earth pressures (they were actually negative). The negligible pressure is likely due to (1) the CMU blocks moving away from the GRS because it was not restrained during compaction and/or (2) the geotextile restraining the soil from moving laterally. If there is no movement of the soil, there will be no pressures exerted on the CMU blocks. Meanwhile FB 6 (Figure 97) and FB 7 (Figure 98) read positive pressures greater than the Rankine active and at-rest values, which indicates that the CMU blocks likely did not move forward as much during backfilling. The lack of movement plus the effects of compaction caused the lateral pressures to be greater than the Rankine active and at-rest values. As the height of backfill increased to about three feet, the CMU blocks likely moved away from the GRS as the pressures in FB7 and FB 8 were essentially zero. However when the backfill height approached 3.5 feet or more, the CMU blocks appear more restrained. This caused FB 7 and FB 8 to read positive pressures that are close to the Rankine active earth pressure.

One caveat to the above observations is that the fatback cells are temperature sensitive. When they are read at different times of the day in Lahaina, Maui with no load on them, the pressures can fluctuate from 0 to in excess of 400 psf (Section 5.3.1.2). During this time, the temperatures in the fatbacks ranged from about 20°C to about 40 °C. However, once the sensors are buried in the ground, the soil temperature does not vary by much and hence the readings should be less affected by the ambient temperature.

After completion of the GRS abutment, lateral earth pressures during key construction events were recorded (Figures 101 and 102 and Table 16 and 17). After construction of the abutment footings were completed (July 10, 2012), all FB cells experienced an increase in lateral earth pressure. This increase is due to placement of rip rap in front of the CMU wall. After all three tub girders were launched across the Kauaula stream (January 10, 2013), the lateral earth pressure increased for all FB cells except FB8. After the majority of the planks were installed on the three tub girders (January 22, 2013), all FB cells experienced a decrease in lateral earth pressure. However after this construction event, all the FB readings remained relatively constant as the end walls and wing walls were constructed.

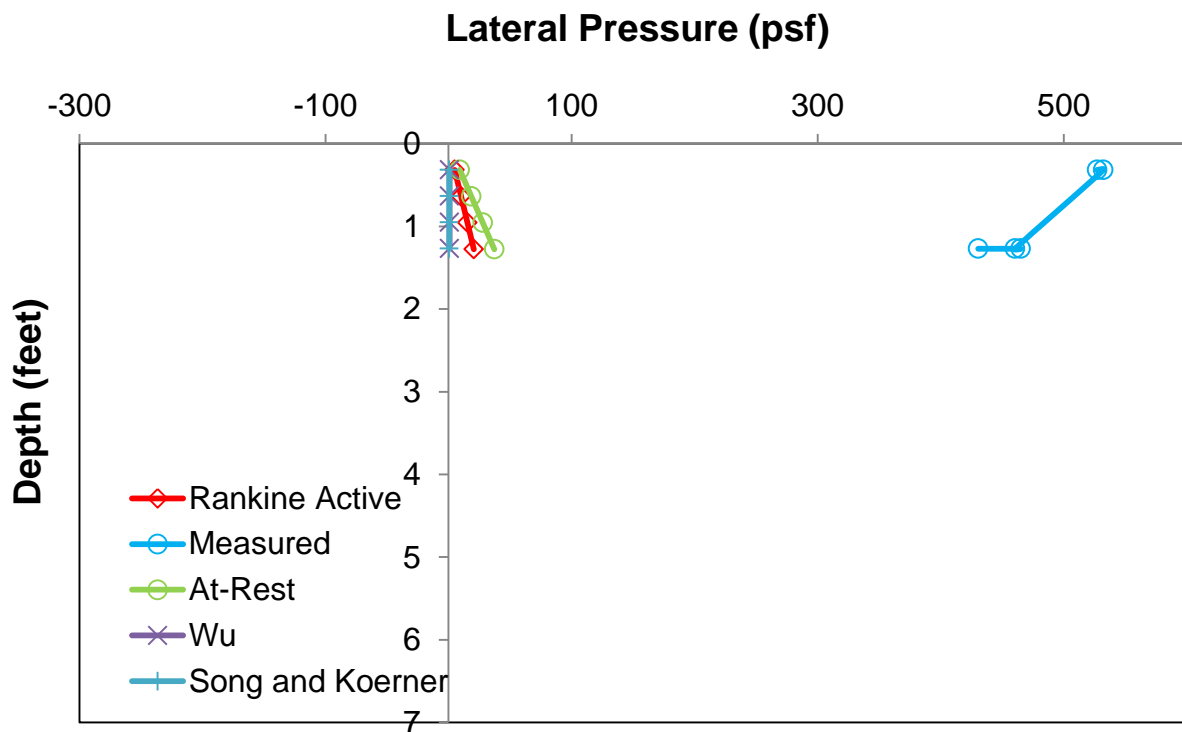


**Figure 97 Measured Lateral Pressures vs Rankine Active, At Rest Pressures, Wu, and Soong and Koerner Estimations (FB 6 at Abutment 1)**

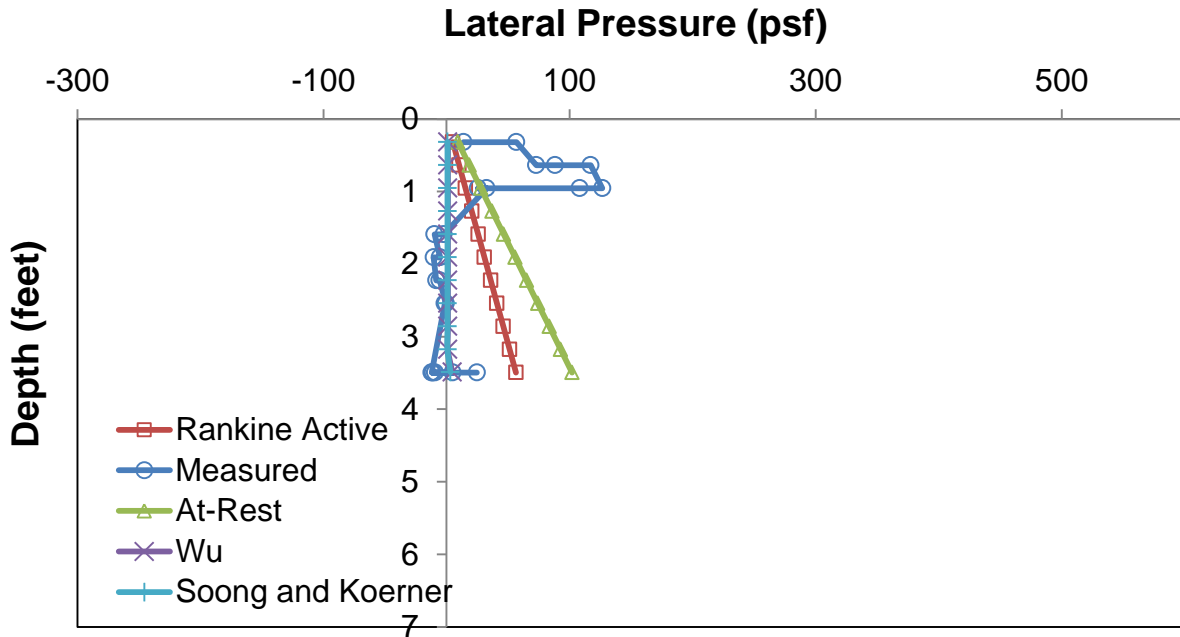


**Figure 98 Measured Lateral Pressures vs Rankine Active, At Rest Pressures, Wu, and Soong and Koerner Estimations (FB 7 at Abutment 1)**

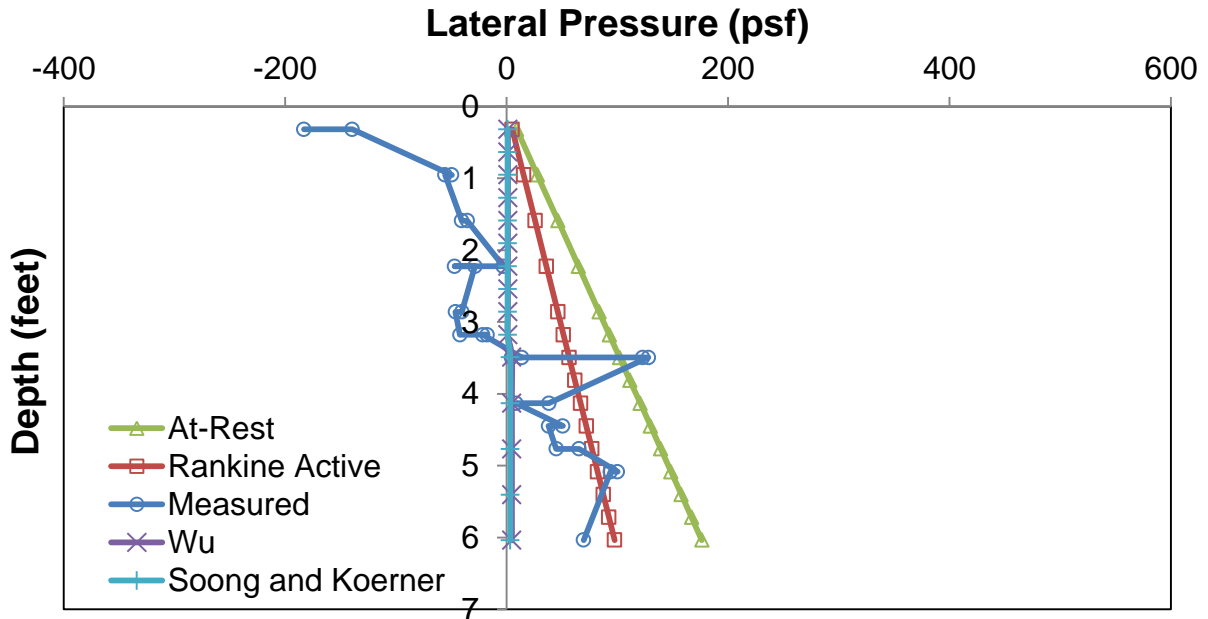


**Figure 99 Measured Lateral Pressures vs Rankine Active, At Rest Pressures, Wu, and Soong and Koerner Estimations (FB 8 at Abutment 1)**

**Table 12 Rankine Active and At Rest Earth Pressures (FB6)**

Abutment 1								
Layer	$\gamma_{d1}^a$ (psf)	$\gamma_{d2}^b$ (psf)	$w_1^a$ (%)	$w_2^b$ (%)	$\gamma$ (psf)	$\sigma_v$ (psf)	$\sigma_{ha}^c$ (psf)	$\sigma_{ho}^d$ (psf)
8.5	142	140	6.6	7.3	150	48	5.11	9.23
9	141	140	6.4	6.7	150	95	10.19	18.41
9.5	143	143	7.0	6.4	152	144	15.35	27.74
10	142	141	7.2	6.2	151	192	20.49	37.03
10.5	141	142	6.4	7.0	151	240	25.62	46.29

<sup>a</sup>Measured on the mountain side with a nuclear gage

<sup>b</sup>Measured on the ocean side with a nuclear gage

<sup>c</sup>Active earth pressure coefficient,  $K_a$ , is 0.08 based on  $\phi = 53.8^\circ$

<sup>d</sup>At-rest earth pressure coefficient,  $K_o$ , is 0.15 based on  $\phi = 53.8^\circ$

**Table 13 Rankine Active and At Rest Earth Pressures (FB7)**

Abutment 1								
Layer	$\gamma_{d1}^a$ (psf)	$\gamma_{d2}^b$ (psf)	$w_1^a$ (%)	$w_2^b$ (%)	$\gamma$ (psf)	$\sigma_v$ (psf)	$\sigma_{ha}^c$ (psf)	$\sigma_{ho}^d$ (psf)
5	141	142	7.1	7.6	152	48.3	3.97	7.33
5.5	143	140	7.1	6.5	151	96.3	7.92	14.6
6	140	142	7.9	7.3	151	144	11.8	21.9
6.5	140	143	7.0	6.5	151	192	15.8	29.2
7	144	143	7.1	6.5	153	241	19.8	36.6
7.5	143	140	7.1	6.8	151	289	23.7	43.9
8	142	140	6.6	7.3	150	337	27.6	51.1
8.5	141	140	6.4	6.7	150	384	31.6	58.4
9	143	143	7.0	6.4	152	433	35.5	65.7
9.5	142	141	7.2	6.2	151	481	39.5	73.0
10	141	142	6.4	7.0	151	529	43.4	80.3

<sup>a</sup>Measured on the mountain side with a nuclear gage

<sup>b</sup>Measured on the ocean side with a nuclear gage

<sup>c</sup>Active earth pressure coefficient,  $K_a$ , is 0.08 based on  $\phi = 53.8^\circ$

<sup>d</sup>At-rest earth pressure coefficient,  $K_o$ , is 0.15 based on  $\phi = 53.8^\circ$

**Table 14 Rankine Active and At Rest Earth Pressures (FB8)**

Abutment 1								
Layer	$\gamma_{d1}^a$ (psf)	$\gamma_{d2}^b$ (psf)	$w_1^a$ (%)	$w_2^b$ (%)	$\gamma$ (psf)	$\sigma_v$ (psf)	$\sigma_{ha}^c$ (psf)	$\sigma_{ho}^d$ (psf)
1	141	140	7.4	5.4	150	47.5	3.91	7.22
2	143	141	7.1	5.7	151	143	11.8	21.8
3	147	140	6.2	6.6	152	240	19.8	36.5
4	143	140	6.8	6.5	151	336	27.6	51.1
5	141	142	7.1	7.6	152	433	35.6	65.7
5.5	143	140	7.1	6.5	151	481	39.5	73.0
6	140	142	7.9	7.3	151	529	43.5	80.3
6.5	140	143	7.0	6.5	151	577	47.4	87.6
7	144	143	7.1	6.5	153	625	51.4	95.0
7.5	143	140	7.1	6.8	151	673	55.4	102
8	142	140	6.6	7.3	150	721	59.3	110
8.5	141	140	6.4	6.7	150	769	63.2	117
9	143	143	7.0	6.4	152	817	67.2	124
9.5	142	141	7.2	6.2	151	865	71.1	131
10	141	142	6.4	7.0	151	913	75.1	139

<sup>a</sup>Measured on the mountain side with a nuclear gage

<sup>b</sup>Measured on the ocean side with a nuclear gage

<sup>c</sup>Active earth pressure coefficient,  $K_a$ , is 0.08 based on  $\phi = 53.8^\circ$

<sup>d</sup>At-rest earth pressure coefficient,  $K_o$ , is 0.15 based on  $\phi = 53.8^\circ$

**Table 15 Abutment 1 Wu and Soong and Koerner Lateral Pressures**

Abutment 1				
Layer	$\gamma$ (psf)	$S_v$ (ft)	Wu (psf)	Soong and Koerner (psf)
9	150	0.32	1.2	0.8
5	150	0.64	4.7	3.3
1	151	0.64	4.8	3.3

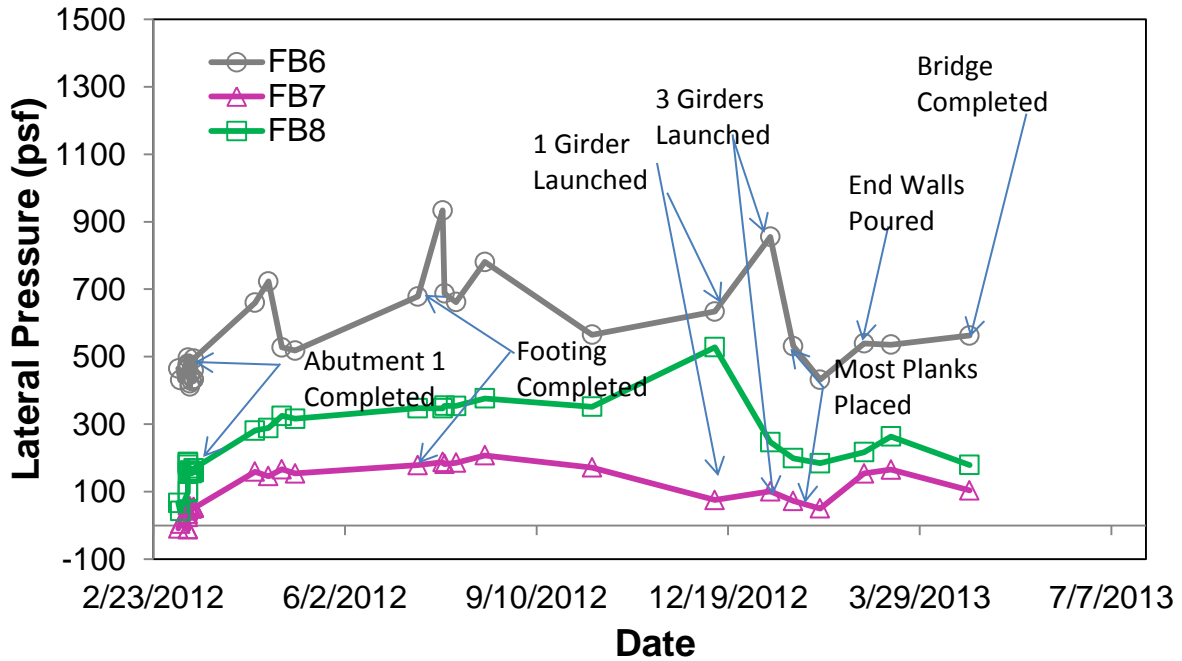


**Figure 100 Abutment 1 Lateral Pressure During Construction**

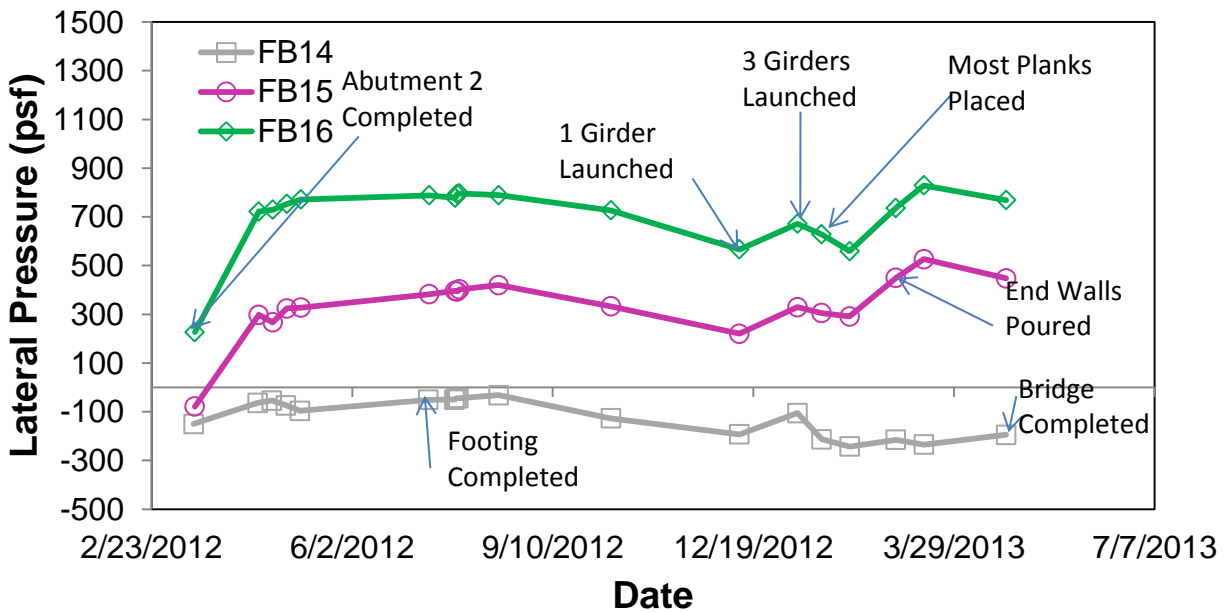


**Figure 101 Abutment 2 Lateral Pressure During Construction**



**Table 16 Abutment 1 Measured Lateral Pressure**

<b>Construction event</b>	<b>FB 6 Measured Pressure (psf)</b>	<b>FB 7 Measured Pressure (psf)</b>	<b>FB 8 Measured Pressure (psf)</b>
<b>Abutment 1 Completed</b>	465	-9.2	67
<b>Footing Completed</b>	678	178	347
<b>1 Girder Launched</b>	634	75	528
<b>3 Girders Launched</b>	855	101	247
<b>Most Planks Placed</b>	531	72	199
<b>End Walls Poured</b>	539	154	217
<b>Bridge Completed</b>	563	104	179

**Table 17 Abutment 2 Measured Lateral Pressure**

<b>Construction event</b>	<b>FB 14 Measured Pressure (psf)</b>	<b>FB 15 Measured Pressure (psf)</b>	<b>FB 16 Measured Pressure (psf)</b>
<b>Abutment 2 Completed</b>	-150	-78.5	227
<b>Footing Completed</b>	-51	382	788
<b>1 Girder Launched</b>	-193	221	567
<b>3 Girders Launched</b>	-106	329	672
<b>Most Planks Placed</b>	-213	305	628
<b>End Walls Poured</b>	-215	449	737
<b>Bridge Completed</b>	-195	448	769

### 5.3.1.2 Post-Construction Lateral Pressures

Figures 102 and 103 display the FB data from April 26, 2013 till September 19, 2013. A summary of the monthly FB data can be found in Tables 18 and 19. All FB cells recorded an increase in lateral earth pressure during this period. For example, FB 7 recorded an increase in average lateral pressure of 59 psf (from 134 psf to 193 psf), which is the smallest increase observed (Table 18). The largest increase of 131 psf occurred in FB 16 (from 813 to 944 psf). This increase consistently occurred in all the CMU fatbacks. It is possible that this slight increase in lateral pressure with time is due to the (1) effects of soil ratcheting or continuous “pounding” of the footing on the GRS backfill caused as a result of superstructure thermal

expansion and contractions; or (2) warming of the ambient temperature from spring to summer (Figure 104).

**Table 18 Monthly Average Lateral Pressure**

Month	Average Lateral Pressure (psf)					
	FB6	FB7	FB8	FB14	FB15	FB16
May	613	134	219	-183	497	813
June	654	156	245	-161	524	850
July	681	171	268	-139	543	878
August	725	190	302	-118	564	922
September	707	193	315	-113	567	944

**Table 19 Monthly Lateral Pressure Range**

Month	Lateral Pressure (psf)											
	FB6		FB7		FB8		FB14		FB15		FB16	
	Max	Min	Max	Min	Max	Min	Max	Min	Max	Min	Max	Min
May	711	553	192	96	267	181	208	155	558	444	874	750
June	770	579	221	105	306	191	183	133	573	465	906	779
July	811	612	252	130	328	221	168	94	595	492	954	814
August	834	654	261	145	368	263	140	78	609	525	980	869
September	842	625	268	137	389	260	136	68	626	506	1015	872

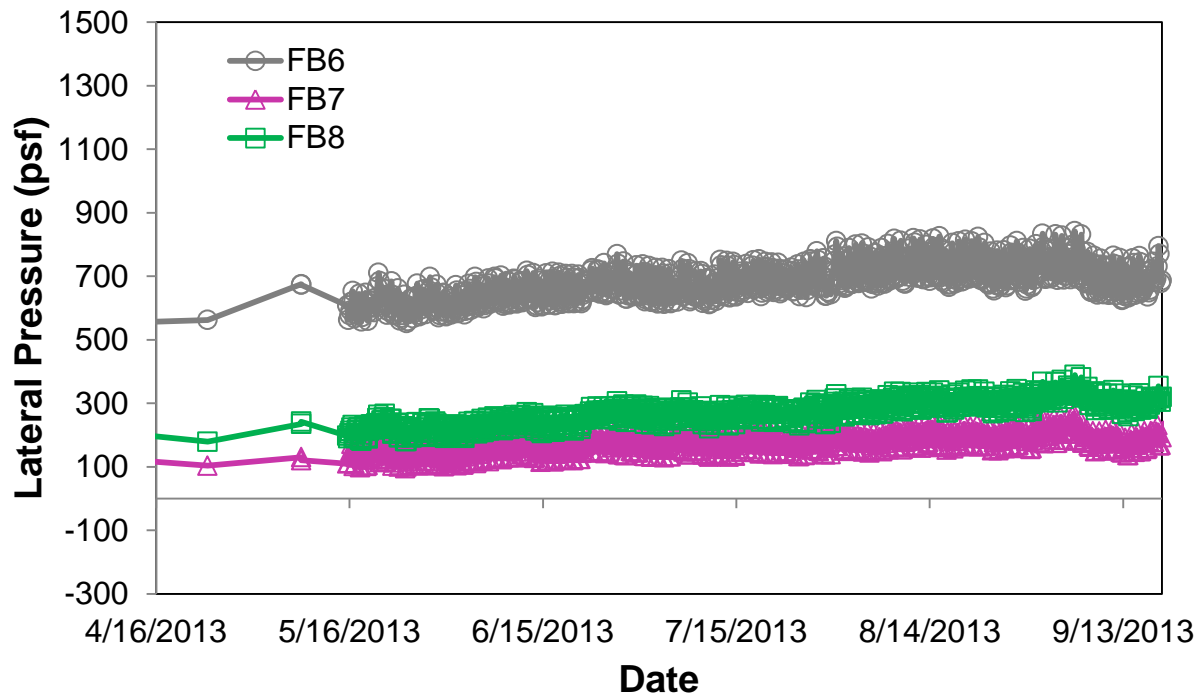


**Figure 102 Abutment 1 Lateral Pressure as a Function of Time**

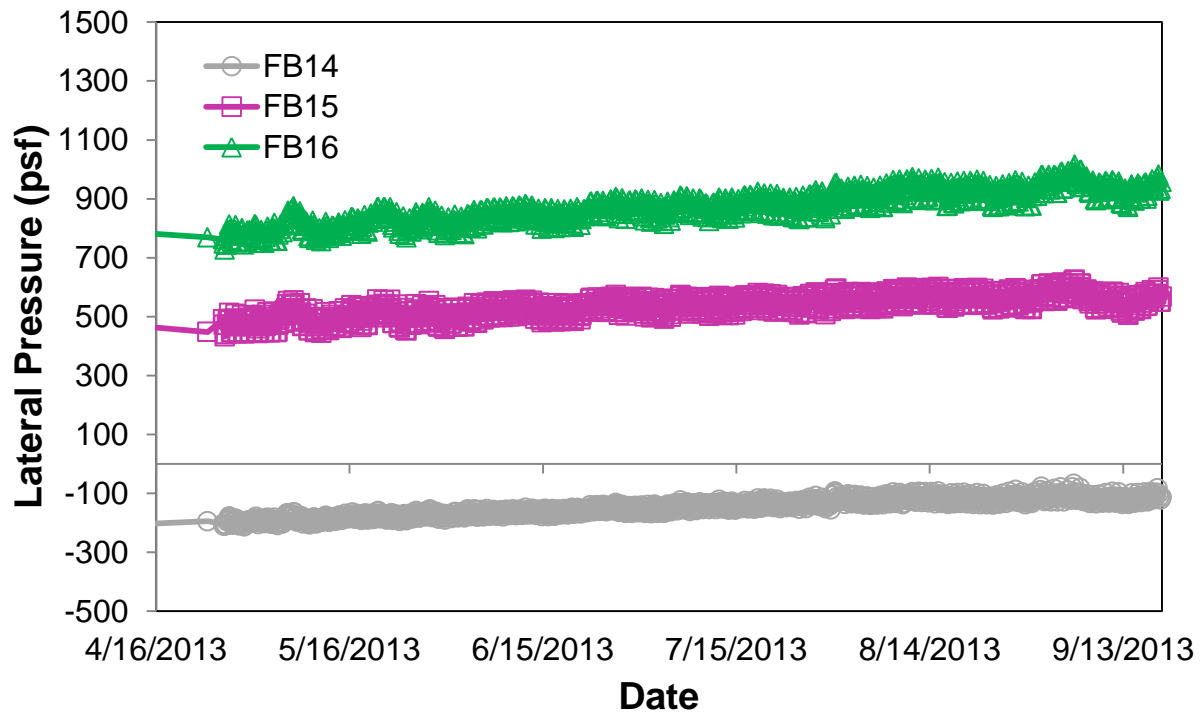


**Figure 103 Abutment 2 Lateral Pressure as a Function of Time**

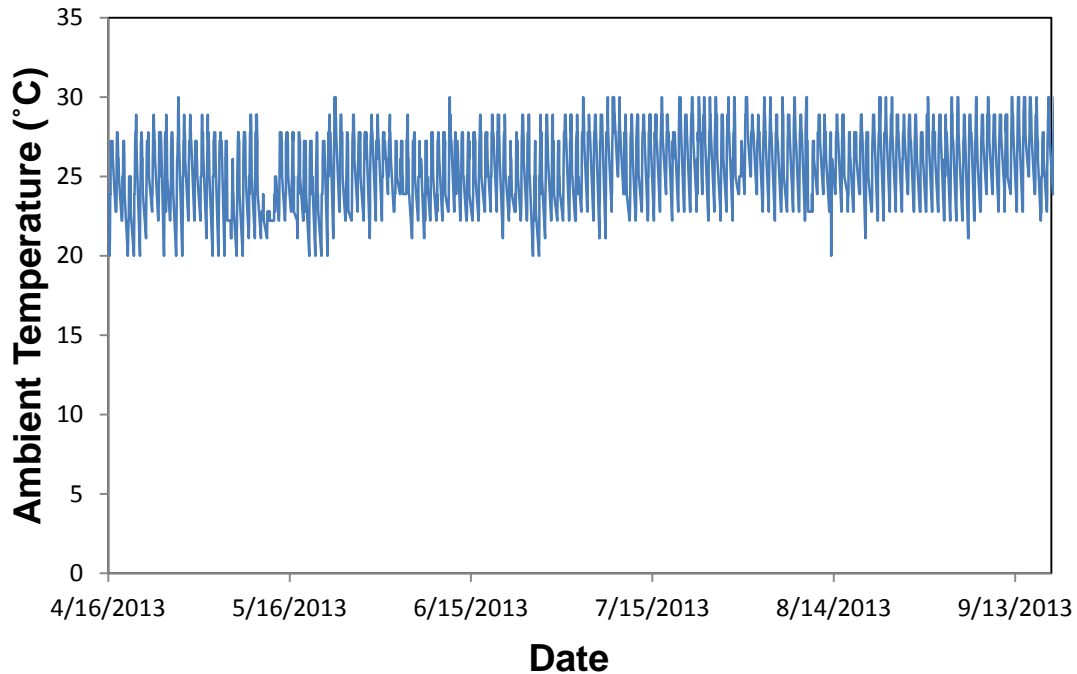


**Figure 104 Ambient Temperature versus Time**

When the FB pressures are plotted together with ambient temperature (Figures 105 and 106), it was observed that the lateral pressure peaked with temperature. It was first realized that the FBs were temperature sensitive during construction of Abutment 2.

After constructing the first five CMU courses at Abutment 2 with FB 15, FB 16 and the backfill behind them compacted in place, the Contractor halted work at Abutment 2. However, FB 15 and 16 were continually monitored. It was found that the FB cells (especially the shallower FB15 with only 4 inches of soil cover) were sensitive to the temperature as shown by Figure 107. The lateral earth pressures are supposed to remain constant due to the absence of construction activity. However the lateral earth pressures would increase as the gage temperature increased. To further investigate the effects of temperature on the FB readings, ten FB cells intended for the end walls were placed out in the sun with no load applied. Periodically, the lateral pressures and the corresponding gage temperatures were recorded. Despite the fact that the pressure on each FB cell should remain 0, it was observed that the lateral pressure increased linearly with increasing temperature. Figure 108 displays the results of this observation. A temperature gradient range of 11.337 psf/°C to 20.564 psf/°C was measured.

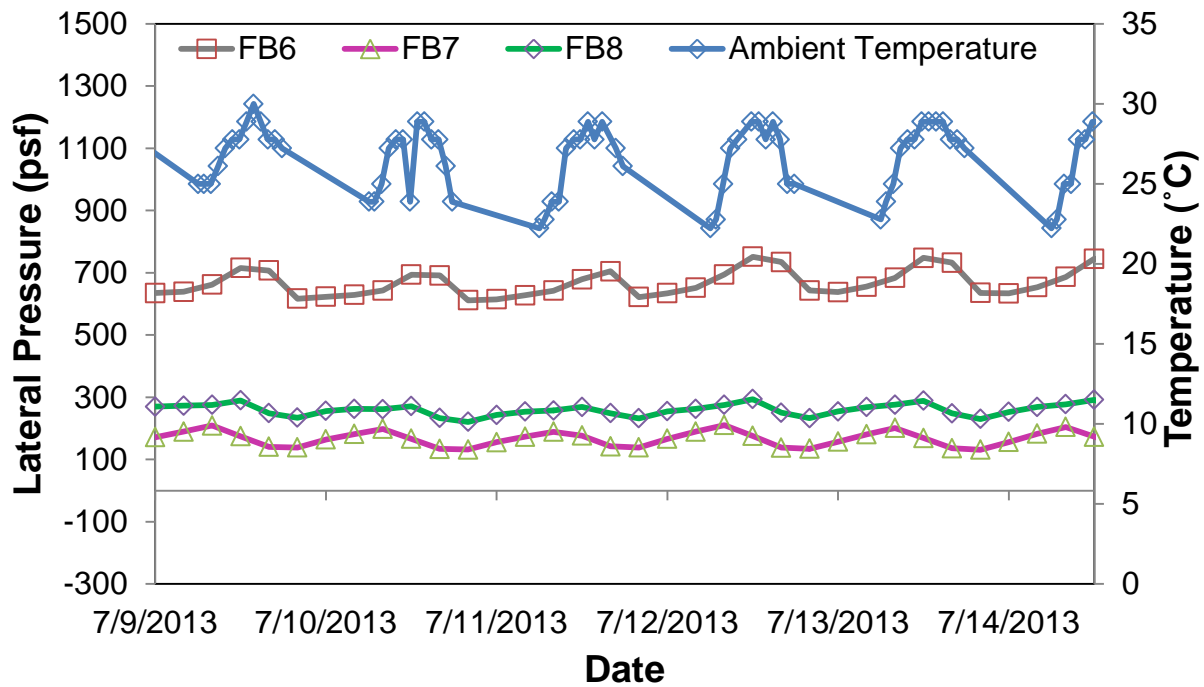


Figure 105 Abutment 1 Lateral Pressure and Ambient Temperature vs Time

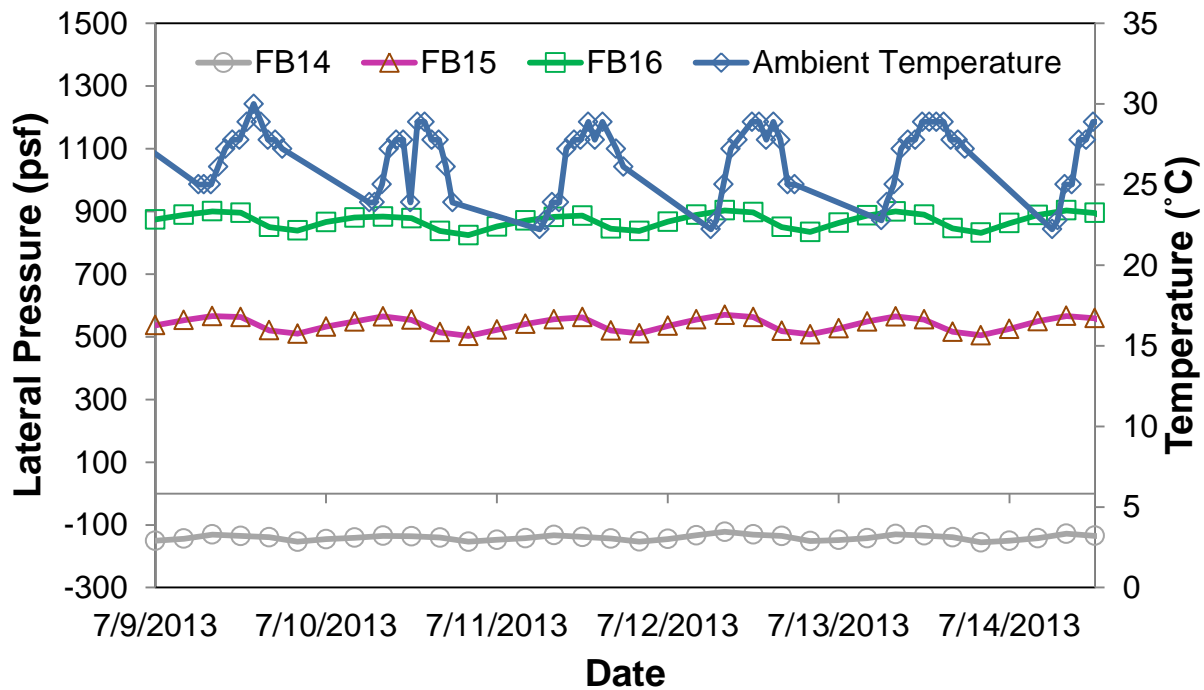


Figure 106 Abutment 2 Lateral Pressure and Ambient Temperature vs Time

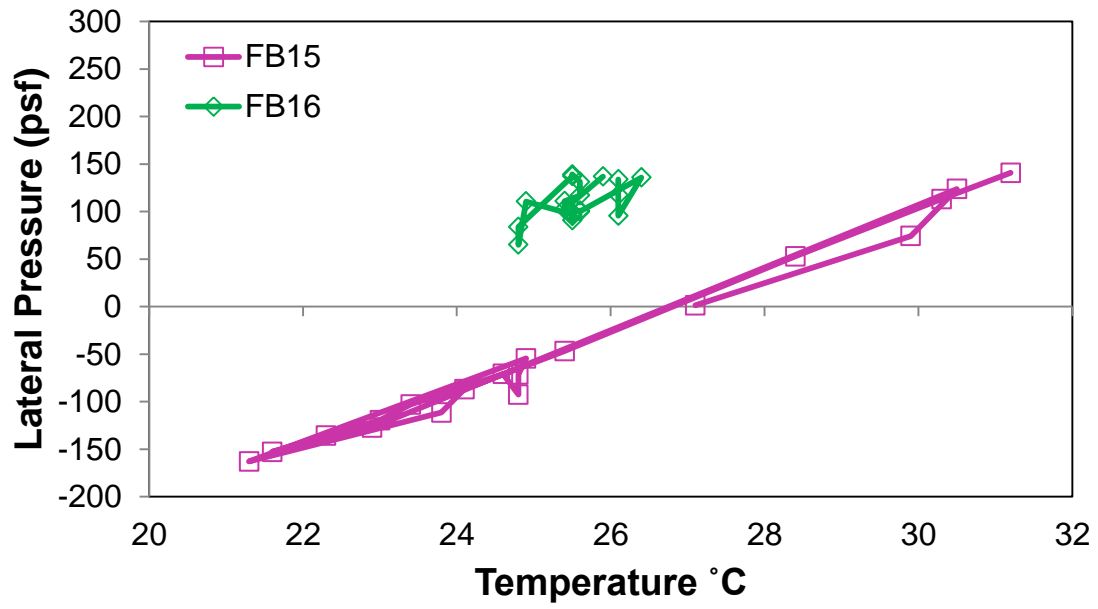


Figure 107 Lateral Pressure vs Temperature



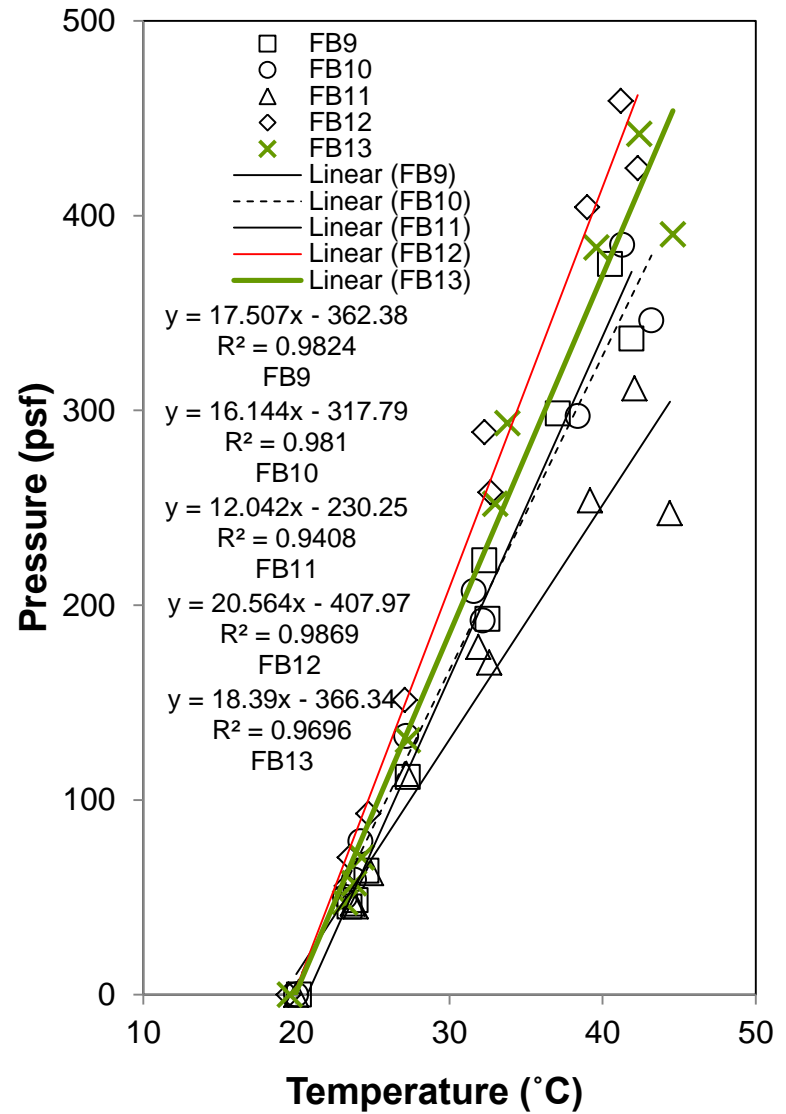
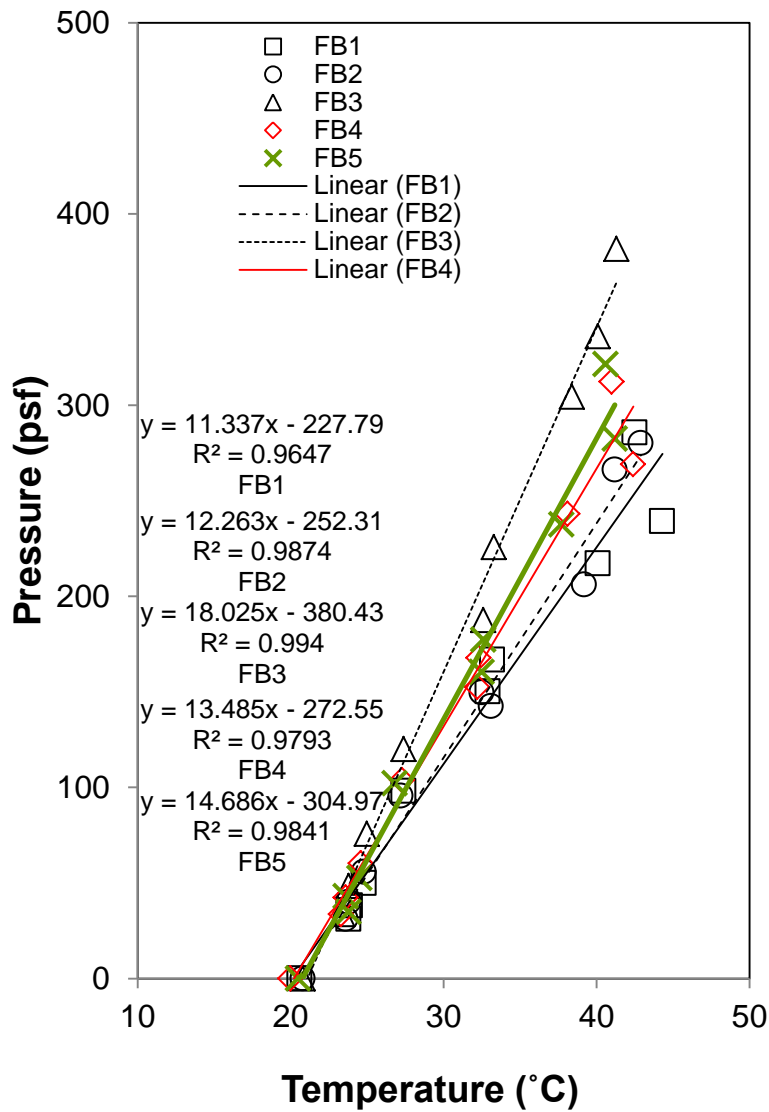


Figure 108 Measured Pressure vs Gage Temperature

### 5.3.2 End Wall

Sections 5.3.2.1 and 5.3.2.2 discuss the lateral pressures behind the end walls during and post-construction, respectively

#### 5.3.2.1 Lateral Pressures During Construction

With the CMU blocks, the lateral pressures behind the end walls were compared to the Rankine active and at-rest pressures. For these comparisons, the temperature gradients from Figure 107 were used to standardize the pressure readings to a temperature of 31°C. This temperature was chosen as it was approximately in the middle of the range of temperatures used to establish the temperature gradients in Figure 108. Figures 109-113 display the measured and standardized lateral pressures. Each FB recorded lateral pressures larger than the at-rest values after being standardized. The lateral earth pressures were larger due to locked-in compaction induced stresses.

The lateral pressures behind the end walls were larger than those behind the CMU. This is because the CMU blocks are partially deformable compared to the end walls. Being more rigid, the end walls did not allow any movement thereby resulting in higher lateral pressures.

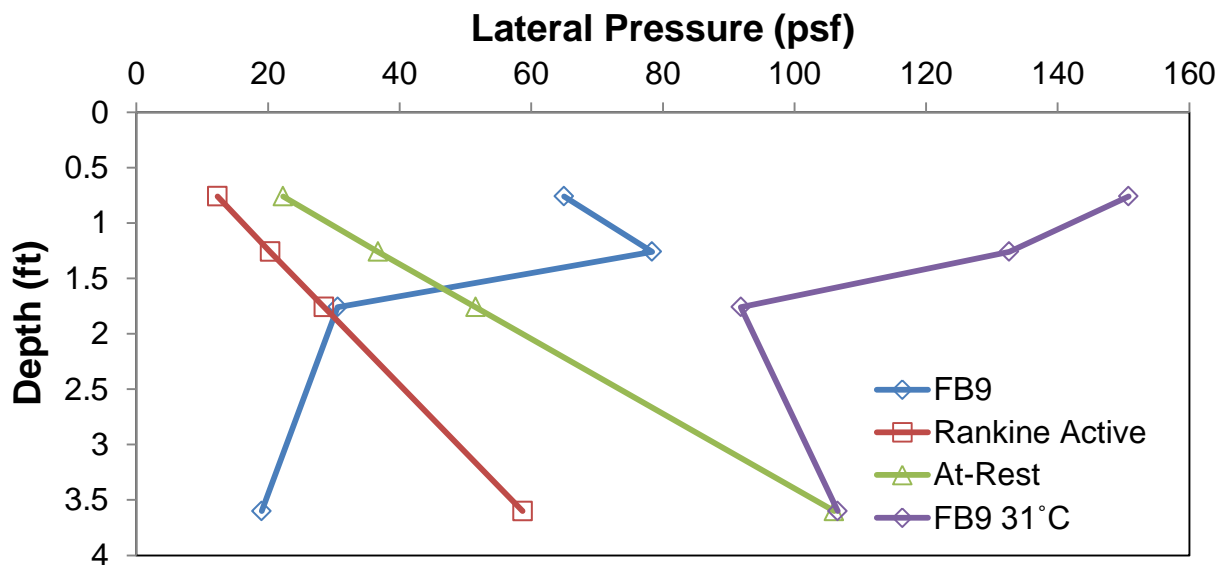


Figure 109 FB9 Lateral Pressure vs Depth

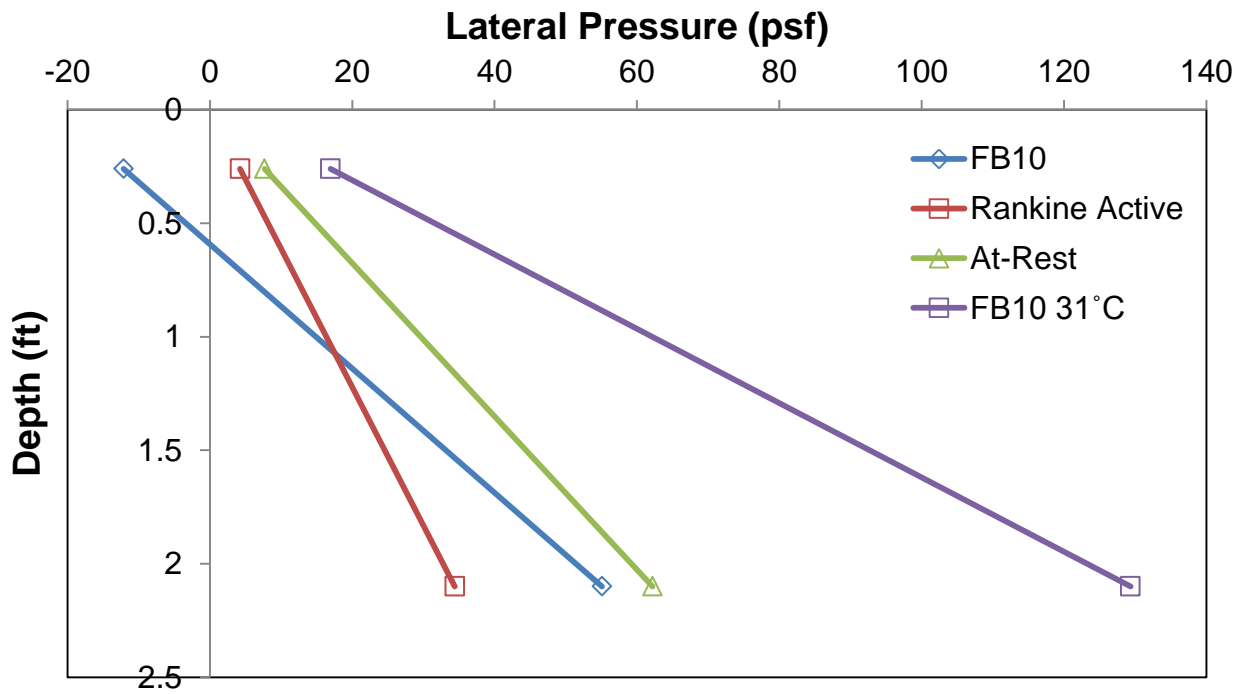


Figure 110 FB10 Lateral Pressure vs Depth

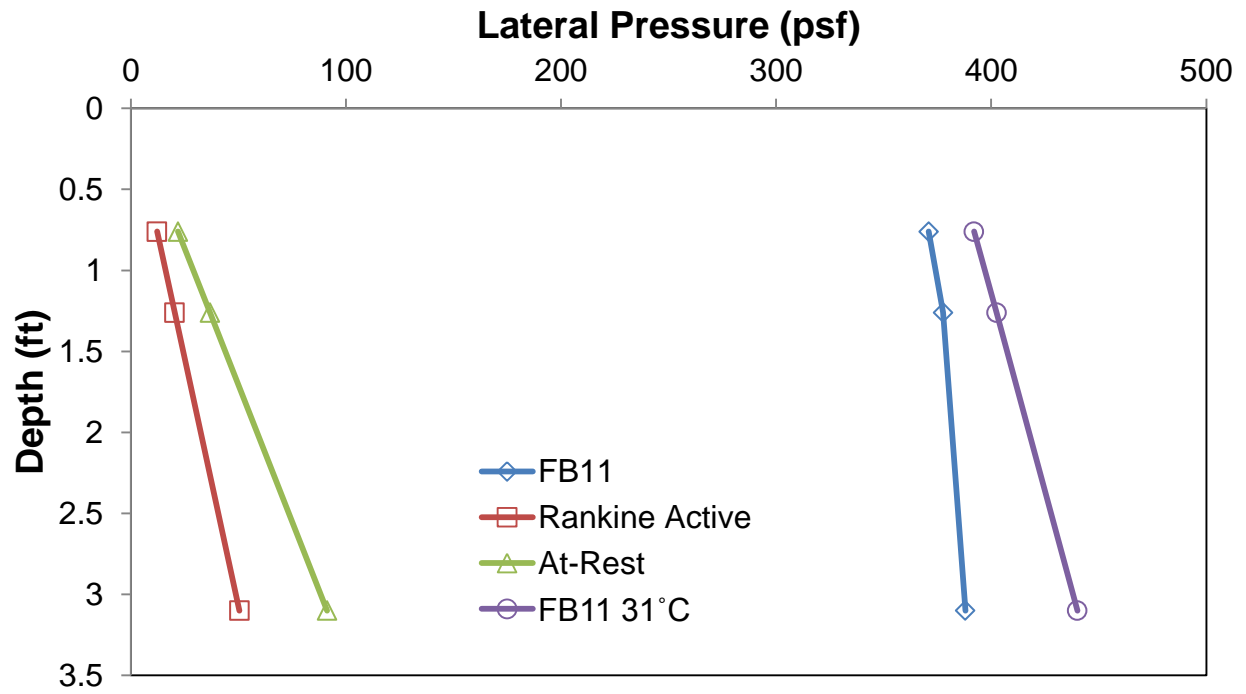
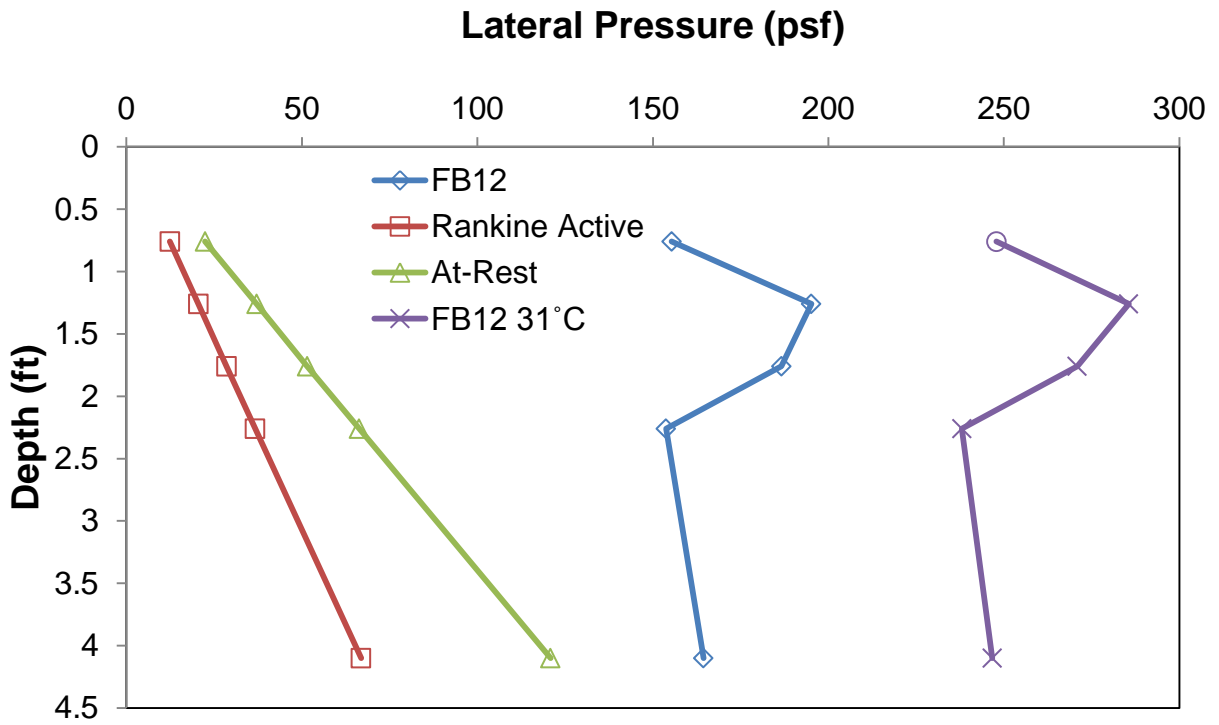
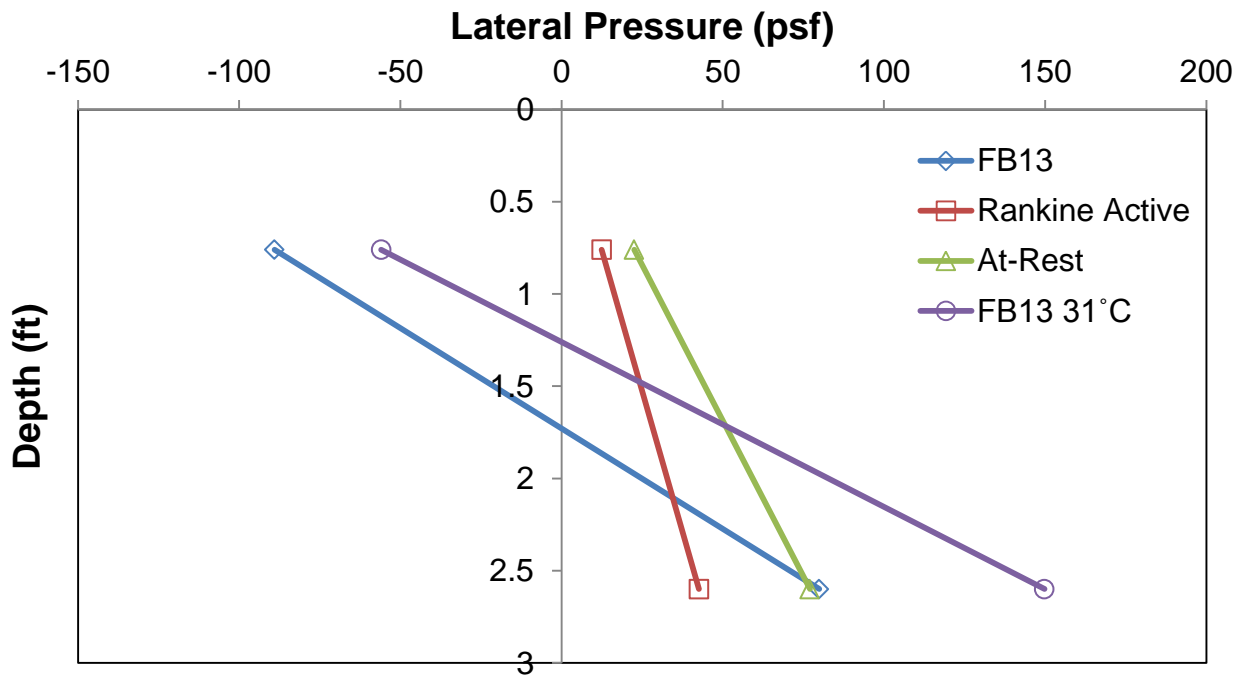


Figure 111 FB11 Lateral Pressure vs Depth



**Figure 112 FB12 Lateral Pressure vs Depth**



**Figure 113 FB13 Lateral Pressure vs Depth**

### 5.3.2.2 Post-Construction Lateral Pressures

Figures 114-117 display the post-construction FB readings behind the end walls starting on April 26, 2013 till September 19, 2013. The average lateral pressures in 7 of the 10 FB cells decreased with time. For example FB13 recorded an average lateral pressure of 176 psf in May. Then in September, the average lateral pressure decreased by 172 psf to 4 psf. It is postulated that the stress reduction is due to shrinkage of the superstructure concrete with time as seen in Figure 127 and explained in Section 5.5. The average lateral pressures in the remaining three FBs (1, 9 and 10) exhibit some erraticism but overall remained fairly constant. A summary of the monthly FB data can be found in Tables 20-23.

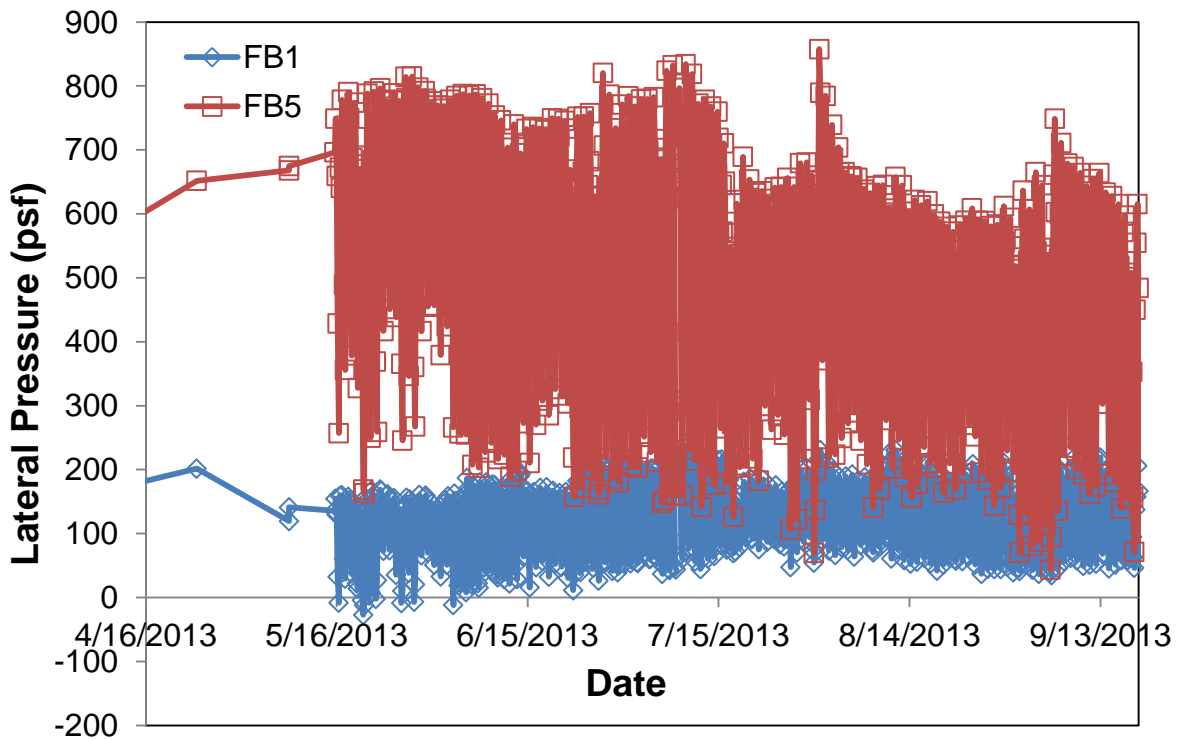


Figure 114 Abutment 1 Outer Tub Girder Lateral Pressures as a Function of Time

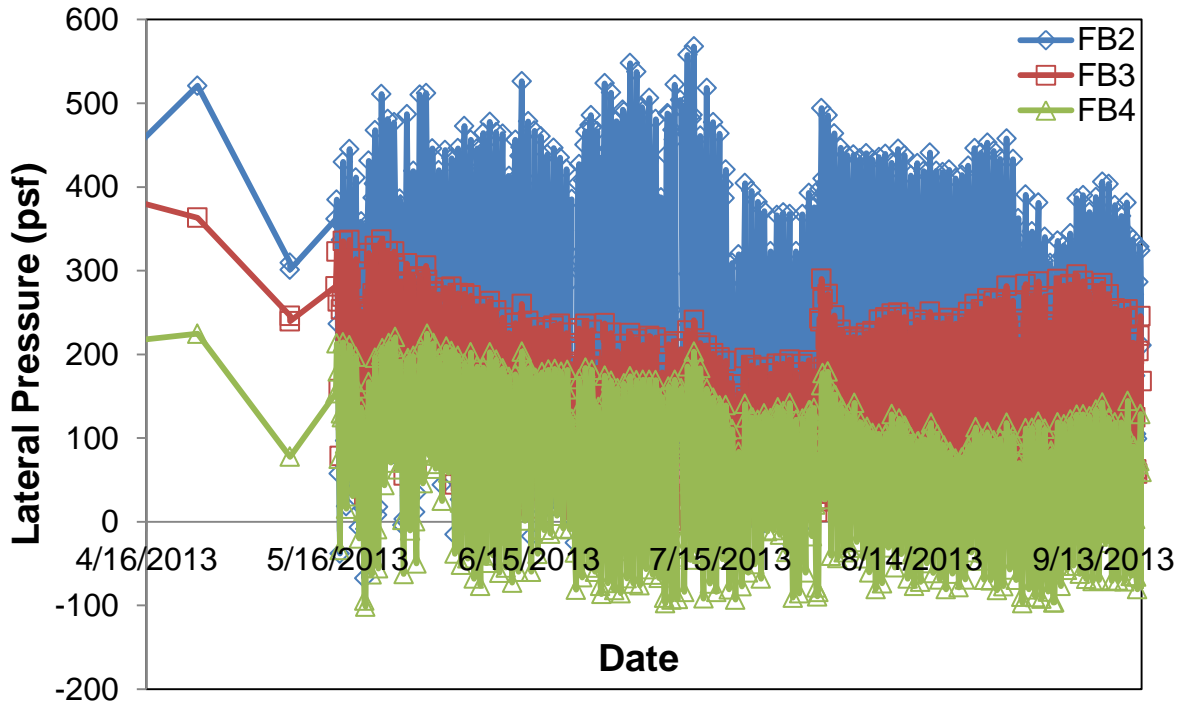


Figure 115 Abutment 1 Middle Tub Girder Lateral Pressures as a Function of Time

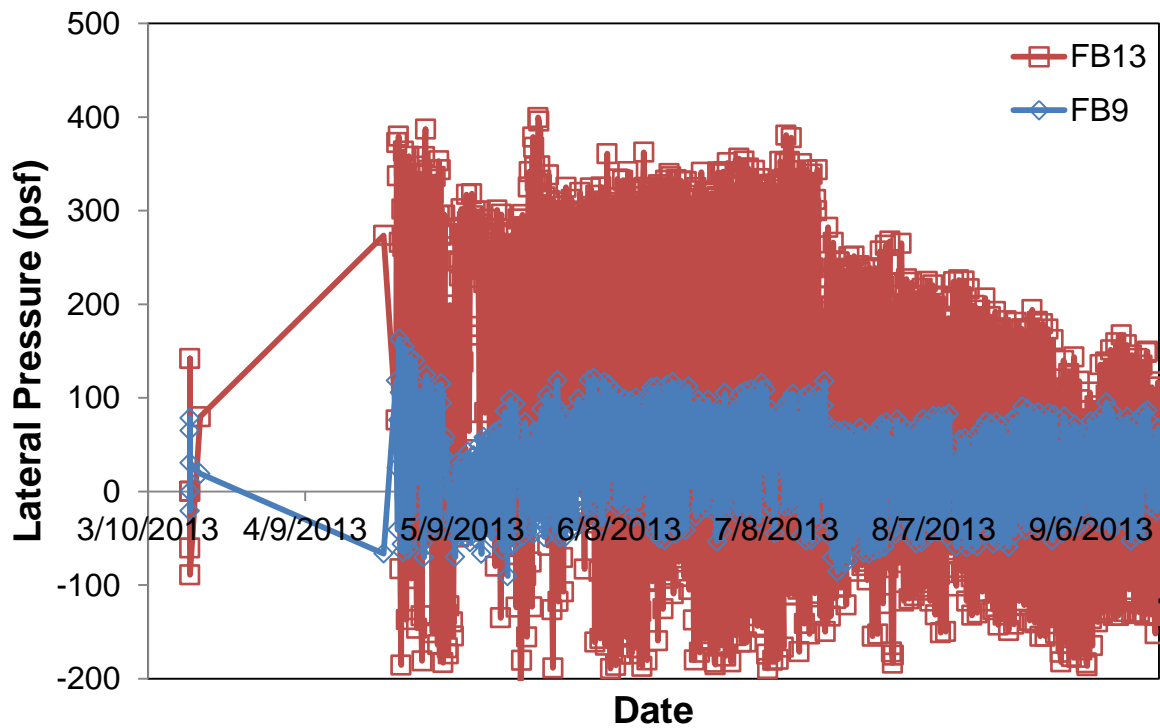


Figure 116 Abutment 2 Outer Tub Girder Lateral Pressures as a Function of Time

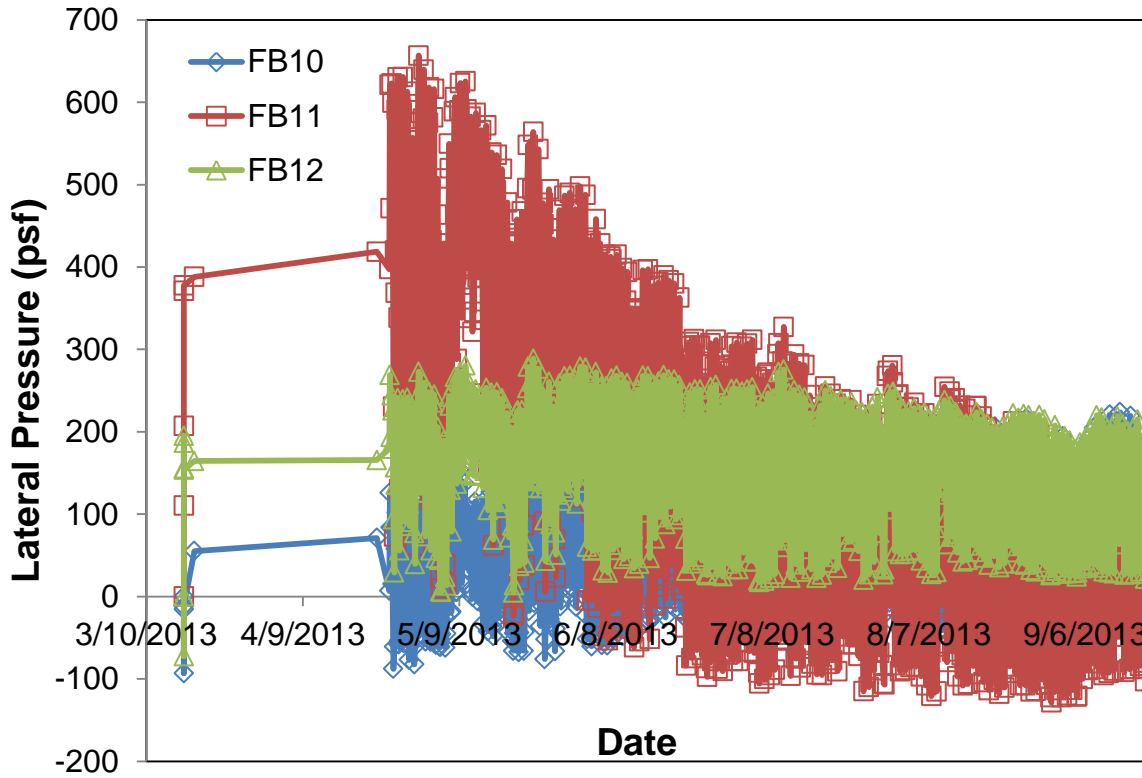


Figure 117 Abutment 2 Middle Tub Girder Lateral Pressures as a Function of Time

**Table 20 Abutment 1 End Walls Average Lateral Pressure**

Month	Avg. Lateral Earth Pressure (psf)				
	FB1	FB2	FB3	FB4	FB5
May	107	264	216	110	605
June	119	270	153	90	541
July	144	246	122	62	508
August	138	296	166	37	456
September	116	239	177	33	439

**Table 21 Abutment 1 End Walls Lateral Pressure Range**

Month	Lateral Pressure (psf)									
	FB1		FB2		FB3		FB4		FB5	
	Max	Min	Max	Min	Max	Min	Max	Min	Max	Min
May	169	-27	512	-68	337	32	225	-101	815	163
June	219	-27	548	-25	281	2	209	-86	820	157
July	247	37	568	-47	290	-9	203	-97	858	70
August	231	37	464	97	284	27	152	-97	739	70
September	224	35	406	84	295	51	144	-96	749	44



**Table 22 Abutment 2 End Walls Average Lateral Pressure**

Month	Avg. Lateral Pressure (psf)				
	FB9	FB10	FB11	FB12	FB13
May	21	58	361	174	176
June	44	77	217	175	158
July	29	74	126	158	136
August	9	88	86	144	66
September	22	78	48	129	4

**Table 23 Abutment 2 End Walls Lateral Pressure Range**

Month	Lateral Pressure (psf)									
	FB9		FB10		FB11		FB12		FB13	
	Max	Min	Max	Min	Max	Min	Max	Min	Max	Min
May	124	-90	171	-82	657	-24	289	5	400	-202
June	121	-53	263	-61	498	-98	279	24	362	-189
July	118	-86	231	-35	327	-115	276	17	381	-189
August	91	-60	216	-41	260	-129	249	26	227	-182
September	95	-52	224	-10	184	-122	220	21	167	-186

The lateral pressures on the end walls displayed a cyclic behavior as a function of time and are more or less in phase with the ambient temperature cycles (Figures 118-121). As the ambient temperature peaked, the lateral pressure reached a maximum. This trend was exhibited by all FBs except FB9. The cyclic lateral pressures must be a result of thermal expansion and contraction of the tub girders since the temperatures in the FBs, once they are buried, are fairly constant over the same period (Figure 122 and 123).

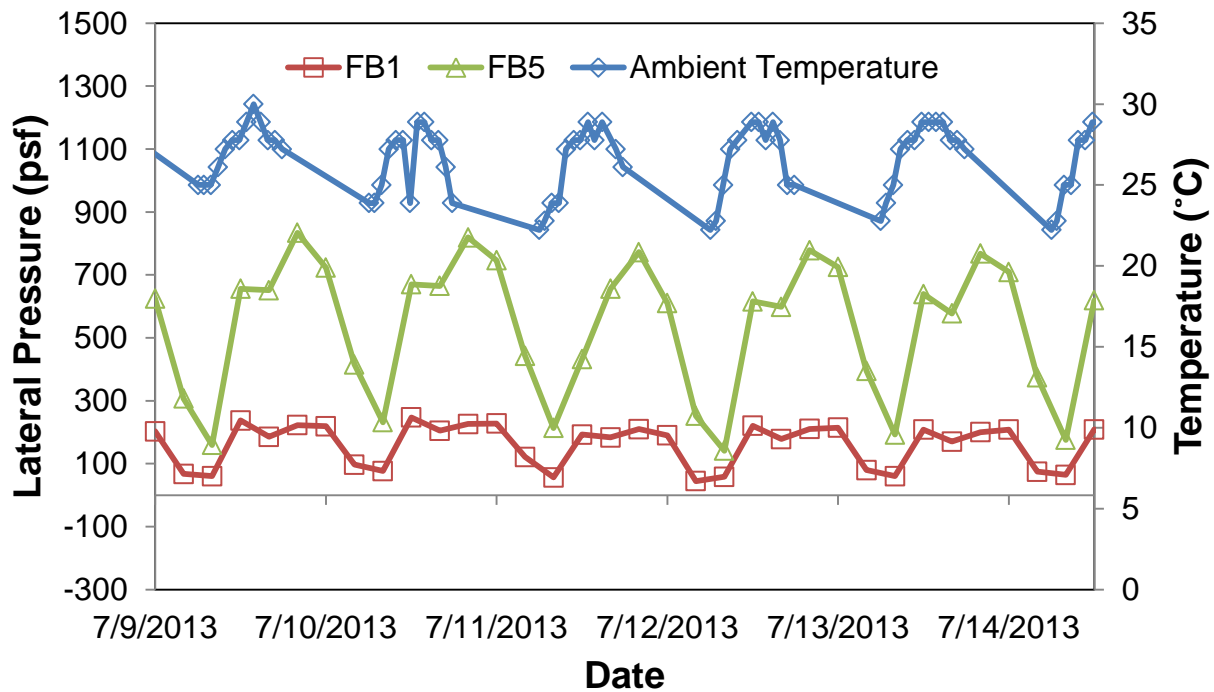


**Figure 118 Abutment 1 Outer Tub Girder Lateral Pressure and Ambient Temperature vs Time**

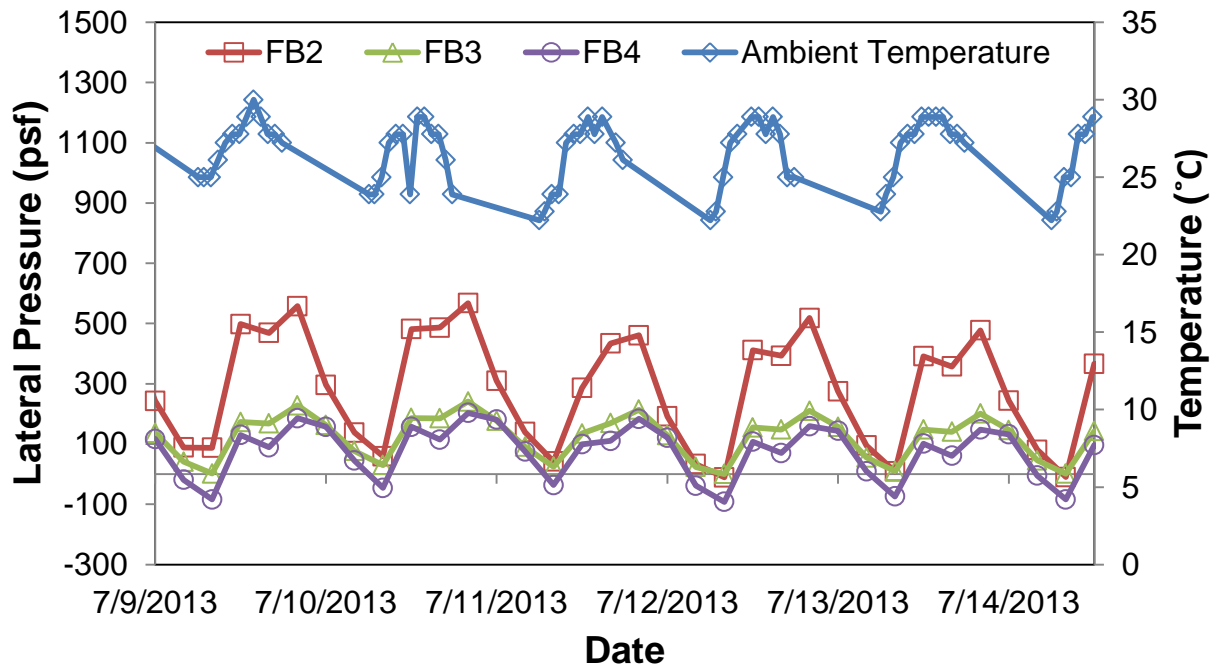


Figure 119 Abutment 1 Middle Tub Girder Lateral Pressure and Ambient Temperature vs Time

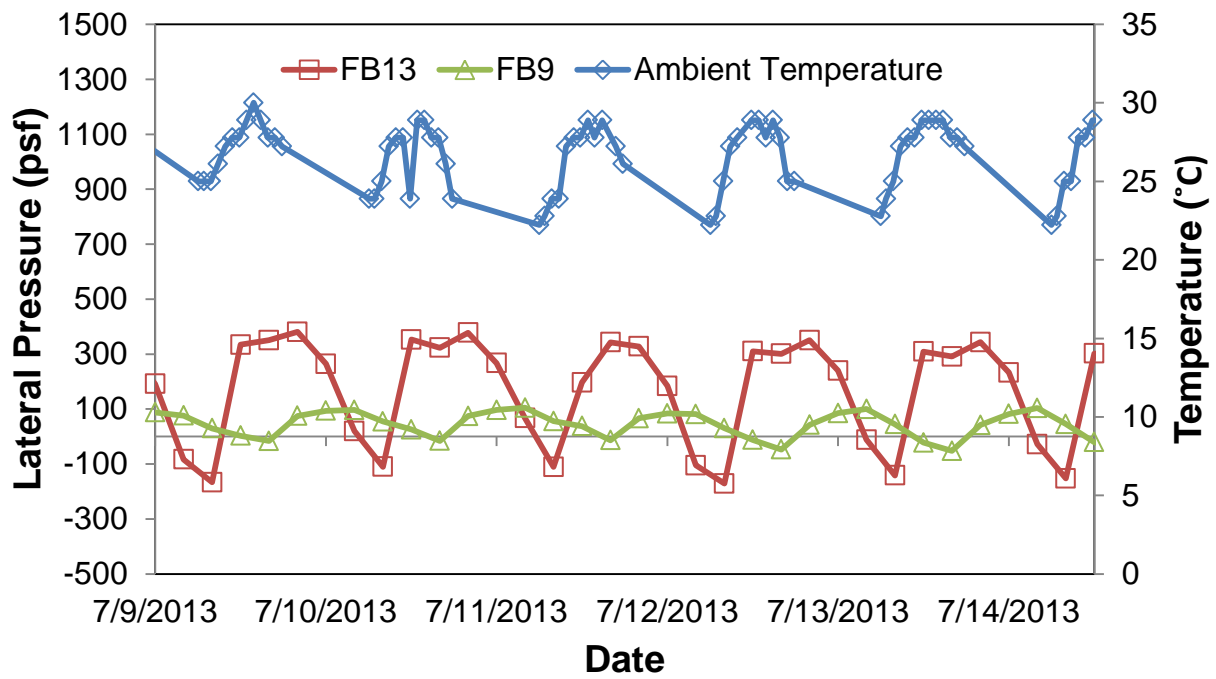


Figure 120 Abutment 2 Outer Tub Girder Lateral Pressure and Ambient Temperature vs Time

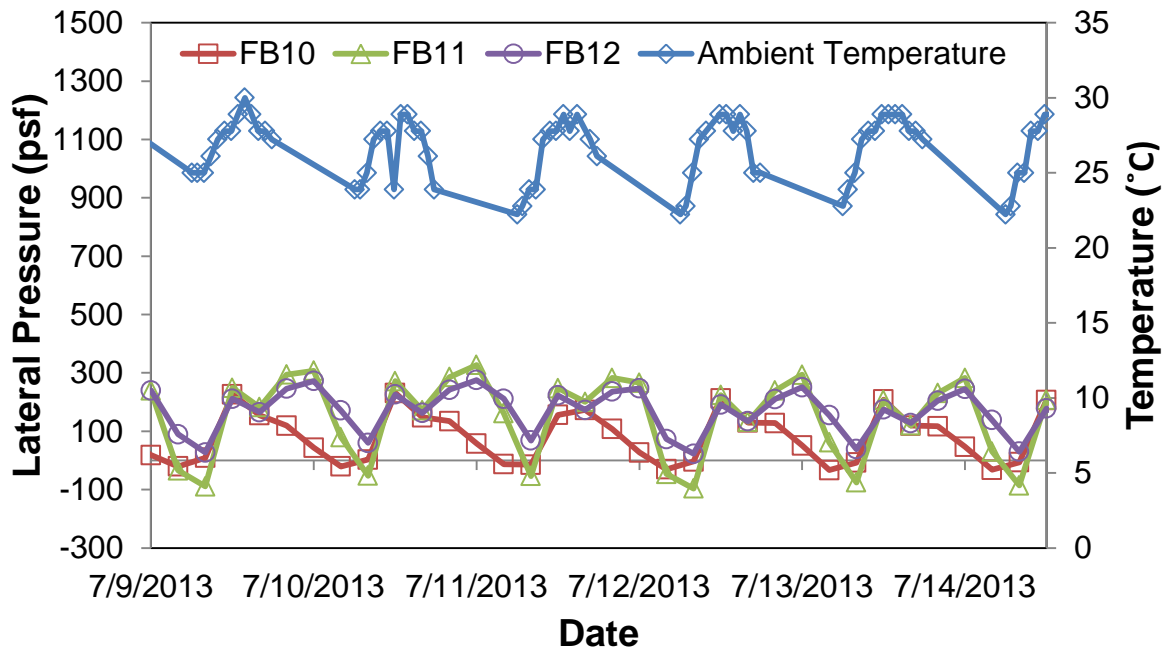


Figure 121 Abutment 2 Middle Tub Girder Lateral Pressure and Ambient Temperature vs Time

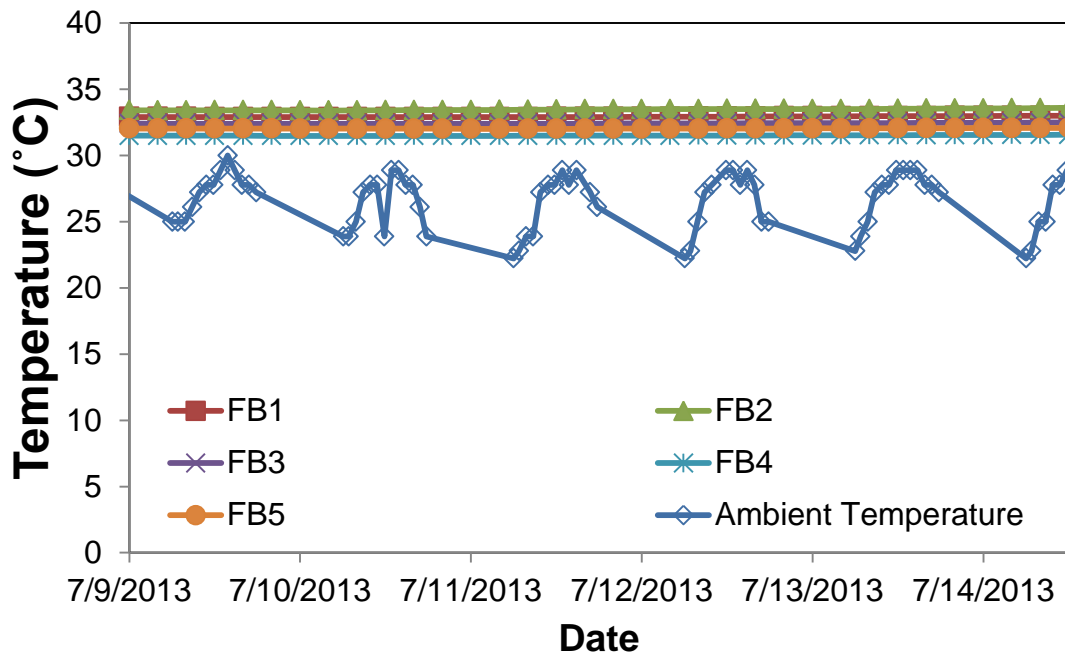
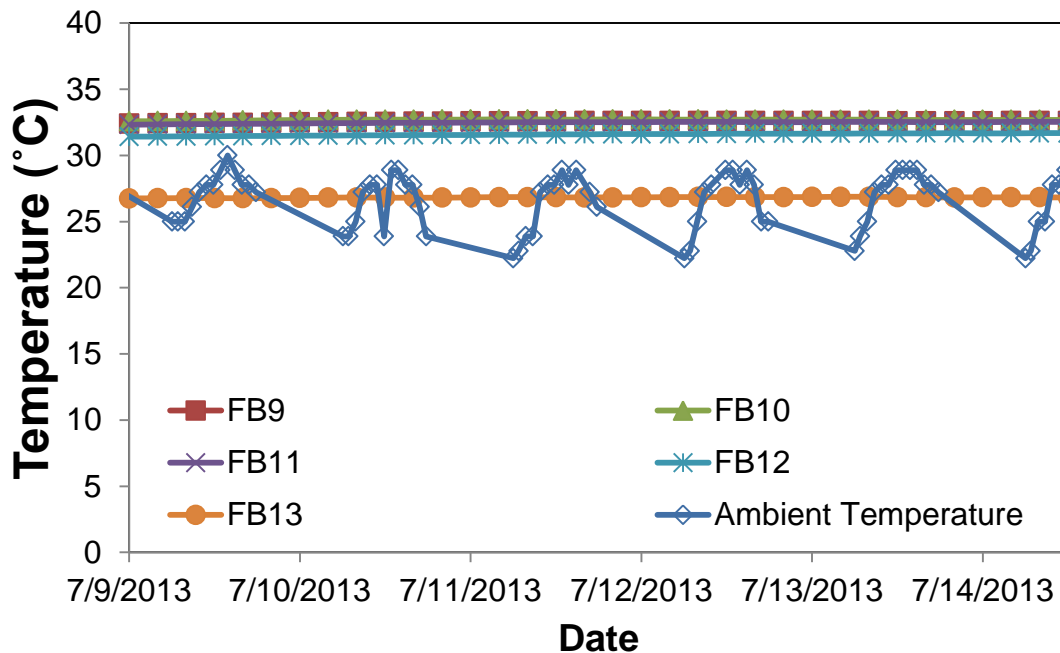


Figure 122 Abutment 1 Middle Tub Girder Instrument and Ambient Temperature vs Time



**Figure 123 Abutment 2 Middle Tub Girder Instrument and Ambient Temperature vs Time**

#### 5.4 Lateral Displacement of Facing Blocks

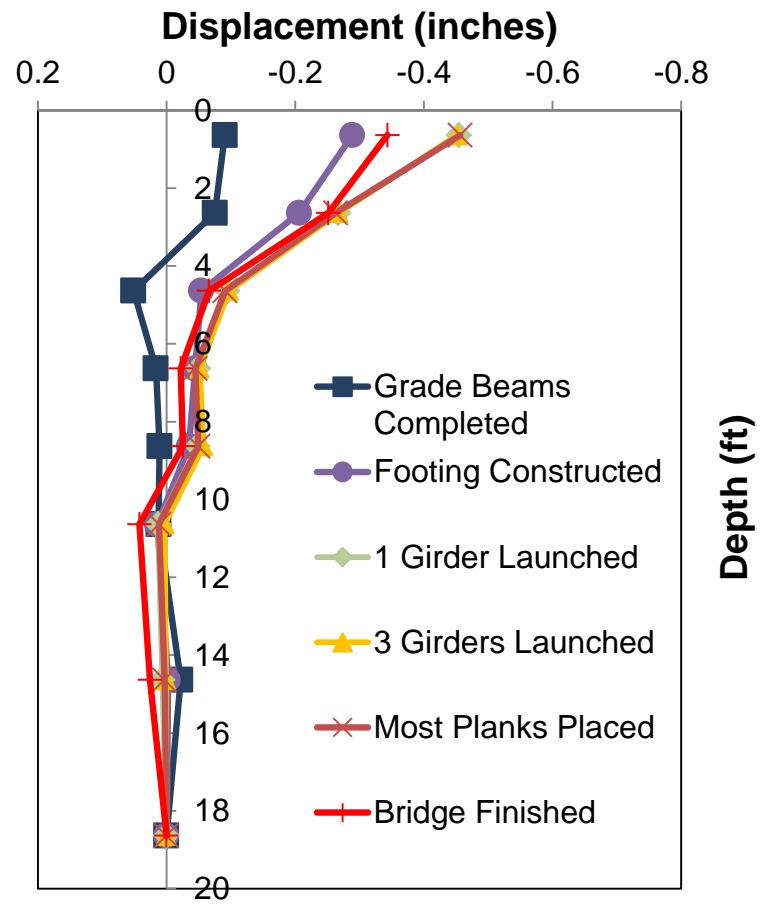
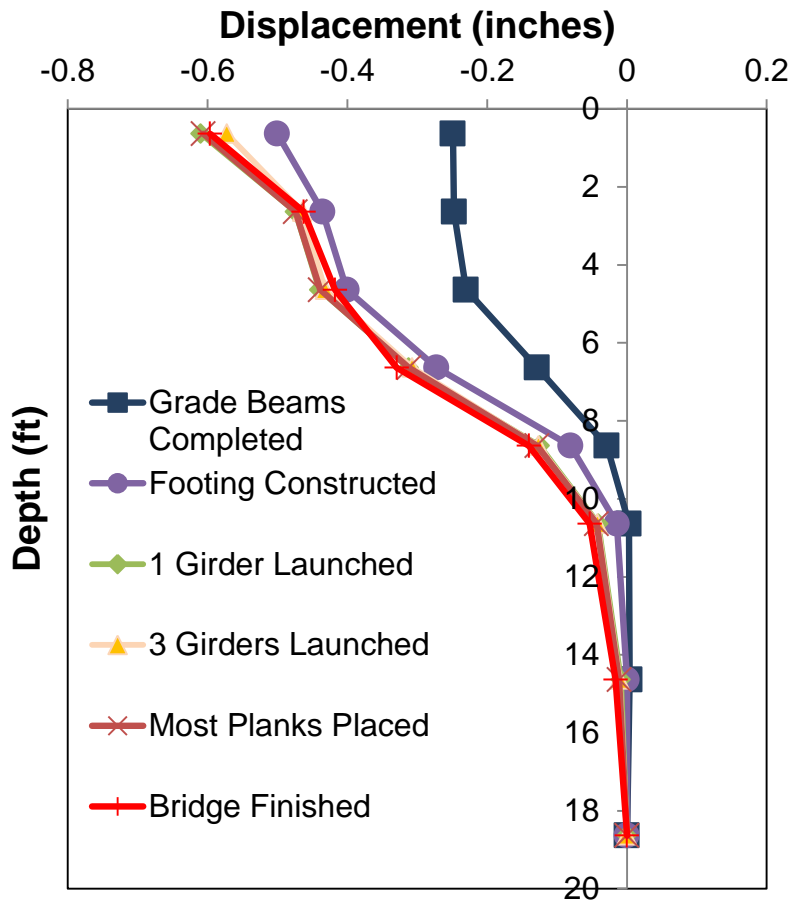
Sections 5.4.1 and 5.4.2 summarize the lateral displacements of the CMU blocks during and post-construction, respectively.

##### 5.4.1 Displacements During Construction

Lateral displacements of the facing blocks were measured with the aid of inclinometers at key construction events as shown in Figure 124 (negative and positive displacements are towards the backfill and stream respectively). It should be noted that the inclinometers were installed after the GRS and CMU wall were erected. Thus, all movements subsequently discussed are in reference to this point in time.

As seen in Figure 124, the largest lateral displacements consistently occurred at the top of the CMU. After completion of the grade beams, lateral displacements were 0.25 inches and 0.09 inches, going towards the GRS fill, at the top of Abutments 1 and 2, respectively. The CMU blocks moved towards the backfill due to rip-rap placement in front of the CMU. This

movement is consistent with observed increases in lateral pressures behind the CMU as seen in Figures 100 and 101. After completion of the footing, lateral displacements towards the GRS fill increased to 0.5 inches and 0.29 inches for Abutments 1 and 2, respectively. The lateral displacement in Abutment 1 was 0.6 inches after the first tub girder was launched and remained constant till bridge completion. Abutment 2 saw an increase to approximately 0.46 inches of lateral displacement after the first tub girder was launched. After the bridge was completed, the lateral displacement was fairly close at 0.34 inches.



(a) (b)  
**Figure 124 Lateral Deflection vs Depth During Construction at (a) Abutment 1 and (b) Abutment 2**

### 5.4.2 Post-Construction Displacements

Figures 125 and 126 display the data collected from each inclinometer starting on April 26, 2013 till September 19, 2013. Each inclinometer recorded a relatively constant lateral displacement during this period. For example I1 at Abutment 1 recorded an average lateral displacement of 0.65 inches in May. In September the average lateral displacement was 0.66 inches. I8 at Abutment 2 experienced less lateral displacement, 0.44 inches, compared to I1 at Abutment 1 of 0.66 inches. A monthly summary of the data can be found in Tables 24 - 27.

The lateral displacements recorded in Abutment 1 remained fairly constant and essentially did not exhibit significant cyclic behavior (Figure 127). However the lateral displacements in Abutment 2 cycled more (Figure 128). Lateral displacements at Abutment 2 appear to have a direct relationship with the ambient temperature. When temperature was highest, the lateral displacement was as well and vice versa.

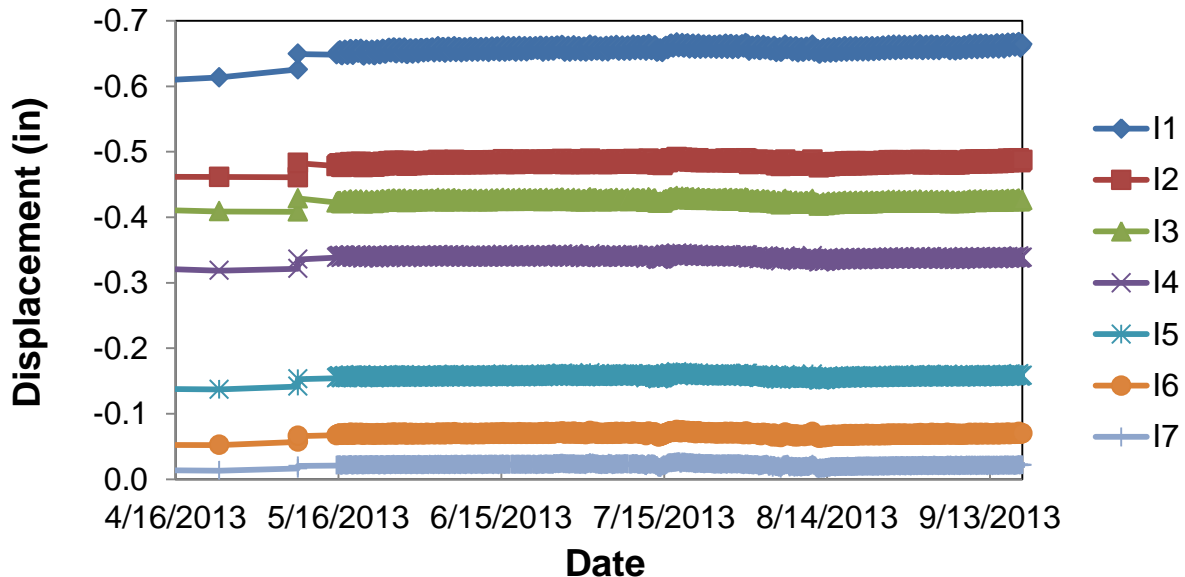


Figure 125 Abutment 1 Lateral Displacement as a Function of Time



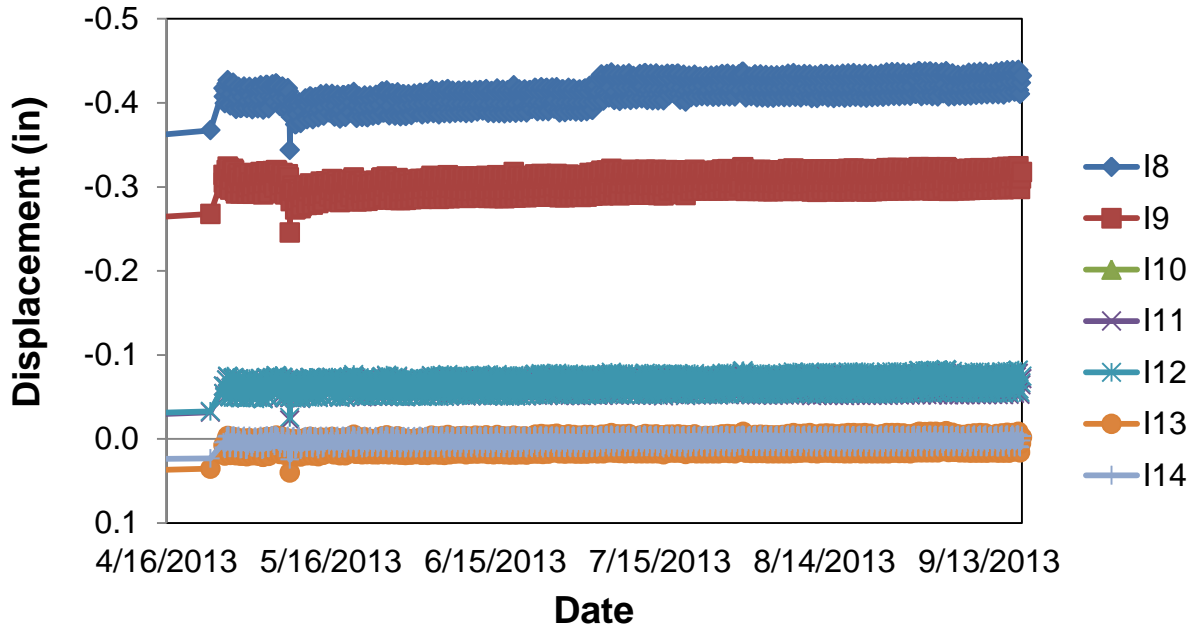


Figure 126 Abutment 2 Lateral Displacement as a Function of Time

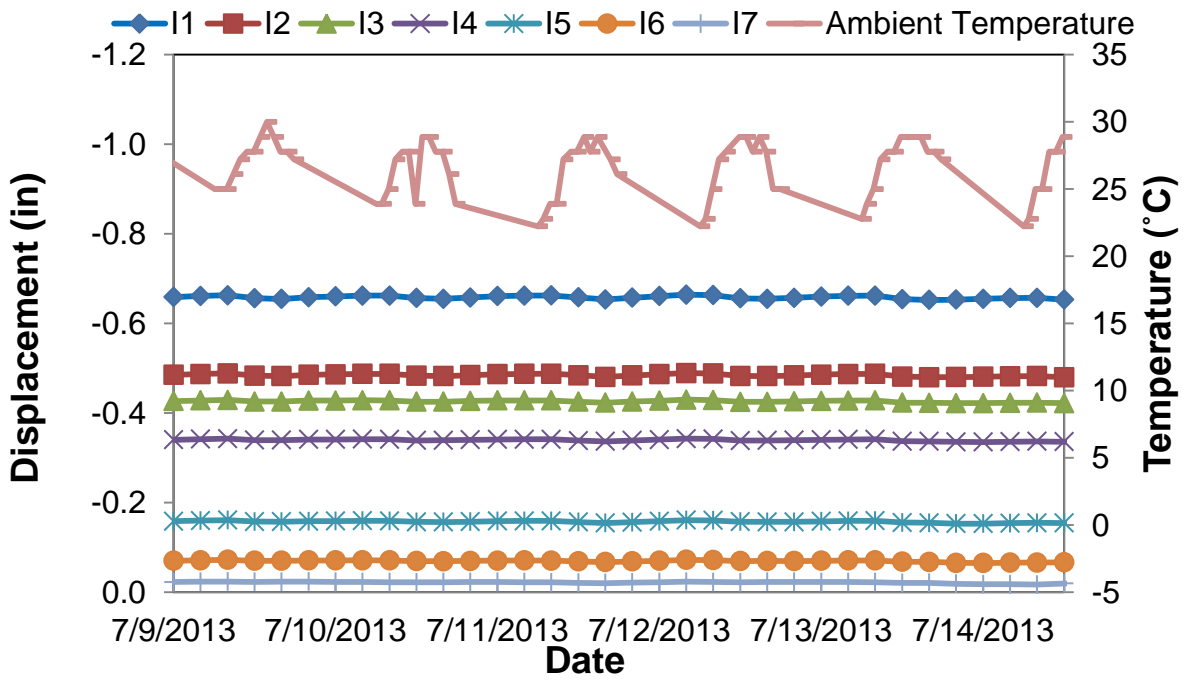


Figure 127 Abutment 1 Lateral Displacement and Ambient Temperature vs Time

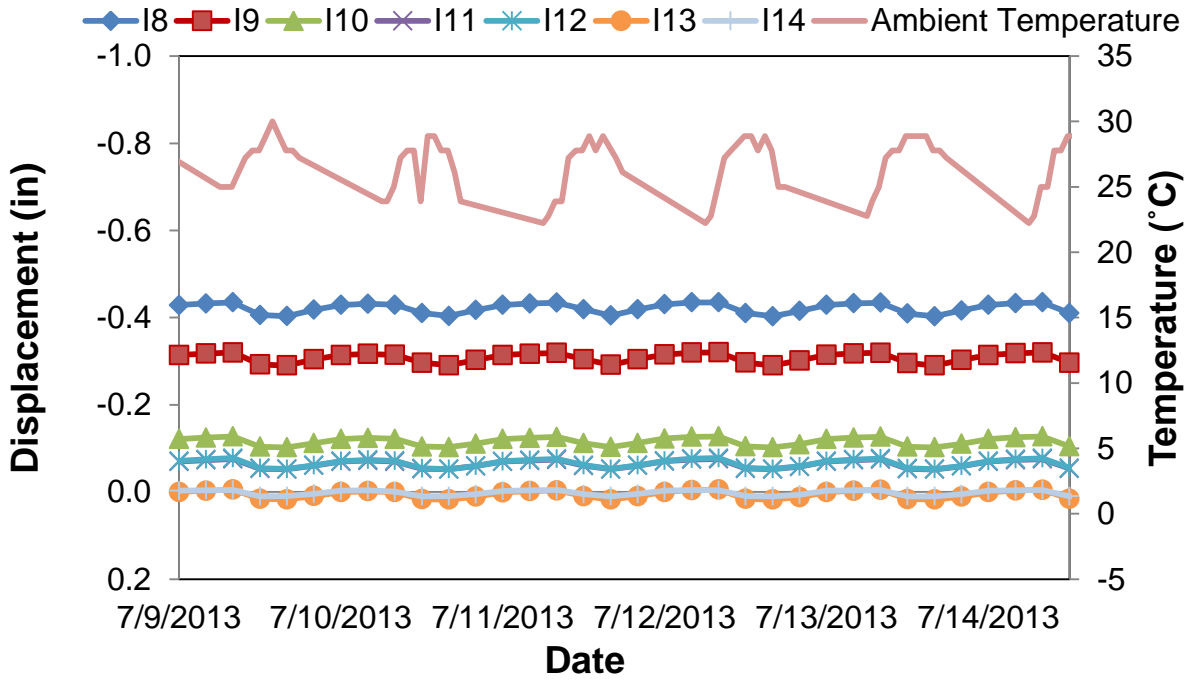


Figure 128 Abutment 2 Lateral Displacement and Ambient Temperature vs Time

**Table 24 Abutment 1 Average Lateral Displacement**

Month	Avg. Lateral Displacement (inches)						
	I1	I2	I3	I4	I5	I6	I7
May	0.65	0.48	0.42	0.34	0.16	0.07	0.02
June	0.66	0.48	0.43	0.34	0.16	0.07	0.02
July	0.66	0.49	0.43	0.34	0.16	0.07	0.02
August	0.66	0.48	0.42	0.34	0.16	0.07	0.02
September	0.66	0.48	0.42	0.34	0.16	0.07	0.02

**Table 25 Abutment 1 Lateral Displacement Range**

Month	Lateral Displacement Range (inches)													
	I1		I2		I3		I4		I5		I6		I7	
	Max	Min	Max	Min	Max	Min	Max	Min	Max	Min	Max	Min	Max	Min
May	0.66	0.63	0.49	0.46	0.43	0.41	0.34	0.32	0.16	0.14	0.07	0.06	0.02	0.02
June	0.66	0.65	0.49	0.48	0.43	0.42	0.34	0.34	0.16	0.16	0.07	0.07	0.02	0.02
July	0.67	0.65	0.49	0.48	0.43	0.42	0.35	0.34	0.16	0.15	0.07	0.07	0.03	0.02
August	0.66	0.65	0.49	0.48	0.43	0.42	0.34	0.33	0.16	0.15	0.07	0.06	0.02	0.02
September	0.67	0.65	0.49	0.48	0.43	0.42	0.34	0.33	0.16	0.16	0.07	0.07	0.02	0.02

**Table 26 Abutment 2 Average Lateral Displacement**

Month	Avg. Lateral Displacement (inches)						
	I8	I9	I10	I11	I12	I13	I14
May	0.40	0.30	0.11	0.06	0.06	0.01	0.00
June	0.40	0.30	0.11	0.06	0.06	0.01	0.00
July	0.42	0.31	0.12	0.06	0.07	0.01	0.00
August	0.42	0.31	0.12	0.06	0.07	0.01	0.00
September	0.42	0.31	0.12	0.07	0.07	0.00	0.00

**Table 27 Abutment 2 Lateral Displacement Range**

Month	Lateral Displacement Range (inches)													
	I8		I9		I10		I11		I12		I13		I14	
	Max	Min	Max	Min	Max	Min	Max	Min	Max	Min	Max	Min	Max	Min
May	0.42	0.34	0.32	0.25	0.13	0.07	0.07	0.02	0.08	0.03	0.04	0.00	0.02	0.00
June	0.42	0.39	0.32	0.29	0.13	0.10	0.08	0.05	0.08	0.05	0.02	0.01	0.01	0.00
July	0.44	0.39	0.32	0.29	0.13	0.10	0.08	0.05	0.08	0.05	0.02	0.01	0.01	0.00
August	0.44	0.41	0.32	0.29	0.13	0.10	0.08	0.05	0.08	0.05	0.02	0.01	0.01	0.00
September	0.44	0.41	0.32	0.29	0.13	0.10	0.08	0.05	0.08	0.05	0.02	0.01	0.01	0.00

5.5 Superstructure Strain

Strains measured in the concrete cylinder, wearing surface, precast planks, and tub girders are discussed below.

5.5.1 Concrete Cylinder

Figure 129 shows a plot of strain versus time for an unreinforced concrete cylinder, sampled during the west tub girder pour. It can be seen that the majority of the compression occurred in the first two days of curing. After the first two days, a strain of -225  $\mu\epsilon$  (negative denotes compression) was recorded. After 28 days the strain increased to -248  $\mu\epsilon$ . After 6 months a strain of -349  $\mu\epsilon$  was recorded. The strain continued to increase throughout the investigation to an average of -362  $\mu\epsilon$  in September 2013 as shown in Table 28.

The strain in the concrete cylinder cycled daily with the ambient temperature (Figure 130). As the temperature increased, the concrete cylinder expanded, causing an increase in the strain. When the temperature decreased, the concrete cylinder compressed, causing a decrease in the strain.

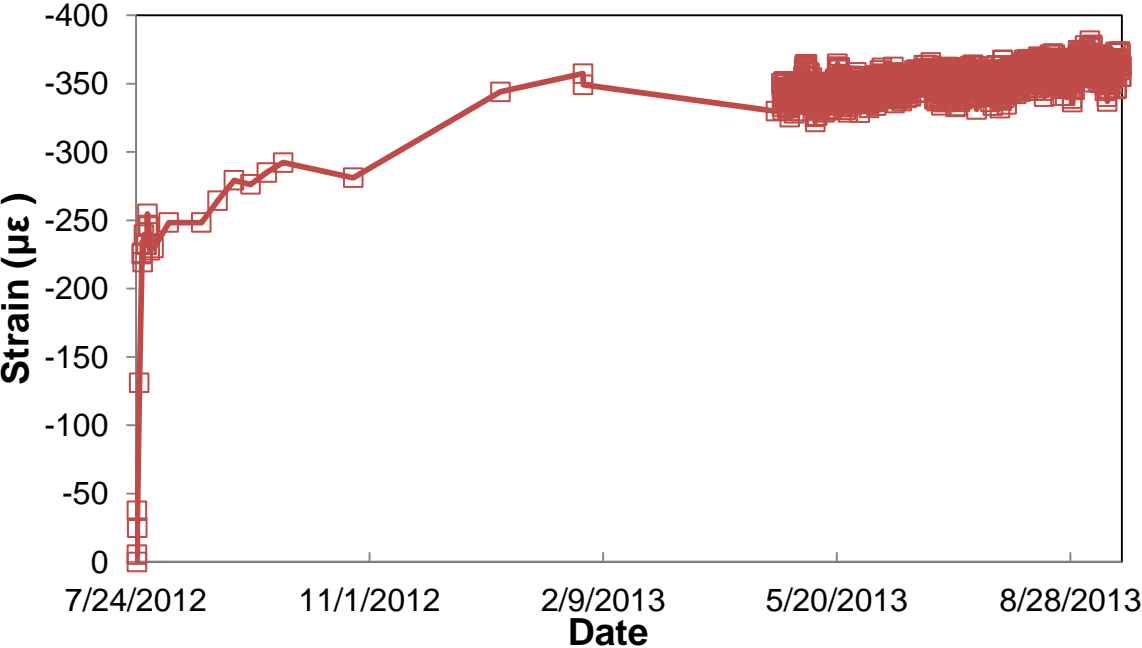
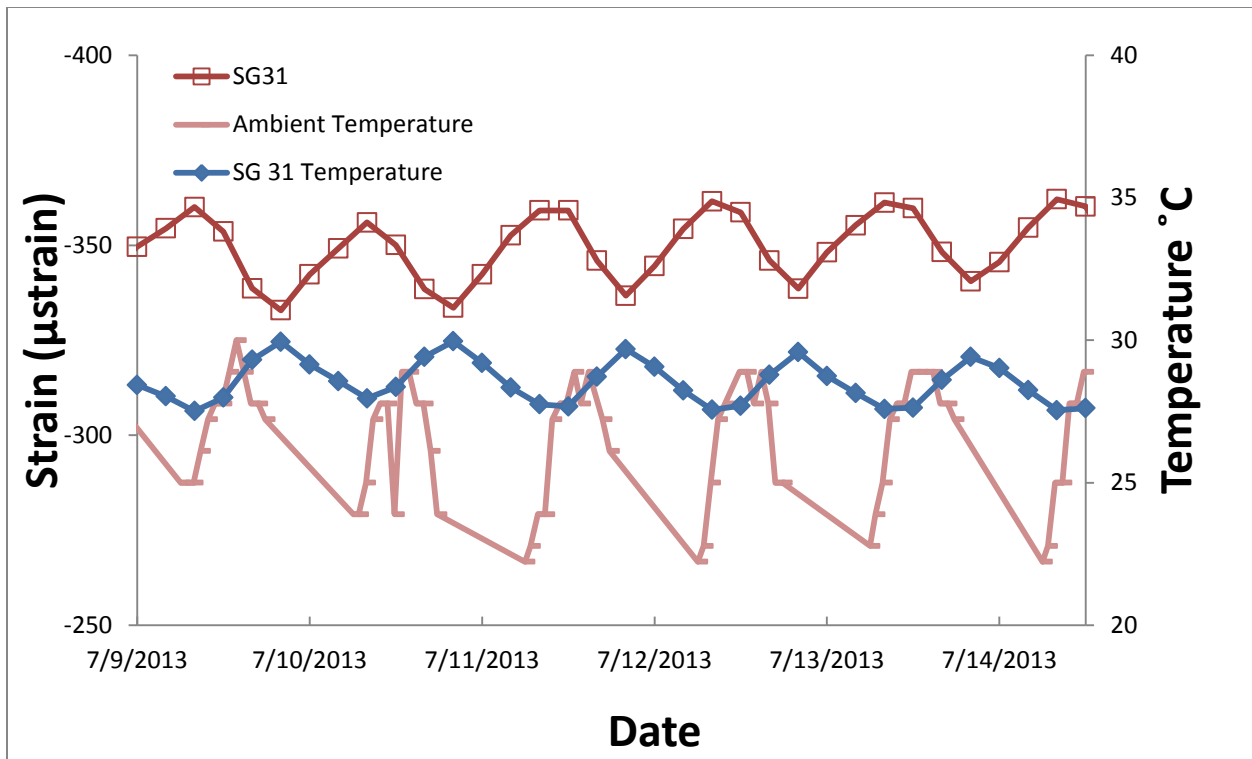


Figure 129 Concrete Cylinder Strain (SG 31) as a Function of Time

**Table 28 Concrete Cylinder (SG 31) Strain Monthly Summary**

Month	Strain Range (- $\mu\epsilon$ )		Strain Avg. (- $\mu\epsilon$ )
	SG31		SG31
	Max	Min	
May	365	322	344
June	365	332	350
July	367	331	351
August	374	336	357
September	381	337	362



**Figure 130 Concrete Cylinder (SG 31) Strain and Ambient Temperature vs Time**

### 5.5.2 Wearing Surface

Figure 131 displays the strains recorded in the wearing surface above the precast planks. Superimposed on this plot are the strains from the unreinforced concrete cylinder which has an identical mix design with the concrete for the precast planks and tub girders but slightly different

than that for the wearing surface as described in Section 4.3. Since this unreinforced concrete cylinder is the only one that was monitored for strain, it is used as a basis for comparing the long term strains in the entire superstructure. Note that the majority of the average strains are marginally lower than the concrete cylinder. For example SG11 experienced on average  $-263 \mu\epsilon$  in September compared to the concrete cylinder with an average strain of  $-362 \mu\epsilon$ . This is due to the fact that the topping has reinforcing that restrains the concrete from shrinking. Strains in the wearing surface appear to steadily increase with time. A monthly summary of the average wearing surface strains can be found in Tables 29 and 30.

### **5.5.3 Precast Planks**

Figure 132 displays the strains recorded in the pre-cast planks placed on top of the tub girders. A larger compression was observed in the pre-cast planks than the concrete cylinder. For example SG22 experienced an average strain of  $-581 \mu\epsilon$  compared to the concrete cylinder experiencing an average  $-362 \mu\epsilon$ . This may be attributable to the weight of and shrinkage of the wearing surface concrete after it was poured on the precast planks. Note that SG17 did not record any data after May 18, 2013. A monthly summary of the precast plank strains can be found in Tables 31 and 32.

### **5.5.4 Tub Girders**

Figures 133-135 display the strains recorded in the tub girders. The strains at the floors of the tub girders were highest with average values ranging from  $-1290 \mu\epsilon$  to  $-1394 \mu\epsilon$  compared to  $-970 \mu\epsilon$  to  $-1243 \mu\epsilon$ , and  $-862 \mu\epsilon$  to  $-1180 \mu\epsilon$ , in the west and east walls, respectively. The strains in the tub girders increased significantly after post-tensioning, which occurred prior to the girder launch in December 2013. They are larger than the strains measured in the concrete cylinder, wearing surface and precast planks. The post-stressing is evident by the significant rise in strain in Figures 132-134. The strains in the floors of the tub girders decreased as more and more load (due to precast planks, wearing surface and jersey barriers) was placed on them after February 5, 2013 as seen in Figure 132. This suggests sagging of the tub girder floors. A monthly summary of the strains in the tub girders can be found in Tables 33-38. After the data acquisition went online in April 2013, Figures 130 through 134 display a trend of strain increasing with time. This suggests the occurrence of ongoing shrinkage in the concrete.

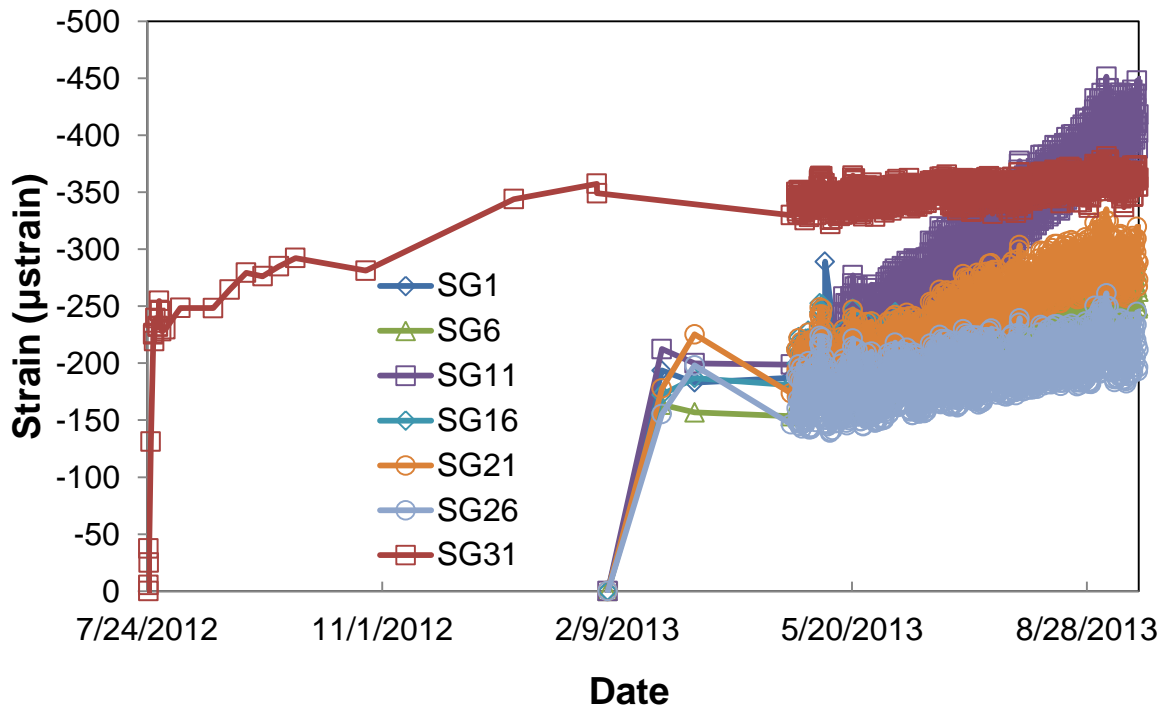


Figure 131 Strain in Top Surface vs Time

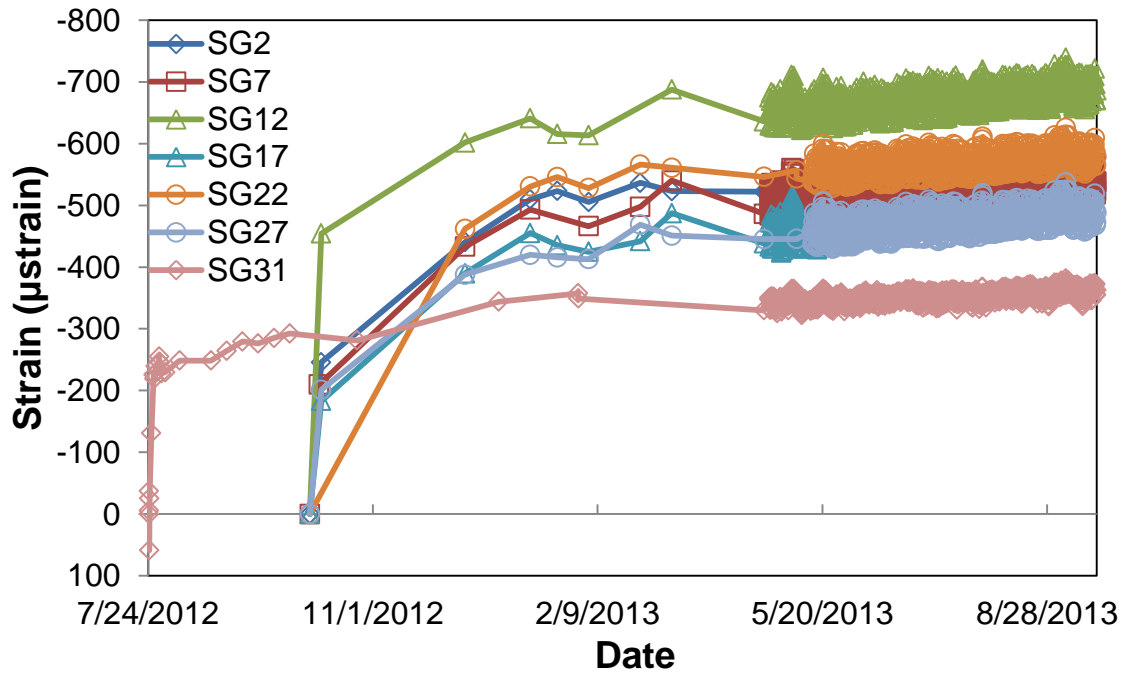


Figure 132 Strain in Pre-Cast Planks vs Time



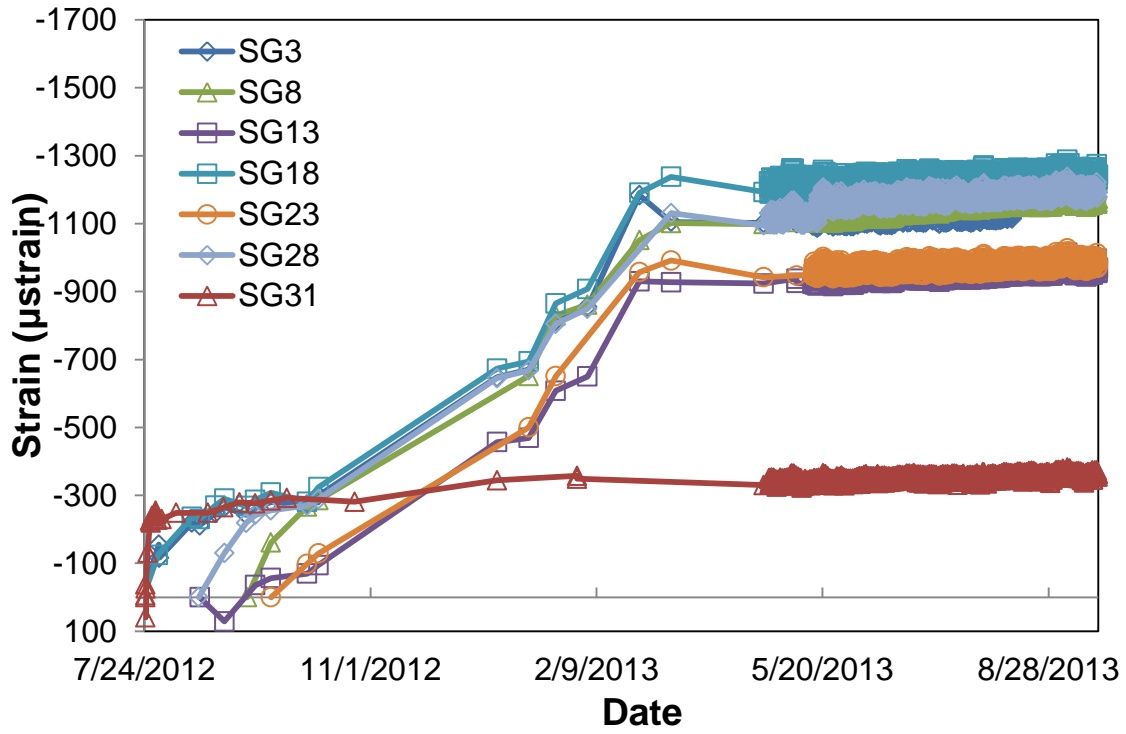


Figure 133 Strain in West Walls of Tub Girders vs Time

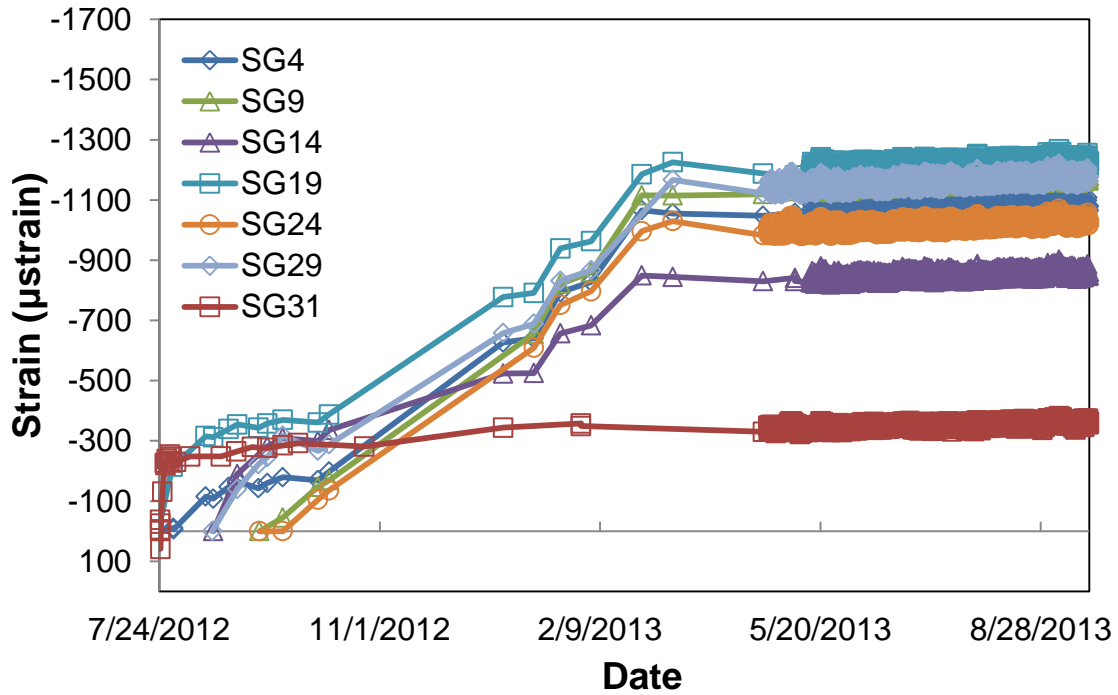


Figure 134 Strain in East Walls of Tub Girders vs Time

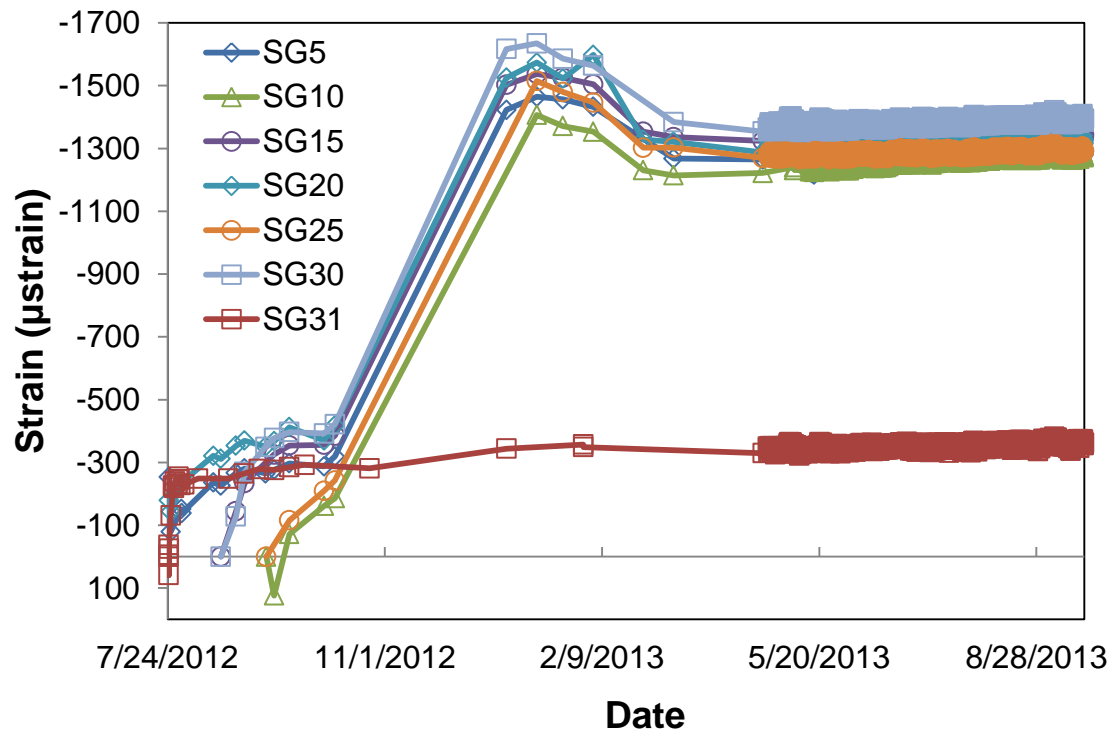


Figure 135 Strain in Floors of Tub Girders vs Time

**Table 29 Average Strain in Wearing Surface**

Month	Avg Strain ( $-\mu\epsilon$ )					
	SG1	SG6	SG11	SG16	SG21	SG26
May	203	180	231	202	199	173
June	209	196	265	210	216	183
July	215	220	308	217	249	193
August	221	248	362	225	273	202
September	232	263	407	236	288	213

**Table 30 Range of Strains in Wearing Surface**

Month	Strain Range ( $-\mu\epsilon$ )											
	SG1		SG6		SG11		SG16		SG21		SG26	
	Max	Min	Max	Min	Max	Min	Max	Min	Max	Min	Max	Min
May	289	164	219	156	277	197	252	165	249	167	224	139
June	252	173	237	163	320	212	250	179	264	176	225	150
July	266	183	273	189	377	259	265	187	303	208	239	161
August	269	194	293	218	432	312	270	199	323	241	250	176
September	282	199	306	236	451	370	282	205	335	257	261	182

**Table 31 Average Strain in Precast Planks**

Month	Average Strain (- $\mu\epsilon$ )					
	SG2	SG7	SG12	SG17	SG22	SG27
May	527	510	657	460	555	458
June	531	515	663		560	465
July	536	521	671		566	471
August	541	528	679		572	479
September	552	538	689		581	488

**Table 32 Range of Strains in Precast Planks**

Month	Strain Range (- $\mu\epsilon$ )											
	SG2		SG7		SG12		SG17		SG22		SG27	
	Max	Min	Max	Min	Max	Min	Max	Min	Max	Min	Max	Min
May	575	490	560	481	711	622	513	423	600	529	506	430
June	574	497	554	484	705	630			599	532	505	434
July	586	504	565	494	720	638			611	539	519	442
August	577	515	572	505	728	652			613	548	524	454
September	602	518	583	509	739	656			625	551	537	458

**Table 33 Average Strain in West Walls of Tub Girders**

Month	Average Strain (- $\mu\epsilon$ )					
	SG3	SG8	SG13	SG18	SG23	SG28
May	1115	1123	939	1216	962	1141
June	1121	1135	946	1222	966	1169
July	1126	1154	953	1226	971	1177
August	1132	1164	961	1233	977	1184
September	1142	1173	970	1243	986	1193

**Table 34 Range of Strains in West Walls of Tub Girders**

Month	Strain Range (- $\mu\epsilon$ )											
	SG3		SG8		SG13		SG18		SG23		SG28	
	Max	Min	Max	Min	Max	Min	Max	Min	Max	Min	Max	Min
May	1157	1088	1159	1102	982	916	1263	1187	1002	939	1206	1096
June	1159	1092	1171	1107	983	920	1259	1192	1001	942	1206	1140
July	1171	1100	1196	1127	996	929	1271	1199	1010	948	1218	1149
August	1175	1109	1200	1145	1002	939	1276	1210	1016	957	1227	1227
September	1187	1114	1211	1150	1014	944	1288	1215	1027	961	1237	1166

**Table 35 Average Strain in East Walls of Tub Girders**

Month	Average Strain (- $\mu\epsilon$ )					
	SG4	SG9	SG14	SG19	SG24	SG29
May	1057	1147	840	1201	1004	1146
June	1062	1157	844	1206	1008	1152
July	1066	1165	848	1211	1015	1161
August	1071	1171	853	1217	1022	1168
September	1080	1180	862	1227	1031	1177

**Table 36 Range of Strains in East Walls of Tub Girders**

Month	Strain Range (- $\mu\epsilon$ )											
	SG4		SG9		SG14		SG19		SG24		SG29	
	Max	Min	Max	Min	Max	Min	Max	Min	Max	Min	Max	Min
May	1099	1028	1184	1126	879	819	1241	1178	1047	980	1192	1118
June	1098	1035	1193	1130	877	821	1241	1181	1042	984	1190	1124
July	1109	1041	1203	1143	887	827	1252	1187	1053	992	1202	1133
August	1112	1048	1208	1152	890	835	1257	1197	1060	1002	1211	1145
September	1124	1052	1219	1156	902	838	1268	1201	1071	1006	1221	1150

**Table 37 Average Strain in Floors of Tub Girders**

Month	Average Strain (- $\mu\epsilon$ )					
	SG5	SG10	SG15	SG20	SG25	SG30
May	1276	1240	1333	1309	1281	1372
June	1281	1251	1333	1311	1282	1375
July	1283	1265	1336	1313	1285	1380
August	1286	1274	1340	1318	1291	1388
September	1290	1279	1344	1324	1295	1394

**Table 38 Range of Strains in Floors of Tub Girders**

Month	Strain Range (- $\mu\epsilon$ )											
	SG5		SG10		SG15		SG20		SG25		SG30	
	Max	Min	Max	Min	Max	Min	Max	Min	Max	Min	Max	Min
May	1306	1217	1260	1225	1359	1318	1337	1290	1308	1265	1402	1352
June	1305	1262	1274	1230	1355	1317	1332	1293	1300	1267	1397	1358
July	1307	1265	1288	1248	1356	1320	1335	1295	1303	1269	1406	1364
August	1313	1270	1295	1259	1362	1327	1343	1303	1311	1276	1415	1373
September	1321	1270	1302	1263	1370	1328	1349	1306	1317	1279	1421	1377

The strains recorded of the tub girders displayed a cyclic behavior as a function of ambient temperature (Figures 136-140). As the temperature was at its highest value, the strain exhibited the highest strain (tendency to go into tension). Conversely when the temperature was at its lowest, the strain exhibited the lowest strain (tendency to compress).

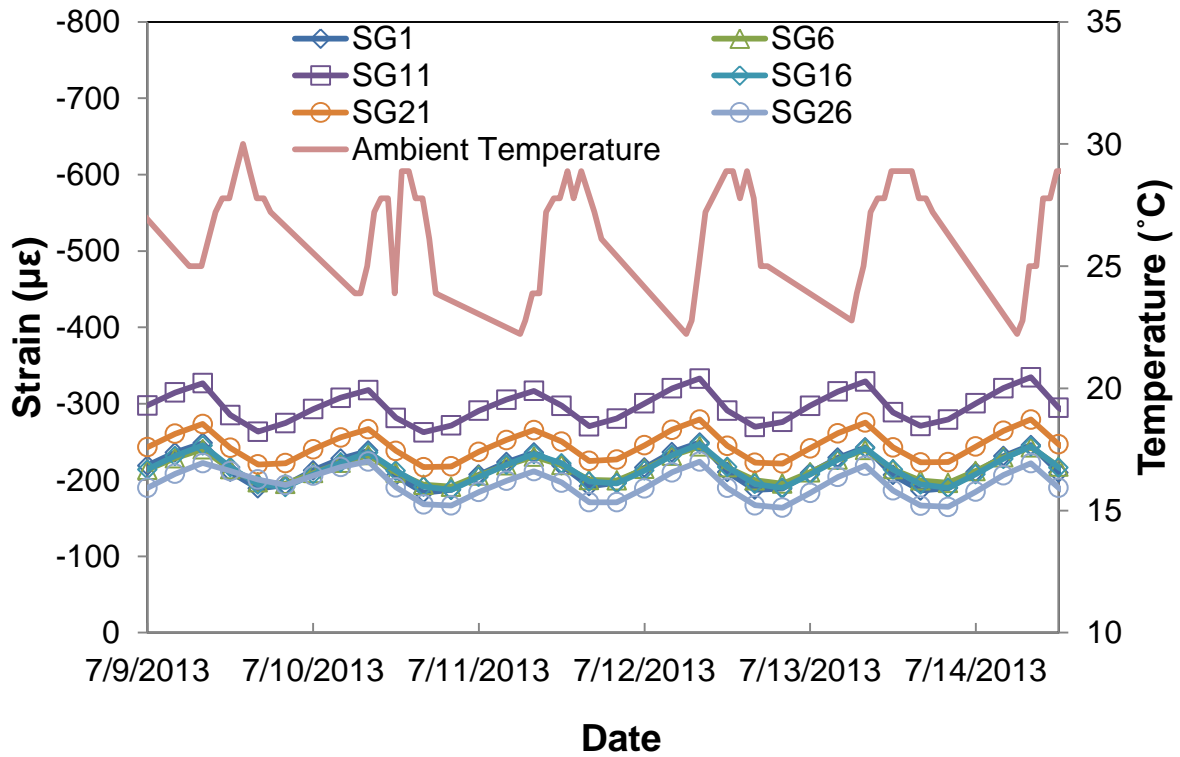


Figure 136 Wearing Surface Strain and Ambient Temperature vs Time



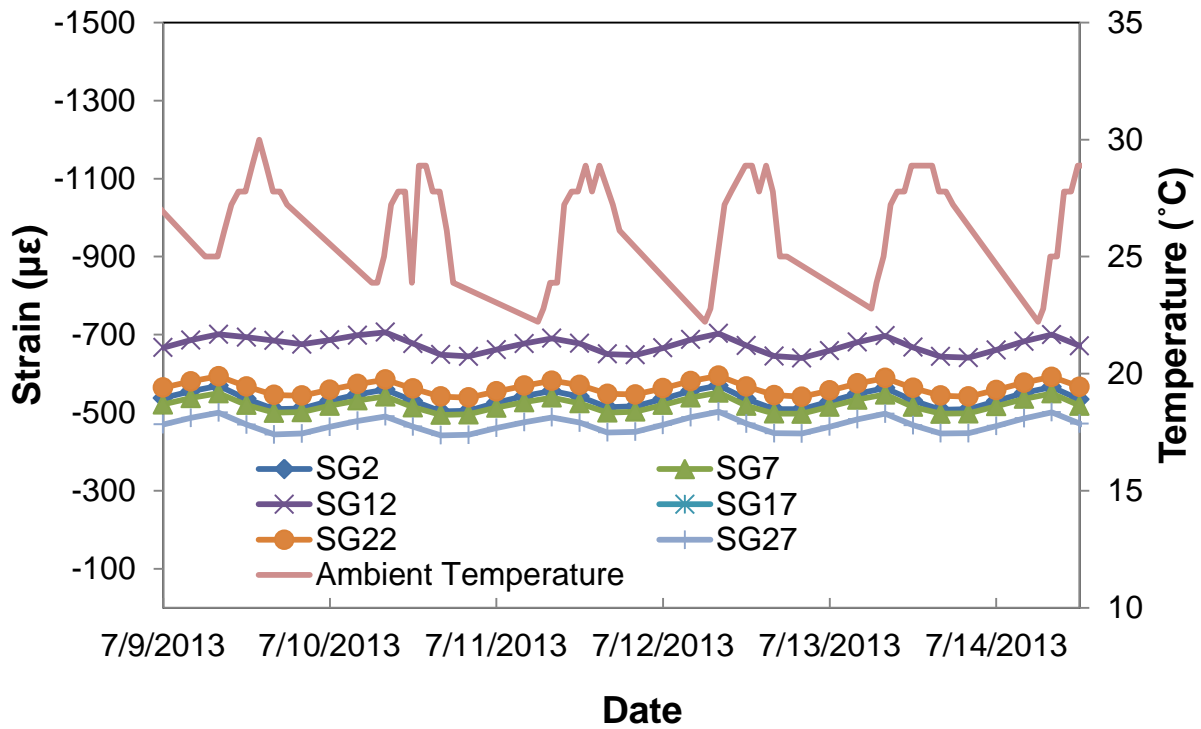


Figure 137 Pre-Cast Plank Strain and Ambient Temperature vs Time

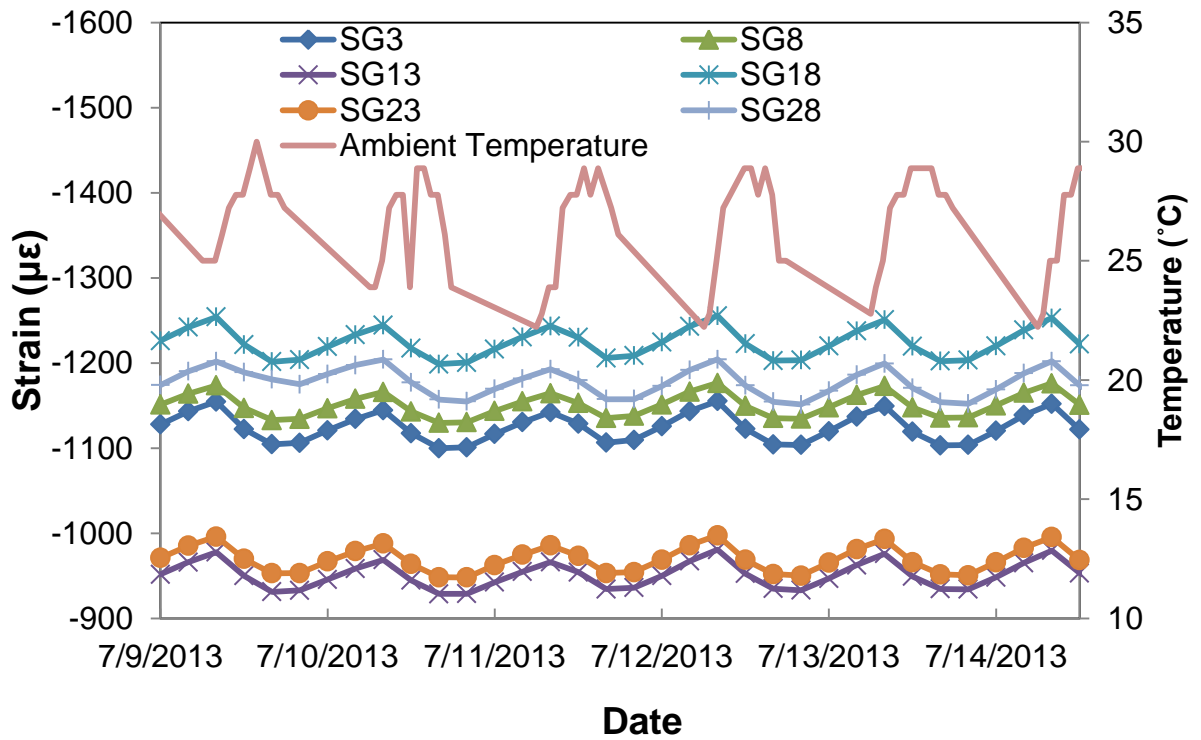


Figure 138 West Wall Strain and Ambient Temperature vs Time

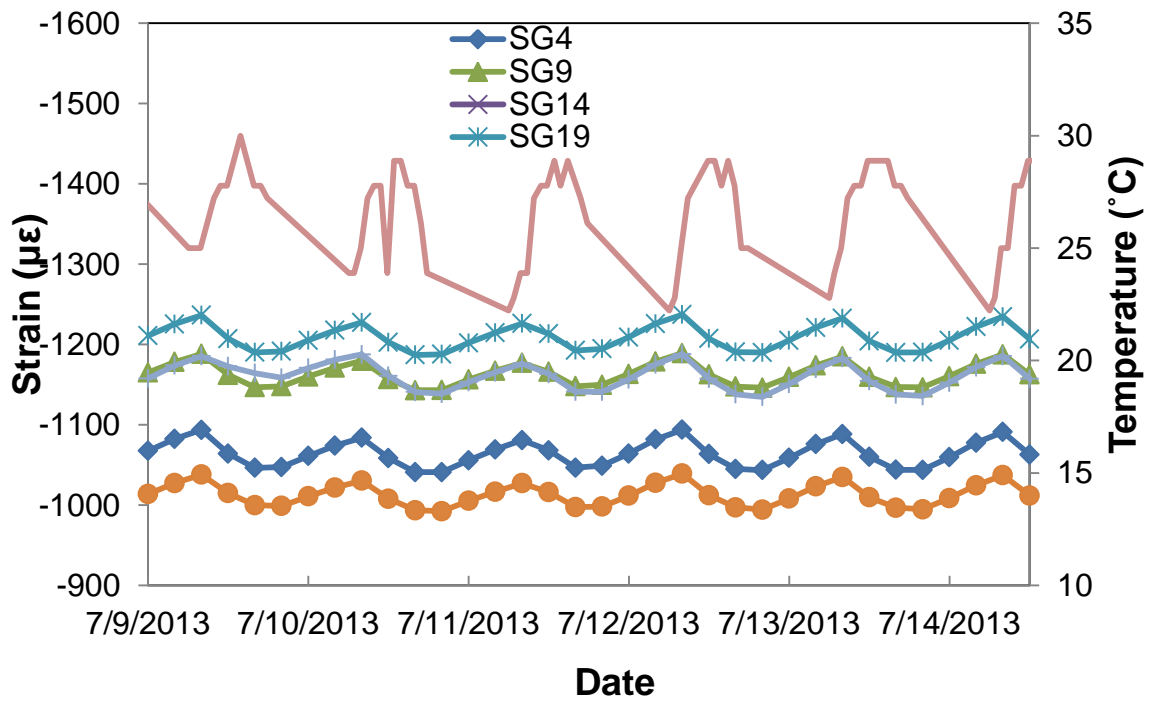


Figure 139 East Wall Strain and Ambient Temperature vs Time

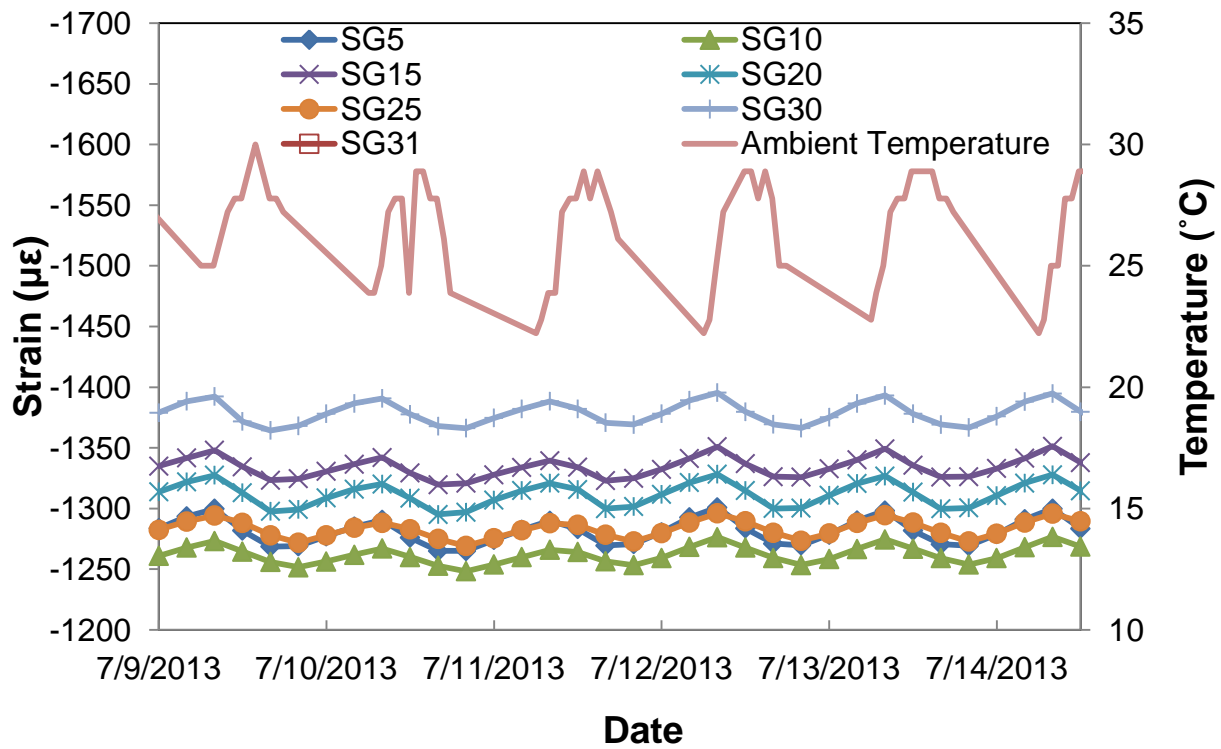


Figure 140 Tub Girder Floor Strain and Ambient Temperature vs Time

Concrete undergoes volumetric strain with changes in temperature. The amount of volume change is governed by the material's coefficient of thermal expansion in accordance with Equation 16. For example the change in length over a 5.6°C (≈10°F) temperature swing, which is typical for Lahaina, and using a coefficient of thermal expansion of 4.4 to 6.7 x 10<sup>-6</sup> in/in/°F for concrete is 0.029 to 0.044 inches. Using the definition of strain (Equation 17), the change in measured strain should be between 44 to 67 με.

$$\Delta L = (\alpha)(L_0)(\Delta T) \quad (16)$$

$\Delta L$  = change in length

$\alpha$  = linear temperature expansion coefficient (reinforced concrete)  
= typically between 4.4 to 6.7 x 10<sup>-6</sup> in/in/°F

$L_0$  = initial length = span length/2 = 109 feet/2 = 654 inches

$\Delta T$  = Change in Temperature

$$\epsilon = \frac{\Delta L}{L_0} = (\alpha)(\Delta T) \quad (17)$$

The strains closest to the theoretical strain associated with a 5.6°C temperature change at 4 P.M. on 7/13/2013 to 4 A.M. on 7/14/2013 are those in the wearing surface and pre-cast planks (Table 39). The wearing surface is exposed to the sun most while the tubs being below and in the shade, are less affected by the ambient temperature.

**Table 39 Comparison of Measured and Calculated Strains Over Half a Temperature Cycle**

	<b>Location</b>	<b>Strain at 4:00 PM on 7/13/13</b>	<b>Ambient Temperature (°C)</b>	<b>Strain at 4:00 AM on 7/14/13</b>	<b>Ambient Temperature (°C)</b>	<b>Measured <math>\Delta\mu\epsilon</math></b>	<b>Calculated <math>\Delta\mu\epsilon</math></b>
SG1	Wearing Surface	-186	27.8	-231	22.2	45	44 - 67
SG2	Precast Planks	-507	27.8	-551	22.2	44	44 - 67
SG3	Tub West Wall	-1103	27.8	-1139	22.2	36	44 - 67
SG4	Tub East Wall	-1044	27.8	-1078	22.2	34	44 - 67
SG5	Tub Floor	-1272	27.8	-1288	22.2	16	44 - 67
SG6	Wearing Surface	-199	27.8	-230	22.2	31	44 - 67
SG7	Precast Planks	-498	27.8	-535	22.2	37	44 - 67
SG8	Tub West Wall	-1136	27.8	-1165	22.2	29	44 - 67
SG9	Tub East Wall	-1147	27.8	-1176	22.2	29	44 - 67
SG10	Tub Floor	-1259	27.8	-1268	22.2	9	44 - 67
SG11	Wearing Surface	-271	27.8	-320	22.2	49	44 - 67
SG12	Precast Planks	-644	27.8	-683	22.2	39	44 - 67
SG13	Tub West Wall	-934	27.8	-965	22.2	31	44 - 67
SG14	Tub East Wall	-831	27.8	-858	22.2	27	44 - 67
SG15	Tub Floor	-1326	27.8	-1341	22.2	15	44 - 67
SG16	Wearing Surface	-194	27.8	-228	22.2	34	44 - 67
SG18	Tub West Wall	-1202	27.8	-1239	22.2	37	44 - 67
SG19	Tub East Wall	-1190	27.8	-1222	22.2	32	44 - 67
SG20	Tub Floor	-1300	27.8	-1321	22.2	21	44 - 67
SG21	Wearing Surface	-233	27.8	-264	22.2	31	44 - 67
SG22	Precast Planks	-544	27.8	-577	22.2	33	44 - 67
SG23	Tub West Wall	-952	27.8	-983	22.2	31	44 - 67
SG24	Tub East Wall	-997	27.8	-1025	22.2	28	44 - 67
SG25	Tub Floor	-1280	27.8	-1289	22.2	9	44 - 67
SG26	Wearing Surface	-166	27.8	-206	22.2	40	44 - 67
SG27	Precast Planks	-447	27.8	-486	22.2	39	44 - 67
SG28	Tub West Wall	-1154	27.8	-1187	22.2	33	44 - 67
SG29	Tub East Wall	-1138	27.8	-1171	22.2	33	44 - 67
SG30	Tub Floor	-1369	27.8	-1388	22.2	19	44 - 67
SG31	Concrete Cylinder	-348	27.8	-362	22.2	14	44 - 67

### 5.5.5 Strain Gage Temperature

Figures 141-146 display the temperatures recorded in the strain gages installed in the wearing surface (SG1, 6, 11, 16, 21 and 26) pre-cast planks (SG2, 7, 12, 17, 22 and 27) and tub girders (SG3, 8, 13, 18, 23, 28 in the west walls; SG 4, 9, 14, 19, 24 and 29 in the east walls; SG 5, 10, 15, 20, 25, 30 in the tub floors), at the third point of each tub girder. In general, the temperatures in the wearing surface were highest, followed by the pre-cast planks, the tub girder walls and the tub girder floors indicating that the temperature of the concrete decreased from the top of the superstructure to the bottom. This is consistent with the strains in Table 39 where the wearing surface was directly affected by the sun while the precast planks and the tub girders were less affected as they were in the shade.

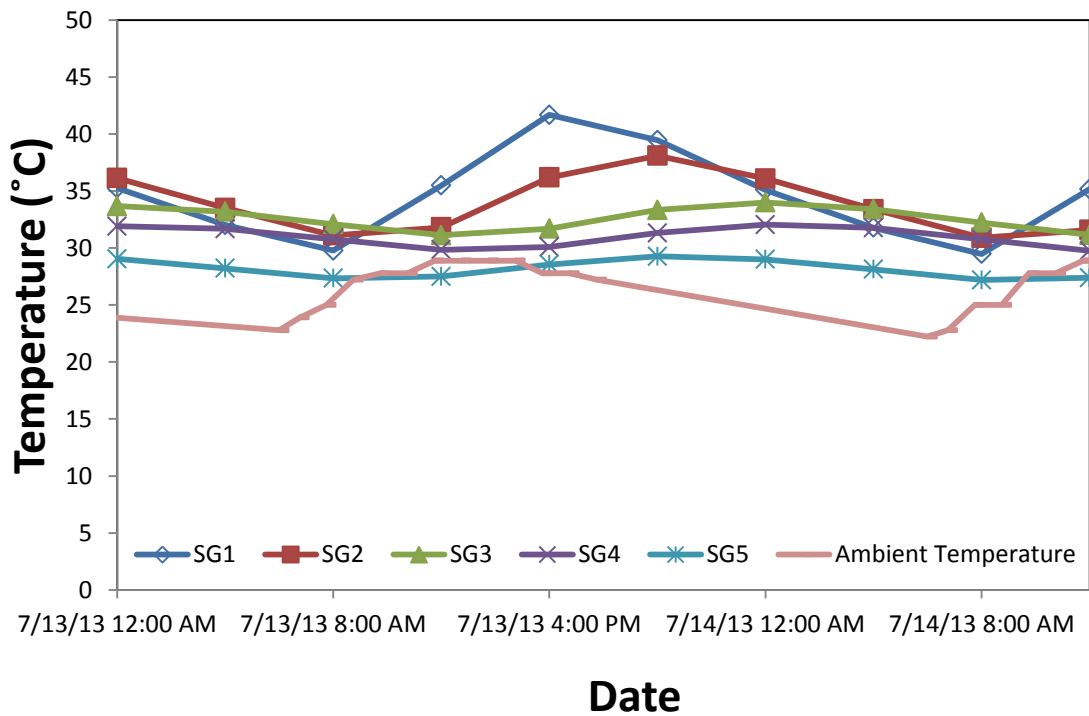


Figure 141 Temperatures in Tub Girder 3 on Abutment 1 Side

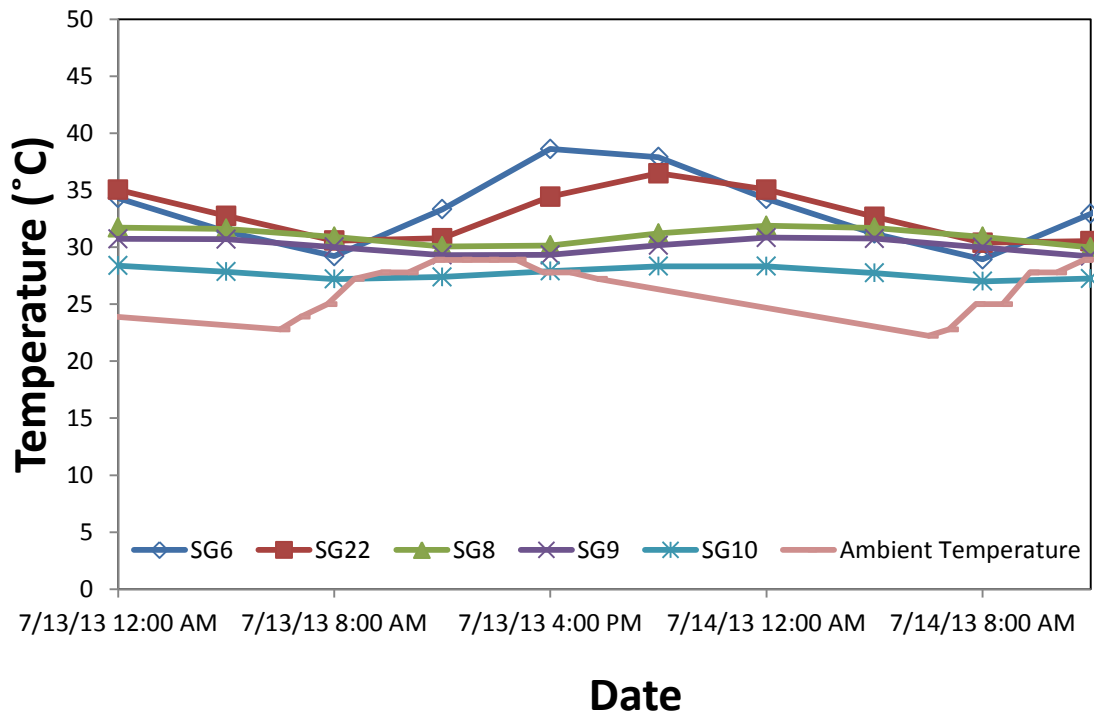


Figure 142 Temperatures in Tub Girder 2 on Abutment 1 Side

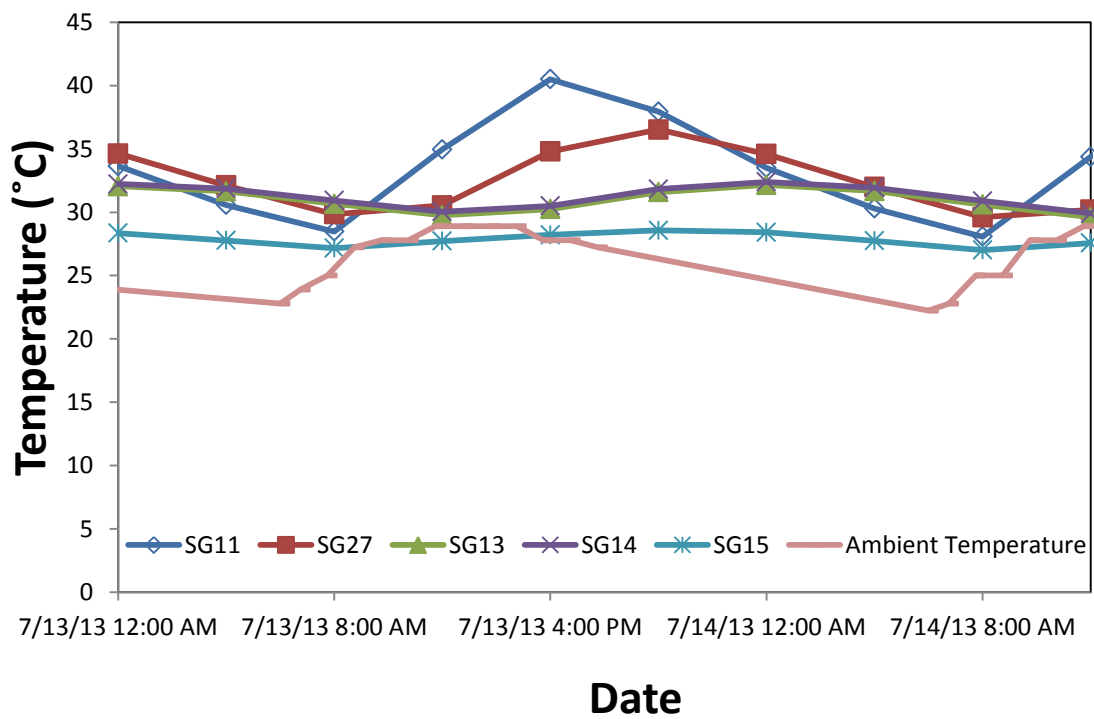
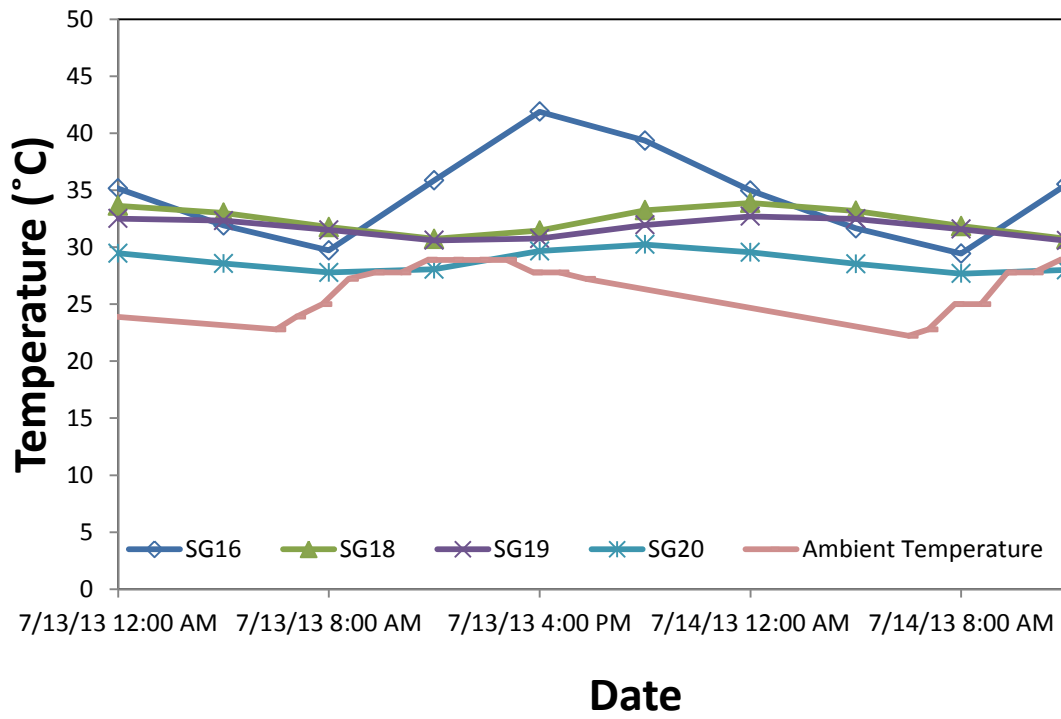
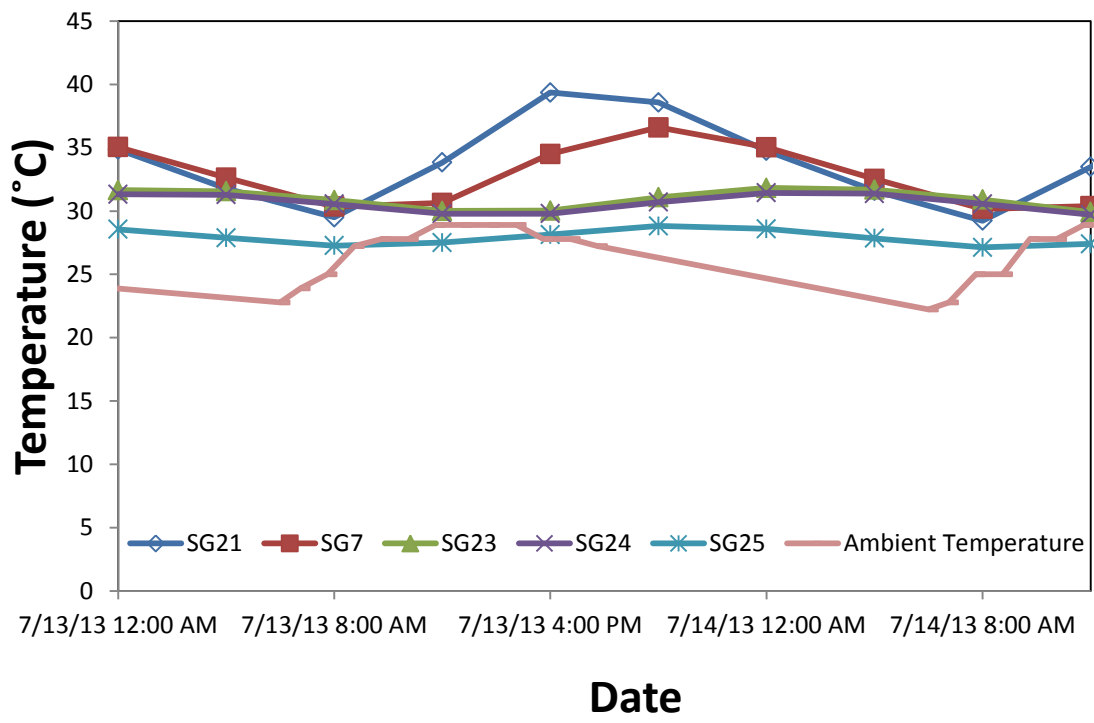


Figure 143 Temperatures in Tub Girder 1 on Abutment 1 Side



**Figure 144 Temperatures in Tub Girder 3 on Abutment 2 Side (SG17 in the precast planks stopped working)**



**Figure 145 Temperatures in Tub Girder 2 on Abutment 2 Side**

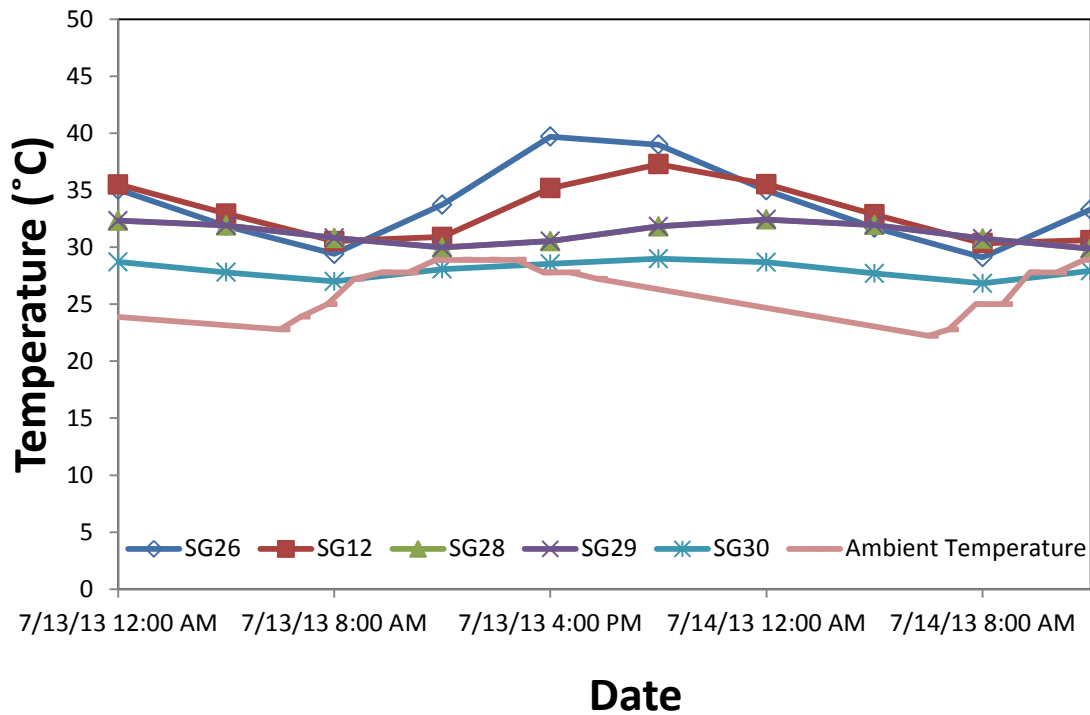


**Figure 146 Temperatures in Tub Girder 1 on Abutment 2 Side**

### 5.6 Verification of GRS-IBS Behavior

Expansion and contraction of the bridge superstructure is believed to cause rotation of the footing about a transverse axis. Figure 147 displays the behavior of the EP cells over a day in July 2013. When the ambient temperature was lowest, contraction of the superstructure caused the footing to rotate with its toe moving down on the GRS. This rotation caused the vertical pressures in EP cells closer to the stream (EP 1 and 2) to increase. When the ambient temperature was highest, expansion of the tub girders caused the footing to rotate with its toe lifting off from the GRS. This rotation caused the vertical pressures experienced by EP 1 and 2 to decrease. Figure 147 is consistent with the behavior described above; the only caveat is that there appears to a slight lag in the minimum pressure reacting to the warmest temperature. However, this may be due to the fact that the temperature and pressure readings were read at discrete time intervals that were not frequent enough. Note that the weight of the bridge does not change; therefore the average pressure should be relatively constant. However, Figure 147



shows that the average vertical pressure still cycles with temperature. This cyclic behavior implies that some of the weight is distributed to the wing wall footings.

The FB readings also showed evidence that a slight rotation of the footing occurred. Figure 148 displays the FB data associated with the middle tub girder of Abutment 2. When the ambient temperature was lowest, the tub girders contracted and a decrease in lateral earth pressure was recorded. Conversely when the ambient temperature was highest, expansion of the tub girders caused an increase in lateral pressure. The top most FB (FB10) experienced a large increase and decrease in lateral pressure over a 24-hour-period. This further supports the theory that there is rotation of the footing about the transverse axis accompanied by rotation of the end wall due to thermal expansion and contraction of the bridge superstructure.

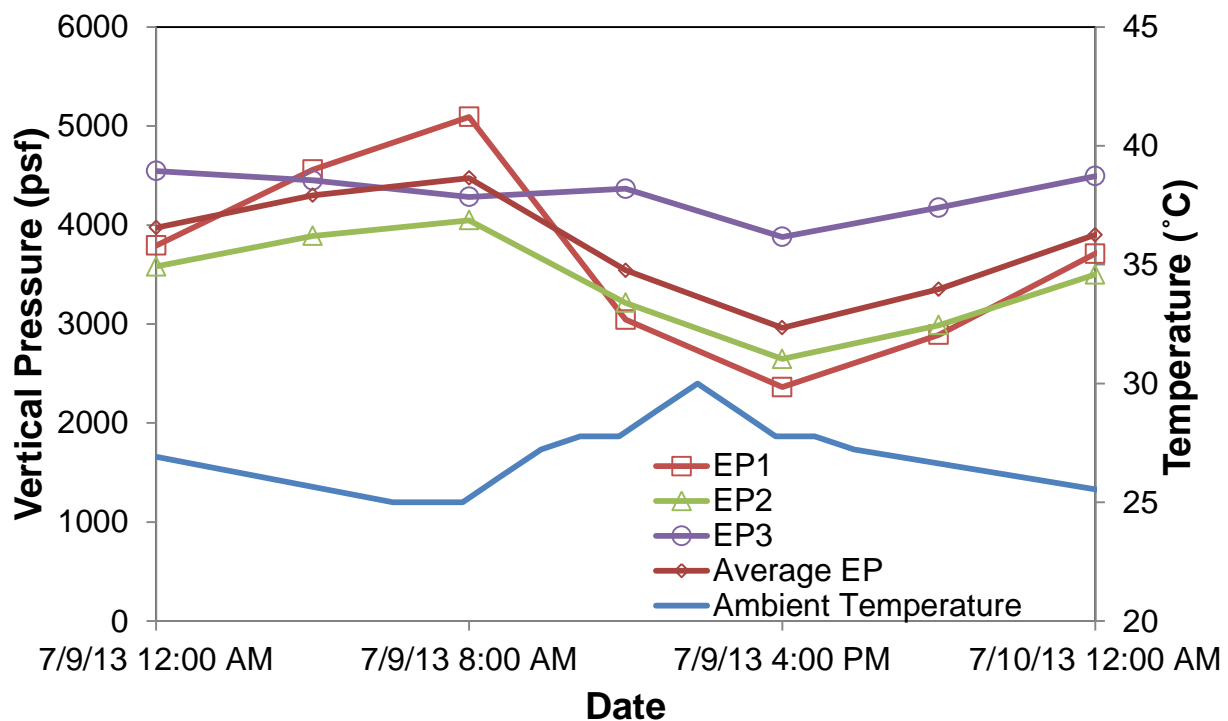


Figure 147 Vertical Pressure Variation Over One Day

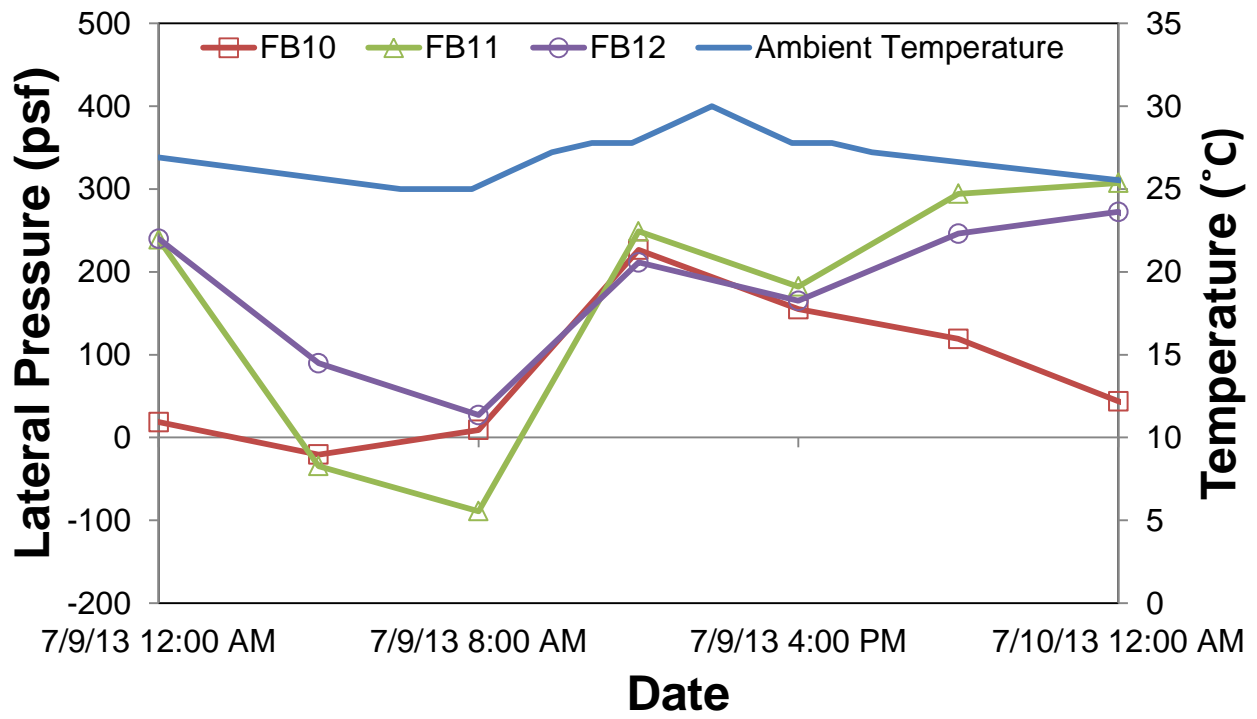


Figure 148 Lateral Pressure Variation Over One Day

## 6 FINITE ELEMENT ANALYSIS

Construction of the GRS abutment described in Chapter 3 was simulated using the finite element method (FEM). The data collected during construction was compared to the numerical analysis results as a check for reasonableness.

### 6.1 Software and Model Parameters

The FEM analysis was conducted in 2-D assuming plane strain conditions. NAVFAC (1989) consider the plane strain assumption as reasonable when the L/b ratio > 5 where L is the length and b is the footing width. The GRS abutment length was 55 feet and the bridge footing width was 5 feet, giving an L/b ratio of 11.

Numerical analyses were performed using PLAXIS 2D 2010 (Brinkgreve, 2011). All soils were modeled using the bi-linear elasto-plastic Mohr-Coulomb model. The geomaterial that influences the GRS behavior most is the abutment fill, which is directly below the footing and adjacent to the CMU. Being further away, the properties of the older alluvium and rip rap have less of a behavioral influence. The unit weight of the fill represents the average value measured from field density testing. The shear strength parameters are from large scale direct shear tests as shown in Figure 24 (Section 3.1.3). The Mohr-Coulomb failure envelope of the abutment fill is actually curved. A cohesion of 1185 psf was inferred using linear regression through the three direct shear test points in Figure 24. The dilatancy angle is estimated using Bolton's expression as follows:

$$\phi_{\text{peak}} = \phi_{\text{crit}} + 0.8\psi \quad (18)$$

where  $\phi_{\text{peak}}$  = peak friction angle,  $\phi_{\text{crit}}$  = fully softened or critical state friction angle and  $\psi$  = dilatancy angle. Since  $\phi_{\text{peak}} = 53.8^\circ$  and  $\phi_{\text{crit}} = 49^\circ$  from Figure 24,  $\psi = 6^\circ$  using Equation 18. In PLAXIS, the Young's modulus of the abutment fill can be specified to increase linearly with depth. Duncan et al (1980) provided the following expression for the initial Young's modulus,  $E_i$ , of a GW material compacted to 100% relative compaction based on standard Proctor which is roughly equivalent to 95% relative compaction based on modified Proctor.

$$E_i = 450 \left( \frac{\sigma_3}{p_a} \right)^{0.4} \quad (19)$$

where  $\sigma_3$  = minor principal stress = horizontal stress and  $p_a$  = atmospheric pressure. Since the PLAXIS Young's modulus is taken at 50% of yield,  $E_{50} \approx 0.5E_i$ ; i.e.;

$$E_{50} = 225 \left( \frac{\sigma_3}{p_a} \right)^{0.4} \quad (19)$$

When plotted versus depth,  $E_{50}$  varies non-linearly as shown in Figure 149. A linear approximation for the modulus can be made by specifying  $E_{50} = 67.3$  ksf at the top and a slope of 19.2 ksf per ft of elevation drop.

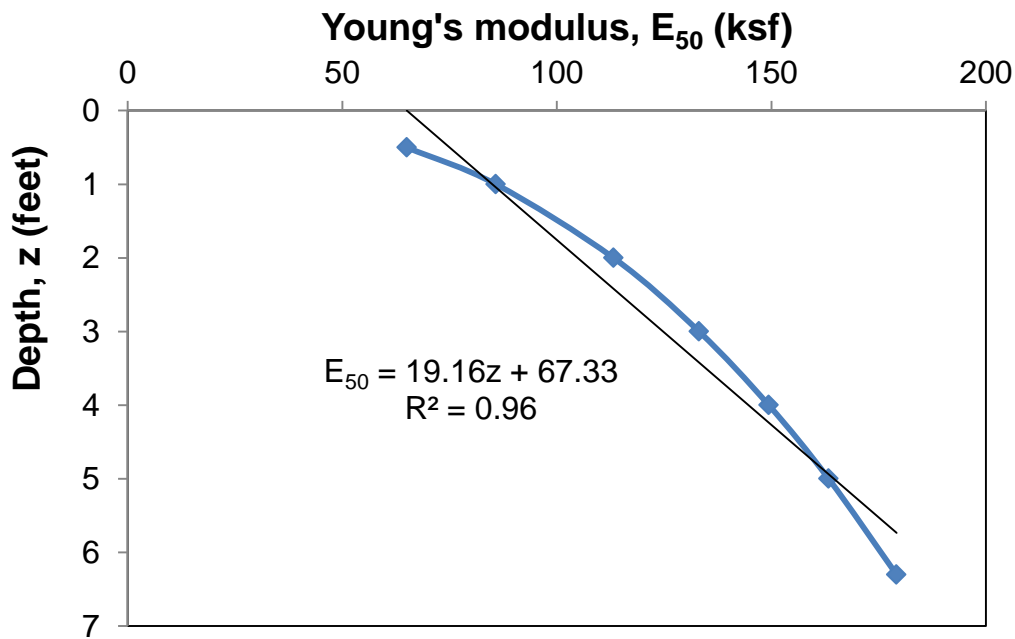


**Figure 149** Abutment Fill's  $E_{50}$  as a Function of Depth

The older alluvium and rip rap were both assigned a large unit weight, a large friction angle and a large Young's modulus. Their dilatancy angle is approximated as  $\phi_{\text{peak}} - 30^\circ$  which is approximately true for quartz according to the PLAXIS materials model manual (PLAXIS, 2011). Clearly, the older alluvium and rip rap are not quartzitic but as indicated earlier, the older

alluvium and rip rap do not have a major influence on the overall GRS behavior; hence this approximation is deemed adequate.

The CMU and footing were modeled as linear elastic. Table 40 summarizes the material properties utilized in the FEM analysis. Calculation of other material properties can be found in Appendix C.

**Table 40 Material Input Parameters for Finite Element Analysis**

Material	Unit weight $\gamma$ (lb/ft <sup>3</sup> )	Cohesion c (psf)	Friction angle $\phi$ (°)	Young's modulus E <sub>50</sub> (lb/ft <sup>2</sup> )	Poisson's ratio v	Dilatancy angle $\psi$ (°)
Abutment Fill	151	1185 <sup>1</sup>	53.8	<sup>1</sup>	0.2	6
Older Alluvium	160	0	55	1.04x10 <sup>6</sup>	0.3	25
CMU Block	93.5	Modeled as Linear Elastic		5.8x10 <sup>8</sup>	0.0	N/A
Footing	150	Modeled as Linear Elastic		5.8x10 <sup>8</sup>	0.0	N/A
Rip Rap	160	0	55	1.04x10 <sup>6</sup>	0.3	25

Note: 1. The modulus of the abutment fill is not a constant. It was assigned a value of 67.3 ksf at the top and increased linearly with depth at a rate of 19.2 ksf per ft.

PLAXIS requires the axial stiffness (EA) and the wide width tensile strength (T<sub>i</sub>) of the geotextile, the values of which are shown in Table 41. The load-deformation relationship of a fabric in a uniaxial tension test is commonly expressed as load/width vs. strain. Since E is the slope of load/area vs. strain curve in a uniaxial test, the slope of load/width vs. strain curve is E\*thickness. In plane strain, the width is taken as 1 unit of length, hence E\*A = E\*thickness\*1 = slope of load/width vs. strain curve. From Appendix B, the tensile strength at 5% strain is 2400 lb/ft (Appendix B). Hence, EA = 2400/0.05 = 48,000 lb/ft.

**Table 41 Geotextile Input Parameters for Finite Element Analysis**

Type of Geotextile	Axial Stiffness EA (lb/ft)	Ultimate Strength T <sub>f</sub> (lb/ft)
Mirafi® PET 70/70	48000	4800

Due to symmetry, only half the bridge was considered in the mesh. All boundaries except the line of symmetry were rough and rigid (fixed both horizontally and vertically) while the line of symmetry was smooth and rigid (fixed horizontally but free to displace vertically). The lateral extent of the finite element mesh was extended until no noticeable difference in the GRS abutment behavior was observed when loaded. The bottom boundary extends 10 feet below the RSF. A medium coarse mesh made up of 15-node triangular elements was utilized.

Interface elements were specified to allow relative movement between the structural elements (CMU) and the soil (abutment fill) that they contact. They have zero thickness and are elastoplastic.

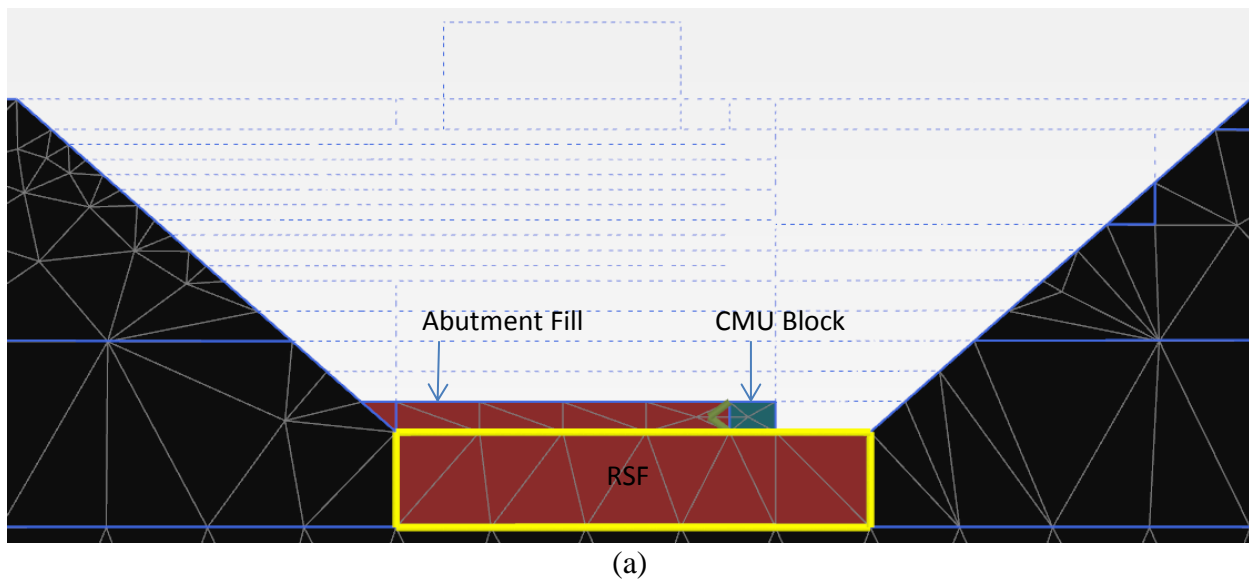
## 6.2 Modeling the Construction Sequence

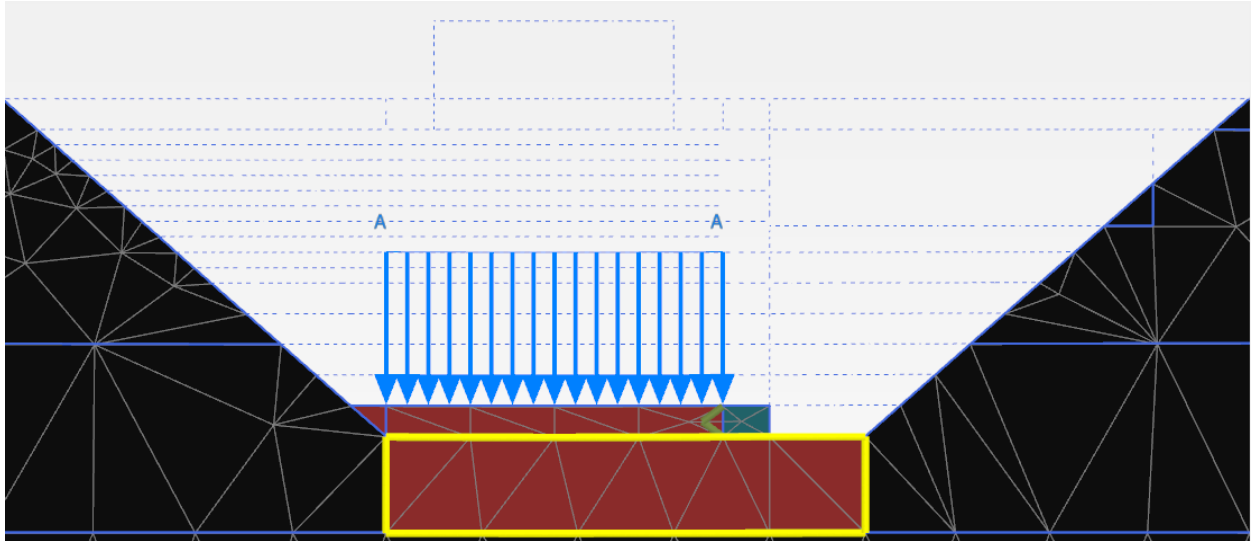
The construction sequencing was modeled as follows:

1. Place first lift of facing blocks and soil. The compaction thickness was 0.64 feet for the first 5 lifts and 0.32 feet for the last 10 (Figure 150a).
2. Activate interface element between soil and CMU.
3. Apply and remove a uniform vertical stress of 2000 psf over the entire surface of the soil layer to simulate compaction (Figure 150b). (The vibratory plate compactor was a Wacker BPU 4045. The centrifugal force was rated at 8992 lbs and the plate area was 4.3 ft<sup>2</sup>).
4. Place a sheet of geotextile to cover the entire soil layer and facing block (Figure 150c).
5. Place another lift of soil and facing blocks over the previous lift (Figure 150d).
6. Repeat steps 2 through 5 until the fifth CMU course is reached.
7. Place the next CMU course and 0.32 ft of soil.
8. Apply and remove a uniform vertical stress of 2000 psf over the entire surface of the soil layer

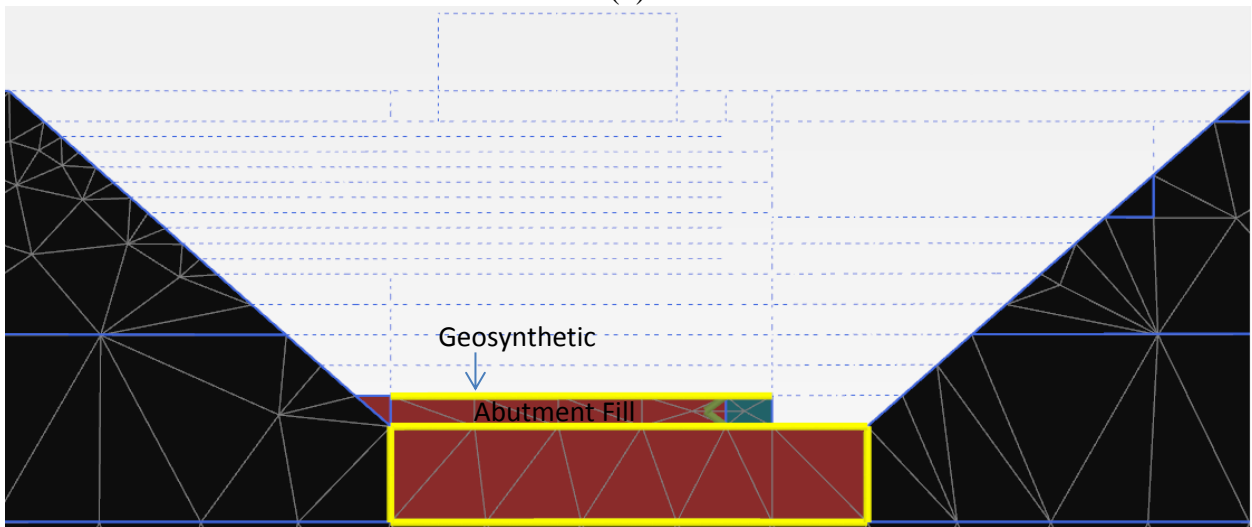
to simulate compaction.

9. Place another 0.32 ft of soil so that it is flush with the top of the CMU.
10. Apply and remove a uniform vertical stress of 2000 psf over the entire surface of the soil layer to simulate compaction.
11. Place a sheet of geotextile to cover the entire soil layer and facing block.
12. Repeat steps 7 through 10 until the top of the GRS abutment is reached (Figure 150e).
13. Place rip-rap in front of GRS abutment (Figure 150f).
14. Place footing on top of GRS abutment (Figure 150g).
15. Apply loads to the footing corresponding to construction events outlined in Table 9 in Section 5.1.1 (Figure 150h)



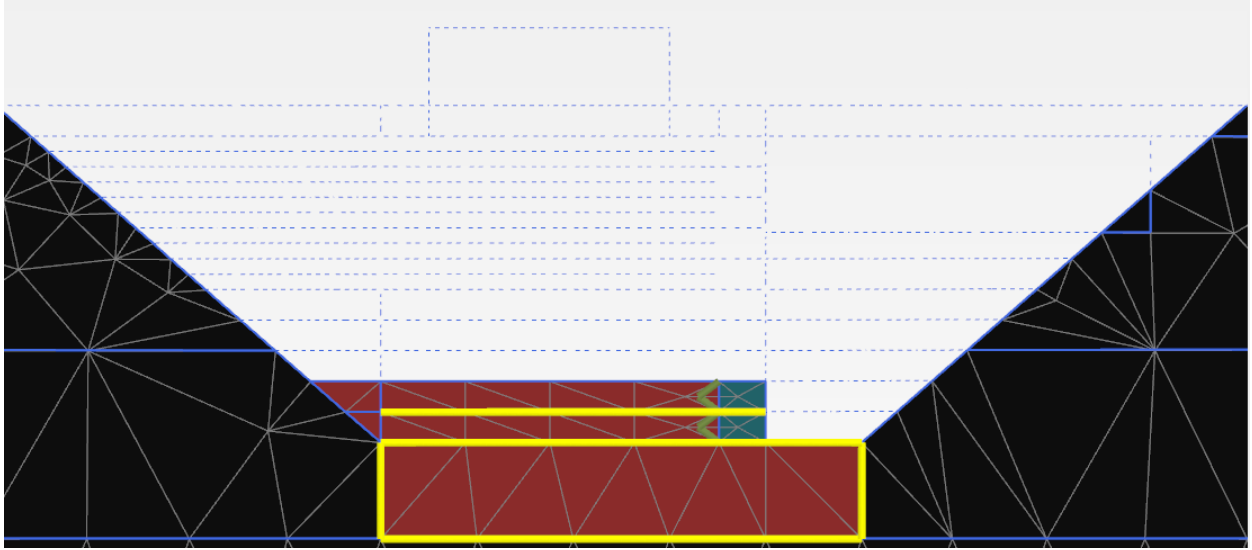


(b)

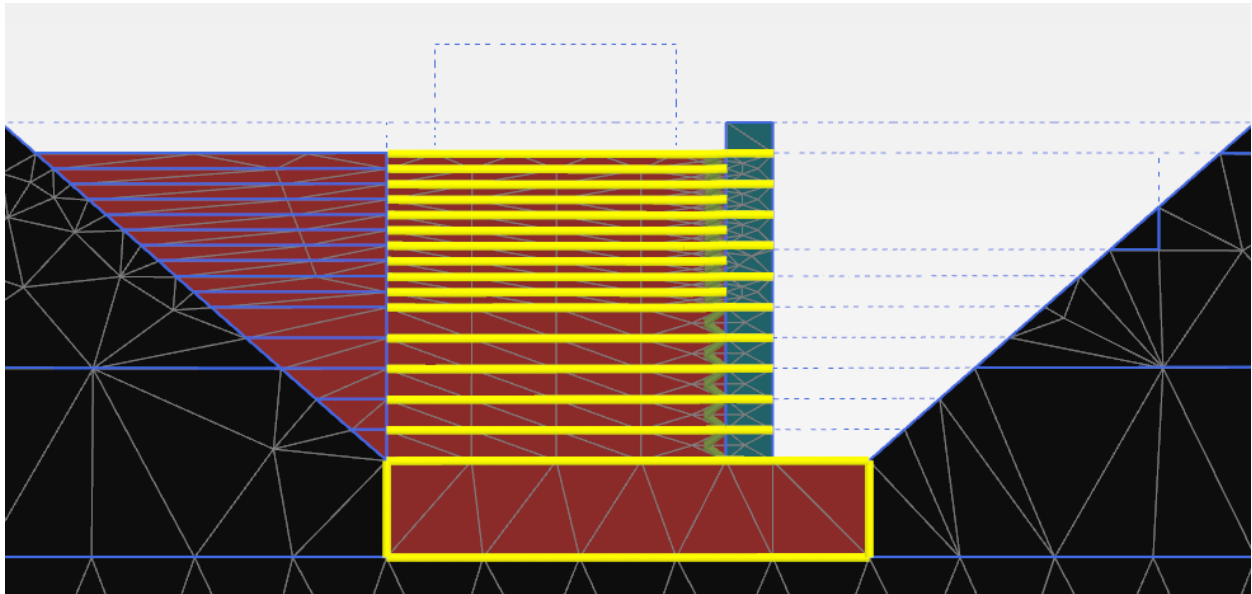


(c)

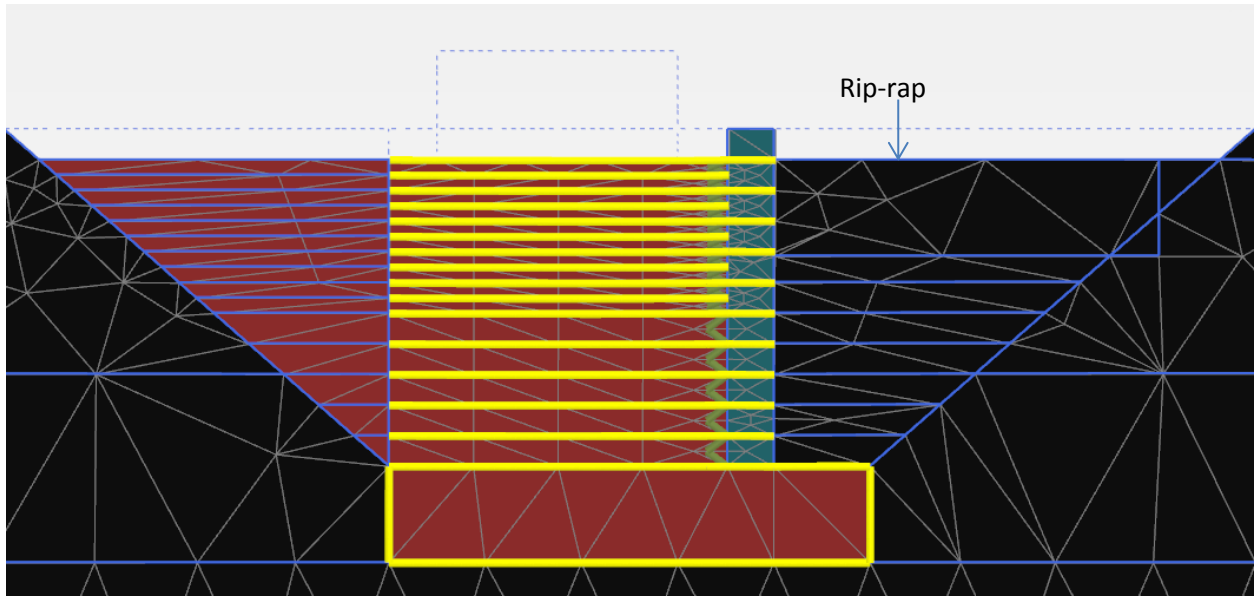




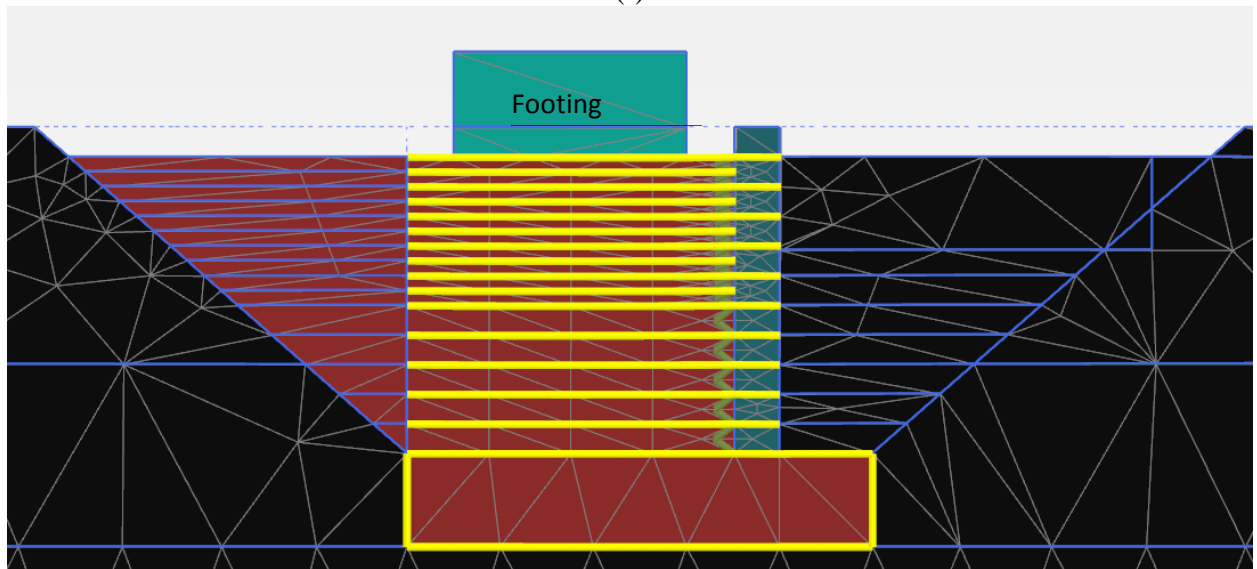
(d)



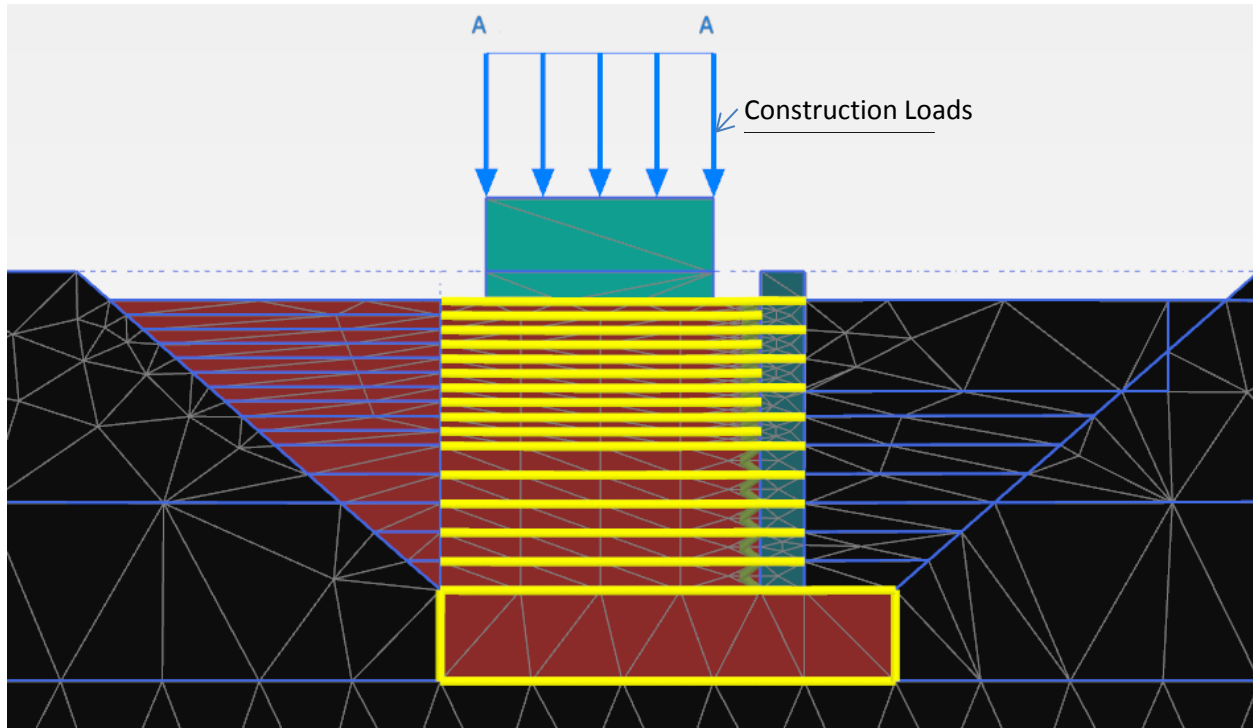
(e)



(f)



(g)



(h)  
**Figure 150 Construction Sequence**

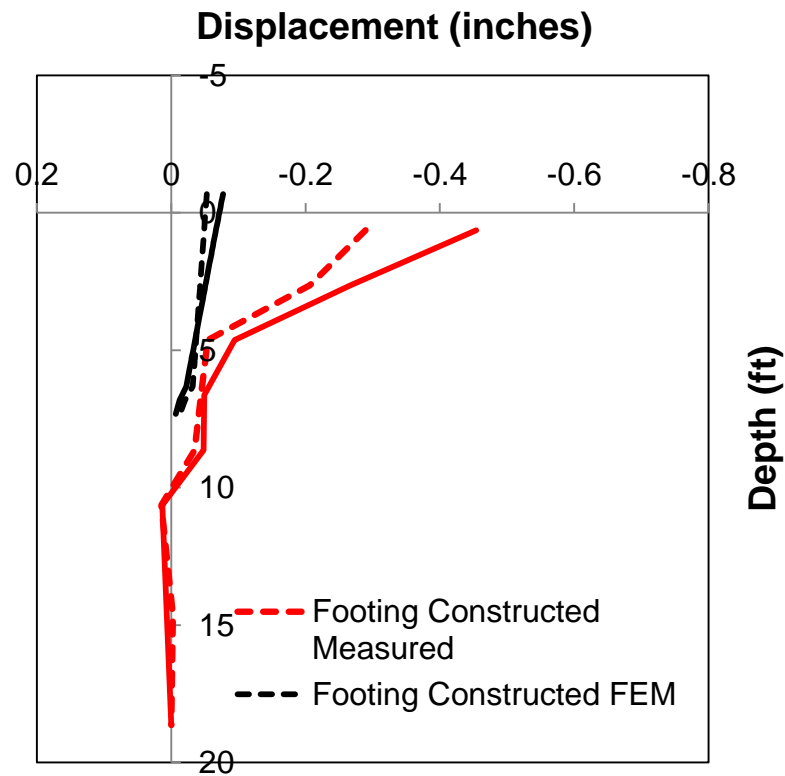
### 6.3 Comparison of Calculated and Measured Behavior

Figures 151a and b compare the calculated and measured lateral displacements during 4 significant construction milestones. It should be noted that the inclinometers were installed only after 10 courses of the CMU blocks and GRS were completed but prior to rip rap placement. Hence, to generate the lateral deflected profile in Figure 145, lateral displacements plotted = lateral displacements at each construction milestone – lateral displacements at the end of GRS construction.

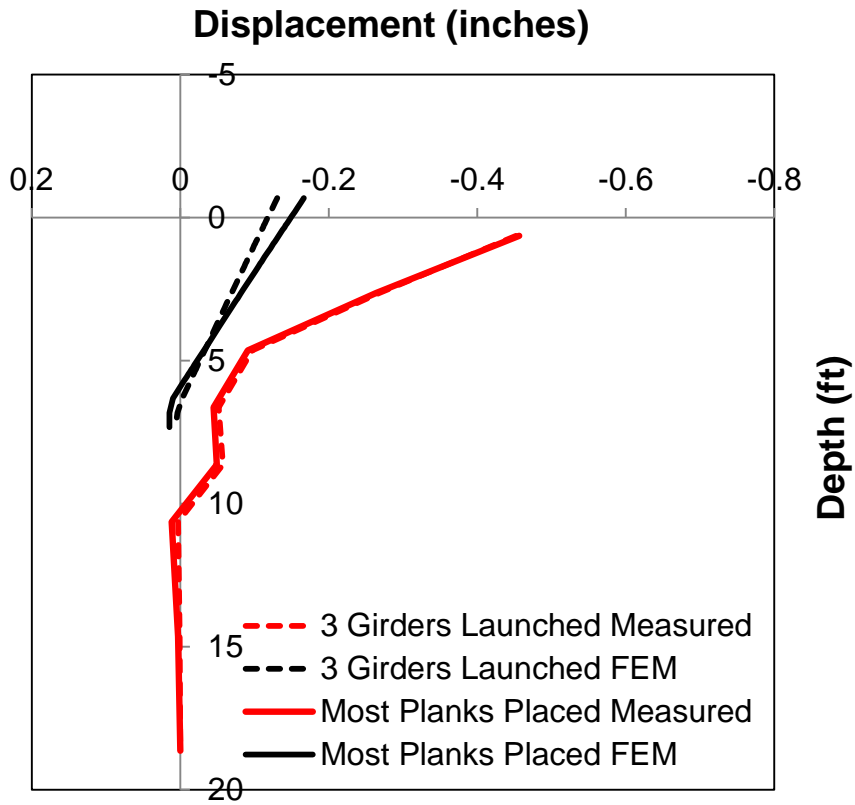
For all 4 cases, the largest lateral displacement consistently occurred at the top of the CMU. The deflected profile of the CMU blocks curved towards the backfill due to the fact that the rip-rap placement in front of the CMU has a large buttressing effect while the superstructure loading has a negligible effect especially under service loads. The calculated lateral displacements are significantly smaller than the measured displacements. However, the predicted and measured lateral earth pressures in the CMU are remarkably similar in magnitude and behavior (Figure

152). Overall, the lateral earth pressures increased as more and more construction milestones were reached.

Figure 153 compares the calculated and measured settlement for 3 construction milestones. The calculated settlements were slightly larger than the measured settlements for all three events. After most planks were in place, a settlement of 0.73 inches was measured but the calculated settlement was 1.0 inch or 0.27 inches larger. Considering that these calculations were made without any stress-strain data from triaxial tests for the abutment fill, overall the results from the FEM analysis can be considered quite consistent with the measured.



(a)



(b)  
**Figure 151 Predicted vs Measured Displacements**

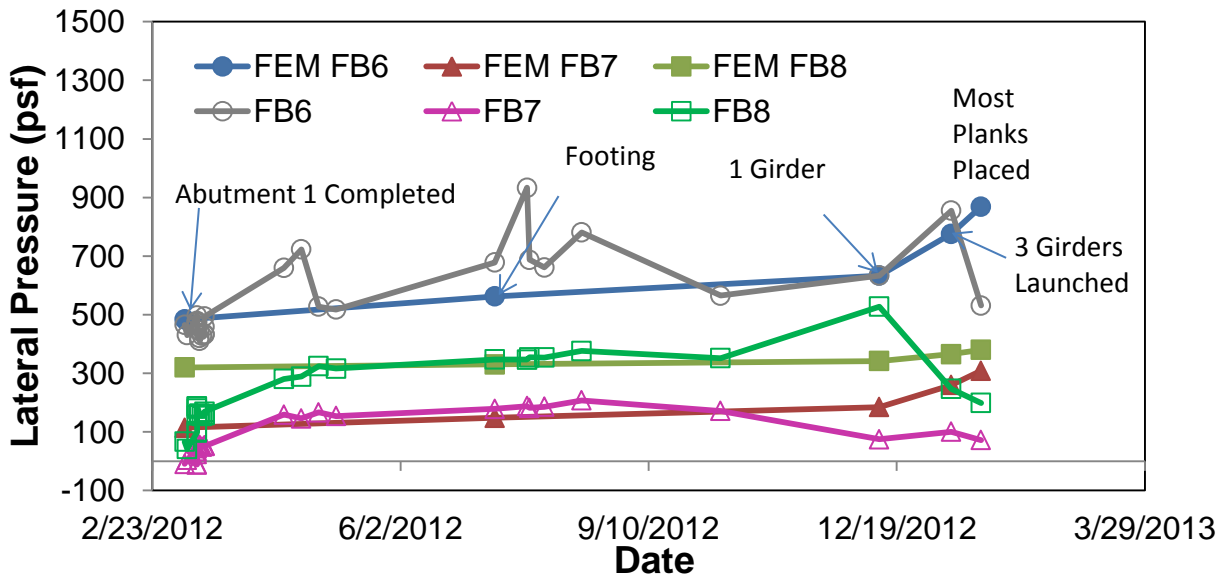


**Figure 152 Calculated vs Measured Lateral Pressures on the Facing**

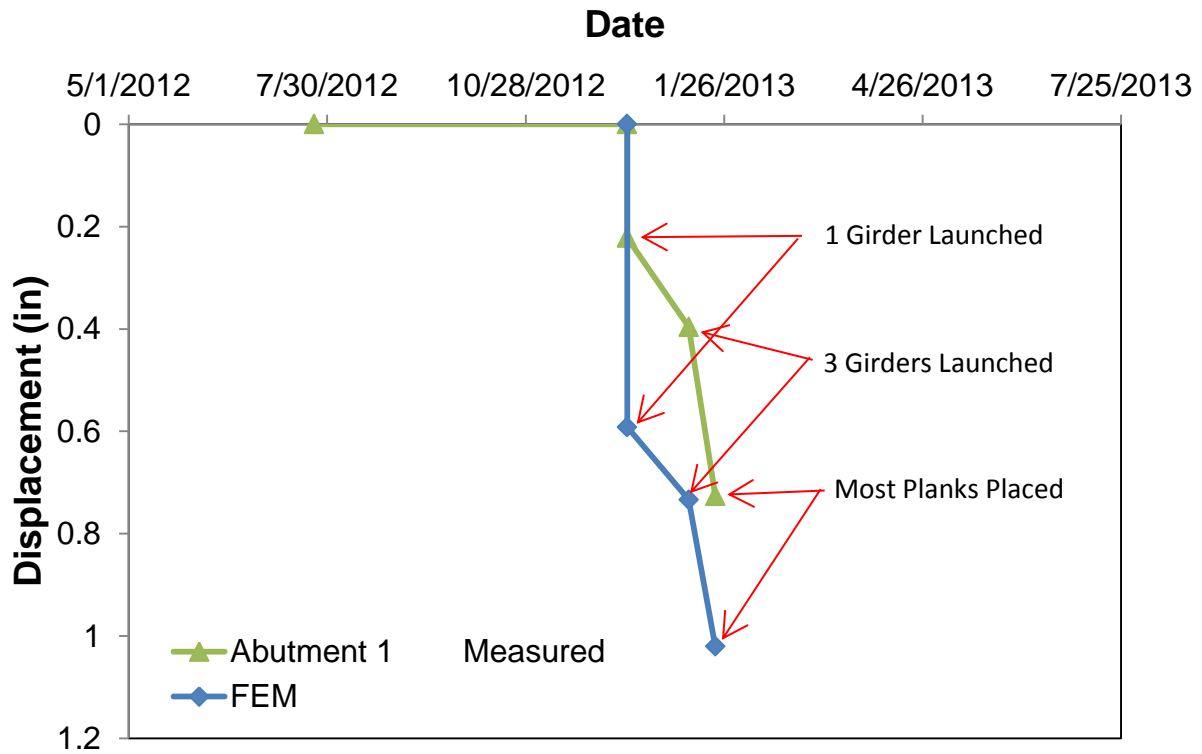


Figure 153 Calculated vs Measured Settlement

## 7 SUMMARY AND CONCLUSIONS

### 7.1 Project Summary

GRS-IBS is a relatively new bridge system promoted by the FHWA for single span bridges. The first GRS-IBS in Hawaii was constructed across the Kauaula Stream in Lahaina on the island of Maui, Hawaii. Structural health monitoring of this bridge was performed during and after construction with the aid of survey points and a comprehensive instrumentation system.

Vibrating wire instruments were placed in the GRS abutments and superstructure to monitor the 1) strains in the tub girders, 2) vertical stresses under the bridge footing, 3) lateral earth pressures on the facing and end walls, 4) lateral displacement of the facing blocks, 5) settlement of the bridge footing. All vibrating wire instruments were connected to a data acquisition system for remote monitoring. A FEM analysis was performed to compare with some of the measured data during construction. The following conclusions are offered as a result of this study.

### 7.2 Conclusions

1. The vertical pressures recorded below the Abutment 2 footing compared reasonably well with calculated values during the various construction events. The percent difference between the calculated and measured pressures ranged from -20 to +7%, excluding the 1 girder launch where it was overestimated by 77%. This discrepancy can be attributed to a rotation of the footing caused by the first tub girder loading only one (east) side of the footing.
2. The measured vertical pressures cycled during the course of a 24-hour period due to ambient temperature changes. As the temperature increased to a maximum in the afternoon, the bridge superstructure expands and hogs causing the footing to rotate about a transverse axis whereby the portion of the footing on the stream side lifts off. The vertical EP cells closer to the stream, EP1 and EP2, experienced a larger pressure fluctuation versus ambient temperature compared to EP3, which is farthest from the stream.
3. To determine whether the vertical pressure fluctuation is genuinely temperature-induced and not due to noise, a dummy EP cell was placed inside the Abutment 2 J-box. The ambient temperature ranged from 22°C to 30°C while the dummy cell instrument temperature ranged from 28.7 °C to 30.6 °C. Since they were buried below the footing, the EP cell temperatures

remained relatively constant. The EP cells installed under the footing continued to fluctuate while the dummy cell essentially read 0. The data suggests that there is little noise from the data acquisition system and the vertical pressure fluctuations in EP cells 1 to 3 appear to be temperature-induced.

4. The GRS abutment footings settled less than 0.9 inches in total at the time of writing. The Abutment 1 and 2 footings settled 0.85 inches and 0.55 inches, respectively.

5. It was found that the FB cells were sensitive to temperature. The lateral pressure recorded increased linearly with increasing temperature even when there was no change in the applied pressure. Temperature gradients varying from 11.3 psf/°C to 20.6 psf/°C were measured in the 10 FB cells installed behind the end walls.

6. Lateral pressures behind the CMU blocks displayed cyclic behavior as a function of ambient temperature. It was observed that the lateral pressures increased with increasing ambient temperature but the variation of lateral pressures from peak to trough over a month were in general 200 psf or less.

7. The lateral pressures recorded on the CMU blocks showed a slight increase with time after construction. It is possible that this slight increase is due to the effects of soil ratcheting or continuous “pounding” of the footing on the GRS backfill or due to a temperature increase as the season transitioned from spring to summer.

8. All FB installed on the end walls recorded lateral pressures larger than the at-rest values after being standardized to a temperature of 31°C. Standardization to a temperature was made to minimize the effects of temperature on the FB readings. The measured end wall lateral pressures were large due to locked-in compaction induced stresses.

9. The average lateral pressures in 7 of the 10 FB cells installed on the end walls decreased with time. The stress reduction is most likely due to shrinkage of the superstructure concrete. The average lateral pressures in the remaining three FBs exhibited some erraticism but overall remained fairly constant.



10. The lateral pressures on the end walls generally cycled with of time and are more or less in phase with the ambient temperature cycles; i.e.; the lateral pressure increased with ambient temperature due to thermal expansion of the tub girders and vice versa. Cycling of the lateral pressures is not due to changes in the gage temperature since the temperatures in the FBs, once they are buried, remained fairly constant. This trend also supports cycling of the vertical pressures due to rotation of the footing about a transverse axis. The top most FB experienced the largest increase and decrease in lateral pressure.

11. The inclinometers in the CMU blocks were installed at the end of GRS construction. This was followed by rip-rap placement in front of the CMU which caused the CMU blocks to laterally displace towards the backfill at the top. This movement away from the stream was recorded by the inclinometers. The lateral displacements increased with each major construction event. However, after construction was completed, the lateral displacements remained constant.

12. When the strains in the wearing surface were plotted with time, they were slightly lower than those of a concrete cylinder that served as a control. This is due to the fact that the topping has reinforcing that restrains the concrete from shrinking whereas the cylinder, being unreinforced, shrank more.

13. Larger compressive strains were observed in the precast planks than the concrete cylinder. This may be attributable to weight of and shrinkage of the wearing surface concrete after it was poured on the precast planks.

14. The strains in the floors of the tub girders were highest among all the locations monitored. They increased significantly after post-tensioning. They are larger than the strains measured in the concrete cylinder, wearing surface and precast planks. The strains in the floors of the tub girders decreased as more and more load (due to precast planks, wearing surface and jersey barriers) was placed on the tubs causing the tub girder floors to sag.

15. All strain gages show a trend of strain increasing with time. This suggests the occurrence of ongoing shrinkage in the concrete.

16. Using typical linear thermal coefficients of expansion for concrete and the ambient temperature change over a 12-hour-period, the calculated strains were compared to measured values. The strains closest to the theoretical are those in the wearing surface and pre-cast planks whereas the strains in the tubs were much lower. The wearing surface is exposed to the sun most while the tubs being below and in the shade, are less affected by the ambient temperature.

17. The average vertical pressure for the three EP cells below the footing also cycled with temperature when theoretically, they are expected to be constant since the weight of the bridge is constant. This can only imply that some of the weight is distributed to the wing wall footings.

18. The FEM analysis yielded nearly identical trends but not necessarily magnitude for vertical and lateral displacements and lateral earth pressure on the CMU facing. This helped verify that the observed trends and measured values are reasonable.

### 7.3 Main Contributions

In a fully integral abutment bridge supported on spread footings, the temperature induced cycling of vertical pressure on the GRS backfill due to the footing rotation about a transverse axis is significant. Design of such footings should consider whether the GRS fill will shakedown or not.

Concrete superstructure strains increase with time due to shrinkage causing the lateral pressures on the end walls to reduce with time.

It was observed that lateral earth pressures behind the CMU were generally close to or less than the Rankine active earth pressure values of the unreinforced abutment backfill during construction of the GRS. Numerical analyses of the GRS construction corroborated these observed lateral pressure measurements. This suggests that the lateral pressures behind the CMU blocks do not follow the Wu (2001), Soong and Koerner (1997), nor classical earth pressure theories for the Maui blocks used in this bridge.

#### 7.4 Recommendations for Future Research

The evidence indicates that due to thermal expansion and contraction of the Kauaula Stream bridge superstructure, the bridge footing rotates constantly about a transverse axis causing the GRS fill to be loaded and unloaded cyclically. From these load cycles, permanent deformation (PD) of the soil may occur. There are three possible outcomes: 1) the applied load is smaller than the shakedown limit, in which case the PD will approach a constant value with increasing load cycles (plastic shakedown), 2) the applied load is larger than the plastic shakedown limit but smaller than the plastic creep limit and the material will eventually fail after a large number of load cycles, or 3) the applied load is large and the deformation is plastic (incremental collapse) (Werkmeister 2003). The deviator stress for the Kauaula Stream Bridge is about 3000 psf for EP 1 and shakedown is expected based on PD testing of a basalt base course of similar gradation (Song, 2009). However, there is concern for GRS-IBS bridges that are constructed on open graded material. Open graded material has a lower shakedown limit than a well-graded material and its susceptibility to PD should be investigated.

It is also recommended that further investigation on the rotation of the footing about a transverse axis be made by installing vertical pressure cells below the wing wall footings of future GRS-IBS bridges. Alternatively, investigate whether the vertical pressures cycle for future GRS-IBS where the superstructure is supported on bearings resting on the footing; i.e.; no moment connection between the superstructure and the abutment wall and footing.

## 8 REFERENCES

- AASHTO. (2010) “LRFD Bridge Design Specifications”, Edition 5, American Association of State Highway and Transportation Officials.
- Abu-Hejleh, N., Zornberg, J. G., N., & Wang, T., McMullen M., Outcalt W. (2001). “Performance of geosynthetic-reinforced walls supporting the Founders/Meadows Bridge and approaching roadway structures”. Denver, Colo.: Research Branch, Colorado Dept. of Transportation.
- Abu-Hejleh, N., Zornberg, J. G., Elias, V., & Watcharamonthein, J. (2003). “Design assessment of the Founders Meadows GRS abutment structure”. In Proc., 82nd Annual TRB Meeting.
- Adams, M., Nicks, J., Stabile, T., Wu, J., Schlatter, W., and Hartmann, J. (2011a). “Geosynthetic Reinforced Soil Integrated Bridge System—Interim Implementation Guide.” Report No.FHWA-HRT-11-026, Federal Highway Administration, McLean, VA.
- Adams, M.T. (2008). “The Bridge of Defiance County,” *Geosynthetics*, 26(2), pp 14–16, 18, 20–21, Industrial Fabrics Association International, Roseville, MN.
- Adams, M.T., Lillis, C.P., Wu, J.T.H, and Ketchart, K. 2002. “Vegas Mini Pier Experiment and Postulate of Zero Volume Change.” Proceedings, Seventh International Conference on Geosynthetics, Nice, France, pp. 389-394
- Adams, M.T., Nicks, J.E., Stabile, T., Wu, J.T.H., Schlatter, W., and Hartmann, J. (2011b). “Geosynthetic Reinforced Soil Integrated Bridge System—Synthesis Report.” Report No.FHWA-HRT-11-027, Federal Highway Administration, McLean, VA.
- Adams, M.T., Schlatter, W., and Stabile, T. (2007). “Geosynthetic-Reinforced Soil Integrated Abutments at the Bowman Road Bridge in Defiance County, Ohio.” Proceedings, Geo-Denver 2007, American Society of Civil Engineers, Denver, CO.
- Berg, R., Christopher, B., and Samtani, N. 2009. “Design of Mechanically Stabilized Earth Walls and Reinforced Soil Slopes – Volume 1”. GEC-11, Report No. FHWA-NHI-10-024, National Highway Institute, Federal Highway Administration, Arlington, VA

Brinkgreve, R.B.J. (2011). "PLAXIS 2D 2010." Plaxis bv, Delft, Netherlands.

Duncan, J.M., Byrne, P., Wong, K.S. and Mabry, P. (1980). "Strength, stress-strain and bulk modulus parameters for finite element analysis of stress and movements in soil masses." UCB/GT/80-01, University of California, Berkeley, CA.

Geo-Institute, Committee on Shallow Foundations. (1999). "Shallow Foundations on Reinforced Soil", American Society of Civil Engineers, Reston, VA.

Hirata and Associates Inc. (2009). "Geotechnical Investigation Honoapilani Highway Realignment, Phase 1B-1 from Lahainaluna Road To Hokiokio Place Lahaina, Maui, Hawaii.

Johnson, A. (2011). "Recommendations for design and analysis of earth structures using geosynthetic reinforcements-EBGEO", München, Germany: Ernst & Sohn.

Kai Hawaii, Inc. (2011). Honoapilani Highway Realignment Phase 1B-1, Lahainaluna Road to Hokiokio Place. Original Design Drawings

Keller, G. R., & Devin, S. C. (2003). "Geosynthetic-reinforced soil bridge abutments". Transportation Research Record: Journal of the Transportation Research Board, 1819(1), 362-368.

KSF Inc. (2011). Honoapilani Highway Realignment Phase 1B-1, Lahainaluna Road to Hokiokio Place. Value Engineered Design Drawings.

Mirafi. (2014). "Mirafi PET70/70".

National Oceanic and Atmospheric Administration. (2013). <http://www.ncdc.noaa.gov/cdo-web/>. Accessed 2013.

NAVFAC, "Soil Mechanics Design Manual 7.01," Naval Facilities Engineering Command, Alexandria, VA, 1986

Opti-cal. (2014). <<http://www.surveyequipment.com>> Accessed December 2013.

Pham, T.Q. (2009). “Investigating Composite Behavior of Geosynthetic Reinforced Soil (GRS) Mass”. Ph.D. Thesis, University of Colorado, Denver.

Song, Y. (2009). “Testing and analysis of recycled materials”. Ph.D. Dissertation, University of Hawaii, Honolulu, HI.

Soong, T., Koerner, M. (1997) “On the Required Connection Strength of Geosynthetically Reinforced Walls” *Geotextiles and Geomembranes* 15, (4-6), pp. 377-393

Survey Control Services. (2014). <[sccsurvey.co.uk](http://sccsurvey.co.uk)> Accessed December 2013.

Tateyama, M., Murata, O., Watanabe, K., and Tatsuoka, F. (1994). “Geosynthetic-Reinforced Retaining Walls for Bullet Train Yard in Nagoya.” *Recent Case Histories of Permanent Geosynthetic- Reinforced Soil Retaining Wall* (Tatsuoka and Leshchinsky, editors) A. A. Balkema Publishers, Rotterdam, The Netherlands, pp. 141–150.

Tatsuoka, F., Uchimura, T., Tateyama, M., and Koseki, J. (1997). “Geosynthetic- Reinforcement Soil Retaining Walls as Important Permanent Structures.” *Mechanically Stabilized Backfill* (Wu, editor) A. A. Balkema Publishers, Rotterdam, The Netherlands, pp. 3–24.

Vennapusa, P., White, D., Klaiber, W., Wang, Shiyun. (2012). “Geosynthetic reinforced soil for low volume bridge abutments”. Ames, IA: Center for Earthworks Engineering Research, Iowa State University.

Warren, K., Schlatter, W., Adams, M., Stabile, T., and LeGrand, D. (2010) “Preliminary Results for a GRS Integrated Bridge System Supporting a Large Single Span Bridge”. *Earth Retention Conference 3*: pp. 612-619.

Werkmeister, S. “Permanent Deformation Behavior of Unbound Granular Materials in Pavement Constructions”. PhD dissertation. Dresden University of Technology, Germany, 2003.

Wu, J.T., Lee, K., Helwany, S., Ketchart, K. (2006). “Design and construction guidelines for geosynthetic-reinforced soil bridge abutments with a flexible facing”, NCHRP Report 556, Transportation Research Board, Washington, D.C.

Wu, J.T.H. (2007). "Lateral earth pressure against the facing of segmental GRS walls". Proc., Geosynthetics in Reinforcement and Hydraulic Application, Geo-Denver 2007: New Peaks in Geotechnics, American Society of Civil Engineers: 1-11.

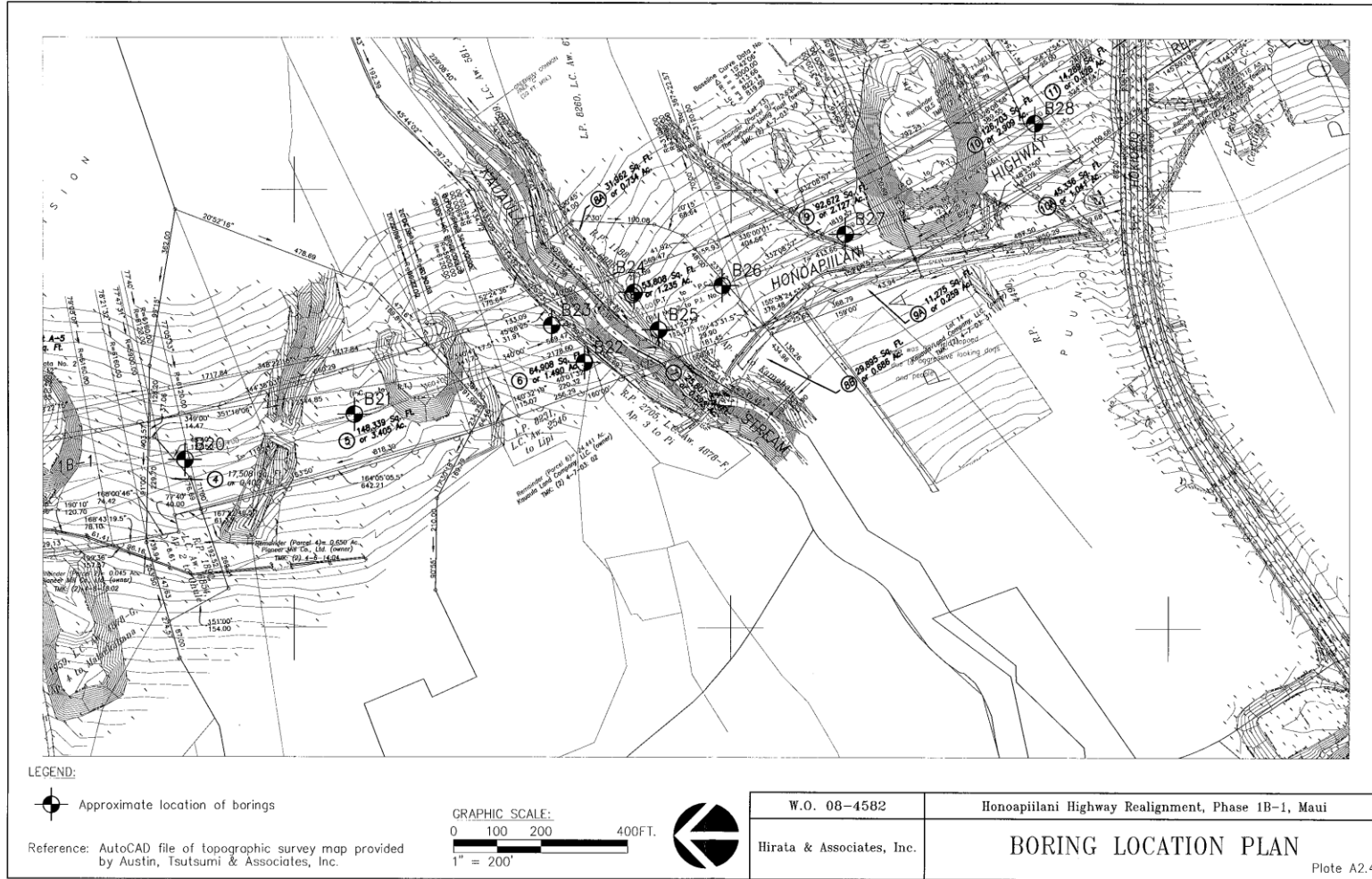
Wu, J.T.H. (1994). "Design and Construction of Low Cost Retaining Walls: The Next Generation in Technology." Report No. CTI-UCD-1-94, Colorado Transportation Institute, Denver, CO.

Wu, J.T.H. (2001). "Revising the AASHTO Guidelines for Design and Construction of GRS Walls, Report No. CDOT-DTD-R-2001-6". Colorado Department of Transportation, Denver, CO.

Wu, J.T.H. (2010). "Myths and facts on on design and construction of segmental GRS walls" Report CDOT-DTD-R-2001-6, Colorado Department of Transportation, 135 pages.

Wu, J.T.H., Pham, T.Q., and Adams, M.T. 2011. "Composite Behavior of a Geosynthetic Reinforced Soil (GRS) Mass. Report No. FHWA-HRT-10-077". Federal Highway Administration, McLean, VA.

**APPENDIX A: BORING LOGS (HIRATA AND ASSOCIATES, 2009)**





HIRATA & ASSOCIATES, INC.

BORING LOG

W.O. 08-4582

BORING NO. B22 DRIVING WT. 140 lb. START DATE 4/23/09  
 SURFACE ELEV. 116± DROP 30 in. END DATE 4/28/09

DEPTH	GRAPH	SAMPLE	BLOWS PER FOOT	DRY DENSITY (PCF)	MOIST. CONT. (%)	DESCRIPTION
0						Clayey SILT (ML) - Reddish brown, slightly moist, stiff, with sand and gravel. Boulder at one foot.
			19/6" 50/5"	95	6	
5			10/No Penetration			COBBLES AND BOULDERS - Mottled brown, dense to very dense, in a matrix of silt, sand, and gravel. (Older Alluvium) Begin HQ coring at 6 feet. 70% Recovery from 6 to 11 feet.
10						70% Recovery from 11 to 16 feet.
15			50/4" 10/No Penetration			88% Recovery from 16 to 21 feet.
20						72% Recovery from 21 to 26 feet.
25			10/No Penetration			88% Recovery from 26 to 31 feet.
30						COBBLES AND BOULDERS - Mottled brown, medium hard to hard, in a matrix of cemented silt, sand, and gravel. (Older Alluvium) Plate A4.31

HIRATA & ASSOCIATES, INC.

BORING LOG

W.O. 08-4582

BORING NO. B22 (Continued) DRIVING WT. 140 lb. START DATE 4/23/09  
 SURFACE ELEV. 116± DROP 30 in. END DATE 4/28/09

DEPTH	GRAPE	SAMPLE	BLOWS PER FOOT	DRY DENSITY (PCF)	MOIST. CONT. (%)	DESCRIPTION
30						35% Recovery from 31 to 36 feet.
35						100% Recovery from 36 to 41 feet.
40						COBBLES AND BOULDERS – Mottled brown, dense to very dense, in a matrix of silt, sand, and gravel. (Older Alluvium) 70% Recovery from 41 to 46 feet.
45						
50			10/No Penetration			COBBLES AND BOULDERS – Mottled brown, medium hard to hard, in a matrix of cemented silt, sand, and gravel. (Older Alluvium) 100% Recovery from 46 to 51 feet.
55						83% Recovery from 51 to 56 feet.
60		▲	90/10"		26	COBBLES AND BOULDERS – Mottled gray, dense to very dense, in a matrix of silt, sand, and gravel. (Older Alluvium) 70% Recovery from 56 to 61 feet.

Plate A4.32

HIRATA & ASSOCIATES, INC.

BORING LOG

W.O. 08-4582

BORING NO. B22 (Continued) DRIVING WT. 140 lb. START DATE 4/23/09  
 SURFACE ELEV. 116± DROP 30 in. END DATE 4/28/09

DEPTH	GRAPH	SAMPLE	BLOWS PER FOOT	DRY DENSITY (PCF)	MOIST. CONT. (%)	DESCRIPTION
60			10/No Penetration			
						End boring at 61 feet.
65						Neither groundwater nor seepage water encountered.
70						
75						
80						
85						
90						

Plate A4.33

HIRATA & ASSOCIATES, INC.

BORING LOG

W.O. 08-4582

BORING NO. B23 DRIVING WT. 140 lb. START DATE 4/14/09  
 SURFACE ELEV. 120± DROP 30 in. END DATE 4/16/09

DEPTH	GRAPH	SAMPLE	BLOWS PER FOOT	DRY DENSITY (PCF)	MOIST. CONT. (%)	DESCRIPTION
0						
		<input type="checkbox"/>	18	84	8	Clayey SILT (ML) – Reddish brown, slightly moist, medium stiff to stiff, with sand and gravel.
		<input type="checkbox"/>	15	105	9	
5		<input type="checkbox"/>	10/No Penetration			COBBLES AND BOULDERS – Mottled brown, dense to very dense, in a matrix of silt, sand, and gravel. (Older Alluvium) Begin HQ coring at 5.5 feet. 47% Recovery from 5.5 to 8 feet.  80% Recovery from 8 to 13 feet.  58% Recovery from 13 to 18 feet.  92% Recovery from 18 to 21 feet.  87% Recovery from 21 to 26 feet.
10						
15						
20						
25						
30						COBBLES AND BOULDERS – Mottled gray, medium hard to hard, in a matrix of cemented silt, sand, and gravel. (Older Alluvium) 90% Recovery from 26 to 31 feet.

Plate A4.34

HIRATA & ASSOCIATES, INC.

BORING LOG

W.O. 08-4582

BORING NO. B23 (Continued) DRIVING WT. 140 lb. START DATE 4/14/09  
 SURFACE ELEV. 120± DROP 30 in. END DATE 4/16/09

DEPTH TH	GRAPH	SAMPLE	BLOWS PER FOOT	DRY DENSITY (PCF)	MOIST. CONT. (%)	DESCRIPTION
30						90% Recovery from 31 to 36 feet.
35						100% Recovery from 36 to 41 feet.
40						100% Recovery from 41 to 46 feet.
45						100% Recovery from 46 to 51 feet.
50						100% Recovery from 51 to 56 feet.
55						100% Recovery from 56 to 61 feet.
60						

Plate A4.35

HIRATA & ASSOCIATES, INC.

BORING LOG

W.O. 08-4582

BORING NO. B23 (Continued) DRIVING WT. 140 lb. START DATE 4/14/09  
 SURFACE ELEV. 120± DROP 30 in. END DATE 4/16/09

DEPTH	GRAPH	SAMPLE	BLOWS PER FOOT	DRY DENSITY (PCF)	MOIST. CONT. (%)	DESCRIPTION
60						100% Recovery from 61 to 66 feet.
65						100% Recovery from 66 to 71 feet.
70						100% Recovery from 71 to 76 feet.
75						100% Recovery from 76 to 81 feet.
80						78% Recovery from 81 to 84 feet.
85						End boring at 84 feet.
90						Neither groundwater nor seepage water encountered.

Plate A4.36

BORING LOG

W.O. 08-4582

BORING NO. B24 DRIVING WT. 140 lb. START DATE 9/8/08  
 SURFACE ELEV. 116± DROP 30 in. END DATE 9/12/08

DEPTH	GRAPH	SAMPLE	BLOWS PER FOOT	DRY DENSITY (PCF)	MOIST. CONT. (%)	DESCRIPTION
0						Clayey SILT (ML) - Brown, moist, medium stiff, with sand and gravel.
1			10/No Penetration			COBBLES AND BOULDERS - Brown, dense to very dense, in a matrix of partially cemented silt, sand, and gravel. (Older Alluvium)  Begin NX coring at 9 feet. 77% Recovery from 9 to 14 feet.  60% Recovery from 14 to 19 feet.  95% Recovery from 19 to 24 feet.  77% Recovery from 24 to 29 feet.  83% Recovery from 29 to 32 feet.
5			10/No Penetration			
10			10/No Penetration			
15						
20						
25						
30						Plate A4.37

HIRATA & ASSOCIATES, INC.

BORING LOG

W.O. 08-4582

BORING NO. B24 (Continued) DRIVING WT. 140 lb. START DATE 9/8/08  
 SURFACE ELEV. 116± DROP 30 in. END DATE 9/12/08

DEPTH	GRAPH	SAMPLE	BLOWS PER FOOT	DRY DENSITY (PCF)	MOIST. CONT. (%)	DESCRIPTION
30						72% Recovery from 32 to 35 feet.
35						COBBLES AND BOULDERS - Mottled gray, medium hard to hard, in a matrix of cemented silt, sand, and gravel. (Older Alluvium) 78% Recovery from 35 to 40 feet.
40						COBBLES AND BOULDERS - Mottled brown, dense to very dense, in a matrix of silt, sand, and gravel. (Older Alluvium) 92% Recovery from 40 to 45 feet.
45						77% Recovery from 45 to 50 feet.
50						75% Recovery from 50 to 52 feet.
55						COBBLES AND BOULDERS - Mottled brown, medium hard to hard, in a matrix of cemented silt, sand, and gravel. (Older Alluvium) 97% Recovery from 52 to 55 feet.
60						95% Recovery from 55 to 60 feet.

Plate A4.38



HIRATA & ASSOCIATES, INC.

BORING LOG

W.O. 08-4582

BORING NO. B24 (Continued) DRIVING WT. 140 lb. START DATE 9/8/08  
 SURFACE ELEV. 116± DROP 30 in. END DATE 9/12/08

DEPTH	GRAPH	SAMPLE	BLOWS PER FOOT	DRY DENSITY (PCF)	MOIST. CONT. (%)	DESCRIPTION
60						100% Recovery from 60 to 65 feet.
65						100% Recovery from 65 to 70 feet.
70						100% Recovery from 70 to 75 feet.
75						100% Recovery from 75 to 80 feet.
80						COBBLES AND BOULDERS – Mottled brown, dense to very dense, in a matrix of silt, sand, and gravel. (Older Alluvium) 87% Recovery from 80 to 85 feet.
85						End boring at 85 feet.  Neither groundwater nor seepage water encountered.
90						Plate A4.39

HIRATA & ASSOCIATES, INC.

BORING LOG

W.O. 08-4582

BORING NO. B25 DRIVING WT. 140 lb. START DATE 5/11/09  
 SURFACE ELEV. 111± DROP 30 in. END DATE 5/13/09

DEPTH FOOT	GRAPH	SAMPLE	BLOWS PER FOOT	DRY DENSITY (PCF)	MOIST. CONT. (%)	DESCRIPTION
0						Clayey SILT (ML) - Reddish brown, slightly moist, stiff, with sand and gravel.
2			10/No Penetration			COBBLES AND BOULDERS - Mottled brown, dense to very dense, in a matrix of silt, sand, and gravel. Partially cemented from 2 to 10 feet, medium hard to hard. (Older Alluvium)
5						
10						Begin HQ coring at 9 feet. 70% Recovery from 9 to 14 feet.
15			12		31	
20						100% Recovery from 16 to 19 feet.  100% Recovery from 19 to 24 feet.
25			50/2"		10	92% Recovery from 24 to 29 feet.
30			50/3"		12	67% Recovery from 29 to 34 feet. Plate A4.40

HIRATA & ASSOCIATES, INC.

BORING LOG

W.O. 08-4582

BORING NO. B25 (Continued) DRIVING WT. 140 lb. START DATE 5/11/09  
 SURFACE ELEV. 111± DROP 30 in. END DATE 5/13/09

DEPTH	GRAPH	SAMPLE	BLOWS PER FOOT	DRY DENSITY (PCF)	MOIST. CONT. (%)	DESCRIPTION	
30							
35						58% Recovery from 34 to 39 feet.	
40			10/No Penetration			92% Recovery from 39 to 44 feet.	
45						70% Recovery from 44 to 49 feet.	
50			25/6" 10/No Penetration		21	83% Recovery from 50 to 54 feet.	
55						83% Recovery from 54 to 59 feet.	
60				10/No Penetration			
						COBBLES AND BOULDERS - Brown, medium hard to hard, in a matrix of cemented silt, sand, and gravel. (Older Alluvium) Plate A4.41	

HIRATA & ASSOCIATES, INC.

BORING LOG

W.O. 08-4582

BORING NO. B25 (Continued) DRIVING WT. 140 lb. START DATE 5/11/09  
 SURFACE ELEV. 111± DROP 30 in. END DATE 5/13/09

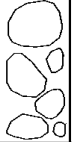
DEPTH	GRAPH	SAMPLE	BLOWS PER FOOT	DRY DENSITY (PCF)	MOIST. CONT. (%)	DESCRIPTION
60						100% Recovery from 59 to 64 feet.
65						End boring at 64 feet.  Neither groundwater nor seepage water encountered.
70						
75						
80						
85						
90						

Plate A4.42

## APPENDIX B: TECHNICAL SHEET (MIRAFI, 2014)



TENCATE GEOSYNTHETICS  
Americas

# Mirafi<sup>®</sup> PET70/70



Mirafi<sup>®</sup> PET70/70 geotextile is composed of high tenacity polyester multifilament yarns which are woven into a stable network such that the yarns retain their relative position. Mirafi<sup>®</sup> PET70/70 geotextile is inert to biological degradation and resistant to naturally encountered chemicals, alkalis, and acids.

TenCate Geosynthetics Americas is accredited by a2La (The American Association for Laboratory Accreditation) and Geosynthetic Accreditation Institute – Laboratory Accreditation Program (GAI-LAP).

Mechanical Properties	Test Method	Unit	Minimum Average Roll Value	
			MD	CD
Tensile Strength (at ultimate)	ASTM D4595	lbs/ft (kN/m)	4800 (70.0)	4800 (70.0)
Tensile Strength (at 5% strain)	ASTM D4595	lbs/ft (kN/m)	1080 (15.8)	2400 (35.0)
Tensile Strength (at 10% strain)	ASTM D4595	lbs/ft (kN/m)	3360 (49.0)	4800 (70.0)
Creep Reduced Strength	ASTM D5262	lbs/ft (kN/m)	2880 (42.0)	
Long Term Design Strength <sup>1,2</sup>	GRI GT-7	lbs/ft (kN/m)	2280 (33.2)	
Factory Sewn Seam	ASTM D4884	lbs/ft (kN/m)	2400 (35.0)	
Permittivity	ASTM D4491	sec <sup>-1</sup>	0.10	
Apparent Opening Size (AOS) <sup>3</sup>	ASTM D4751	U.S. Sieve (mm)	40 (0.43)	
UV Resistance (at 250 hours)	ASTM D4355	% strength retained	50	

<sup>1</sup> Machine Direction

<sup>2</sup> Long Term Allowable Design values are for sand, silt and clay

<sup>3</sup> ASTM D4751: AOS is a Maximum Opening Diameter Value

Note: To obtain Secant Modulus, divide tensile strength by the appropriate strain level (i.e. Secant Modulus at 5% = 1080/0.05=21,600 lb/ft)

Physical Properties	Unit	Typical Value
Roll Dimensions (width x length)	ft (m)	15 x 300 (4.5 x 91.5)
Roll Area	yd <sup>2</sup> (m <sup>2</sup> )	500 (418)
Estimated Roll Weight	lb (kg)	234 (107)

© 2013 TenCate Geosynthetics Americas  
Mirafi<sup>®</sup> is a registered trademark of Nicolon Corporation

**Disclaimer:** TenCate assumes no liability for the accuracy or completeness of this information or for the ultimate use by the purchaser. TenCate disclaims any and all express, implied, or statutory standards, warranties or guarantees, including without limitation any implied warranty as to merchantability or fitness for a particular purpose or arising from a course of dealing or usage of trade as to any equipment, materials, or information furnished herewith. This document should not be construed as engineering advice.

Creep Reduced Strength (ASTM D5262), Long Term Design Strength (GRI GT-7), Factory Sewn Seam (ASTM D4884) and UV Resistance (ASTM D4355) are not covered by our current A2LA accreditation.



365 South Holland Drive  
Pendergrass, GA 30567

Tel 706 693 2226  
Tel 888 795 0808

Fax 706 693 4400  
[www.tencate.com](http://www.tencate.com)



GAI-LAP-25-97

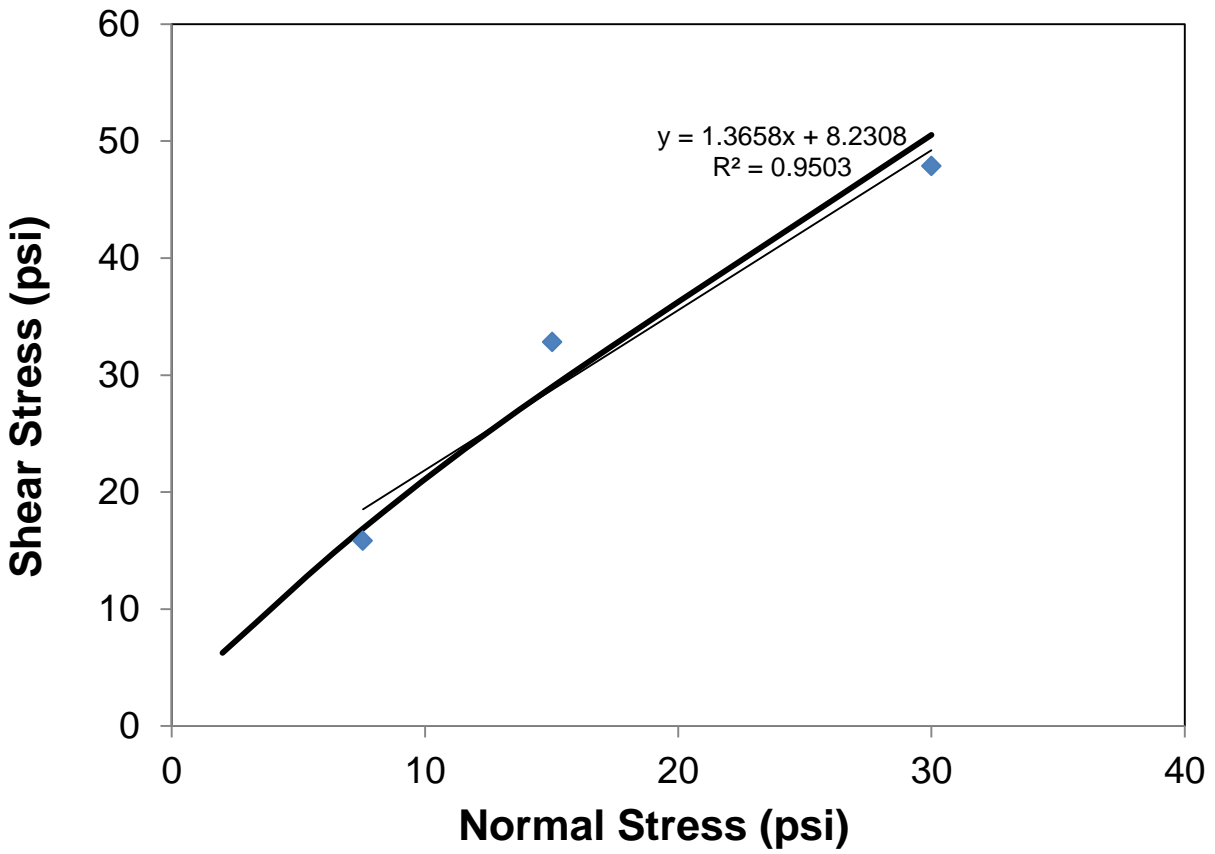


Testing Lab 1291.01 & 1291.02

FGS000035  
ETQR8

## APPENDIX C: SAMPLE CALCULATIONS

### Fill Properties



$$\phi = \tan^{-1}1.3658$$

$$\phi = 53.8$$

$$c = 8.23 \text{ psi} = 1,185 \text{ psf}$$

### CMU Block

$$V = 7.625 \times 11.625 \times 15.625 = 1,385 \text{ in}^3 = 0.80 \text{ ft}^3$$

$$W = 75 \text{ lb}$$

$$\gamma = \frac{W}{V} = \underline{93.5 \text{ pcf}}$$

### Footing

$$\begin{aligned} E \text{ (in psi)} &= 57,000\sqrt{f_c} \\ &= 57,000\sqrt{5000 \text{ psi}} \\ &= 4,030,509 \text{ psi} \\ &= \underline{580400000 \text{ psf}} \end{aligned}$$

### Geotextile

$$\begin{aligned} EA &= \frac{T}{\varepsilon} \\ &= \frac{2,400}{0.05} \\ &= \underline{48,000 \text{ lbf/ft}} \end{aligned}$$